CBPF

Centro Brasileiro de Pesquisas Físicas

Measurement of $\nu_\mu/\bar{\nu}_\mu$CC double-differential cross sections on MINERvA hydrocarbon target for the shallow inelastic scattering background region

Daniel Souza Correia

Advisor: Dr. Hélio da Motta

Thesis submitted to Centro Brasileiro de Pesquisas Físicas in partial fullfilment for the degree of Doctor of Science.

Rio de Janeiro
March, 2026

CBPF Centro Brasileiro de Pesquisas Físicas

MINISTÉRIO DA CIÊNCIA, TECNOLOGIA E INOVAÇÃO

GOVERNO FEDERAL BRASIL UNIÃO E RECONSTRUÇÃO

"Measurement of v_μ/v̄_μ CC double-differential cross sections on MINERvA hydrocarbon target for the shallow inelastic scattering background region"

DANIEL SOUZA CORREIA

Tese de Doutorado em Física apresentada no Centro Brasileiro de Pesquisas Físicas do Ministério da Ciência Tecnologia e Inovação. Fazendo parte da banca examinadora os seguintes professores:

Hélio da Motta Filho - Orientador/CBPF

Jonathan Paley – FERMILAB

gov.br Documento assinado digitalmente
LAURA PAULUCCI MARINHO
Data: 30/03/2026 11:15:50-0300
Verifique em https://validar.iti.gov.br

Laura Paulucci Marinho - ITA

Vittorio Paolone – U. OF PITTSBURGH/USA

José Abdalla Helayël-Neto - CBPF

Rio de Janeiro, 25 de março de 2026.

Abstract

Cross section measurements are essential for all neutrino oscillation experiments. In fact, uncertainties associated to cross section model parameters constitute one of the dominant sources of errors in current oscillation analyses. In particular, understanding neutrino-induced pion production in the kinematic regime known as shallow inelastic scattering (SIS) is critical for improving neutrino interaction modeling in event generators. In this study, 416,233 (237,468) muon neutrino (antineutrino) interactions are measured in a SIS background region, predominantly made of baryon resonances. The analyzed datasets were collected from 2013 to 2019, comprising neutrinos generated by the Fermilab NuMI facility, with mean energy of 6 GeV, and the interactions occurred on the MINERvA hydrocarbon target. The measurements are presented as double-differential cross sections in terms of the outgoing muon longitudinal and transverse momentum components, as well as the Bjorken x and y variables. Comparisons between the extracted data and predictions from several generators reveal significant discrepancies across most kinematic bins.

Keywords: Particle Physics. Neutrinos. MINERvA.

Dedicated to my family.

Será possível conhecer todo o universo? Meu Deus, achar o caminho no bairro já é difícil.

- Woody Allen

Acknowledgements

I would like to thank my advisor, Hélio da Motta-Filho, for accepting me as his student, for his guidance and advice, and for granting me the privilege of coming to Fermilab.

To Dr. Adrian Lozanos, muchas gracias por su asistencia en mi análisis y por su amistad.

To all MINERvA collaborators who made the experiment possible, I am sincerely grateful. In particular, I would like to thank Jorge Morfín for his longstanding support of the Latin American community; Abbey Waldron and Rik Gran (MINERvA co-spokes), Jeff Nelson and Minerba Betancourt for their physics insights, which greatly benefited this analysis.

I thank Profs. Ana Machado and Ettore Segreto for hosting me at Unicamp during part of my hardware work, and the Engineer Cézar, who patiently trained me to operate the liquid argon purification system (without destroying it).

A special thanks goes to Jon Paley, whose support made my research at Fermilab possible, and also Leo Bellatoni for his contributions.

I would like to thank Profs. Helayël and Tião for the amazing lectures on electroweak theories and QCD, and to all CBPF staff, in particular Sônia, Taíssa, Bete, and Larissa.

To the friends from all over the world whom I met in the Fermilab Village, thank you for the meals we shared and for the cultural exchanges – I hope our paths cross again someday.

Finally, a few words to those who, despite the distance, have stood by me for more than a decade since I left my hometown: my family. Obrigado pelo apoio durante todos esses anos. O incentivo de vocês foi essencial para que eu pudesse completar essa (longa) jornada.

I would like to thank Coordenação de Aperfeiçoamento de Pessoal de Nível Superior (CAPES) for the PhD scholarship.

List of Publications

During my PhD, apart from my analysis presented in this thesis, I had the opportunity to contribute to liquid argon neutrino detector development, which resulted in the following publications:

- D. Cardoso *et al.*, "Innovative proposal for N_2 capturing in liquid argon using the Li-FAU molecular sieve," J. Instrum. **19**, C08001 (2024);
- P. Bianchi Neto *et al.*, "Exploring N_2 capturing in liquid argon using Li-FAU mol sieve in the ICEBERG cryostat," J. Instrum. **20**, C06045 (2025).

The following papers are associated with the content of this thesis:

- A. Lozano *et al.* (MINERvA Collaboration), "Measurement of charged-current ν_μ and $\bar{\nu}_\mu$ cross sections on hydrocarbon in a shallow inelastic scattering region," arXiv:2503.20043 [hep-ex] (2025);
- J. Kleykamp *et al.* (MINERvA Collaboration), "Measurement of the A dependence of the muon neutrino charged-current quasielastic-like cross section as a function of muon and proton kinematics at $\langle E_\nu \rangle \sim 6$ GeV," arXiv:2503.15047 [hep-ex] (2025);
- A. S. Meyer *et al.* (MINERvA Collaboration), "The nucleon axial form factor from elementary target data," arXiv:2512.14097 [hep-ex] (2025).

List of abbreviations and acronyms

AMU DIS	Aligarh Muslim University Deep Inelastic Scattering interaction model
DIS	Deep Inelastic Scattering interaction channel
CC	Charged Current
FSI	Final State Interactions
GEANT4	GEometry ANd Tracking
GENIE	Generates Events for Neutrino Interaction Experiments
MINERvA	Main Injector Neutrino ExpeRiment to study v-A interactions
MINOS	Main Injector Neutrino Oscillation Search
NC	Neutral Current
NuMI	Neutrinos at the Main Injector
NR1π	Non-resonant single-pion production
PPFX	Package to Predict the FluX
QE	Quasi-Elastic interaction channel
QH	Quark-Hadron duality
RES	Resonant pion production interaction channel
RPA	Random Phase Approximation
2p2h	Two-particle Two-hole
SIS	Shallow Inelastic Scattering

Contents

List of Figures

List of Tables

1 Introduction

Neutrinos are, after photons, the most abundant particles in the Universe: roughly 60 billion of them pass through every square centimeter of the Earth surface each second [1]. Proposed theoretically in 1930 by W. Pauli as a solution to the problem of energy conservation in β-decay, neutrinos were observed experimentally for the first time more than 20 years later, at the Savannah River nuclear reactor in South Carolina (EUA) [2, 3]. According to the Standard Model of particle physics, neutrinos are described as spin-$1/2$ fermions with zero electric charge and are assumed to be massless. They occur in three flavors, each associated with a charged lepton: the electron, muon, and tau [4].

From the late 1960s, several independent observations confirmed that neutrinos undergo oscillations: after traveling a certain distance, a neutrino produced in one flavor state can be detected as another (for example, a muon neutrino transforming into an electron neutrino) [5–7]. These measurements provided compelling evidence that neutrinos have non-zero masses, and opened a new frontier in particle physics. Despite significant progress in recent years [7–13], neutrinos remain among the most mysterious particles in nature. Fundamental questions are still open: what mechanism gives rise to their tiny masses compared to those of other elementary particles? Which of the three neutrino mass eigenstates is the heaviest? Is charge–parity symmetry violated in the leptonic sector?

To address these questions, precise measurements of neutrino cross sections are crucial, as they constitute one of the dominant sources of systematic uncertainty in oscillation experiments [14, 15]. In fact, neutrino event generators are not able to reproduce measurements across the full kinematic range, with final-state interactions (secondary re-scatterings following the primary interaction; see Sec. 2.4), remaining poorly understood [16]. In particular, the modeling of pions $-$ the same particle that C. M. G. Lattes contributed to discover in the 1940s [17, 18] $-$, produced in the so-called shallow inelastic scattering (SIS) region, has received minimal attention.

SIS is defined as a kinematic regime above the $\Delta(1232)$ resonance and below the onset of deep inelastic scattering (DIS) processes [19, 20]. This transition region comprises an overlap of different processes, including a Δ and higher baryonic resonances background, non-resonant and multi-quark interactions. Historically, the neutrino community has primarily focused on meson (typically pion or kaon) production through the Δ resonance, while the SIS region has been the least explored [21–25]. Despite its complexity and the challenges of modeling multiple contributing effects simultaneously, two approaches can be taken to describe the physics of SIS: the first possibility is through the concept of quark-hadron duality; and the other is by explicitly considering non-perturbative quantum chromo dynamics (QCD) contributions [26, 27]. Studying interactions in this kinematic regime is highly relevant, as it has a direct impact on current neutrino event simulations and future oscillation experiments.

This thesis reports measurements of double-differential neutrino cross sections in a SIS region dominated by resonances background. The primary goal of this work is to provide experimental inputs to improve neutrino interaction model simulations. The measurements are performed for both muon neutrinos and antineutrinos using the MINERvA data, which have mean energy of around 6 GeV, generated by the NuMI beam, and interacting on the MINERvA hydrocarbon target. The results are presented as a function of the Bjorken variables x and y, as well as the parallel and transverse components of the outgoing muon momentum, measured with both the MINERvA and MINOS near detector.

The thesis is organized as follows. Chap. 2 reviews the main neutrino-nucleus interaction mechanisms in the few-GeV energy regime. Chap. 3 defines the SIS region and discusses its physics aspects and implications. Chap. 4 describes the MINERvA experiment. Chap. 5 and 6 detail the cross section extraction procedure and the systematic uncertainties associated to the measurements, respectively. Chap. 7 presents and discusses the final results. Finally, the thesis concludes in Chap. 8 with the conclusions and future perspectives. In Append. A, the extracted data cross sections are used to test other models; Append. B presents background constraint results; Append. C shows the uncertainties on the data cross sections; and Append. D outlines the main results regarding a hardware work on liquid argon detectors.

<u>Remarks & Conventions</u>:

- ♢ Throughout the document natural units are adopted (*i.e.*, $\hbar = c = 1$).

2 Neutrino-nucleus interactions

This chapter provides the theoretical foundation for performing and interpreting neutrino cross section analyses. Sec. 2.1 summarizes the mechanisms through which neutrinos interact within the Standard Model. In Sec. 2.2, the primary interaction channels relevant for neutrino-nucleus scattering in the intermediate energy regime (0.1–20 GeV) are introduced. Nuclear medium effects that modify these interactions, including final-state interactions, are discussed in Sec. 2.3. Finally, Sec. 2.5 defines the kinematic variables used in this analysis. A more extensive and comprehensive discussion of these topics can be found in [4, 28].

2.1 Neutrinos in the Standard Model

In the Standard Model, neutrinos and their interactions are described by the Glashow-Salam-Weinberg model [29–31]. Based on theoretical arguments and experimental evidences, they propose the existence of four massless gauge-invariant particles as mediators of the electroweak interaction. These mediators are denoted by $W_\mu^{(1)}, W_\mu^{(2)}, W_\mu^{(3)}$ and A_μ, with $\mu = 0, 1, 2, 3$, and have as mathematical basis the $\mathsf{SU_L}(2) \bigotimes \mathsf{U_Y}(1)$ symmetry group.

The interaction with the Higgs field provides mass to three of them, $W_\mu^{(+)}$, $W_\mu^{(-)}$, and Z_μ^0, leaving the photon, A_μ, massless. After the spontaneous symmetry breaking, the relevant part of the Lagrangian coupling the $W_\mu^{(\pm)}$ e Z_μ^0 bosons and leptons is written as

$$\mathcal{L} = \sum_{\alpha=e,\mu,\tau} \left[\overline{\nu}_{\alpha,L} i\gamma^\mu \partial_\mu \nu_{\alpha,L} + \frac{g_w}{\sqrt{2}} \Big(\overline{\nu}_{\alpha,L} \gamma^\mu l_{\alpha,L} W_\mu^{(+)} + h.c. \Big) + \frac{g_w}{2\cos\theta_w} \overline{\nu}_{\alpha,L} \gamma^\mu \nu_{\alpha,L} Z_\mu^0 \right]. \quad (2.1)$$

Eq. 2.1 describes how neutrinos interact with matter via the weak force: l_α denotes charged leptons ($\alpha =$ electron, muon e tau), and ν_α ($\overline{\nu}_\alpha$) are their associated neutrinos (antineutrinos). Because neutrinos produced in weak interactions are always left-handed [32], then only left-handed leptons components appear in this equation.

In Eq. 2.1, the first term is a kinetic term describing the free propagation of neutrinos; the second term is the charged-current (CC) vertex, where lepton flavors switch within the same family by exchanging a $W^{(\pm)}$ boson; the third term is the neutral-current (NC) vertex, whose Z^0 exchanging produces no lepton flavor shift; g_w is the weak isospin gauge coupling constant; θ_w is called as the Weinberg angle, one of the fundamental parameters of the Standard Model.

Moreover, notice that there is no mass term in this Lagrangian because in the Standard Model neutrinos are assumed massless (Majorana or Dirac mass terms require extending the model). Neutrino–nucleus scattering processes, discussed in Sec. 2.2, are derived by combining these interaction terms with the quark content of nucleons, which are described by the quantum chromodynamic SU(3) group. The CC and NC processes are illustrated in Fig. 1 by their Feynman diagrams.

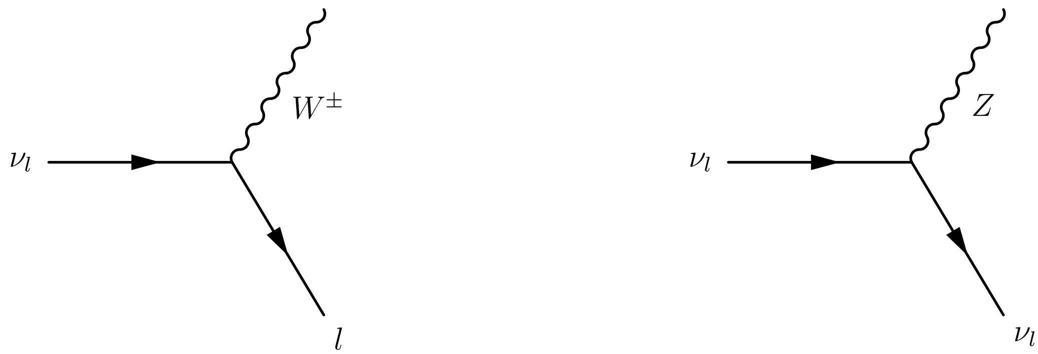

Figure 1 – Feynman diagrams illustrating neutrino interactions via the weak force. The left figure shows charged-current processes, while the right figure shows neutral-current processes.

2.2 Neutrino-nucleon scattering mechanisms

Over the years, the neutrino physics community has identified a broad range of mechanisms through which neutrinos interact with matter. Given the extension and complexity of these processes, the discussion in this section is divided into three parts and limited to those most relevant for this cross section analysis (only charged-current processes are considered), namely:

i) Primary neutrino-nucleon interactions,

ii) Nuclear medium effects,

iii) Final-state interactions.

The focus of this section is to introduce the main features of neutrino–nucleon scattering in the 0.1–20 GeV energy range. In this regime, neutrino cross sections are understood to be dominated by three primary interaction channels: quasi-elastic scattering, resonant meson production, and deep inelastic scattering, each discussed below. Nuclear medium effects and the final-state interactions that may follow these primary interactions are introduced in the next section.

2.2.1 Quasielastic scattering

Charged-current quasielastic (CCQE) scattering is the predominant process for neutrino energies in the sub-GeV region (~ 1 GeV). In CCQE interactions, a neutrino (antineutrino) scatters off a neutron (proton) target inside the nucleus, producing a charged lepton, one proton (neutron) and no pions in the final state[1], as described by Eq. 2.2. Fig. 2 illustrates the corresponding Feynman diagram for the process.

$$\nu_l + n \to l^- + p, \qquad \bar{\nu}_l + p \to l^+ + n. \tag{2.2}$$

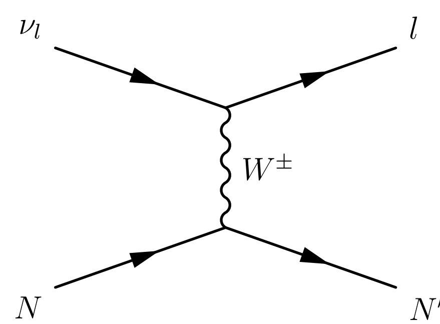

Figure 2 – Feynman diagram for the charged-current quasielastic scattering.

Historically, the investigations of CCQE scatterings started in the 1970s and 1980s using bubble chambers filled with hydrogen and deuterium to explore the vector-axial nature of the weak interaction, and to determine the axial vector form factor of the nucleon. Key references on these earlier measurements are [39–41].

Despite neutrinos communicate with quarks through the exchange of a $W^\pm$ boson, protons and neutrons are usually used as effective degrees of freedom, and the theoretical description of the process is given in terms of fundamental ingredients known as (nucleon) axial and vector form factors, which generally depend on the squared of four-momentum transfer, Q^2.

Although well-motivated alternatives exist [42, 43], the convention for the axial form factor is to use the Llewellyn Smith dipole form *ansatz* [33], given by Eq. 2.3. In this equation, $g_\mathsf{A} = \mathsf{F_A}(\mathsf{Q}^2 = 0) = 1.2723(23)$ is the axial coupling constant, determined by neutron beta decay [44], and $\mathsf{M_A}$ is the axial mass, the only remaining free parameter, measured from fits to neutrino-deuterium scattering [39]. GENIE nominal values and vector form factor parameterization are listed in Tab. 3.

$$\mathsf{F_A}(\mathsf{Q}^2) = \frac{g_\mathsf{A}}{(1 + \mathsf{Q}^2/\mathsf{M}_\mathsf{A}^2)^2}. \tag{2.3}$$

2.2.2 Resonant pion production

Given enough energy, the struck nucleon may transition into excited baryonic states (resonances), generally represented by N*. At low hadronic invariant mass, W, defined in Eq. 2.11c, the $\Delta(1232)$

[1] Historically, CCQE interactions were defined assuming scattering from a free or stationary bound nucleon [33, 34]. With the advent of high-statistics measurements, it was shown that nuclear effects such as Fermi motion, multinucleon interactions, and final-state interactions – discussed in Sec. 2.3 – play a significant role and must be included for precise neutrino energy reconstruction. Recent works have investigated nuclear medium effects using transverse (to the neutrino beam) kinematic variables [35–38].

resonance gives the largest contribution. As W increases, higher-mass resonances, such as N*(1440), N*(1535) and N*(1520), start to become relevant.

In their way back to the ground state, these resonances emit mesons, which are typically pions or kaons. Among these final states, particular attention has been given to single-pion production, as it constitutes one of the main backgrounds in oscillation analyses (see Sec. 3.4). Eq. 2.4 describes the single-pion production via Δ, and Eq. 2.5 lists some important channels; Fig. 3 illustrates the corresponding Feynman diagram.

$$\nu_l + N \rightarrow l + \Delta \rightarrow l + N + \pi. \tag{2.4}$$

$$\begin{aligned} &\nu_l p \rightarrow l^- p\pi^+, && \bar{\nu}_l p \rightarrow l^+ p\pi^-, \\ &\nu_l n \rightarrow l^- p\pi^0, && \bar{\nu}_l p \rightarrow l^+ n\pi^0, \\ &\nu_l n \rightarrow l^- n\pi^+, && \bar{\nu}_l n \rightarrow l^+ n\pi^-. \end{aligned} \tag{2.5}$$

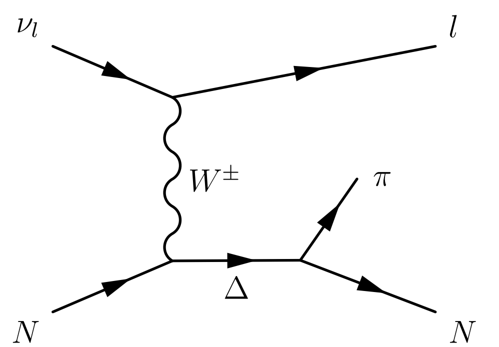

Figure 3 – Feynman diagram for single-pion production via $\Delta(1232)$ resonance.

The cross section model widely used to simulate neutrino interactions in the resonance region is due to Rein and Sehgal, from 1981 [45]. In this model, the authors derive 18 resonances up to W $= 2.0$ GeV, assuming that the outgoing lepton is massless. The fundamental ingredients of the theory are the vector and axial vector form factors, and, similarly to QE scatterings, they are parameterized assuming a dipole form (Eq. 2.3). GENIE conventions to simulating resonant pion production are listed in Tab. 3.

2.2.3 Non-resonant pion production

Non-resonant interactions are another source of pions. These processes are at the center of this analysis, and detailed discussion in presented in Chap. 3. Differently from resonant production, in these reactions pions emerge directly from weak interaction amplitudes, without forming an intermediate baryon resonance, as described by Eq. 2.6.

$$\nu_l + N \rightarrow l + N' + \pi. \tag{2.6}$$

Attempts to model such interactions involve, for instance, Born graphs, shown in Fig. 4. Recent works have explicitly derived non-resonant contributions to the neutrino cross section − see Refs. [46, 47] −, however, despite the efforts toward a theoretically-motivated treatment, the models are either valid in a limited kinematic regime or needs empirical adjustment to match the data. Alternative approaches to describe non-resonant interactions, such as quark-hadron duality and non-perturbative QCD effects, exist and are discussed in Sec. 3.2.

Another intrinsic difficulty in this kinematic regime is that resonant and non-resonant single-pion production lead to identical final states and interfere at the amplitude level. Moreover, given the overlap of processes, their experimental separation is effectively impossible. All these limitations force event generators to use external hadronic and bubble-chamber data to tune non-resonant contributions (see Sec. 3.3).

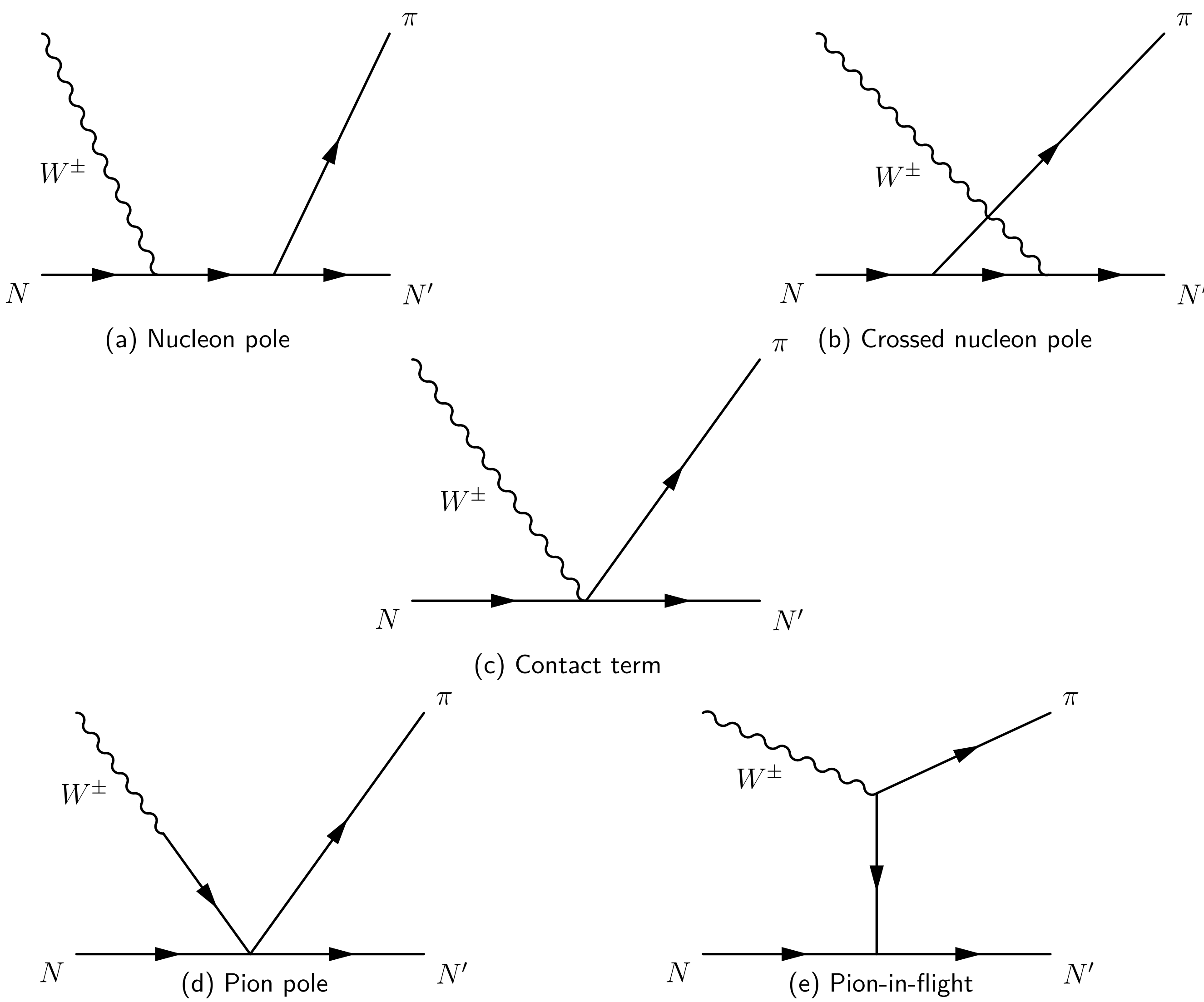

Figure 4 – Non-resonant single-pion production mechanisms: nucleon pole, crossed nucleon pole, contact term, pion pole, and pion-in-flight contributions.

Although their sub-leading contribution to the total SIS cross section (< 3 %), other mechanisms, such as coherent and diffractive processes, can also produce pions; they are discussed in Sub-sec. 2.2.5.

2.2.4 Deep inelastic scattering

At even higher energies, neutrinos start to resolve the internal structure of the nucleon and can scatter directly off quarks. This process is known as deep inelastic scattering (DIS). DIS reactions are described by Eq. 2.7 and represented by the Feynman diagram in Fig. 5. The signature of these events in the detector are a hadronic shower (charged or neutral pions, kaons, protons and neutrons), and a lepton in the final state.

$$\nu_l + N \to l^- + X, \qquad \bar{\nu}_l + N \to l^+ + X. \tag{2.7}$$

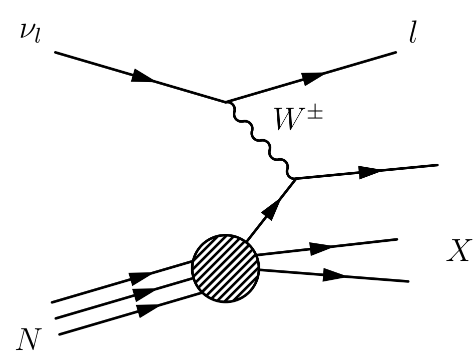

Figure 5 – Feynman diagram for the deep inelastic scattering channel.

The cross section formula for DIS processes are generally written in terms of three structure function $F_{1,2,3}(x, y)$, which describe the quark distribution of the struck nucleon $-$ x and y are Lorentz-invariant parameters called as Bjorken variables, and defined in Sec. 2.5. Complementary to electromagnetic interactions, which require only two structure functions, $F_{1,2}$, the use of neutrino and antineutrino data allows extracting F_3, a structure function describing the valence quark content due to $W^{\pm}$ axial-vector coupling. The structure functions implemented in GENIE are derived by Bodek and Yang [48], and details of the simulation listed in Tab. 3.

2.2.5 Other interactions

The list of neutrino interactions is not limited to the ones presented above. In fact, other processes occur at intermediate energies, although their contribution to the total cross section is minimum. It is worth mentioning two possible additional scenarios neutrinos can be involved in, and that are eventually considered in simulations: coherent and diffractive single-pion productions.

In the first case, neutrinos scatter off the entire nucleus, transferring negligible energy to it. As the target remains in the ground state, the observed final state does not contain a nuclear recoil; only the usual lepton and a forwarded-scattered pion appear in the detector. Such a reaction is described by Eq. 2.8, and the corresponding Feynman diagram is shown on the left side of Fig. 6.

Similarly, if neutrinos scatter off a free proton producing a lepton and a single pion in the final state, then the interaction is said to be diffractive. Compared to the coherent scattering, because the proton mass is less than the whole nucleus, in this process the proton does recoil, which is observed by energy depositions in the detector. The diffractive single pion production is described by Eq. 2.9, and its cross section calculated by using the Feynman diagram on the right side of Fig. 6.

$$\nu_l A \rightarrow l^- \pi^+ A, \qquad \bar{\nu}_l A \rightarrow l^+ \pi^- A. \tag{2.8}$$

$$\nu_l p \rightarrow l^- \pi^+ p, \qquad \bar{\nu}_l p \rightarrow l^+ \pi^- p. \tag{2.9}$$

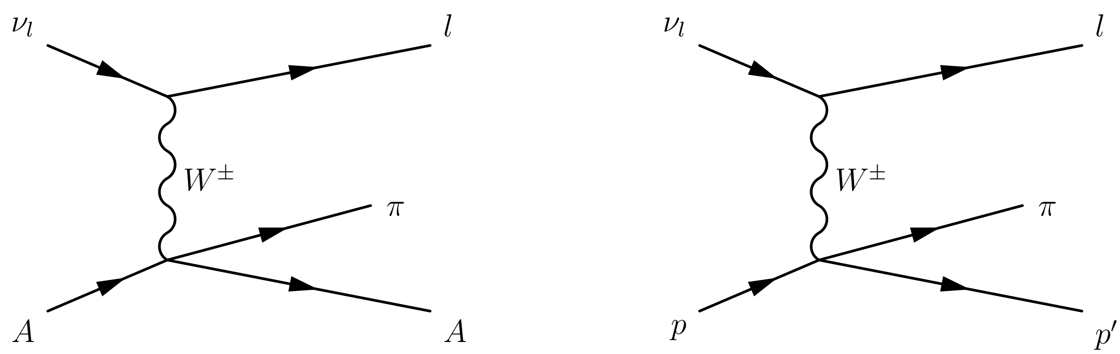

(a) Coherent single pion production.

(b) Diffractive single pion production.

Figure 6 – Feynman diagrams for coherent and diffractive charged-current single pion production.

2.3 Nuclear medium effects

2.3.1 Initial state of nucleons

Nucleons are individually described by a relativistic Fermi gas model [49]. The key aspects of this model are

1. Nucleons are described as quantum states inside a potential well with walls coinciding with the nuclear radius, and they must obey the Pauli exclusion principle;

2. Before the interaction with the incident neutrino, a nucleon has an initial momentum distribution from 0-250 MeV (Fig. 7); and

3. To be ejected from the nucleus, nucleons must have momenta greater than 250 MeV, which means that neutrino-nucleus interactions with low four-momentum transfer are suppressed.

The relativistic Fermi gas does not describe interactions between nucleons, which can carry momenta above the typical Fermi momentum cutoff of approximately 250 MeV. To account for this, Bodek and Ritchie introduced a high-momentum tail to the nucleon momentum distribution to describe multi-nucleon correlations [50] (see Fig. 7).

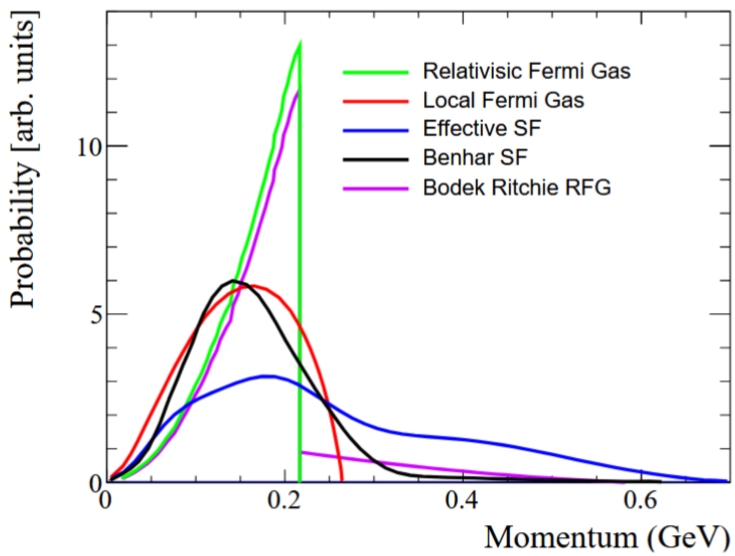

Figure 7 – Nucleon momentum distributions in a ^{12}C nucleus for several initial nucleon state models. Figure reproduced from [51].

2.3.2 Random phase approximation and two-particle-two-hole

In 2010, the MiniBooNE Collaboration showed that, at lower four-momentum transfer, the relativistic Fermi gas description of nucleons as being a collection of non-interacting fermions no longer holds, and nucleon-nucleon correlations must be considered [34]. Two models are used to describe these correlations: random phase approximation (RPA) and two-particle-two-hole (2p2h).

The RPA model predicts how the whole nucleus responds collectively when a neutrino exchanges a $W^{\pm}$ or Z boson with a nucleon [52]. Analogous to how an electric field induces polarization in a dielectric medium – reducing the effective field seen by an electron –, the nuclear medium can "polarize" in response to the weak current: nucleons move to oppose or enhance the external field. As a result, the electroweak coupling appears weakened (screened) at low momentum transfer because the nucleus "rearranges" itself to partially cancel the effect of the probe.

In the 2p2h model, neutrinos interact with a correlated pair of nucleons, which in turn interact with each other via meson-exchange currents (usually a pion) [53]. Given enough momentum transfer, the two nucleons can be ejected from the nucleus and two holes in the Fermi sea are created. The 2p2h contributions to the total cross section were first shown experimentally by MINERvA in 2016, and later incorporated in newer versions of GENIE [54]. Refer to Sub-sec. 4.4.4 to see the performance of these models in describing the data.

2.4 Final-state interactions

The neutrino interactions with one or more nucleons via weak force, discussed in the last two sections, lead to hadrons production inside the nuclear environment. Before being observed in the detector, these hadrons may interact with other hadrons via strong force on their way out of the nucleus. These secondary scatterings are called as final-state interactions, and are responsible for modifying both the kinematics and type of measured particles [27]. The modeling of these processes is quite challenging, and thus constitutes one of the major efforts in the neutrino community.

Four mechanisms have been identified in which hadrons, produced in the primary interaction, may undergo: elastic and inelastic re-scattering, absorption and charge exchange. According to estimates, the probability of pions produced via Δ-resonance re-interact is $\sim$ 75 % on carbon and $\sim$ 80 % on argon; for protons it is about $\sim$ 40-50 % [55]. For this reason, pions are used as a probe to investigate final-state interaction effects. Fig. 8 illustrates the aforementioned four processes. Several models have been proposed to simulate these re-interactions [56]. In particular, the one adopted in this work is described in Sub-sec. 4.4.2.

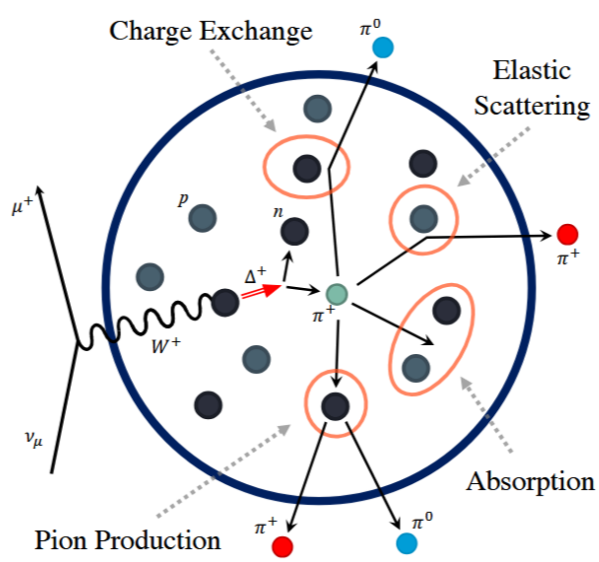

Figure 8 – Four possible final-state interaction processes pions may undergo as they traverse the nuclear medium on their way out of the nucleus. Figure reproduced from [51].

2.5 Analysis variables

In this analysis, cross sections are extracted for neutrinos and antineutrinos interacting on the hydrocarbon target of MINERvA (the precise signal definition is given in Sub-sec. 5.1.1). Interactions are distributed in terms of the pairings: transverse (p_μ^{T}) and parallel (p_μ^{Z}) components of muon momenta (Eq. 2.10a), and for the Lorentz-invariant dimensionless quantities Bjorken x and y (Eq. 2.10b).

$$p_\mu^{\mathsf{T}} = |\vec{p}_\mu| \sin\theta_\mu \qquad p_\mu^{\mathsf{Z}} = |\vec{p}_\mu| \cos\theta_\mu \tag{2.10a}$$

$$x = \frac{\mathsf{Q}^2}{2\mathsf{M_N E_{had}}} \qquad y = \frac{\mathsf{E_{had}}}{\mathsf{E}_\nu} \tag{2.10b}$$

In Eq.s 2.10, $\vec{p}_\mu$ and θ_μ represent the momentum and angle of the muon with respect to the incoming neutrino; Q^2 is the square of the four-momentum transferred from the neutrino to the hadronic system, defined in Eq. 2.11a; E_ν is the neutrino energy (Eq. 2.11b), given in terms of muon and hadronic energies, $\mathsf{E_{had}}$ and E_μ, respectively. Additionally, it is important to define the invariant mass of the hadronic system (Eq. 2.11c), a quantity from which the SIS region is defined. In all these equations, $\mathsf{M_N} = 939.04$ MeV is the nucleon mass at rest, and $\mathsf{M}_\mu = 105.7$ MeV is the muon mass. Fig. 9, illustrates the coordinate system in which the projections of the muon momentum are taken.

$$\mathsf{Q}^2 = 2\mathsf{E}_\nu(\mathsf{E}_\mu - p_\mu \cos\theta_\mu) - \mathsf{M}_\mu^2, \tag{2.11a}$$

$$\mathsf{E}_\nu = \mathsf{E}_\mu + \mathsf{E_{had}}, \tag{2.11b}$$

$$\mathsf{W}^2 = \mathsf{M_N^2} + 2\mathsf{M_N E_{had}} - \mathsf{Q}^2. \tag{2.11c}$$

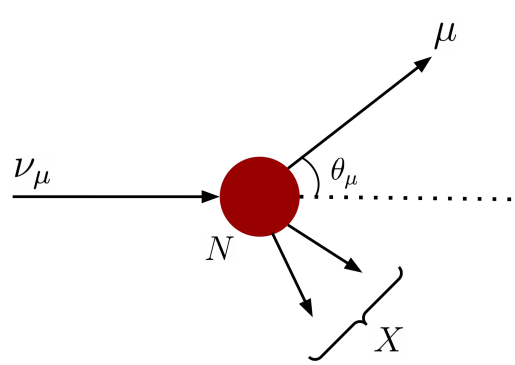

Figure 9 – Kinematics of the charged-current reaction $\nu_\mu N \rightarrow \mu X$ in the laboratory system: the incoming muon neutrino strick a nucleon at rest producing an outgoing muon and a jet of hadrons in the final state.

Both sets of variables have advantages in describing physical aspects of neutrino interactions on the SIS region, and have some nuances that deserve been emphasized. On one hand, the muon momentum variables are reconstructed with higher precision because they are measured directly in both the MINERvA and MINOS near detectors (see Chap. 4); $(p_\mu^{\mathsf{T}}, p_\mu^{\mathsf{Z}})$ does not depend on the hadronic system, and, therefore, provide more model-independent tests of the interaction model and nuclear effects. On the other hand, the (x, y) pairing choice is useful because it probes structure functions and QCD effects directly, but is heavily model-dependent: the Bjorken variables rely on an uncertain neutrino and hadronic energies reconstruction.

The physical interpretation of the Bjorken variables is rooted in the quark-parton model, the fundamental description of deep inelastic lepton-nucleon scattering [57]. In late 1960s, investigations of electron-proton scattering in the Stanford Linear Accelerator Center showed that the structure functions, discussed in Sub-sec. 2.2.4, at $\mathsf{Q}^2 > 2$ GeV^2 and $\mathsf{E_{had}} > 2$ GeV depend only on x [58]. This behavior, also observed in high-energy neutrino scattering, was predicted by Bjorken and is termed as scaling invariance [59]. The physical interpretation for this phenomenon was given by Feynman[2].

According to Feynman, the Bjorken x variable can be thought as the fraction $(0 < x < 1)$ of the proton momentum carried by the struck quark in the parton model [62]. In another words, low-x values $(x < 0.1)$ mean individual partons (quarks/gluons) carry a small fraction of proton momentum, and the regime is dominated by a sea of quarks and gluons, defining the DIS regime. At intermediate energies $(0.1 < x < 0.3)$, the scattering with the proton constituents transition from the DIS onset to the barionic resonances region. Finally, for $0.3 < x < 1$, parton carries a large fraction of proton momentum, and the interaction is classified as QE scattering. In the limit $x = 1$, the lepton interacts with the whole nucleon.

As for the Bjorken y variable, according to the definition in Eq. 2.10b, it represents the fractional energy loss of the incoming neutrino to the hadronic system. Low-y regime $(y \lesssim 0.2)$ means low hadronic activity, with the outgoing lepton retaining most of the neutrino energy. This region is populated by QE processes. Intermediate-y $(0.2 \lesssim y \lesssim 0.6)$ characterizes the resonance production region, and, at $y \gtrsim 0.6$, most of the neutrino energy is transferred to the hadronic system (DIS interactions). Fig. 10 shows a distribution of the main interaction channels in terms of Bjorken variables for neutrino energy $\langle \mathsf{E}_\nu \rangle \sim 6$ GeV (corresponding to the peak of MINERvA medium energy flux).

[2] Several experiments on deep inelastic lepton–nucleon scattering showed that partons, in the Feynman model, are actually identical to the quarks proposed by Gell-Mann and Zweig in 1964 [60, 61].

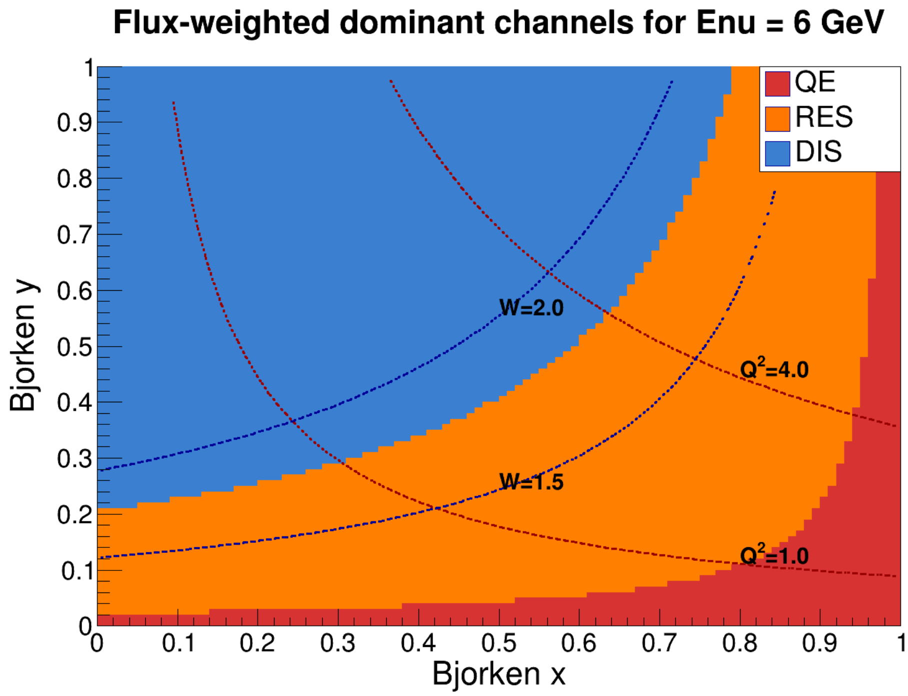

Figure 10 – Map of QE, RES and DIS interaction channels in terms of Bjorken variables x and y. On the plot, dashed lines are also shown for some values of the invariant mass of the hadronic system and four-momentum squared. The peak of the neutrino energy distribution is at around 6 GeV.

3 The shallow inelastic scattering region

In Chap. 2, a variety of neutrino-nucleus interactions in the few-GeV energy region were discussed. In particular, it was shown that neutrinos can induce meson production (typically pions or kaons) either by exciting the struck nucleon to a baryon resonance state − such as the $\Delta(1232)$ or higher-mass resonances − or through non-resonant processes. Historically, single-pion production via the Δ resonance has been the primary focus of the neutrino community, with only a limited number of studies devoted to multiple-pion and non-resonant production processes [27].

The kinematic region encompassing higher resonances, multi-quark and non-resonant pion production processes − referred to as shallow inelastic scattering (SIS) − is the topic of this thesis. This chapter provides a brief overview of SIS, but a more detailed and comprehensive discussion can be found in the Ref. [19]. Building on that review, the chapter begins with Sec. 3.1, which presents the definition of the SIS region. The relevance and how neutrino interactions in this regime can be studied are then discussed in Secs. 3.2, 3.3, and 3.4. These sections connects the physics of SIS with the so-called quark-hadron duality, list the roles of two non-perturbative QCD effects in the transition region, and emphasize its impact on improving neutrino interaction modeling for current and future neutrino oscillation experiments. The chapter concludes with Sec. 3.5, which highlights the first high-statistics SIS cross section measurements performed with the MINERvA detector.

3.1 Definition of shallow inelastic scattering

The systematic experimental investigations of neutrino-nucleus interactions in the SIS region are relatively recent. These studies started a few years ago within the MINERvA Collaboration, with its formal definition being established by J. Morfín *et al.* [19]. According to the authors, the kinematic regime corresponding to SIS is defined operationally in terms of the four-momentum transfer squared, Q^2, and its phase space has two components emphasizing specific physical processes. Namely, they are

I. A $Q^2 > 0$ GeV^2 region comprising mainly higher baryonic resonances, non-resonant and multi-quark meson productions, and also includes a $\Delta(1232)$-resonant background;

II. A $Q^2 > 1$ GeV^2 domain that enhances the multi-quark meson production and reduces the resonant background.

Additionally, the definition is supplemented with kinematic constraints on the invariant mass of the hadronic system, W, to further isolate higher-resonance masses and non-resonant interactions from other processes, such as the single-pion production via $\Delta(1232)$-resonance and DIS interactions. Therefore, one can select a SIS sample by requiring W to be in the energy range:

$$1.5 < \mathrm{W} < 2.0 \text{ GeV}. \tag{3.1}$$

In Eq. 3.1, the lower $\mathrm{W} = 1.5$ GeV cut is imposed to reduce the contamination of events originating from the Δ-resonance, while the upper $\mathrm{W} = 2.0$ GeV limit is adopted to avoid events from the DIS onset. With these conditions, one is left with an inclusive sample that includes the intrinsic overlap of different reaction mechanisms, for which there is no experimental tool to tell them apart in present day. Fig. 11 illustrates the available SIS regions for typical 6 GeV neutrino-nucleon scatterings.

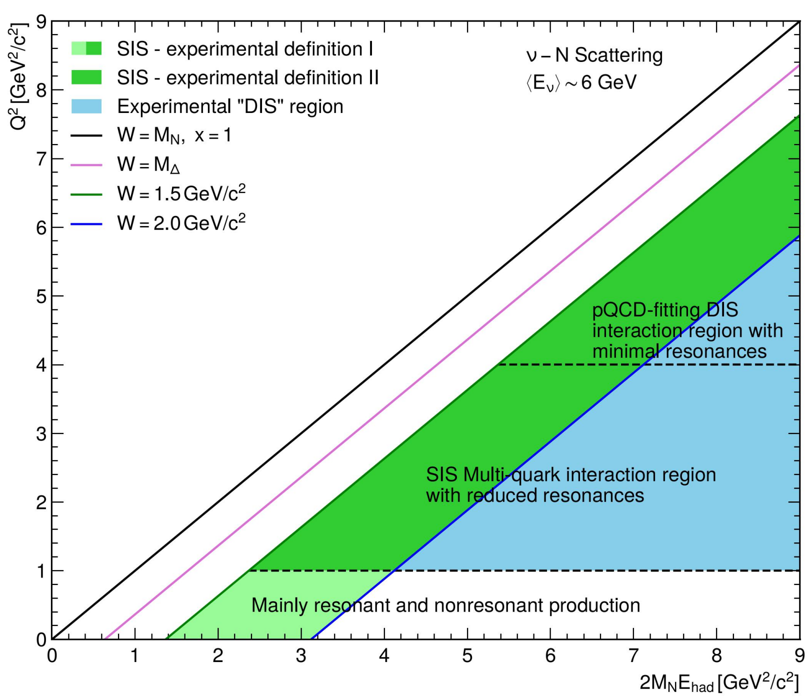

Figure 11 – Allowed kinematic regions in the $(\mathrm{Q}^2, 2\mathrm{M_N E_{had}})$ plane corresponding to the experimental SIS definitions I and II, and their relation to other interaction regimes. The dominant processes are also indicated on the figure, and separated by horizontal dashed lines corresponding to $\mathrm{Q}^2 = 1$ GeV^2 and $\mathrm{Q}^2 = 4$ GeV^2. Figure taken from [20].

3.2 Tools to studying the physics of SIS

Neutrino interactions in the SIS region are extremely complex to model. In this regime, multiple mechanisms contribute simultaneously: resonance excitations, non-resonant and multi-quark pion productions. On the top of the absence of a first-principles theory, the observables in the final state are heavily subjected to nuclear effects, especially FSI (see Sec. 2.4).

Despite these difficulties, there are two possible ways of approaching neutrino interactions in the SIS region, and describe its rich physics content: first, it can be explored by applying the concept of quark-hadron duality; and, secondly, one can extend the DIS structure functions down to the transition region, coupled with non-perturbative QCD corrections. These two methods are discussed below.

3.2.1 Quark-hadron duality

The concept of quark-hadron duality was originally proposed in the 1960s to connect lower- and higher-energy pion-proton scatterings, and is intrinsically associated to the SIS transition region [63]. Years later, Bloom and Gilman used duality to describe electron-nucleon data, and its formal definition was coined by them [26].

Duality establishes that the nucleon resonance structure functions, when averaged over the resonance bumps on an specific energy interval, coincide with the DIS scaling curve at high-Q^2, in the same energy limits. In another words, what this hypothesis suggests is that the physics of hadrons and quarks would have a common origin, with duality being a bridge connecting them. Therefore, if duality holds true for neutrinos, then the SIS transition region could be approximately described by the perturbative QCD formalism. Fig. 12 illustrates the resonance bumps ("peaks" and "valleys") and their average curve.

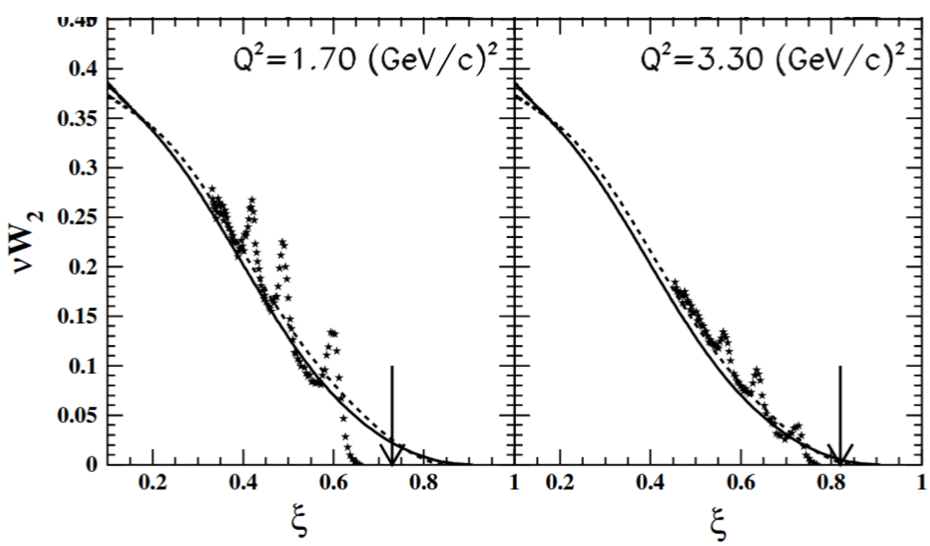

Figure 12 – Experimental verification of quark-hadron duality using electron-nucleon data [64]. The hydrogen structure function, νW_2 (equivalent to F_2), is plotted as a function of the Nachtmann variable (Eq. 3.3) for $Q^2 = 1.70$ GeV^2, and $Q^2 = 3.30$ GeV^2. The solid (dashed) line represents the DIS scaling curve fit at $Q^2 = 10$ GeV^2 ($Q^2 = 5$ GeV^2), and arrows indicate elastic kinematics.

In practical terms, duality can be tested by defining a ratio of integrals of the nucleon structure functions as in Eq. 3.2. If duality is satisfied, then this ratio would be equal to 1. The integral limits, $[\xi_{\rm min}, \xi_{\rm max}]$, must be the same for both the numerator and denominator. To achieve that one must properly adjust the Q^2 values for the resonance and DIS regions in the Nachtmann variable, ξ, which is defined in Eq. 3.3.

$$\mathrm{I}_i(\mathrm{Q}^2_{\rm RES},\, \mathrm{Q}^2_{\rm DIS}) = \frac{\displaystyle\int_{\xi_{\rm min}}^{\xi_{\rm max}} d\xi\; \mathsf{F}_i^{\rm RES}(\xi, \mathrm{Q}^2_{\rm RES})}{\displaystyle\int_{\xi_{\rm min}}^{\xi_{\rm max}} d\xi\; \mathsf{F}_i^{\rm DIS}(\xi, \mathrm{Q}^2_{\rm DIS})}. \tag{3.2}$$

$$\xi(x, \mathsf{Q}^2) = \frac{2x}{1 + \sqrt{1 + 4x^2 \mathsf{M}_\mathsf{N}^2/\mathsf{Q}^2}}. \tag{3.3}$$

In the early 2000s, with the success of QCD and the quark-parton model firmly established, new experimental investigations of the quark-hadron duality in the resonance region started. At the Jefferson Lab, several measurements of resonance structure functions were made from electron scatterings off nucleon and nucleus [64–68]. In these tests, the data seem to be consistent with the duality hypothesis, and the main observed features can be summarized as: the resonance data, on average, are equivalent to the DIS scaling curve, with increasing agreement towards high Q^2 values.

While duality has been observed in the charged leptonic sector, it has not yet been confirmed in neutrino scattering processes. Despite its existence in the weak structure functions was suggested more than three decades ago, a series of limitations have hampered a final conclusion on the topic [69]. Among the issues there is a lack of high statistics data in the resonance region – the only available neutrino-induced resonance production measurements are from the 1970s and 1980s, which are limited by statistics [70, 71]. In the case of neutrino-nucleus scatterings, most measurements are rather concentrated on single-pion production via the $\Delta(1232)$-resonance [21, 22, 72].

On the other hand, on theory grounds, the literature about duality in the neutrino sector is limited to a few studies [73–75, 77]. A summary of the most relevant theoretical findings is given below.

- A collaborative work between Giessen and Ghent groups [75], using the GiBUU neutrino event generator [76], found that the ratio defined in Eq. 3.2 gets closer to 1 when one considers single-pion non-resonant background contributions, induced by electron-nucleon interactions. The same conclusion is drawn for neutrino-nucleon scatterings: as shown on the right side of Fig. 13, considering only the Δ-resonant contribution, duality is around 70%.

- In the Wrocław group work [73], the Rein-Sehgal model is used to predict the Δ-resonant pion production from neutrino-nucleon interactions (see discussion in Sec. 2.2.2). The authors found that duality is not satisfied for neutron targets; for isoscalar targets (equal number of neutrons and protons) the ratio in Eq. 3.2 is closer to ideal duality; and, although not fully satisfactory, the scenario for proton targets seems to be the best one.

- Duality in the case of neutrino-nucleus interactions is much less clear. The Giessen and Ghent groups have also conducted investigations on this regard [77]. Using iron as a nuclear target, they found that the ratio in Eq. 3.2 is about 0.4 only for resonant pion production, without including non-resonant interactions — this value is much lower than the one for the free nucleon case, which is around 0.7. In general, the target characteristics[1] and nuclear medium effects, discussed in Sec. 2.3, should be considered when interpreting duality in neutrino-nucleus scatterings.

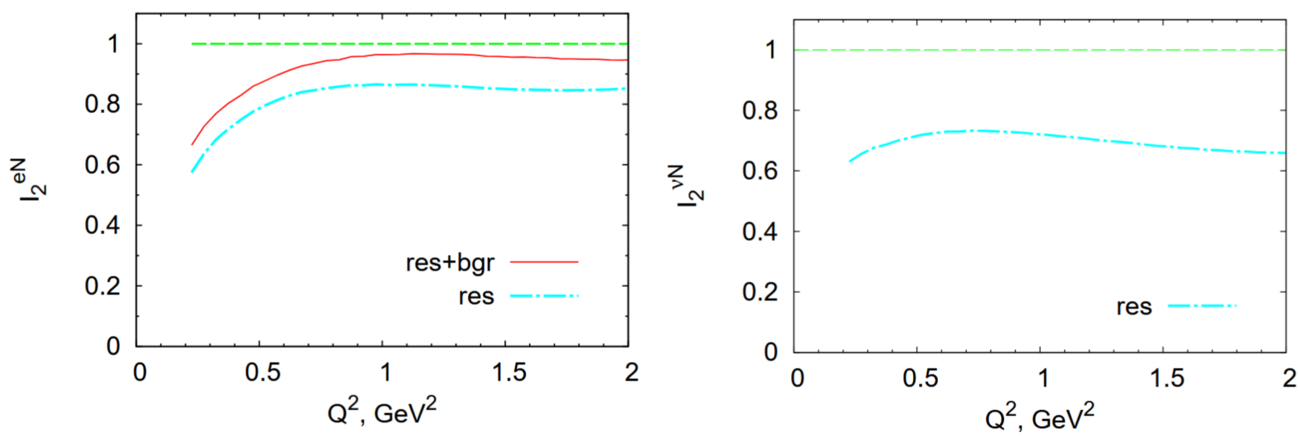

(a) Electron-nucleon prediction.

(b) Neutrino-nucleon prediction.

Figure 13 – Theoretical tests of quark-hadron duality for electron-nucleon (left) and neutrino-nucleon (right) scattering using GiBUU neutrino event generator. The ratio defined in Eq. 3.2 is first calculated separately for Δ-resonant single-pion production ("res", cyan dashed line), and then including non-resonant single-pion background contributions ("res+bgr", red line). Ideal duality is illustrated by the horizontal green dashed line. Figures taken from [75].

3.2.2 Non-perturbative QCD

As discussed in the last subsection, duality is one of the approaches to describe the physics of the SIS transition region, but its confirmation in the weak sector is still an open question; even, it may be valid only under specific circumstances. In the meantime, the inclusion of non-perturbative QCD effects in the DIS structure functions represents an alternative route. In fact, in the SIS regime, non-perturbative phenomena — such as higher twist effects and target mass corrections —

[1] Iron has an excess of neutrons, for which the strength of the resonance structure functions is lower than the DIS ones.

are present, and their consideration is essential for a precise SIS modeling [19, 27]. In a similar fashion as duality, the DIS structure functions, derived in the perturbative QCD regime ($\mathsf{Q}^2 > 4$ GeV^2; Fig. 11), can be extrapolated down to low invariant masses $\mathsf{W} < 2$ GeV region, and then SIS can be properly described with the addition of these non-perturbative effects.

a) **Higher twist effects**

The concept of *twist* was introduced by Gross and Treiman in 1971, when they noticed that "it is no longer the dimension alone that determines the importance of an operator near the light-cone, but rather the difference between the dimension and spin" [78, 79]. Twist is then defined as $\tau = \mathsf{d} - \mathsf{J}$, where d and J are the dimension and spin associated to an operator, respectively. In the DIS context, unpolarized structure functions can be expanded in powers of $1/\mathsf{Q}^2$ through the operator product expansion formalism. They are organized as follows.

$$\mathsf{F}_i(x, \mathsf{Q}^2) = \mathsf{F}_i^{\tau=2}(x, \mathsf{Q}^2) + \frac{1}{\mathsf{Q}^2}\mathsf{H}_i^{\tau=4}(x) + \frac{1}{\mathsf{Q}^4}\mathsf{H}_i^{\tau=6}(x) + \cdots, \quad i = 1, 2, 3. \tag{3.4}$$

In Eq. 3.4, at high-Q^2 the higher twist contributions are suppressed, and the dominant term is $\mathsf{F}_i^{\tau=2}(x, \mathsf{Q}^2)$. This term is referred to as leading twist ($\tau = 2$), and its physics meaning corresponds to neutrino scatterings off a single, quasi-free parton (quark). The leading twist is calculable with perturbative QCD, and described in terms of parton distribution functions (the usual F_1, F_2, and F_3). On the other hand, at moderate Q^2, the higher twist terms ($\tau = 4, 6, ...$) start to contribute, and the QCD factorization fails to describe the functions $\mathsf{H}_i(x)$. These functions are associated to multi-parton correlations, and, because they cannot be calculated from first principles, they are rather extracted from fits on low-Q^2 data [80–82].

b) **Target Mass Corrections**

Another non-perturbative effect that comes into play in the SIS energy regime is the target mass correction (TMC). TMC arises from the fact that the target nucleon, M_N, has a finite mass. In fact, at moderate Q^2, terms involving $\mathsf{M}_\mathsf{N}/\mathsf{Q}^2$ in the DIS cross section formula are relevant, and the Bjorken x is no longer the correct scaling variable; the structure functions must receive kinematic corrections as a function of the Nachtmann variable (Eq. 3.3). There exist a number of theoretical ingredients necessary to derive TMC effects $-$ Ref. [83] is a great review on the topic. Such effects were first calculated for electroweak structure functions by Georgi and Politzer in 1976 [84], and they are typically implemented in the leading twist term. For an application of TMC in lepton- nucleons and nuclei, the reader may refer to the publication [85].

3.3 Simulations in the SIS region

Neutrino interaction simulations (generators) implement cross section and nuclear models to transform an incident neutrino flux distribution into predictions of final-state particles produced in the detector material (see Sec. 4.4 for more details). Due to the variety of models and methods to simulate these interactions, there are many generators in the market. A meticulous study comparing some of the main predictions for the SIS transition region can be found in [86]. This study found significant differences between NEUT [87], NuWro [88] and GENIE [119], as illustrated in Fig. 14.

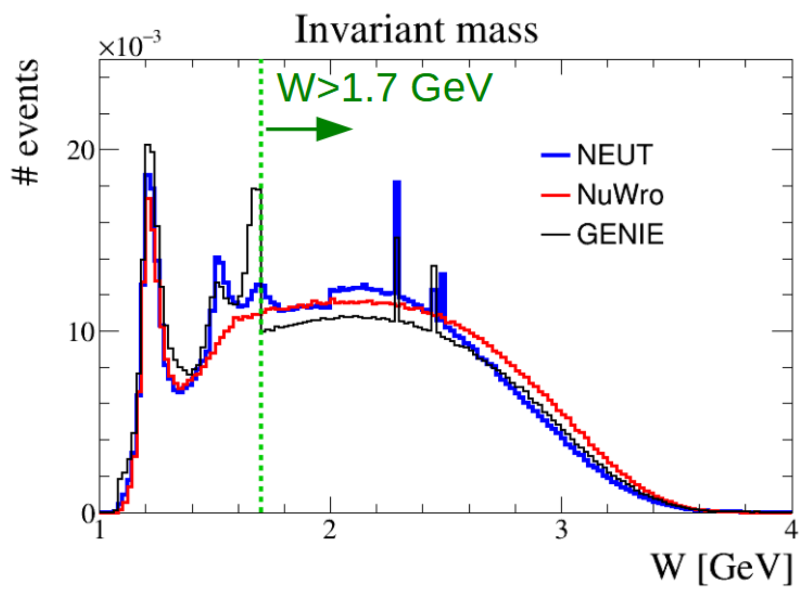

Figure 14 – Number of charged-current neutrino interactions simulated by NEUT, NuWro, and GENIE as a function of the hadronic invariant mass, W. Events are shown for the resonant and DIS regions only, and were generated using 6 GeV muon neutrinos scattering off an iron target. The vertical green dashed line at W $= 1.7$ GeV corresponds to the GENIE convention for the onset of the DIS regime. Figure taken from [86].

Fig. 14 displays predictions for the three aforementioned simulation programs in terms of the invariant hadronic mass, W. These event distributions were generated by 6 GeV muon neutrinos interacting on iron through charged-current resonant and DIS processes only (QE, 2p2h, etc not included). Overall, a visual inspection points out to differences in shape and normalization across the generators. Quantitatively, the treatment of the resonant and DIS regions also differs among them. Below, the conventions adopted by each generator are discussed, and Tab. 1 summarizes their main differences.

3.3.1 NEUT 5.3.4

NEUT utilizes the Rein and Sehgal model to simulate resonance channels in the W < 2.0 GeV region. The region also includes a DIS background, which is predicted by the Koba-Nielsen-Olesen scaling model [89]. In the W > 2.0 GeV regime, events are considered purely DIS and modeled according to the Glück-Reya-Vogt prescription with modification proposed by Bodek and Yang [48];

3.3.2 NuWro 11q

In NuWro, the resonance region is defined by W < 1.6 GeV. In the low W region (W < 1.3 GeV), only the single-pion production via $\Delta(1232)$-resonance excitation is simulated using the Graczyk and Sobczyk form factors [90]. A linear function in terms of W is proposed to describe the transition region $1.3 <$ W < 1.6 GeV, which combines the $\Delta(1232)$ excitation model with the single-pion production part of the DIS cross section [91]. The DIS regime is defined above W $= 1.6$ GeV, and is simulated by the Bodek and Yang DIS model.

3.3.3 GENIE 2.10

Similarly to NEUT, GENIE uses the Rein-Sehgal model to predict baryon resonances. However, differently from the former, the convention followed in this generator defines the resonance region as W < 1.7 GeV. The region also includes a DIS background, which, in this case, is described by the AGKY model [119]. Above W $= 1.7$ GeV, no resonances are considered, but only DIS events, which is simulated by the Bodek-Yang model.

Table 1 – Physics treatment of the resonance and RES–DIS transition regions in generators.

Generator \ Model aspect	Resonance region	Resonance model	Transition to DIS
NEUT 5.3.4	W < 2.0 GeV	Rein-Sehgal	discontinuous at W $= 2.0$ GeV
NuWro 11q	W < 1.6 GeV	Graczyk-Sobczyk	linear in W $= [1.3, 1.6]$ GeV
GENIE 2.10	W < 1.7 GeV	Rein-Sehgal	discontinuous at W $= 1.7$ GeV

If the quark-hadron duality hypothesis is proved true for neutrinos, then the DIS formalism can be extended down to the higher resonance masses region, and there will be no longer a need of several approaches to simulate the same neutrino interactions in the SIS transition region; only the $\Delta(1232)$ resonance would require a separate treatment.

3.4 Connection with oscillation phenomena

The fact that neutrinos change flavors as they travel is known as neutrino oscillation. This phenomenon was discovered in 1998, and confirmed the existence of neutrino masses [6]. It can be understood from a two-flavor transition case in the vacuum, as described by the oscillation probability in Eq. 3.5: after propagating through a certain distance L, a neutrino α turns into a neutrino β. In this equation, θ is the mixing angle, Δm^2 is the mass-squared splitting between the two mass eigenstates and E is the neutrino energy (a more detailed discussion involving matter effects, charge-parity violating phase, etc can be found, for instance, in [92]).

$$\mathrm{P}(\nu_\alpha \rightarrow \nu_\beta) \simeq \sin^2(2\theta)\sin^2\left(\frac{\Delta \mathrm{m}^2 \mathrm{L}}{4\mathrm{E}}\right). \tag{3.5}$$

In particular, the appearance of electron neutrinos in a muon neutrino beam ($\nu_\mu \rightarrow \nu_e$) constitutes one of the main oscillation channels studied in long-baseline experiments, with ν_e being reconstructed from electromagnetic showers. However, pions produced in neutrino interactions can also yield photons in their decay (*e.g.*, $\pi^0 \rightarrow \gamma\gamma$), thereby mimicking an electron-neutrino signal [93].

Moreover, pions – as any other hadrons produced at the primary vertex – are subjected to final-state interactions (Sec. 2.4), which can cause the event topology to be misidentified, for instance, as quasielastic scattering [94]. Ultimately, if not thoroughly studied, neutrino-induced pion production can hinder precise reconstruction of the neutrino energy, and consequently the extraction of the oscillation parameters in current and future experiments such as T2K, NOvA, DUNE, and HyperKamiokande [95–98].

As illustrated in Fig. 15, pion production in the SIS region contributes a significant fraction of events in DUNE.

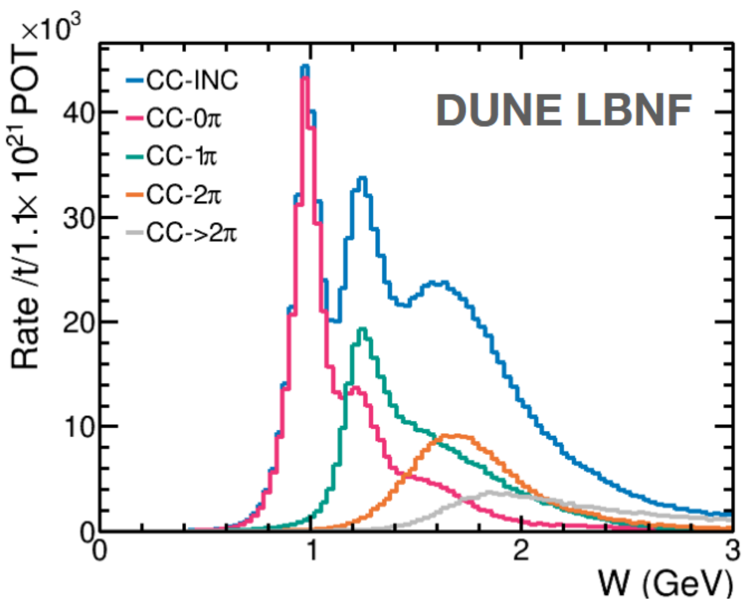

Figure 15 – Number of charged-current neutrino interactions as a function of the hadronic invariant mass, W. The simulation assumes a typical nominal DUNE beam exposure of 1.1×10^{21} protons on target, and is broken down into different pion production final states. Figure taken from [99].

3.5 First MINERvA measurements

As mentioned in Sec. 3.2, neutrino data in the resonance region are very limited, with the only available measurements dating from the 1970s and 1980s [70, 71]. The MINERvA Collaboration has published the first high-statistics neutrino-nucleus cross section measurements in the SIS region [20, 100, 101]. This work, carried out by collaborators at CBPF, represents a major milestone to the neutrino community: first, it fills a longstanding gap in data in the SIS transition region; secondly, the measurements are expected to foster model developments, thereby contributing to improved control of systematic uncertainties in oscillation analyses.

The final samples contain 383,494 (235,017) muon neutrinos (antineutrinos) interacting on a hydrocarbon target, and the cross sections are reported as functions of several kinematic variables. Significant tensions were observed between the measured data and predictions from a number of simulation programs. Fig. 16 illustrates one such example for the squared four-momentum transfer.

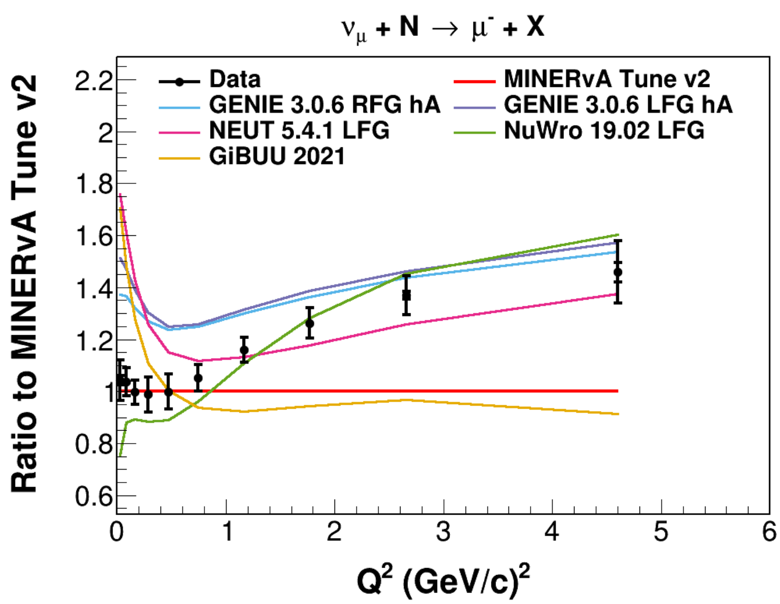

Figure 16 – MINERvA first SIS cross section measurement for charged-current muon neutrino interactions on hydrocarbon. Example taken from [20], and shows data-to-MINERvA Tune v2 simulation as a function of the four-momentum transfer squared. Illustrated also on the plot, there are five generator predictions the data are compared against.

4 MINERvA Experiment

As seen in Chap. 2, neutrinos are neutral particles, and their masses are utterly negligible for laboratory detection — given its tiny cross section ($\sigma \sim 10^{-44}$ cm^2, 13–18 orders of magnitude smaller than the cross section for the electron, the lightest lepton), it was believed that neutrino detection would be impossible [102]. Therefore, neutrinos can only be measured statistically, through their interactions in massive detectors with intense flux sources.

This chapter presents a brief overview about MINERvA (Main Injector Neutrino ExpeRiment to study v-A interactions), a neutrino cross section experiment that was located at Fermilab, and which collected data from 2009 to 2019. An extensive discussion and all details regarding the experimental apparatus can be found in the Refs. [103–105].

4.1 The NuMI beam

The neutrino interactions observed in the MINERvA detector are induced by neutrinos produced from the Fermilab NuMI beam. The beam is generated through a multi-step process, described in detail in Ref. [106]. First, protons are accelerated in the Main Injector to an energy of 120 GeV, as illustrated in Fig. 17. They are then directed into a stationary carbon target, where hadronic particles — primarily pions and kaons — are produced (see Fig. 18).

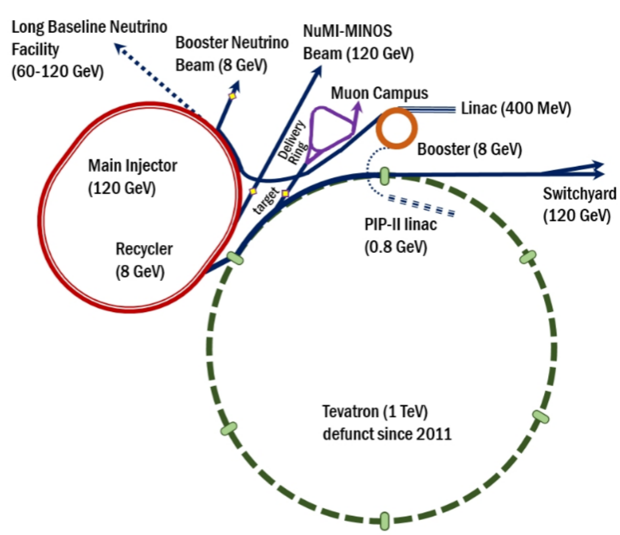

Figure 17 – Fermilab Accelerator complex. Figure taken from [107].

Since hadrons are produced over a wide range of angles, two magnetic horns are used to focus and select hadrons of a given electric charge towards a 675 m long vacuum decay pipe; depending on the horn current polarity, either positively on negatively charged hadrons are focused. The pions and kaons subsequently decay predominantly into neutrinos and muons. Residual hadrons are attenuated by a 5 m thick absorber, and the muons are stopped by approximately 240 m of rock downstream of the absorber.

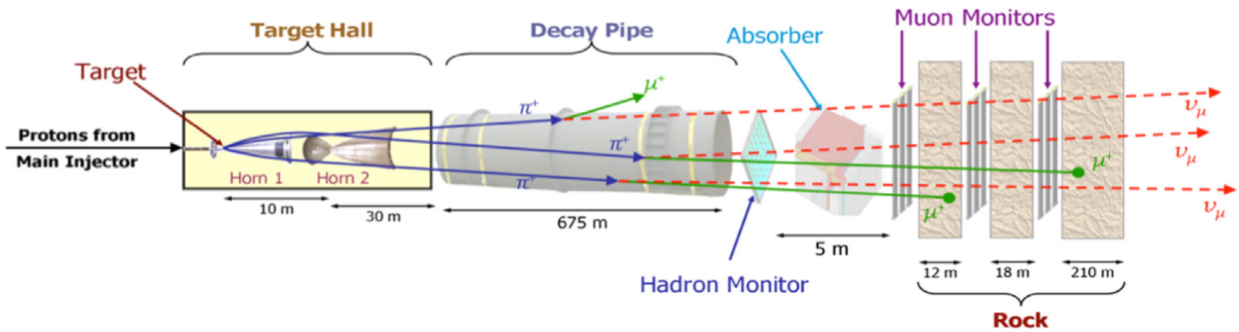

Figure 18 – Schematic of the NuMI Beam. Figure taken from [106].

4.2 The MINERvA detector

The MINERvA detector lies 110 m underground, and consists of a broad range of targets to study neutrino interactions with matter: it has liquid helium (He), water (H_2O), iron (Fe), lead (Pb), carbon (C), and hydrocarbon (CH, scintillator). Except for He, which is located upstream of the detector, all other targets are surrounded by electromagnetic and hadronic calorimeters, as shown on the schematic Fig. 19.

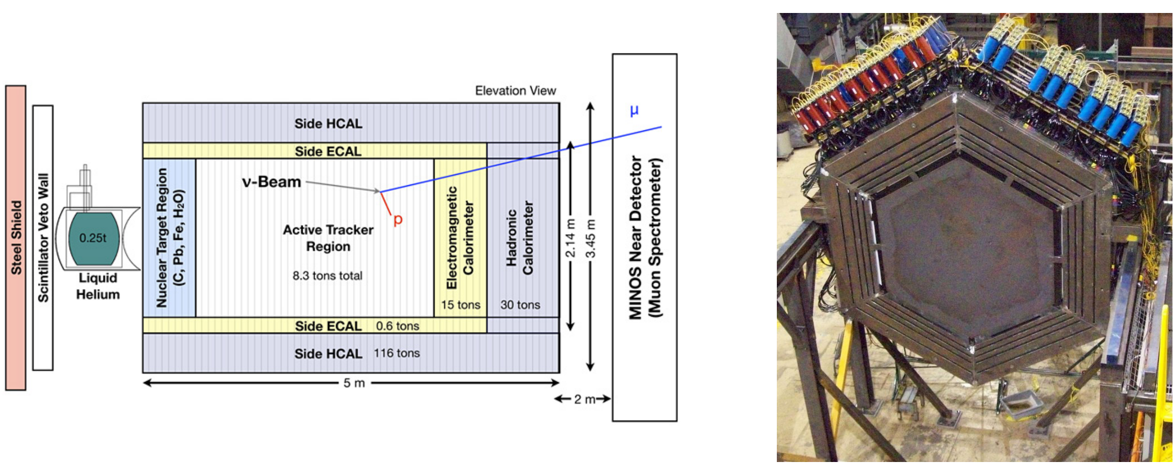

Figure 19 – The MINERvA detector. Figures taken from [103].

The analysis reported in this thesis is focused on neutrino interactions in the MINERvA active tracker region, comprised purely of plastic scintillator strips. Such strips have an isosceles triangle shape (base of 3.3 cm and height of 1.7 cm), whose center pass an wavelength-shifting fiber responsible for transmitting light signals to photo-multiplier tubes mounted above the detector (red and blue components on the upper part of right-side Fig. 19).

A total of 127 strips are glued together to form an hexagonal plan, arranged according to the orientations in Tab. 2, and illustrated in Fig. 20 – this arrangement allows 3-dimensional reconstruction of the interaction vertex, and is especially relevant for the nuclear targets. In the tracker region, there are 124 planes grouped two-by-two (UX-VX) in 62 modules, and numbered from 23 to 84. All details about fiducial mass specifications, electronics, readout, and data calibration can be found in the Ref. [103].

Table 2 – Scintillator plane views as a function of strip orientations.

Plane view	Strip orientation
X-view	Anti-parallel to gravity direction.
U-view	Rotated 60° clockwise w.r.t central axis of the detector.
V-view	Rotated 60° counterclockwise w.r.t central axis of the detector.

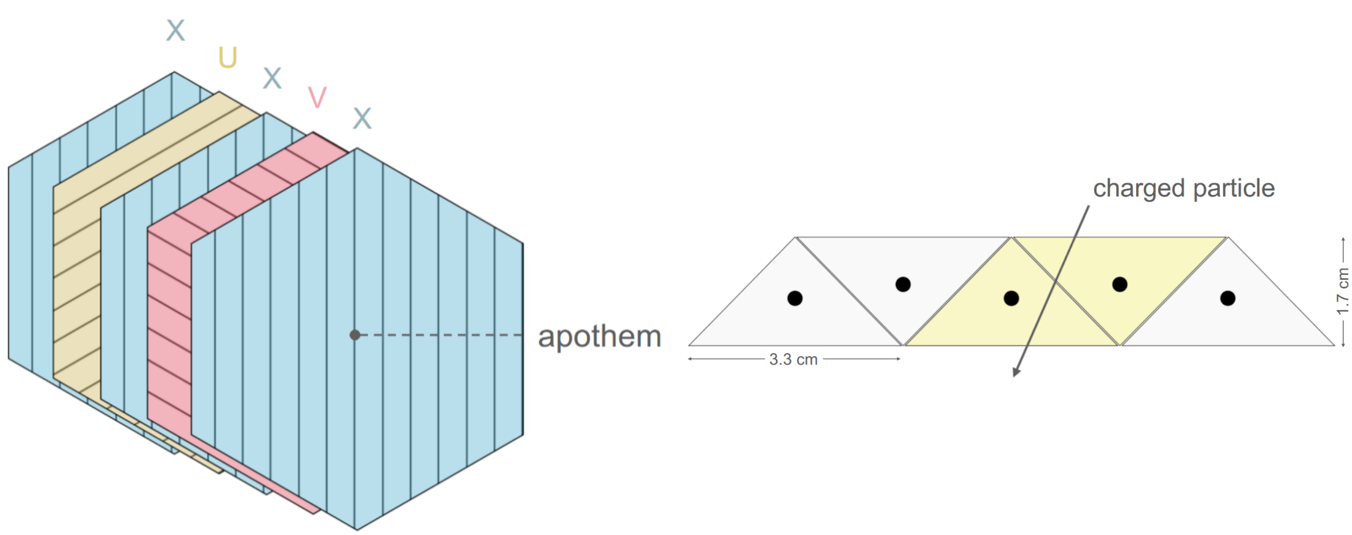

Figure 20 – Figure on the left illustrates how the MINERvA scintillator planes are assembled, according to the orientations listed in Tab. 2. The figure on the right shows a cross section of the strips' configuration, and indicates the ones activated (in yellow) by the passage of a charged particle; the generated scintillation light is transmitted to PMTs through optical fibers, located at the strip's center (black circles). Figures reproduced from A. Klustová, [108], CC BY-NC 4.0.

Neutrino interactions are reconstructed from combined measurements of energy depositions in both the MINERvA and MINOS near detectors (discussed in Sec. 4.3). As detailed in Ref. [103], the reconstruction starts by identifying muon track candidates. An algorithm is used to group energy deposits (hits) into five cluster categories, which two of them (trackable and heavily ionizing) are used to form a muon track – it must span at least 11 planes. Once the muon track is formed, the remaining energy activity is attributed to the hadronic recoil system via a calorimetry procedure encoded by Eq. 4.1.

$$\mathrm{E}^{\mathrm{cal}}_{\mathrm{recoil}} = \alpha \sum_i c_i \mathrm{E}_i. \tag{4.1}$$

In Eq. 4.1, α is an effective, first-order approximation parameter, determined through a fitting process, and represents an average correction for nuclear binding energy, invisible neutrons, FSI-induced missing energy, and other lost activities in the instrumented volume; E_i is the visible energy deposited in sub-detector i, and c_i is a calorimetric constant that converts the measured visible energy into an estimate of the true deposited energy, determined from detector calibration studies. Further details can be found in section 8 “Recoil energy reconstruction” of Ref. [103].

Event displays of representative candidates for charged-current muon neutrinos (antineutrinos) interactions in the SIS region, as reconstructed in the MINERvA and MINOS detectors, are presented in the top (bottom) panels of Fig. 21. Notice that, the muon track appear in the detector as a straight long line.

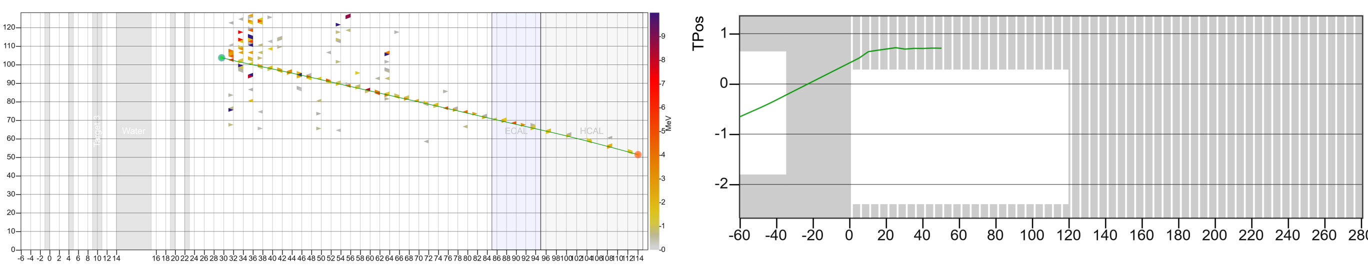

(a) **Neutrino** mode.

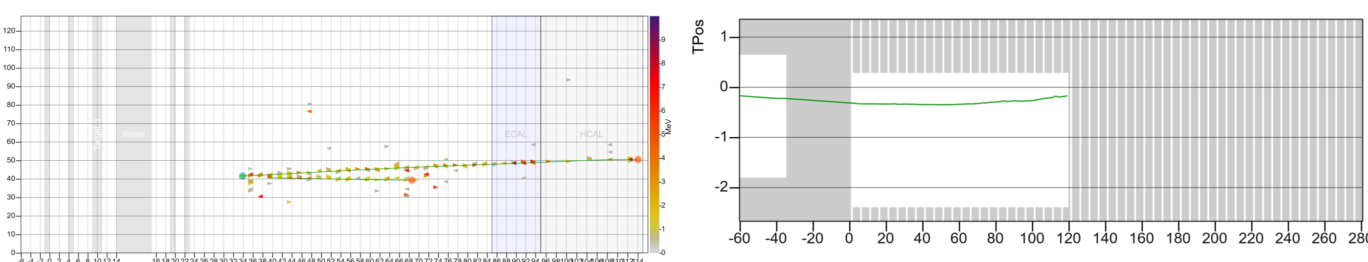

(b) **Antineutrino** mode.

Figure 21 – Tracks of SIS data event candidates seen in events displays. Top (bottom) figure shows the tracks for neutrino (antineutrino) mode. The x-axis indicates the module numbers, whereas the y-axis the strip number. Individual triangles in Arachne represents an energy cluster, with their colors related to the size of the deposit, according to the scale at the right. The green lines are the projections of the tracks' three-dimensional directions onto the UZ-plane.

4.3 The MINOS near detector

MINOS was a two-detector neutrino oscillation experiment designed to measure ν_μ and $\bar{\nu}_\mu$ disappearance, and operated from February 2005 to April 2012 [109]. Its near detector was located 2 m downstream of MINERvA, at Fermilab, and the second detector 735 km away, in the Soudan Underground Laboratory, northern Minnesota.

Consisting of 282 steel planes, the MINOS near detector was used in the MINERvA experiment as a muon spectrometer. The momentum and charge of the muon were measured by using a 1.3T toroidal magnetic field, produced in the coil hole indicated in Fig. 22, and the resulting track must be matched to the one measured in MINERvA – to meet this requirement, the difference between the end-point detector tracks must be less than 40 cm.

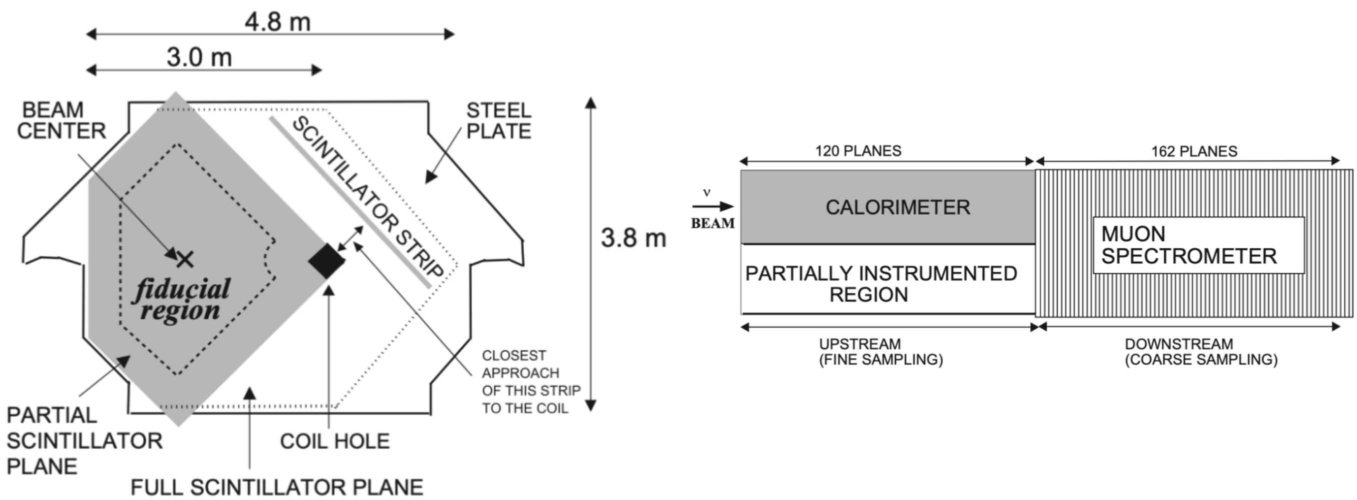

Figure 22 – (*left*) Transverse view of the MINOS near detector plane. The shaded area shows a partially instrumented active scintillator plane and the dashed line within shows the boundary of the fiducial region. The dotted line shows the outline of a fully instrumented scintillator plane The MINOS near detector. (*right*) Top view of the detector, showing the calorimeter and muon spectrometer. The drawing is not to scale. Figures taken from [110].

In MINOS, based on its energy, muon momentum and charge can be reconstructed either by range or curvature. In the first method, if the muon is contained within the calorimeter, the energy deposited in the MINOS active scintillator (see right Fig. 24) is used to get

$$p_{\mu,\text{range}} = \sqrt{\text{E}^2_{\mu,\text{range}} - \text{m}^2_\mu}. \tag{4.2}$$

On the other hand, if the muon has enough energy to escape the calorimeter region, then the second method is used. In the reconstruction by curvature, first track candidates are subjected to a filter algorithm, and from that the radius, R, is measured, and the momentum given by

$$\frac{1}{\mathsf{R}} = 0.3\frac{|\vec{B}|}{p_{\mu,\mathsf{curv}}}, \tag{4.3}$$

where $|\vec{B}|$ is the mean magnetic field along the trajectory, given in Gauss.

Based on the polarity of the magnetic field, and on their charge, muons will be focused towards the coil or deflected to the sides of the detector. Fig. 23 shows the case where the forward magnetic field focuses μ^- towards the center, and μ^+ are deflected to the sides – for reverse current, the outcome is the opposite.

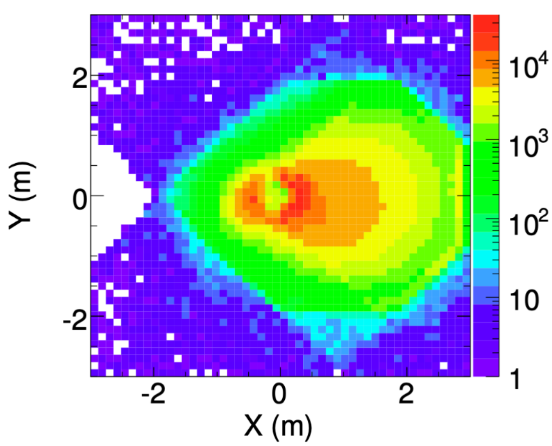

(a) μ^- tracks are focused towards the center.

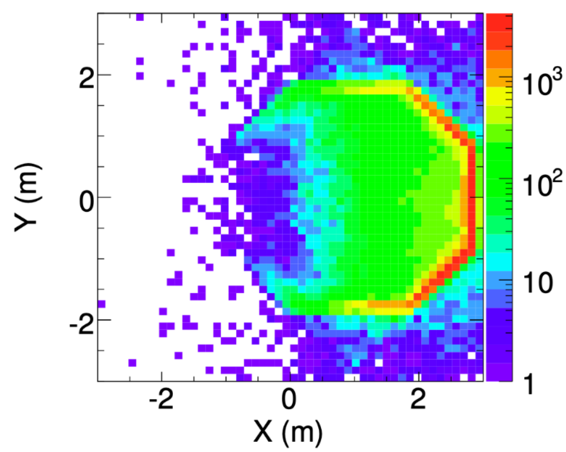

(b) μ^+ tracks are deflected to the sides.

Figure 23 – Simulated positions of μ^- and μ^+ tracks generated with the MINOS near detector magnetic field set in the forward polarity. The magnetic coil is positioned at the center $(\mathsf{X}, \mathsf{Y}) = (0, 0)$ m. Figures taken from [111].

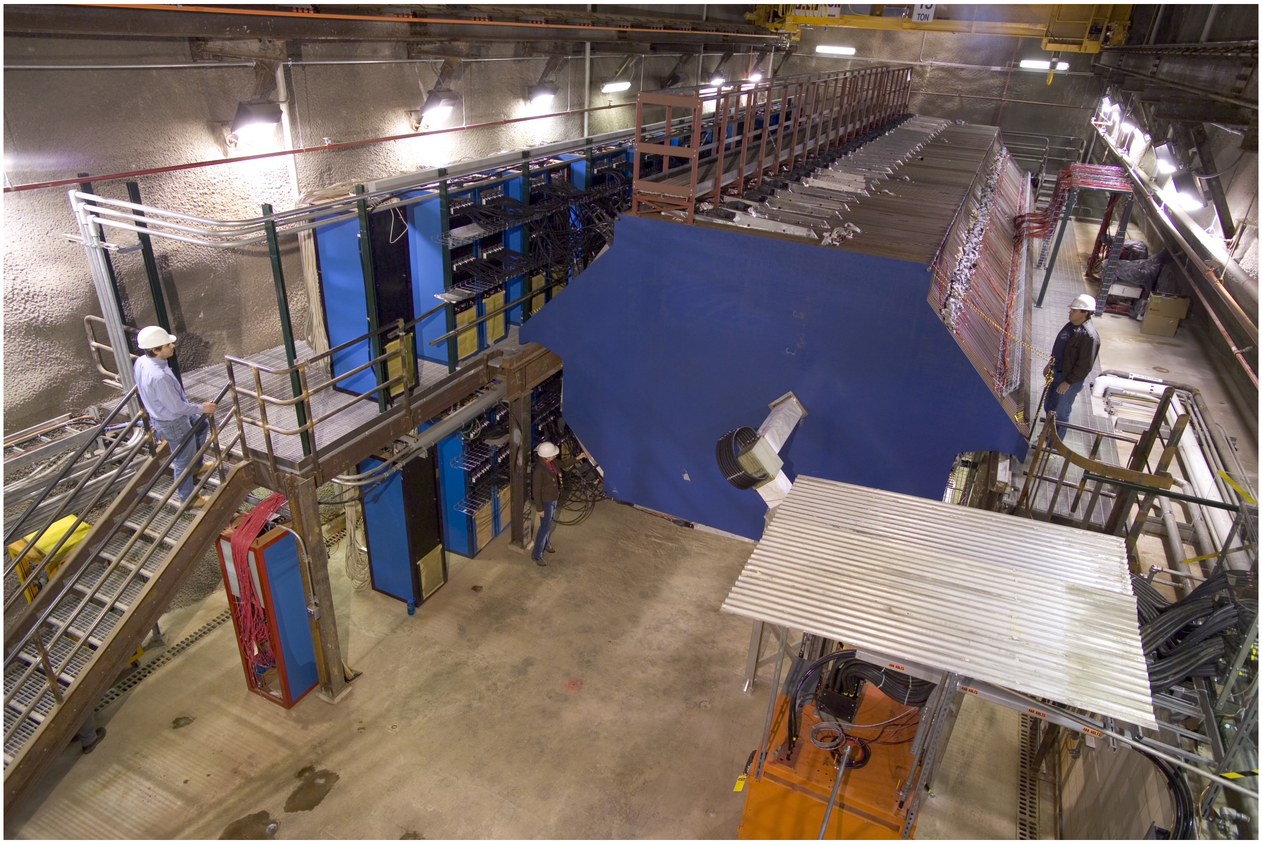

Figure 24 – Two collaborators look over the complete MINOS near detector. Picture taken before the MINERvA detector installation, and reproduced from [112].

4.4 Simulations

4.4.1 Neutrino flux simulation

The neutrino beam is simulated by g4numi, a GEANT4-based software [113, 114]. The simulation predicts 120 GeV proton-carbon interactions, providing the kinematics and propagation through the beamline system of primary particles. The thickness of the carbon target allows the primary hadrons undergo re-interactions, and several components of the beamline system are sources of uncertainties. MINERvA handles these uncertainties with the PPFX package, and constrain the flux using neutrino-electron scattering, and inverse muon decay data [115–118]. More details on the flux uncertainties are discussed in Sec. 6.2.

4.4.2 Neutrino interactions simulation

At present date, MINERvA analyses use the GENIE simulation program, version 2.12.6, to predict neutrino interactions in its detector [119]. GENIE takes as input the neutrino flux simulation, the detector's material target information, and other parameters to predict the cross section interaction models, discussed in Chap. 2. The main cross section model parameters assumed to generate the simulation used in this work are listed in Tab. 3. Additionally, a series of tunings is applied on the top of the baseline simulation; they are discussed in Sub-sec. 4.4.4.

Table 3 – Cross section models, parameters, and conventions implemented in GENIE v2.12.6.

Process	Parameters and Conventions
QE scattering	The process uses an implementation of the Llewellyn Smith model [33]. The axial form factor is parameterized as a dipole form, with axial mass $\mathsf{M_A} = 0.99^{+25\%}_{-15\%}$ GeV. Vector form factors are modeled with the BBBA05 parameterization [126].
Multi-nucleon scattering	2p2h interactions are simulated using an implementation of the Valencia 2p2h model [53].
RES pion production	Resonant single-pion production is simulated using the Rein-Sehgal model [45]. Following a recommendation from PDG, it includes 16 resonances up to $\mathsf{W} = 1.7$ GeV [44]. The vector and axial form factors assume a dipole function, with their corresponding masses $\mathsf{M_V} = (0.84 \pm 0.08)$ GeV and $\mathsf{M_A} = (1.12 \pm 0.22)$ GeV.
non-RES pion production	Non-resonant single-pion production is calculated using the Bodek-Yang model. 1π and 2π data from ANL and BNL bubble chamber experiments are used to tune the model in the region $1.4 < \mathsf{W} < 1.7$ GeV [70, 71].
Deep inelastic scattering	DIS interactions are defined in the kinematic region of $\mathsf{Q}^2 > 1$ GeV^2 and $\mathsf{W} > 2$ GeV, and implements the Bodek-Yang model to calculate the cross sections [48]. The AGKY model and PYTHIA program are used to describe hadronization processes [119].
Final-state interactions	FSI, discussed in Sec. 2.4, involving nucleons and pions are modeled using an intranuclear cascade simulation called INTRANUKE [119].

4.4.3 Detector simulation

The detector simulation consists of taking the final state particles, predicted by GENIE, and propagate them through the detector, considering its geometry. This part of the simulation is done by GEANT4, and uses information such as particles direction and their associated energy, tracker, calorimeters, and nuclear targets to produce objects that can be used by the reconstruction algorithms. More details on each step involved in the detector simulation can be found in Ref. [120].

4.4.4 MINERvA Tune v2

MINERvA Tune v2 (MnvTunev2) is the central value of this analysis, and corresponds to a series of corrections applied to the GENIE baseline simulation based on previous *in-situs* and external measured data. The ingredients comprising this specific MINERvA tuning are detailed below, and Fig. 29 illustrates the corresponding effect from each tuning component.

4.4.4.1 Random phase approximation suppression

This is a modification applied to QE processes in the low-Q^2 region using random phase approximation calculations from Nieves, Amaro, and Valverde [121]. In 2016, using neutrino-carbon dataset, MINERvA demonstrated that at low energy (q_0) and low momentum $(|q_3| < 0.5$ GeV) transfer, a 25-30 % suppression is needed to correctly describe the data [54]; see Fig. 25.

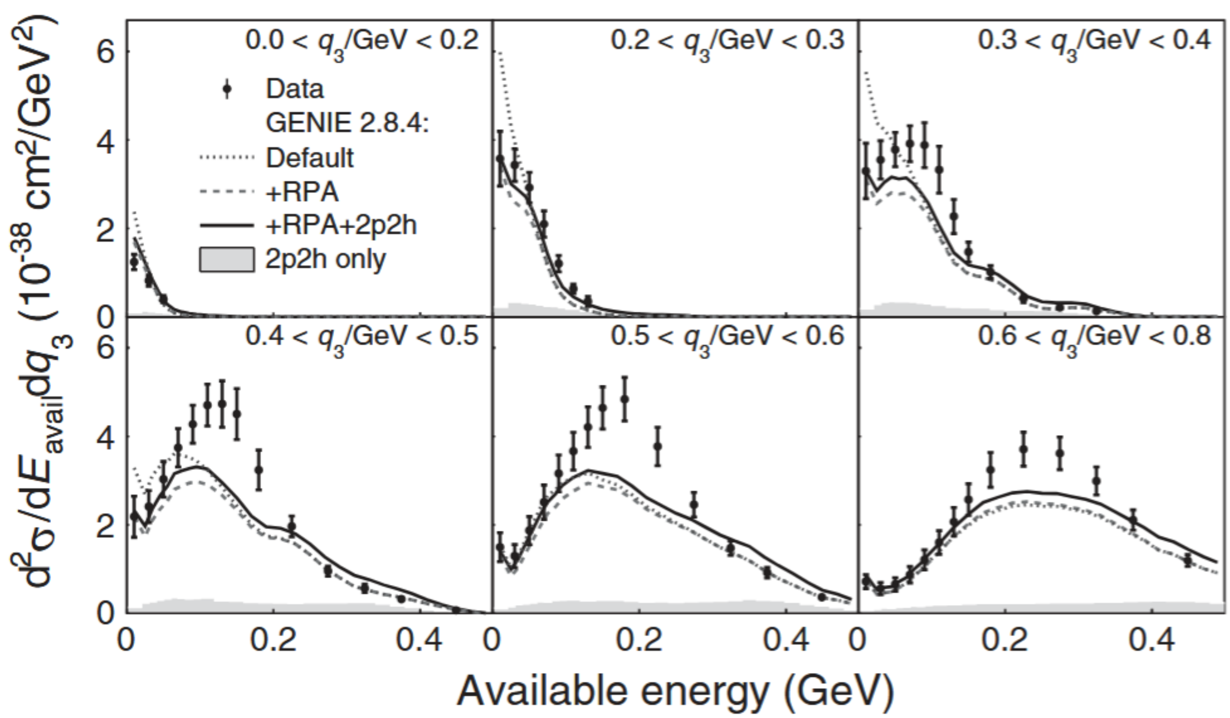

Figure 25 – Neutrino double-differential cross section in terms of available energy and three-momentum transfer. The prediction is from GENIE 2.8.4 model, with the baseline simulation shown as small dot line. The suppression from the RPA model is illustrated as long-dashed line, and the combination of quasielastic-like events with the 2p2h component as a solid line. The 2p2h component is shown separately as a shaded region. Figure reproduced from [54].

4.4.4.2 Two-particle-two-hole enhancement

The 2p2h process, discussed in the Sec. 2.3.2, is enhanced in specific regions of energy and three-momentum transfer by 50 % over the nominal Valencia prediction, based on MINERvA neutrino and antineutrino data [122, 123]; see Fig. 26.

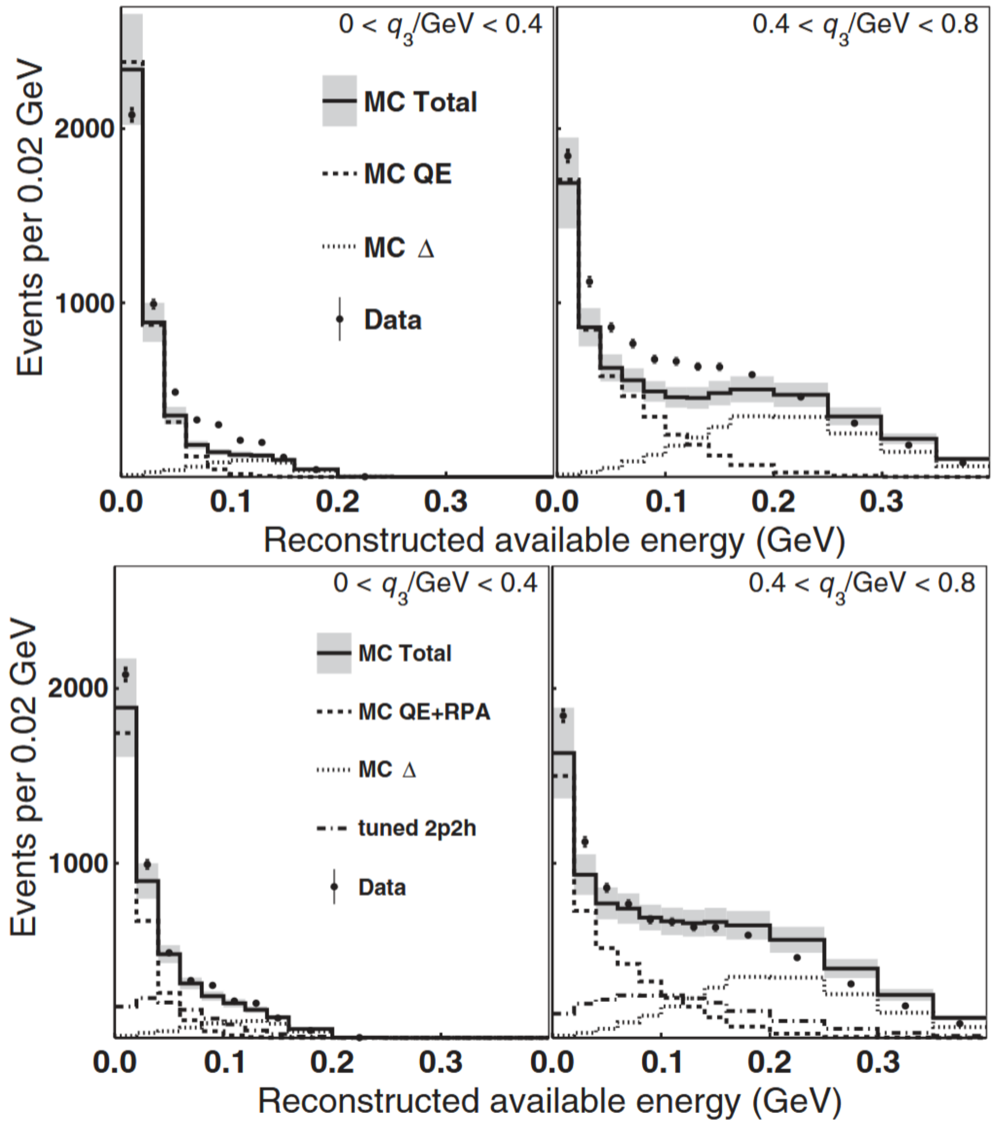

Figure 26 – Reconstructed antineutrino interactions as a function of available energy and three-momentum transfer. The panels on the left show the base GENIE Monte Carlo simulation. The right panels illustrate the tuned simulation MnvGENIE-v1: the region between the predicted CCQE process (dashed) and the $\Delta(1232)$ resonance (dotted) is filled by events generated from the Valencia 2p2h process plus additional 2p2h events (dot-dashed). Figure reproduced from [123].

4.4.4.3 Non-resonant background normalization suppression

The GENIE non-resonant background normalization contribution to the total cross section (or for short, NR1Pi) is reduced by 43 % through a fit applied to re-analyzed 12 neutrino-induced pion datasets from ANL/BNL experiments [124]; see Fig. 27.

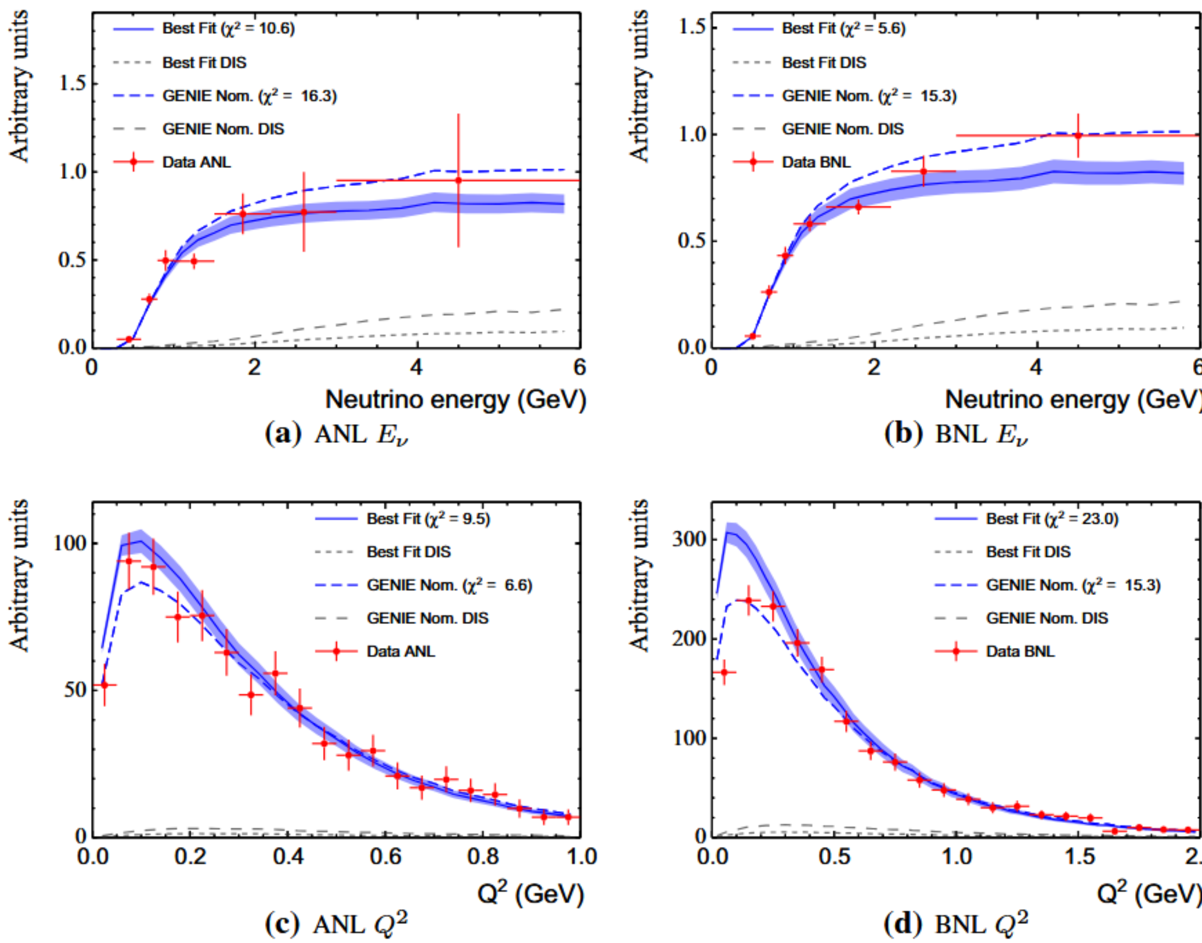

Figure 27 – One fit example taken from [54]. The plots include four $\nu_\mu p \rightarrow \mu^- p \pi^+$ datasets from ANL/BNL, and the event distributions are shown in terms of neutrino energy (top panels) and four-momentum transfer (bottom panels). The GENIE v2.8.2 nominal prediction is represented by a dashed blue line, whereas the best fit distributions are illustrated as a solid blue line, along with their corresponding χ^2. The non-resonant background prediction (GENIE Nom. DIS) before (after) fit is shown as long-dashed (short-dashed) gray line. The data are illustrated as red dots.

4.4.4.4 Low-Q^2 suppression to GENIE Δ-resonant pion production

This is an *ad-hoc* correction implemented in the GENIE resonant single-pion production model (Rein-Sehgal). Using MINERvA measurements of four charged-current single-pion production channels, a suppression is applied in the $Q^2 < 0.7$ GeV^2 region as an attempt to resolving longstanding tensions observed in MiniBooNE and MINOS experiments [125].

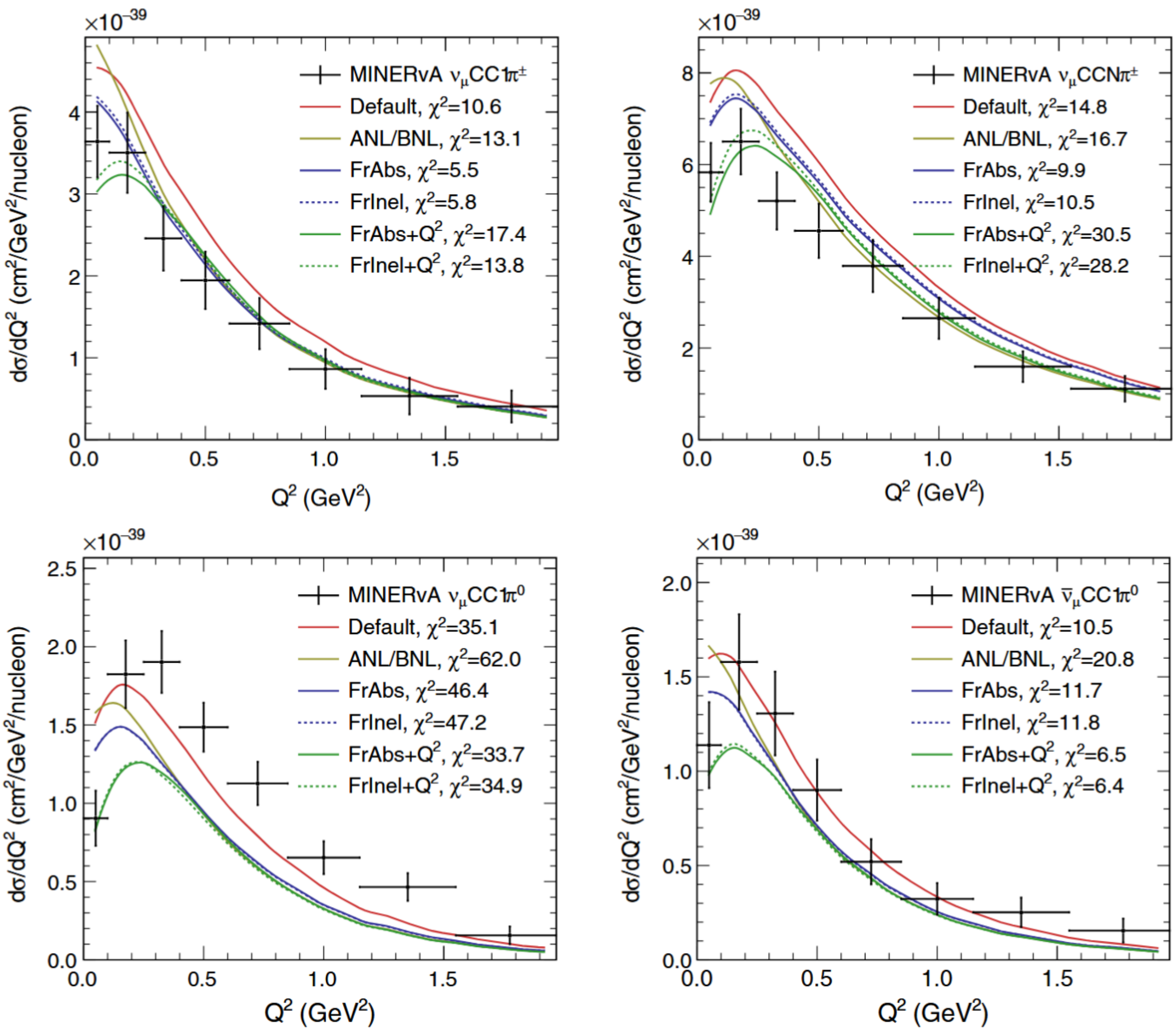

Figure 28 – Differential data cross sections measured by MINERvA (black points), and different model predictions. Default GENIE 2.12.6 model is shown in red solid line, ANL/BNL tune in yellow/olive solid line, and the GENIE FSI dials (Tab. 16) varied in the analysis are: fractional absorption (FrAbs, blue solid), fractional inelastic scattering (FrInel, blue dotted). The corresponding versions including the Low-Q^2 reweighting are shown in green solid and green dotted lines. Figure reproduced from [125].

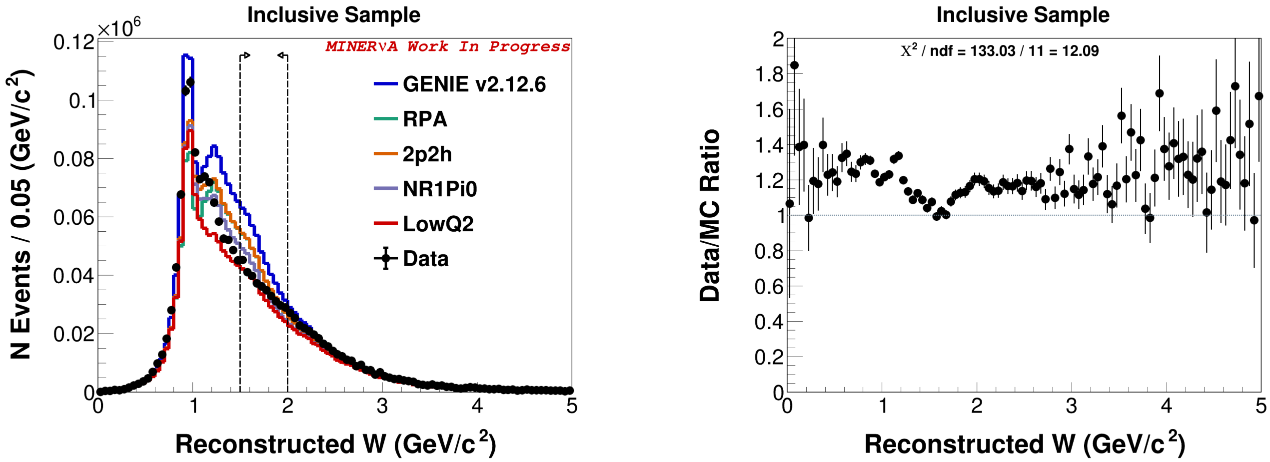

Figure 29 – (*left*): Effect of corrections (weights) applied to GENIE v2.12.6 to reduce disagreement with data; the weights are applied cumulatively in the order shown in the legend (from top to bottom); the final result, corresponding to this analysis central value (MnvTunev2), is represented by the red line; SIS region is the region between the vertical dashed lines, defined by $1.5 < \mathrm{W} < 2.0$ (GeV/c^2). (*right*): ratio between MnvTunev2 and data; the χ^2 value shown at the top is calculated for the SIS region only.

5 Data analysis

This chapter describes each step of the double-differential cross section measurement in the SIS region. In two dimensions, the cross section is defined according to the Eq. 5.1, whose terms, described in Tab. 4, will be progressively discussed in the following sections. Among the references consulted while writing this chapter there is a helpful review of various cross section extraction methods adopted by current neutrino experiments, available at [127]. Following these steps, two analyses are performed in neutrino and antineutrino modes: one for the components of the outgoing muon momentum, $(p_\mu^{\mathsf{T}}, p_\mu^{\mathsf{Z}})$ – transverse and parallel components with respect to the neutrino beam direction, respectively –, and one for the Bjorken variables (x, y), which are defined in Sec. 2.5. The final cross section results are presented and discussed in Chap. 7.

$$\left(\frac{d^2\sigma}{dxdy}\right)_i = \frac{1}{T\Phi\Delta x_i \Delta y_i}\frac{1}{\epsilon_i}\left[\sum_j \mathsf{U}_{ij}\left(\mathsf{N}^{obs} - \mathsf{N}^{bkg}\right)_j\right]. \tag{5.1}$$

Table 4 – Double-differential cross section ingredients and their descriptions.

Ingredient	Description	Section
N_j^{obs}	Number of SIS events reconstructed in bin j.	5.1
N_j^{bkg}	Number of tuned backgrounds reconstructed in bin j.	5.2
U_{ij}	Unfolding matrix element that maps reconstructed bin j into true bin i.	5.3
ϵ_i	Efficiency reconstruction and detector acceptance corrections.	5.4
$\Delta x_i \Delta y_i$	Bin widths of variables x_i and y_i.	
Φ	Integrated neutrino flux.	5.5
T	Number of targets in the fiducial volume.	

The dataset analyzed in this work was collected by the MINERvA Collaboration between September 2013 and February 2019, period also referred to as Medium Energy phase, in which the neutrino mean energy peaked at around 6 GeV. The muon momentum and Bjorken variables are binned according to the list below. The criteria adopted to determine the bin limits and edges include the kinematic constraints imposed by the analysis signal definition and selection cuts, described in the next section. Moreover, each bin must contain sufficient statistics so that the results are not dominated by statistical uncertainty. In practice, the optimization of the migration matrices (shown in Sec. 5.3) is done under two requirements: (i) more than 70% of signal events must be in the diagonal entries[1], and (ii) the fractional errors must remain below 5%.

[1] A stricter condition increases the per-bin statistics, but produces coarser binning, thereby reducing the resolution of the distributions shapes.

- p_μ^{T} (GeV) $= \{0.07, 0.15, 0.25, 0.325, 0.40, 0.475, 0.55, 0.70, 0.85, 1.0, 1.25, 1.5, 2.5\}$ (12 bins)
- p_μ^{Z} (GeV) $= \{2.5, 3.0, 3.5, 4.0, 4.5, 5.0, 6.0, 8.0, 10.0, 15.0, 20.0\}$ (10 bins)
- Bjorken-x $= \{0.01, 0.031, 0.084, 0.186, 0.36, 0.70\}$ (5 bins)
- Bjorken-y $= \{0.00, 0.15, 0.25, 0.35, 0.50\}$ (4 bins)

5.1 Event selection

The starting point of any cross section analysis consists of establishing a precise definition for the signal events of interest and an estimate of all possible sources of background (*i.e.*, those events that do not attend the signal definition criteria). Based on these definitions and on the detector ability to identify those signal events, one designs and applies a set of cuts to select, among all reconstructed events, those interactions classified as signal while keeping the background contamination as low as possible. In this section, two terms of Eq. 5.1 are determined for this analysis: N^{obs} and N^{bkg}, the reconstructed SIS events, and their corresponding backgrounds.

5.1.1 Analysis' signal and backgrounds

As discussed in Sec. 3.1, the SIS transition region is made of higher-resonances, non-resonant and multi-quark meson production via lepton-nucleon interactions. In particular, this analysis is focused at muon neutrinos and antineutrinos interacting in the SIS region via charged-current processes with the MINERvA hydrocarbon target.

These processes are generally described by Eq. 5.2. The SIS interaction signature left in the detector is characterized by a muon (or anti-muon) in the final state, μ (μ^+), and the hadronic system, X, contains one or multiple pions.

$$\nu_\mu + \mathrm{CH} \rightarrow \mathrm{X} + \mu. \tag{5.2}$$

Since as of today it is not possible to experimentally separate resonant from non-resonant pion production (and their interference terms), in practice these processes are investigated in this analysis under a kinematic constraint that emphasizes interactions in the SIS region.

Such a constraint is stated by item 1. on the list below, and reflects the experimental definition of SIS – a lower limit of 1.5 GeV on the invariant mass of the hadronic system, $\mathrm{W}_{\mathrm{true}}$, is chosen to avoid the $\Delta(1232)$-resonant background, whereas the upper limit of 2.0 GeV is set to reduce the contamination of single-quark DIS events. The remaining conditions on the signal definition list are detector-related constraints, adopted to detect high-statistics neutrino interactions with acceptable efficiency.

1. $Q^2_{\text{true}} > 0$ GeV^2 and $1.5 < W_{\text{true}} < 2.0$ GeV;
2. Charged-current $\nu_\mu/\bar{\nu}_\mu$;
3. Muon energy $2 < E_{\mu^\pm,\text{true}} < 20$ GeV;
4. Muon angle $\theta_{\mu^\pm,\text{true}} < 20°$;
5. Interaction on hydrocarbon target.

Given that the analysis' signal is essentially defined by a W kinematic range isolating SIS interactions, then any other interaction channel is classified as a background event. Again, in terms of the experimental version (nucleon at rest) of GENIE 2.12.6 prediction for the invariant mass of the hadronic system, 3 regions are designed to represent non-SIS events: QE, $\Delta(1232)$-RES, and DIS interactions. Furthermore, one should add neutral-current, electron-neutrinos, and wrong flavor interactions, altogether labeled as non-CC$\nu_\mu/\bar{\nu}_\mu$, and the total sources of background are 4.

These backgrounds are listed in Tab. 5, and illustrated in Fig. 30. Since the non-CC$\nu_\mu/\bar{\nu}_\mu$ background events do not contribute significantly to the SIS region (see Sec. 5.1.2), they will not be included in the background tuning process. Moreover, it is worth noting that events escaping the muon angle and energy regions, as well as those SIS interactions outside of the fiducial volume will be accounted for during the efficiency correction step, a later stage of the cross section extraction procedure, discussed in Sec. 5.4.

Table 5 – Based on GENIE 2.12.6 interaction channels, the background is classified by kinematic cuts on the invariant mass, W. The regions around the signal is enriched with QE, $\Delta(1232)$-RES, and DIS events, and are depicted in Fig. 30.

W regions	Plot legend labels
$0.00 < W_{\text{true}} < 1.15$	QE$_{bkg}$
$1.15 < W_{\text{true}} < 1.50$	RES$_{bkg}$
$W_{\text{true}} > 2.00$	DIS$_{bkg}$
non-CC$\nu_\mu/\bar{\nu}_\mu$	

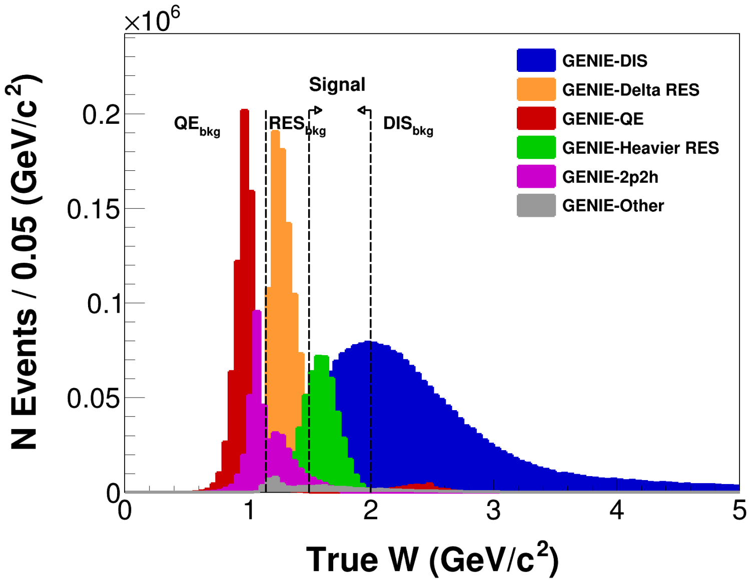

Figure 30 – Using GENIE 2.12.6, the inclusive sample is split into the true SIS signal and background, modeled according to the W limits defined in Tab. 5: regions populated by QE, $\Delta(1232)$-RES and DIS events. Illustration made using a neutrino prediction.

5.1.2 Selection cuts

Having established the signal definition and identified the main sources of background contamination based on physics processes, a series of selection cuts is applied to both reconstructed simulation and data events. These cuts are designed to reject as much background as possible while maintaining high signal efficiency.

As described in Chap. 4, at neutrino interactions are reconstructed by combining measurements of energy depositions in two detectors: at MINERvA and MINOS near detectors. Over the years, extensive studies within MINERvA have led to a standardized set of selection cuts that are common to several cross section analyses. These cuts account for operational characteristics of both the MINERvA and MINOS detectors, and are summarized in Tab. 6; in particular, the final entry in the table is introduced to select events in the SIS region.

Table 6 – Selection cuts applied to reconstructed simulation and data events.

Cut	Description
Helicity	The curvature of a muon track, observed in MINOS, is used to distinguish neutrino and antineutrino interactions: negative (positive) curvatures are associated to muon neutrino (antineutrino). This cut is essential to reduce the contamination of a different neutrino helicity for a given neutrino flavor.
Muon angle and energy	The muon angle (with respect to the incident neutrino) must be less than 20°, and its energy between 2 and 20 GeV. Previous studies [103] showed that these cuts are necessary because the MINOS detection acceptance and efficiency drop significantly for values outside the specified range.
Muon coil and curvature	Muons observed in MINOS must fall in the fiducial volume defined by the radius interval $210 < \mathrm{R} < 2500$ mm and have a curvature significance level of at least 5σ in order to reduce resolution tails. Previous studies (available internally to the collaboration only) showed that these cuts improve the muon resolution by 20 %.
Fiducial volume	In order to make sure the neutrino interactions take place on MINERvA hydrocarbon target, the interaction vertex must be located within the detector hexagonal area defined by apothem of 850 mm and between the modules 27 and 80.
Dead time	This cut ensures all PMTs upstream the reconstructed interaction vertex (in the MINERvA detector) are not in a "dead time" state, a period of time in which the PMTs are insensitive to new signals after recording an event. If more than one PMT is in dead time, the event is rejected. This is essential to track and prevent rock muons, which typically enter from upstream, making sure the muon track observed in MINOS and MINERvA was originated in the interaction vertex, located in the fiducial volume.
SIS	Events must be reconstructed in the SIS signal region, *i.e.* their invariant mass, $\mathrm{W}_{\mathrm{reco}}$, must be within 1.5 and 2.0 GeV, and the four-momentum transfer squared $\mathrm{Q}^2_{\mathrm{reco}} > 0$ GeV^2.

The implementation of these cuts results in 673,940 (362,802) reconstructed neutrino (antineutrino) interactions in the data sample, and 584,523 (314,805) reconstructed simulated neutrino (antineutrino) events. From these raw numbers, it is clear that, at this stage of the cross section extraction process, the simulation underestimates the data; this effect is illustrated in Figs. 31 and 32. Despite this, the simulation can be used to examine the sample composition in more detail − specifically, to estimate the fraction of events that are true SIS, their classification according to GENIE interaction types, and the extent of background contamination.

In Tab. 7, the simulated events are divided into true SIS signal and background: about 64 % (68 %) is signal, and 36 % (32 %) is background in the neutrino (antineutrino) sample. Since these percentages are calculated with respect to the total reconstructed simulated events, the signal fractions represent the sample purity, a metric defined in Eq. 5.3.

The simulated signal is further categorized according to GENIE processes, with the RES channel subdivided into Delta and heavier resonances. From this classification, it is evident that GENIE-DIS contributes the majority of the SIS signal in both neutrino and antineutrino modes, followed by GENIE-Heavier RES. Meanwhile, RES$_{bkg}$ and DIS$_{bkg}$ together correspond to nearly half of the true SIS signal, making this analysis particularly challenging, as these components must ultimately be constrained and removed from the sample.

The events listed in Tab. 7 are illustrated in Figs. 31 and 32 as stacked plots for the neutrino mode: true SIS in green, QE$_{bkg}$ in red, RES$_{bkg}$ in yellow and DIS$_{bkg}$ in blue – the nonCC$\nu_\mu/\bar{\nu}_{\mu,bkg}$ category is not shown in the figure and will not be included in the background tuning process due to its negligible contribution.

For both the Bjorken and muon distributions, the DIS$_{bkg}$ component is present across all panels. In the former case, it shows up most prominently in the highest y-bin, as expected (see Sec. 2.5). The next major background components, RES$_{bkg}$ and QE$_{bkg}$, dominate the low-energy regime. In terms of Bjorken variables, they are concentrated in the lowest y-panels and decreases as the neutrino energy increases; in terms of muon momentum components, due to the binning, only the RES$_{bkg}$ background remains visible.

Table 7 – Simulated SIS signal and background in neutrino and antineutrino samples. Columns 2 and 4 contain the raw numbers of events; columns 3 and 5 show the corresponding percentage values. The SIS signal is broken down according to GENIE interaction processes, with the resonant category further divided into Delta and heavier baryonic masses.

	ν_μ-mode		$\bar{\nu}_\mu$-mode	
Process	# Events	(%)	# Events	(%)
Signal				
True SIS signal	374,591	**64.08**	215,298	**68.39**
GENIE signal composition				
QE	138	0.02	42	0.01
RES (total)	132,121	22.60	78,484	24.93
Δ RES	31,356	5.36	13,489	4.28
Heavier RES	100,766	17.24	64,995	20.65
DIS	226,312	38.72	126,461	40.17
2p2h	7,469	1.28	3,351	1.06
Other	8,550	1.46	6,961	2.21
Backgrounds (total)	209,932	**35.92**	99,507	**31.61**
Background composition				
QE_{bkg}	17,830	3.05	9,992	3.17
RES_{bkg}	89,098	15.24	40,666	12.92
DIS_{bkg}	102,621	17.56	48,424	15.38
nonCC $\nu_\mu/\bar{\nu}_\mu$	382	0.07	425	0.13

$$\text{Purity} = \frac{\text{Signal events in the reconstructed sample}}{\text{All events in the reconstructed sample}} \tag{5.3}$$

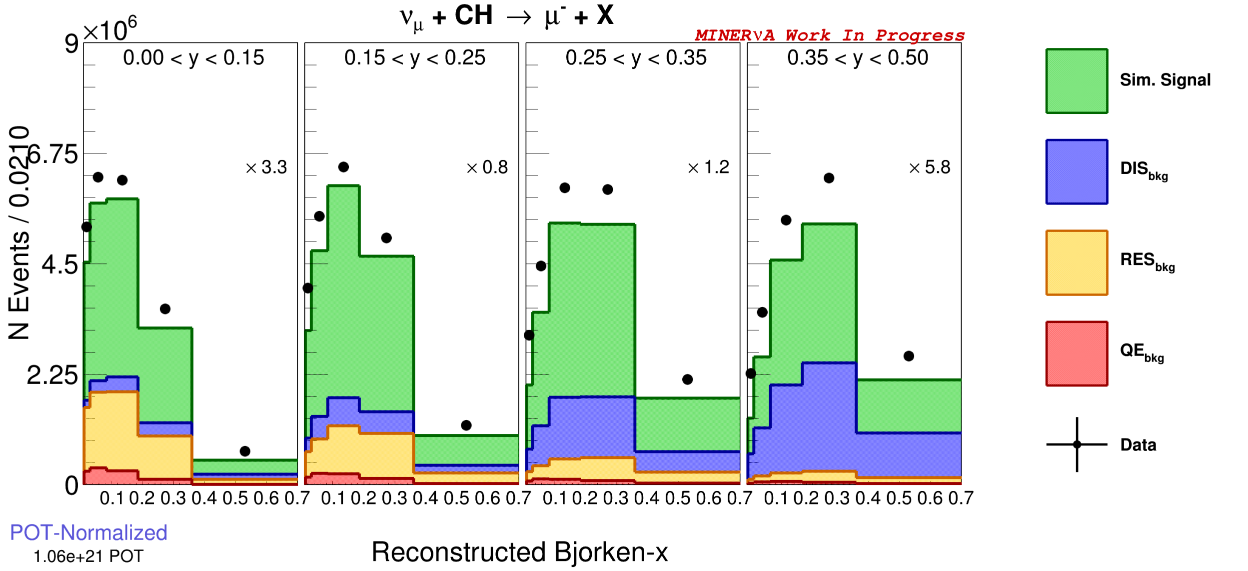

Figure 31 – Selected **neutrino events in the signal region** shown in terms of **Bjorken variables**. The plot displays the data points (black) and the simulated events, stacked in descending order of contribution: signal (green), DIS$_{bkg}$ (blue), RES$_{bkg}$ (yellow) and QE$_{bkg}$ (red). At this stage, the data points carry only statistical uncertainties, represented by (non-visible) error bars.

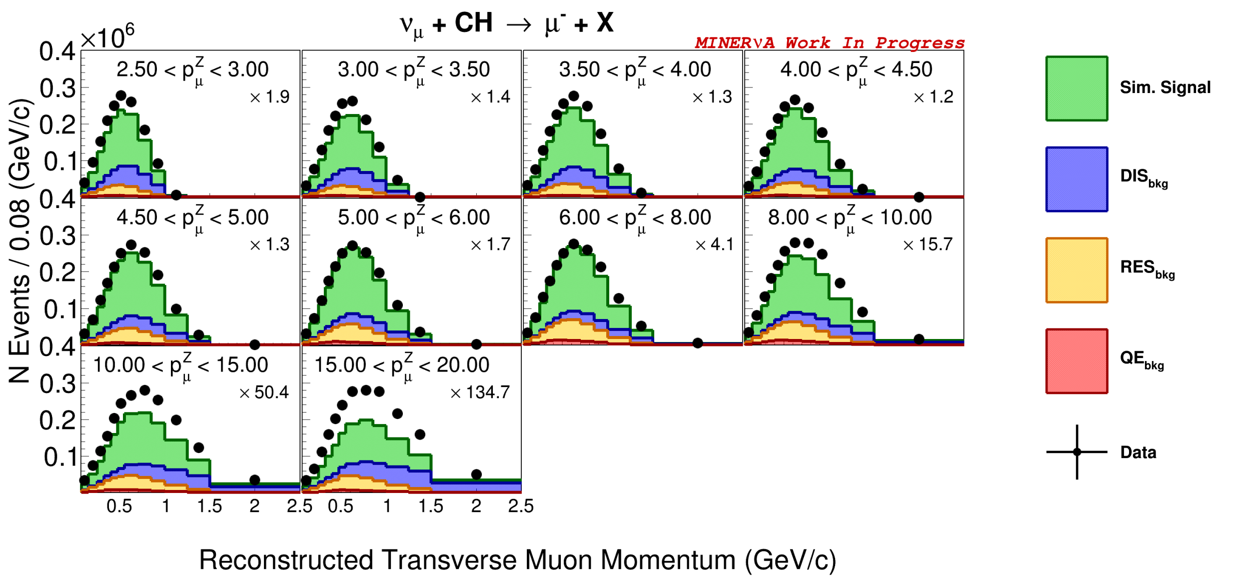

Figure 32 – Selected **neutrino events in the signal region** shown in terms of **muon momentum components**. The plot displays the data points (black) and the simulated events, stacked in descending order of contribution: signal (green), DIS$_{bkg}$ (blue), RES$_{bkg}$ (yellow) and QE$_{bkg}$ (red). At this stage, the data points carry only statistical uncertainties, represented by (non-visible) error bars.

5.2 Background subtraction

The next step in the cross section extraction procedure is the removal of residual background from both reconstructed data and simulated samples, ensuring the measurement reflects the true number of signal events. In Eq. 5.1, the background contribution is denoted by N^{bkg}. As shown in Tab. 7, the estimated fraction of background events in the neutrino (antineutrino) sample is 35 % (32 %), and similar fractions are assumed to be present in the reconstructed data sample as well.

In simulation, isolating the signal is not a big deal: non-signal events are removed directly from the selection. However, in data, given the large background contamination and its inference from truth-level generator prediction, an intermediate step is crucial to extract data signal cross sections with minimum bias – as it will be shown in Secs. 7.1 and 7.2, the simulation does not model neutrino interactions properly; that is why a data-driven correction is fundamental: to make sure the result does not depend on the adopted generator, and its assumptions and conventions.

The backgrounds are constrained and validated through a *sideband tuning* technique, where the data are used to adjust (tune) the normalization and/or shape of the MC-predicted backgrounds in regions of phase space enriched in non-signal events, but poor in signal. By using the data to measure certain *scale factors* in these background-rich regions, referred to as *sidebands*, the tuned simulation represents less biased, more accurate, realistic estimate for non-signal events in the selected data sample. Moreover, it should be noted that, according to this cross section extraction procedure, from now on the data carry both the statistical and systematic uncertainty components, whose sources will be detailed in Chap. 6.

5.2.1 Sidebands definitions

For this analysis, three sidebands are used to adjust the background in the data sample. They are defined in Tab. 8 and correspond to regions enriched in non-SIS events – specifically DIS, RES and QE events – according to the classification in Tab. 5. This time, it is not the true version of the simulation, but its reconstructed counterpart, used to define these kinematic ranges, based on studies of signal purity, contamination and efficiency, discussed in the Append. B.

Fig. 33 shows the reconstructed invariant mass distribution, W_{reco}, divided into the SIS signal region and sidebands populated by specific background sources. Notice that two gaps ($1.30 < W_{reco} < 1.50$ and $2.00 < W_{reco} < 2.30$) are intentionally left to minimize the signal contamination in the sideband regions.

Table 8 – Using the simulation, three background-rich regions are defined in terms of the reconstructed invariant mass, $\mathsf{W}_{\mathsf{reco}}$. These regions, also referred to as sidebands, are predominantly populated by QE, Delta RES, and DIS events, as shown in Fig. 33.

$\mathsf{W}_{\mathsf{reco}}$ regions	Label
$0.00 < \mathsf{W}_{\mathsf{reco}} < 1.15$	Sideband 0
$1.15 < \mathsf{W}_{\mathsf{reco}} < 1.30$	Sideband 1
$2.30 < \mathsf{W}_{\mathsf{reco}} < 3.00$	Sideband 2

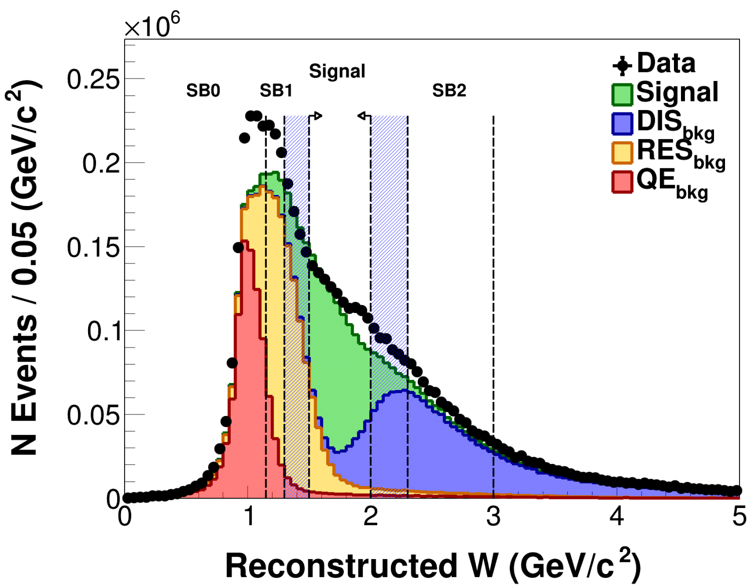

Figure 33 – Simulated neutrino inclusive sample as a function of the reconstructed invariant mass, $\mathsf{W}_{\mathsf{reco}}$. Three regions adjacent to the SIS signal are defined to characterize the analysis background: sidebands 0, 1 and 2, as specified in Tab. 8.

5.2.2 Background constraint method

The MC-predicted backgrounds are corrected by applying scale factors determined through the minimization of a χ^2 function. The reconstructed four-momentum transfer squared, $\mathsf{Q}^2_{\mathsf{reco}}$, was selected to define this function. It was identified as the most effective tuning variable for this analysis, as it reduces data–MC discrepancies while keeping statistical uncertainties under control.

The minimization is performed using ROOT in-built library `Minuit2` [128], applying a bin-by-bin approach to a global χ^2, defined in Eq. 5.4. This bin-by-bin method provides both a normalization correction and an adjustment of the MC distribution shape.

$$\chi^2 = \chi^2_{\mathsf{Sideband\ 0}} + \chi^2_{\mathsf{Sideband\ 1}} + \chi^2_{\mathsf{Sideband\ 2}}, \tag{5.4}$$

where $\chi^2_{\mathsf{Sideband\ k}}$ $(k = 0, 1, 2)$ for each sideband is computed through

$$\chi^2_{\mathsf{Sideband\ k}} = \sum_{i=1}^{\mathsf{nBins}} \frac{(\mathsf{MC}_i - \mathsf{Data}_i)^2}{\mathsf{Data}_i}.$$

The scale factors, w_i^j, correct only the major sources of background $j =$ QE$_{bkg}$, RES$_{bkg}$, and DIS$_{bkg}$, and are extracted from

$$\text{MC}_i = \text{MC}_i^{\text{Sim. Signal}} + \text{MC}_i^{\text{nonCC}\nu_\mu} + \sum_j w_i^j \times \text{MC}_i^j. \tag{5.5}$$

The resulting scale factors are shown in Figs. 34 and 35 for neutrino and antineutrino modes, respectively[2]. From these figures, it is evident that, in the $\text{Q}^2_{\text{reco}} < 1$ GeV^2 region, the DIS$_{bkg}$ background component receives the largest correction, reflecting its underprediction by the simulation – an effect that is even more pronounced in the antineutrino case. As Q^2_{reco} increases, the other two background components, QE$_{bkg}$ and RES$_{bkg}$, depart to opposite directions, indicating that QE events are overpredicted at high-Q^2, while Δ resonant single-pion production in MC falls with Q^2. The last two bins, being low populated, are particularly subject to statistical fluctuations – for a more detailed discussion, see Sec. 7.3. The corresponding scale factor values, accompanied by their statistical and systematic errors, are listed in Tab. 9, for neutrino and antineutrino modes, respectively.

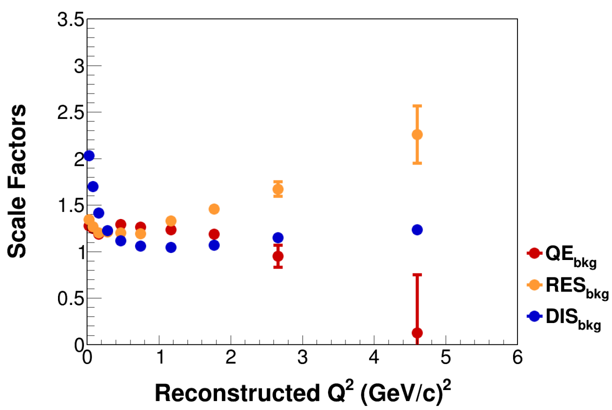

Figure 34 – Scale factors for neutrino mode.

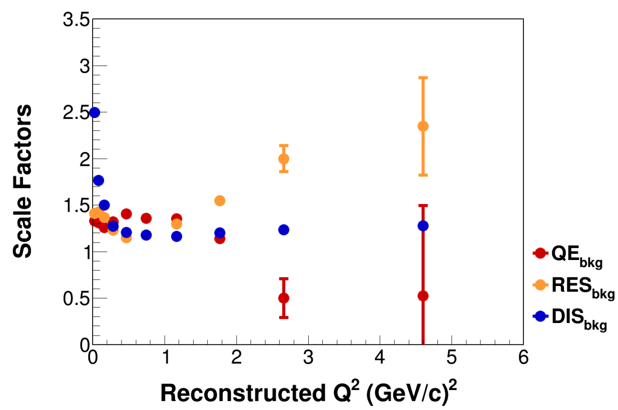

Figure 35 – Scale factors for antineutrino mode.

- Q^2 (GeV^2) $= \{0.00, 0.05, 0.11, 0.21, 0.36, 0.58, 0.91, 1.42, 2.12, 3.20, 6.00\}$ (10 bins)

[2] Error bars refer to statistical uncertainties only.

Table 9 – Scale factor values with their corresponding statistical and systematic uncertainties, measured using a data-driven technique, as described in the text.

Neutrino sample (FHC)			
Bin	QE_{bkg}	RES_{bkg}	DIS_{bkg}
1	1.278 ± 0.008 ± 0.406	1.604 ± 0.011 ± 1.211	2.033 ± 0.030 ± 2.187
2	1.253 ± 0.006 ± 0.399	1.638 ± 0.011 ± 1.403	1.711 ± 0.019 ± 1.505
3	1.190 ± 0.005 ± 0.378	1.521 ± 0.009 ± 1.217	1.431 ± 0.011 ± 1.109
4	1.221 ± 0.005 ± 0.385	1.406 ± 0.008 ± 0.756	1.241 ± 0.008 ± 0.740
5	1.294 ± 0.006 ± 0.407	1.269 ± 0.008 ± 0.448	1.125 ± 0.006 ± 0.673
6	1.266 ± 0.007 ± 0.393	1.198 ± 0.010 ± 0.513	1.062 ± 0.005 ± 0.732
7	1.243 ± 0.012 ± 0.362	1.322 ± 0.016 ± 0.511	1.044 ± 0.004 ± 0.924
8	1.197 ± 0.031 ± 0.266	1.442 ± 0.030 ± 0.877	1.070 ± 0.005 ± 1.157
9	0.975 ± 0.118 ± 0.101	1.638 ± 0.079 ± 2.069	1.148 ± 0.007 ± 1.952
10	0.171 ± 0.621 ± 0.465	2.177 ± 0.307 ± 6.483	1.236 ± 0.009 ± 5.827
Antineutrino sample (RHC)			
Bin	QE_{bkg}	RES_{bkg}	DIS_{bkg}
1	1.328 ± 0.008 ± 0.586	1.409 ± 0.011 ± 0.670	2.497 ± 0.049 ± 3.823
2	1.311 ± 0.006 ± 0.579	1.424 ± 0.011 ± 0.726	1.768 ± 0.028 ± 1.525
3	1.261 ± 0.005 ± 0.555	1.369 ± 0.009 ± 0.701	1.499 ± 0.017 ± 0.934
4	1.321 ± 0.005 ± 0.577	1.230 ± 0.009 ± 0.676	1.274 ± 0.011 ± 0.648
5	1.405 ± 0.006 ± 0.606	1.151 ± 0.009 ± 1.104	1.208 ± 0.009 ± 1.003
6	1.359 ± 0.009 ± 0.568	1.177 ± 0.012 ± 0.907	1.178 ± 0.008 ± 0.871
7	1.351 ± 0.017 ± 0.512	1.297 ± 0.020 ± 0.697	1.163 ± 0.008 ± 0.851
8	1.143 ± 0.050 ± 0.269	1.546 ± 0.045 ± 1.539	1.200 ± 0.010 ± 1.469
9	0.501 ± 0.209 ± 0.359	1.999 ± 0.139 ± 5.256	1.235 ± 0.014 ± 4.606
10	0.525 ± 0.970 ± 0.590	2.346 ± 0.523 ± 6.147	1.280 ± 0.021 ± 5.698

A technical detail: once extracted, these scale factors are applied in both sideband and signal regions by extending the phase space from two to three dimensions, introducing the tuning variable Q^2 as the third coordinate, (x,y,Q^2). The original two-dimensional space is then recovered by projecting $(x,y,Q^2) \mapsto (x,y)$.

5.2.3 Background tuning result

Let's analyze the performance of this background constraint method by considering, for instance, the most important sideband region of this analysis: sideband 2 − the tuning effect for all other sidebands are shown in Append. B.2, which includes both the Bjorken and muon analyses, in neutrino and antineutrino modes. Fig. 36 shows the events distribution in terms of Bjorken variables before the tuning, and Fig. 37 displays the data/MC ratios before (red) and after (black) the tuning; the muon momentum components case is shown in Figs. 38 and 39.

The ratio plots in Figs. 37 and 39 clearly show that the tuned simulation reduces the data/MC discrepancies for both Bjorken and muon distributions. While the scale factors struggle to repair the shape/model mismatches in some y-bins – specifically, the first two Bjorken-y panels –, for the muon momentum distributions they provide a better description of the data – especially in the $p_{\mu}^{T} < 0.7$ GeV region. And that is not a surprise. As discussed in Chap. 2, the Bjorken variables are derived, hadronic-energy-dependent quantities, with much stronger model dependence than the muon kinematics. The same observations apply to antineutrino distributions, shown in the aforementioned appendix.

The scale factors, extracted from the sideband data, are then used to correct the three background processes in the simulated signal region. The pos-fit distributions are shown in Figs. 40 and 42, and Fig.s 41 and 43 display the data/MC ratios before (red) and after (black) the Q^2 fit. From these plots, the general remark is that the scaling of the background sources by those weights improves the SIS data modeling.

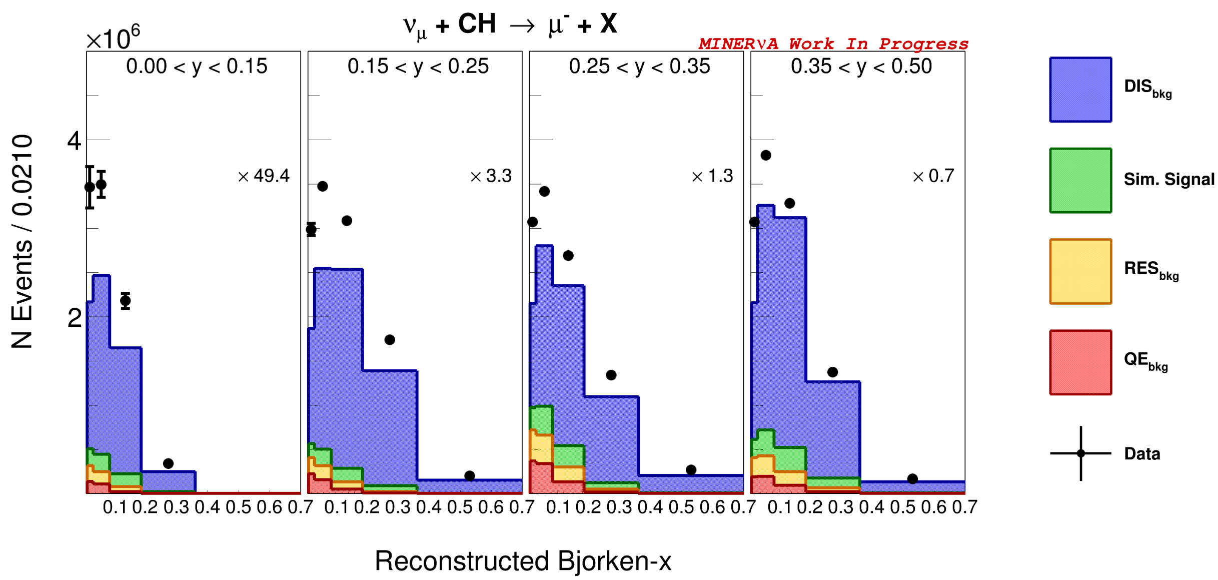

Figure 36 – Selected **neutrino events in Sideband 2** (DIS-rich) shown in terms of **Bjorken variables**. The plot displays the data points (black) and the simulated events, stacked in descending order of contribution: DIS$_{bkg}$ (blue), signal (green), RES$_{bkg}$ (yellow), and QE$_{bkg}$ (red). The error bars on the data represent statistical uncertainties only.

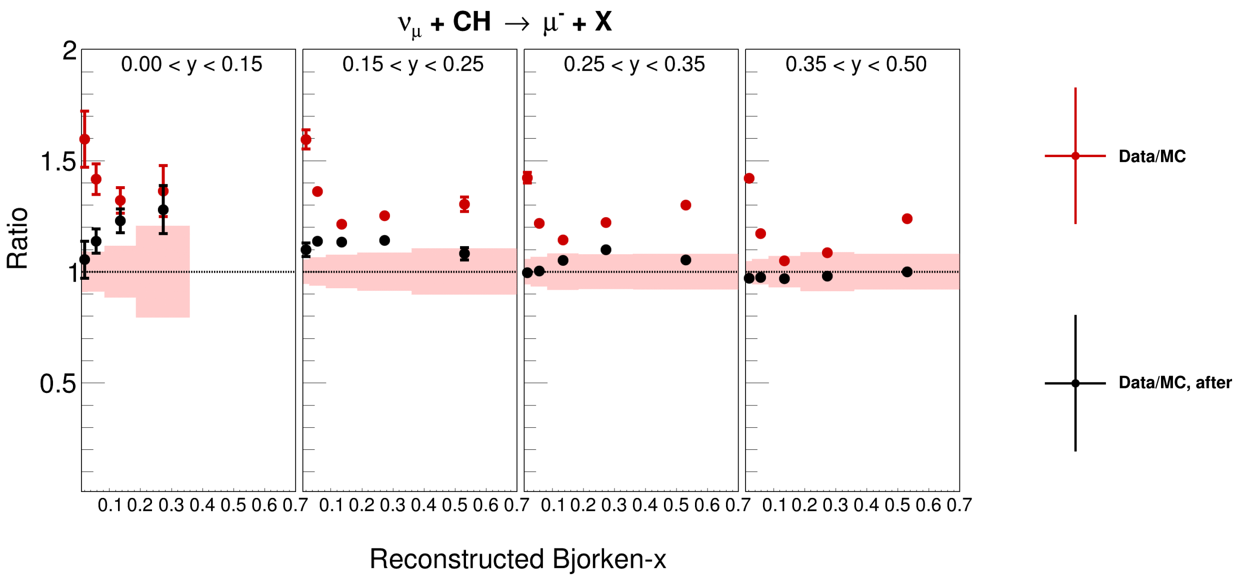

Figure 37 – Data-to-MC ratios in **Sideband 2** as a function of **Bjorken variables**. Red (black) dots represent the data/MC ratio before (after) tuning the background. Error bars indicate statistical uncertainty, while the pink error band around line one represents the total (statistical+systematic) uncertainty on the simulation. Results are shown for **neutrino mode**.

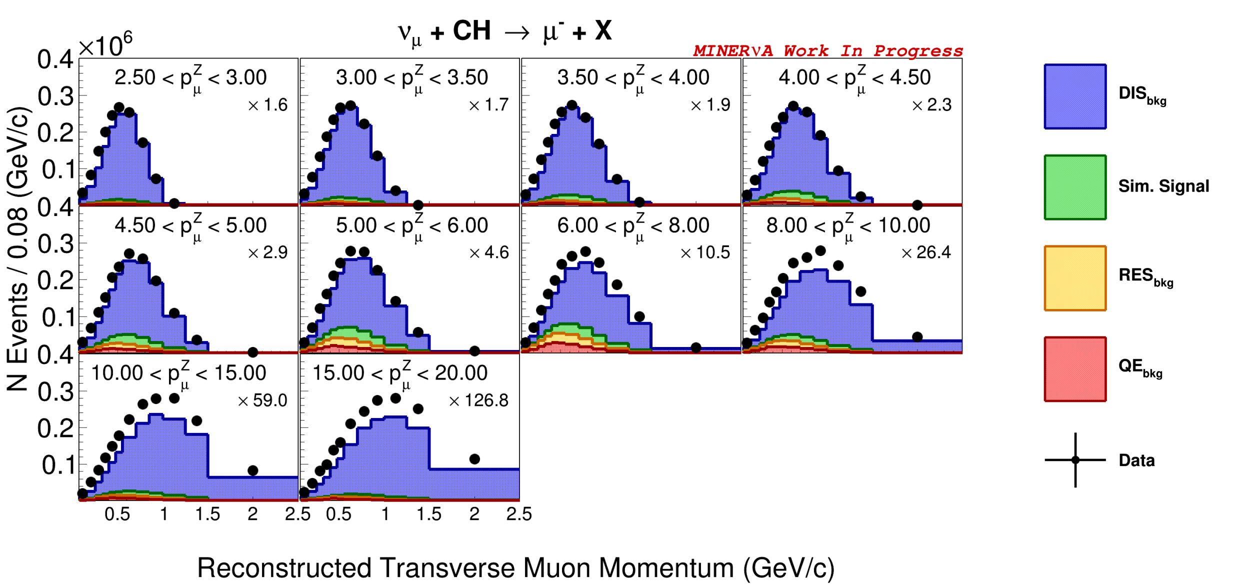

Figure 38 – Selected **neutrino events in Sideband 2** (DIS-rich) shown in terms of **muon momentum components**. The plot displays the data points (black) and the simulated events, stacked in descending order of contribution: DIS_{bkg} (blue), signal (green), RES_{bkg} (yellow), and QE_{bkg} (red). The error bars on the data represent statistical uncertainties only.

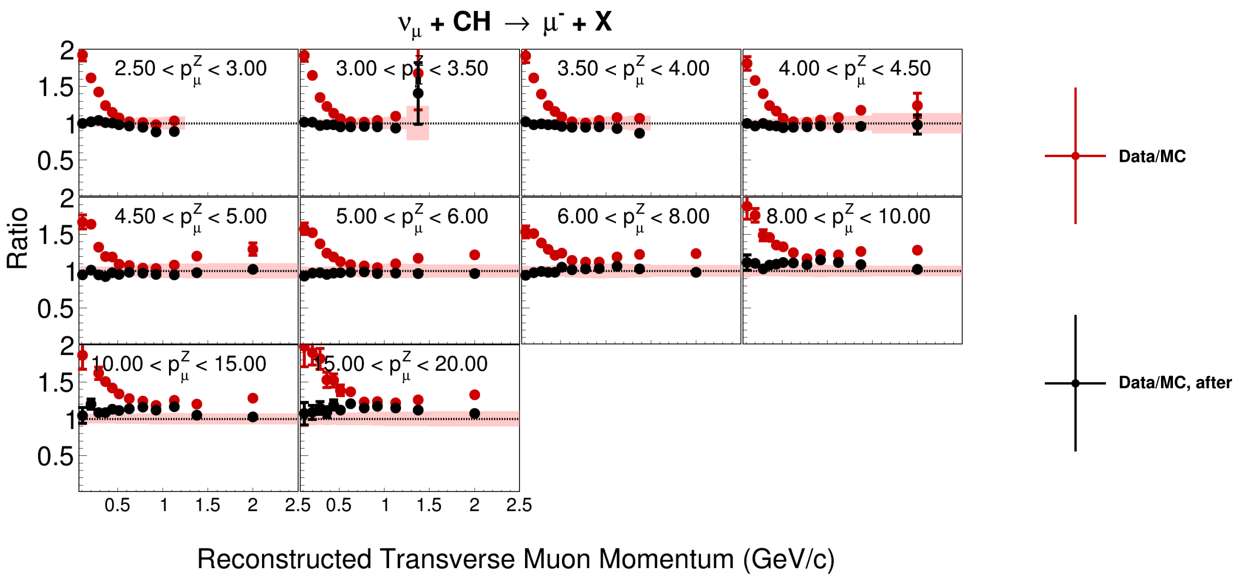

Figure 39 – Data-to-MC ratios in **Sideband 2** as a function of **muon momentum components**. Red (black) dots represent the data/MC ratio before (after) tuning the background. Error bars indicate statistical uncertainty, while the pink error band around line one represents the total (statistical+systematic) uncertainty on the simulation. Results are shown for **neutrino mode**.

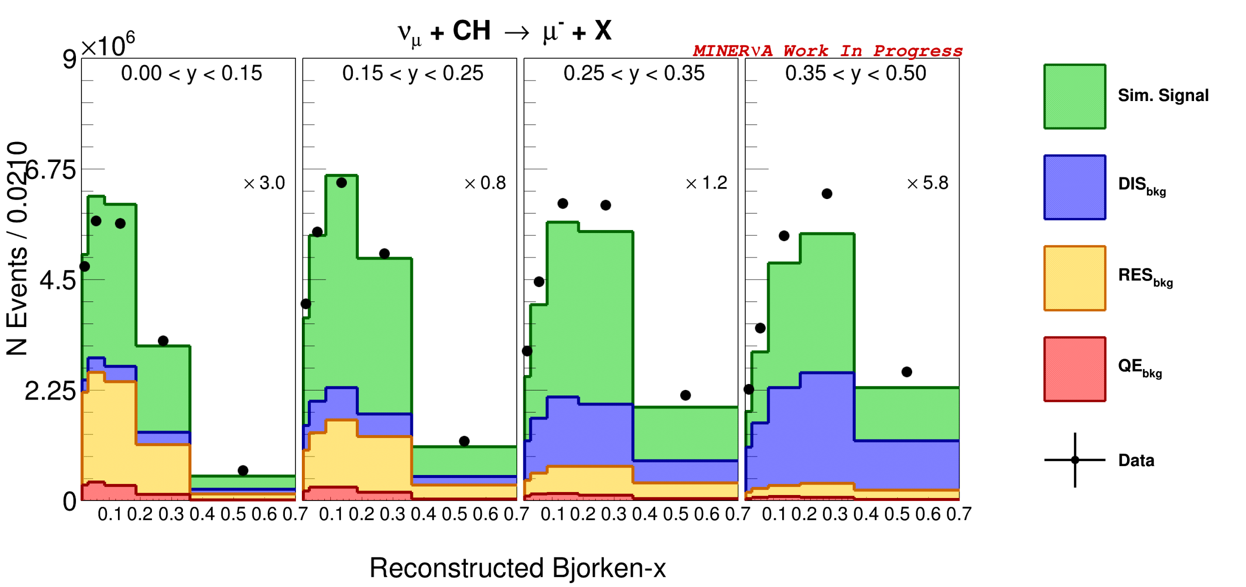

Figure 40 – Selected **neutrino events in the signal region** shown in terms of **Bjorken variables**. The plot displays the data points (black) and the **tuned simulated events**, stacked in descending order of contribution: signal (green), DIS$_{bkg}$ (blue), RES$_{bkg}$ (yellow) and QE$_{bkg}$ (red). The error bars on the data represent statistical uncertainties only.

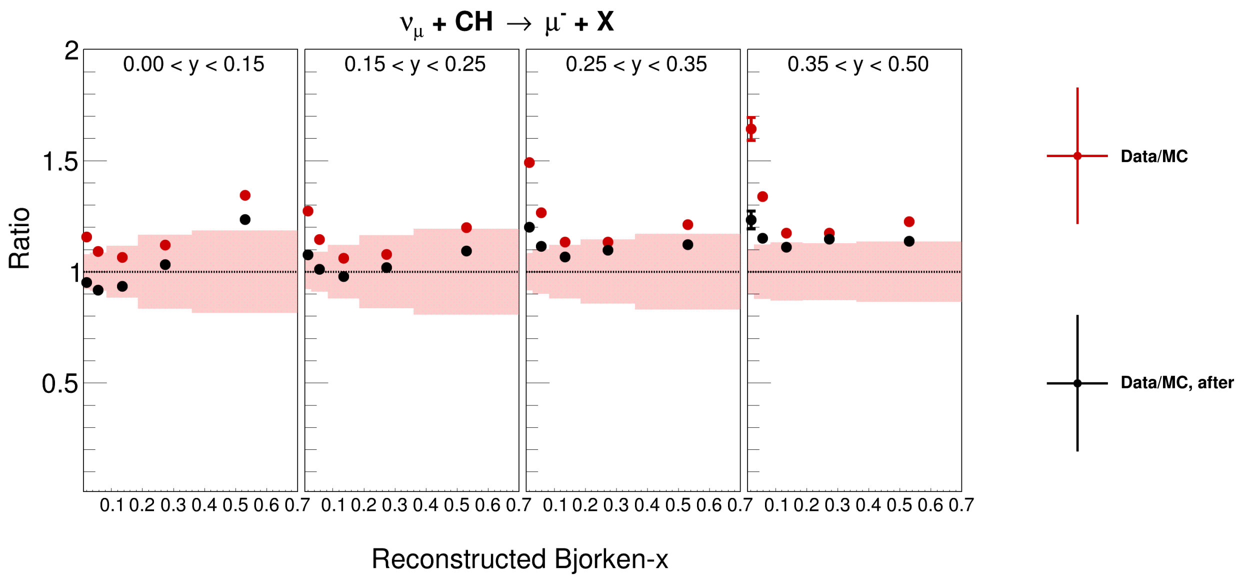

Figure 41 – Data-to-MC ratios in the **signal region** as a function of **Bjorken variables**. Red (black) dots represent the data/MC ratio before (after) tuning the background. Error bars indicate statistical uncertainty, while the pink error band around line one represents the total (statistical+systematic) uncertainty on the simulation. Results are shown for **neutrino mode**.

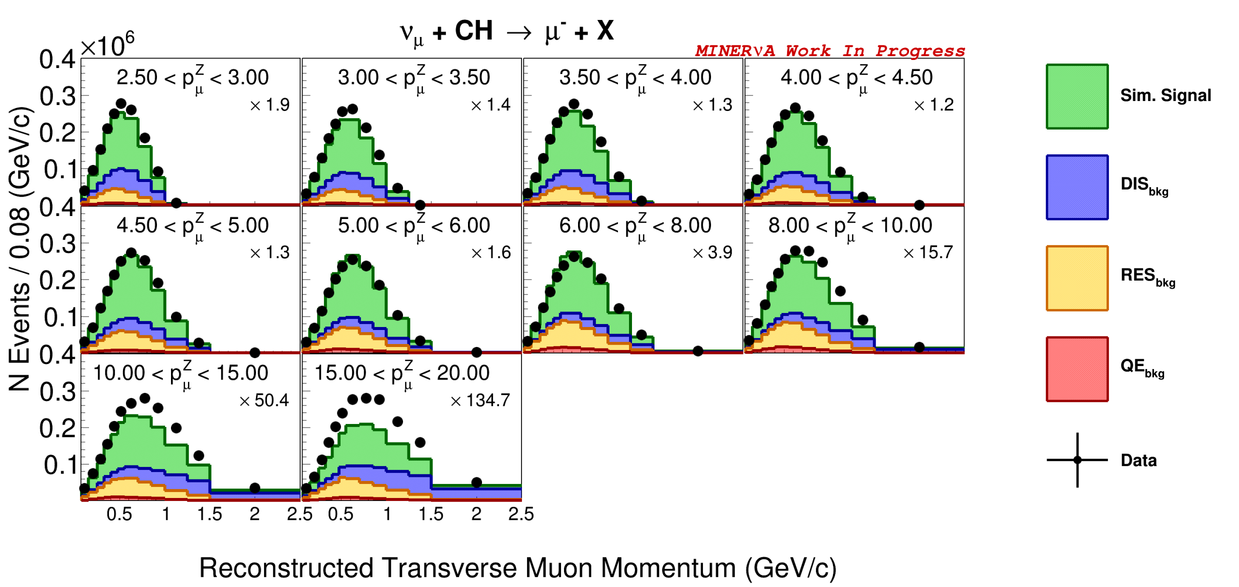

Figure 42 – Selected **neutrino events in the signal region** shown in terms of **muon momentum components**. The plot displays the data points (black) and the **tuned simulated events**, stacked in descending order of contribution: signal (green), DIS_{bkg} (blue), RES_{bkg} (yellow) and QE_{bkg} (red). The error bars on the data represent statistical uncertainties only.

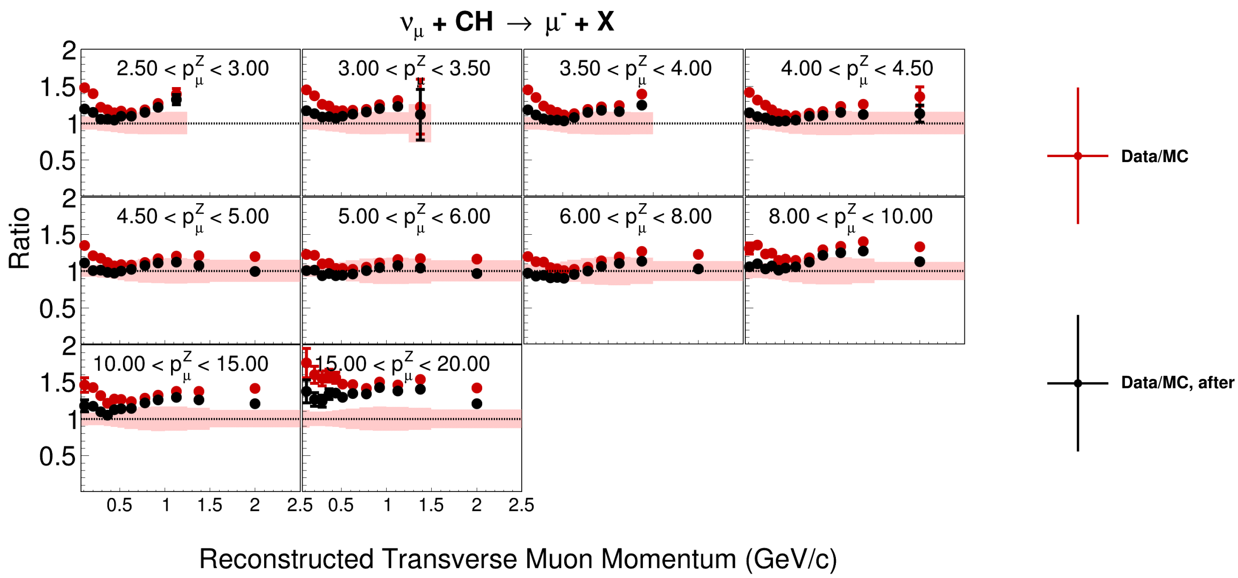

Figure 43 – Data-to-MC ratios in the **signal region** as a function of **muon momentum components**. Red (black) dots represent the data/MC ratio before (after) tuning the background. Error bars indicate statistical uncertainty, while the pink error band around line one represents the total (statistical+systematic) uncertainty on the simulation. Results are shown for **neutrino mode**.

5.2.4 Background-subtracted distributions

The tuned backgrounds are then removed from the data sample. The aftermath of this procedure leaves a total of 416,233 (237,468) reconstructed interactions in the neutrino (antineutrino) background-subtracted data samples. They are shown in Figs. 44 and 46, followed by their corresponding data-to-simulation ratio plots in Figs. 45 and 47.

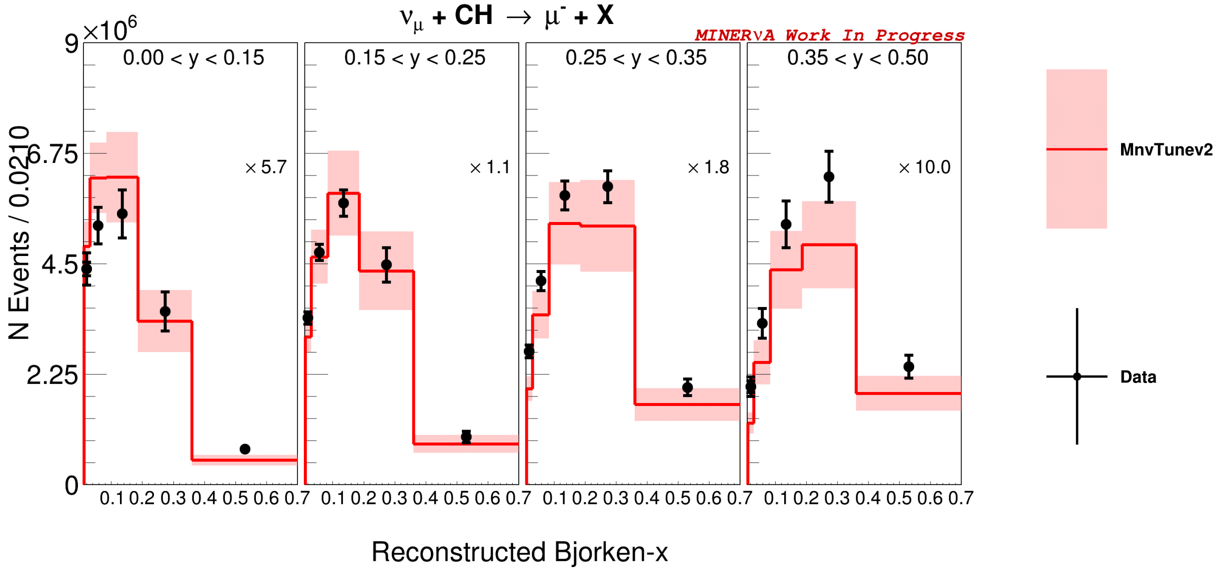

Figure 44 – Background-subtracted distributions as a function of **Bjorken variables**. The data points (black) include both statistical uncertainties (represented by inner error bars) and total uncertainties, statistical plus systematic (outer error bar). The simulated **neutrino** sample is shown as solid red line, with the surrounding pink band indicating its total (statistical + systematic) uncertainty.

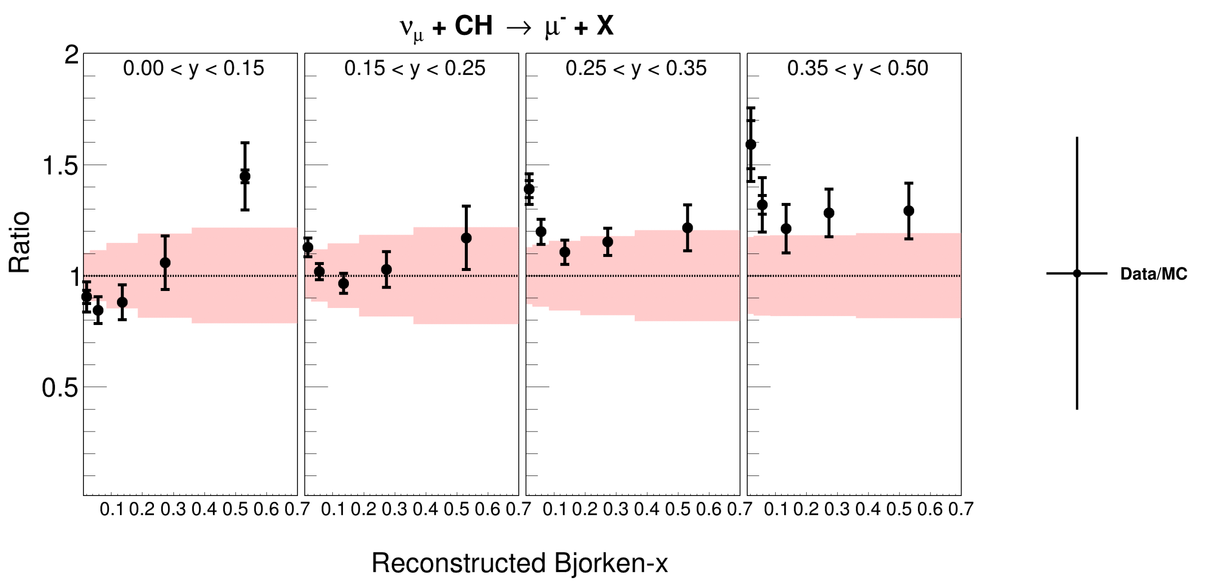

Figure 45 – Background-subtracted data-to-MC ratios as a function of **Bjorken variables**. The data points (black) carry both statistical (represented by inner error bar) and total (statistical + systematic, represented by outer error bar) uncertainties. The pink error band around line one represents the total (statistical+systematic) uncertainty on the simulation. Results are shown for **neutrino mode**.

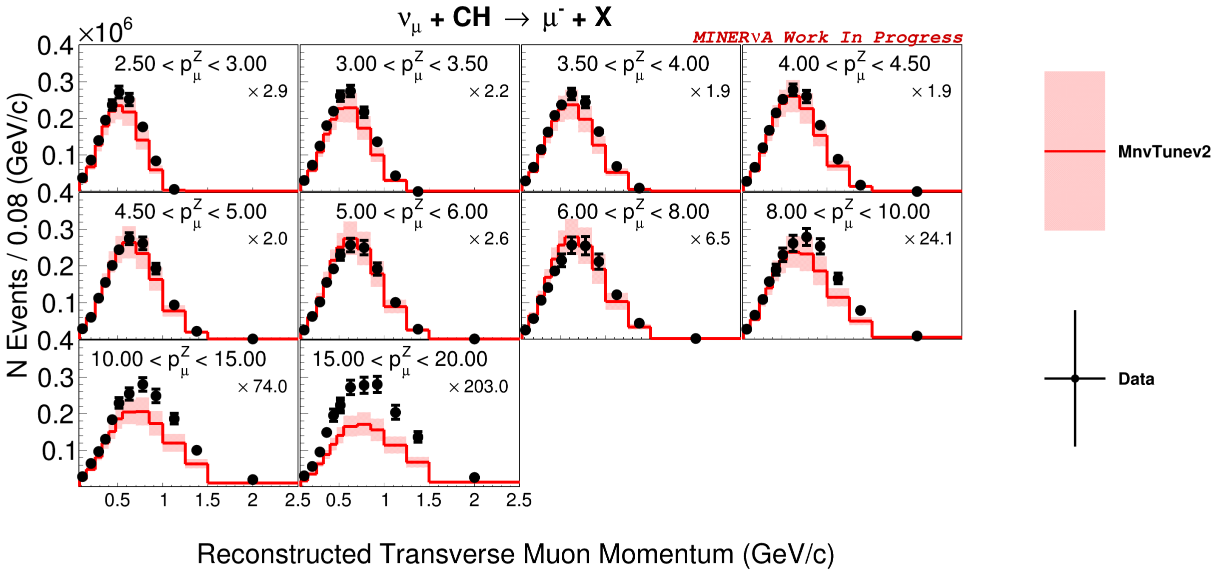

Figure 46 – Background-subtracted distributions as a function of **muon momentum components**. The data points (black) include both statistical uncertainties (represented by inner error bars) and total uncertainties, statistical plus systematic (outer error bar). The simulated **neutrino** sample is shown as solid red line, with the surrounding pink band indicating its total (statistical + systematic) uncertainty.

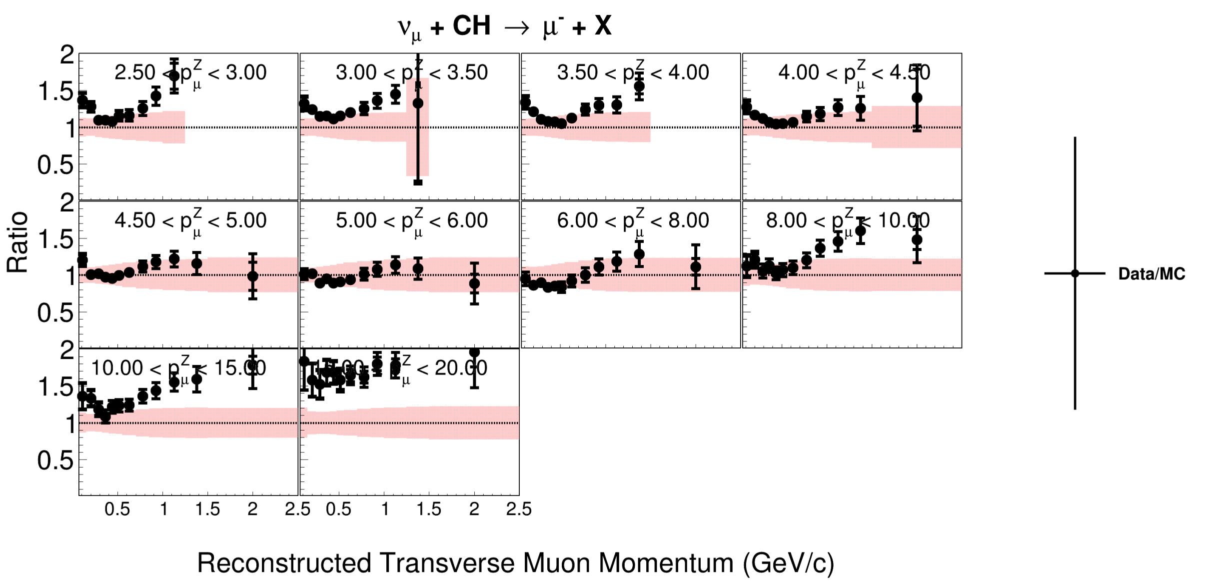

Figure 47 – Background-subtracted data-to-MC ratios as a function of **muon momentum components**. The data points (black) carry both statistical (represented by inner error bar) and total (statistical + systematic, represented by outer error bar) uncertainties. The pink error band around line one represents the total (statistical+systematic) uncertainty on the simulation. Results are shown for **neutrino mode**.

5.3 Unfolding

At this stage, the true signal has been isolated in both reconstructed simulated and data samples through the background subtraction process. Despite that, the samples still include (or are affected by) three detector/reconstruction-related limitations, which will be addressed in this and in the next section. The first one is known as smearing, an effect present in any particle detector: given that no detector can measure a physical quantity with exact precision, the reconstructed data distribution is shifted away from its true value. "Unfolding" is then the process that corrects for the detector smearing, ensuring that the measurements are detector-independent and remain comparable to theoretical predictions. In Eq. 5.1, U_{ij} denotes the elements of the unfolding matrix. The two remaining detector effects are addressed in Sec. 5.4.

5.3.1 Detector smearing

The detector smearing can be identified and estimated by using the true and reconstructed versions of the simulated signal to build a matrix, shown in Fig. 48. In this figure, the rows (columns) correspond to true (reconstructed) signal events, and the numbers displayed on each entry are row-normalized event percentages – each row is normalized to 1 (underflow and overflow bins, corresponding to events outside the signal region, are not shown). The detector smearing is manifested as non-zero off-diagonal occurrences. If the detector were perfect, these matrices would be the identity (only diagonal entries), which means that the predicted and measured values for a given observable match up with 100% probability. So, the more smeared the reconstructed distribution, the larger is the off-diagonals spread.

Consider, for instance, the second reconstructed Bjorken-x bin in Fig. 48a. One sees that 72% of true events were measured in the right bin (bin 2); 23% of the events the detector should had placed in bin 1 also ended up being reconstructed in bin 2; and 9%, supposed to belong to bin 3, migrated to bin 2. Therefore, the reconstructed bin 2 is a mixture: it contains contributions from truth bins 1, 2 and 3. Likewise, taking the reconstructed bins 6 and 7 of p_μ^T in Fig. 48c one sees that: the former has contributions from 3 neighboring bins, whereas the latter has 4. At end of the day, in essence, the detector smearing has a probabilistic nature – one reconstructed bin can come from many possible truth bins, and vice versa.

In order to have a detector-independent cross section measurement, one needs to account for the smearing effect. Given the previous discussion, one cannot deterministically redistribute counts from where the detector put them back to where they originated, but *statistically infer* the most likely truth-level distribution that could have produced the measured reconstructed distribution (data and/or MC). This is called as "unfolding". And the migration matrix itself is used in this process: by multiplying its inverse by the reconstructed distribution, one can get the events in true phase space. In theory, one could get the inverse matrix using Linear Algebra. However, direct inversion calculations are mathematically unstable: small changes in the measured distribution cause big fluctuations in truth. Instead, several regularized unfolding alternatives provide stable solutions (*e.g.*, Iterative Bayesian unfolding, Singular Value Decomposition unfolding, Tikhonov regularization, and, more recently, Machine Learning-based unfolding). In particular, MINERvA adopts the iterative Bayesian unfolding (D'Agostini method), discussed below.

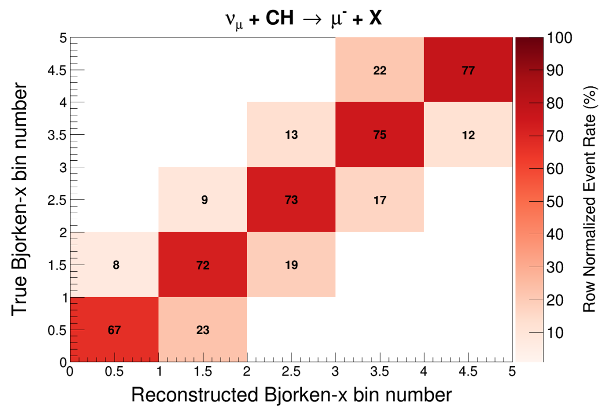

(a) Bjorken-x migration matrix.

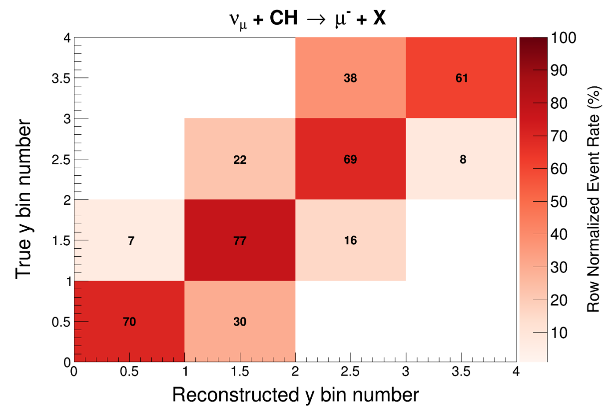

(b) Bjorken-y migration matrix.

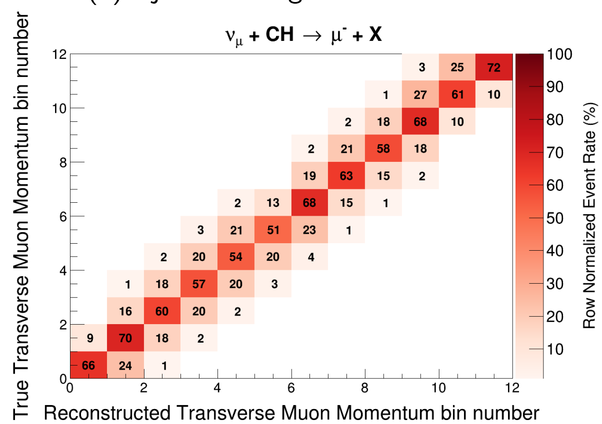

(c) p_μ^T migration matrix.

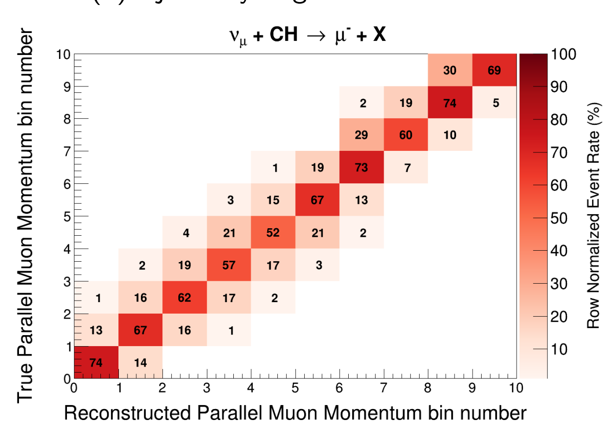

(d) p_μ^Z migration matrix.

Figure 48 – Row-normalized one-dimensional migration matrices for Bjorken-x and Bjorken-y (top), and p_μ^{T} and p_μ^{Z} (bottom) variables.

5.3.2 D'Agostini iterative Bayesian unfolding

D'Agostini method uses Bayes theorem in an iterative way to construct an effective inverse matrix [129, 130]. Defined in Eq. 5.6, the unfolding matrix is built from elements of the migration matrix, M_{ij}, and from an initial guess of the truth-level distribution, $\pi_i^{(k)}$. Starting from iteration $k = 0$, this prior is successively updated according to Eq. 5.7, where $\epsilon_i = \sum_j \mathrm{M}_{ij}$ is the detection efficiency for a true bin i, and $\mathrm{N}_j^{\mathrm{reco}}$ is the measured spectrum. For one iteration ($k = 1$), the unfolding procedure gives a result biased by the prior. On the other hand, if one lets the number of iterations $k \to \infty$, the solution is then equivalent to direct matrix inversion, as each iteration amplifies statistical fluctuations. Therefore, choosing the right stopping point, k, where the bias-to-variance trade-off is balanced, is critical for the unfolding solution.

$$\mathsf{U}_{ij} = \frac{\mathsf{M}_{ij}\,\pi_i^{(k)}}{\sum_\ell \mathsf{M}_{\ell j}\,\pi_\ell^{(k)}} \tag{5.6}$$

$$\pi_i^{(k+1)} = \frac{1}{\epsilon_i}\sum_j \mathsf{U}_{ij}\mathsf{N}_j^{\mathrm{reco}} \tag{5.7}$$

5.3.3 Determining the unfolding regularization parameter, k

The ideal regularization parameter, k (Eqs. 5.6 and 5.7), is the one that minimizes the total modelling error (bias^2+variance). To determine it, a series of studies is carried out, where a family of alternative truth models are used to reweight the baseline MnvTunev2 simulation. The underlying reason for that is because the regularization parameter must be model-independent. In fact, the migration matrices, shown in Fig. 48, assume MnvTunev2 as the baseline MC to estimate the smearing of true kinematics by the detector. It turns out that this model is in disagreement with the SIS background-subtracted data, as shown in Figs. 44 and 46, which means that the smearing matrices are biased and the probabilities they encode may not perfectly represent the data. Therefore, using variations of the simulation to determine the regularization parameter ensures it is robust against this model dependence, and makes possible its use to unfold both the reconstructed MC and data distributions.

The reweighted reconstructed predictions, also referred to as "warped" simulations, are built by systematically varying some parameters or components of the cross section models implemented in the nominal model (MnvTunev2). The family of models used in this work to generate the warped distributions are listed in Tab. 10, and a comparison to the baseline MnvTunev2 simulation is shown in Fig. 49. These models are provided as input to Eq.s 5.6 and 5.7, where the migration matrices are kept to MnvTunev2. To mimick the randomness of real data collection and ensure the stability of the unfolding procedure, these warped reconstructed distributions are unfolded 500 times for $k = 1, 2, 3, ..., 100$ iterations, each time with bin contents fluctuated according to Poisson statistics.

Given a model, for each k iteration, the bias–variance trade-off is quantified by computing a χ^2 between the unfolded and its corresponding true ($\mathsf{N}^{\mathsf{true}}$) distributions using Eq. 5.8, with $(\mathsf{C}^{-1})_{ji}$ an element of the inverse unfolding covariance matrix. The optimal regularization parameter is found to be the minimum value of a median χ^2 that matches the number of degrees of freedom (equal to the number of bins) and remains stable after that. Two results corresponding to the

Low-Q^2(NUBARPi0) and MnvTunev2-NR1Pi warps are shown in Fig. 50 for the Bjorken variables.

$$\chi^2 = \sum_i \sum_j (\pi^{(k)} - \mathrm{N}^{\mathrm{true}})_j \cdot (\mathrm{C}^{-1})_{ji} \cdot (\pi^{(k)} - \mathrm{N}^{\mathrm{true}})_i \tag{5.8}$$

Table 10 – Warped models used to determine the D'Agostini regularization parameter.

Warped Model	Description
AMU	This is a DIS ($W > 2.0$ GeV, $Q^2 > 1.0$ GeV^2) model developed at Aligarh Muslim University (AMU). The authors use a microscopic nuclear model that incorporates Fermi motion, binding energy, nucleon correlations, meson cloud contributions, and shadowing to compare electromagnetic and weak structure functions for iron nuclei [131].
EMC	This refers to the equation 9 of the paper [132], which is implemented to reweight the GENIE DIS cross section component. That equation is a multiplicative correction factor applied to DIS events on iron targets, used in the NuTeV experiment's analysis, to ensure that the measured structure functions $F_2(x, Q^2)$ and $xF_3(x, Q^2)$ are appropriately adjusted for the nuclear medium effects.
Low-Q^2(JOINT$^+$)	The default JOINT channel at the MnvTunev2 Low-Q^2 weight is shifted by $+5$%. The Low-Q^2 weight is part of this analysis central value, which is described in Sub-sec. 4.4.4
Low-Q^2(JOINT$^-$)	This warped simulation is generated similarly to the previous one: the default JOINT channel at the MnvTunev2 Low-Q^2 weight is shifted by -5%.
Low-Q^2(NUBARPi0)	The Low-Q^2 default JOINT channel at MnvTunev2 is replaced by the channel prevenient from the $\bar{\nu}_\mu$CC1π^0 dataset [].
MnvTunev1	The Low-Q^2 suppression in the $Q^2 < 0.7$ GeV^2 region at MnvTunev2 is turned OFF. The Low-Q^2 weight is described in Sub-sec. 4.4.4.
MnvTunev4	This is the same as MnvTunev1, including the reanalysis of the deuterium bubble chamber from ANL/BNL [67, 68]. The resonant axial mass changes from 1.12 GeV [42, 43] to $M^{A}_{RES} = 0.94$ GeV, and the cross section normalization factor is set to 1.15 [201].
MK18	This is a model for single pion production in neutrino–nucleon interactions that coherently combines resonant and non-resonant amplitudes. In addition, it includes lepton mass effects, and predicts cross sections and pion distributions more consistent with data than the Rein–Sehgal model implemented in GENIE [133].
MnvTunev2-NR1Pi	The non-resonant single pion production reduction by 43 % at MnvTunev2 is turned OFF. The NR1Pi weight is described in Sub-sec. 4.4.4.

Theses studies lead to the conclusion that the regularization parameter for the two analyses must be 4. Using this number of iterations, the distributions are unfolded and the results shown in Figs. 51 and 53.

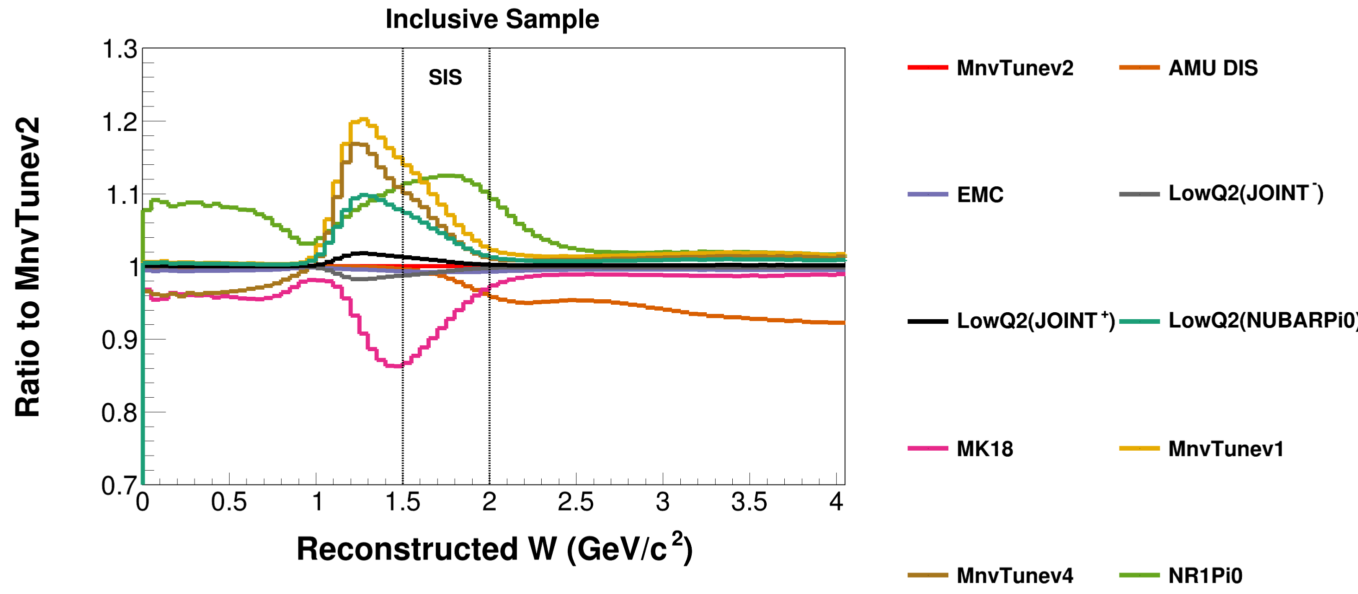

Figure 49 – Comparison between warped models and MnvTunve2 baseline as a function of the reconstructed invariant mass, W. These warped simulations are described in Tab. 10; they are used to test the unfolding procedure, and to determine the D'Agostini regularization parameter. The SIS region is located between the two vertical dashed lines, corresponding to $W_{reco} = 1.5$ GeV and $W_{reco} = 2.0$ GeV.

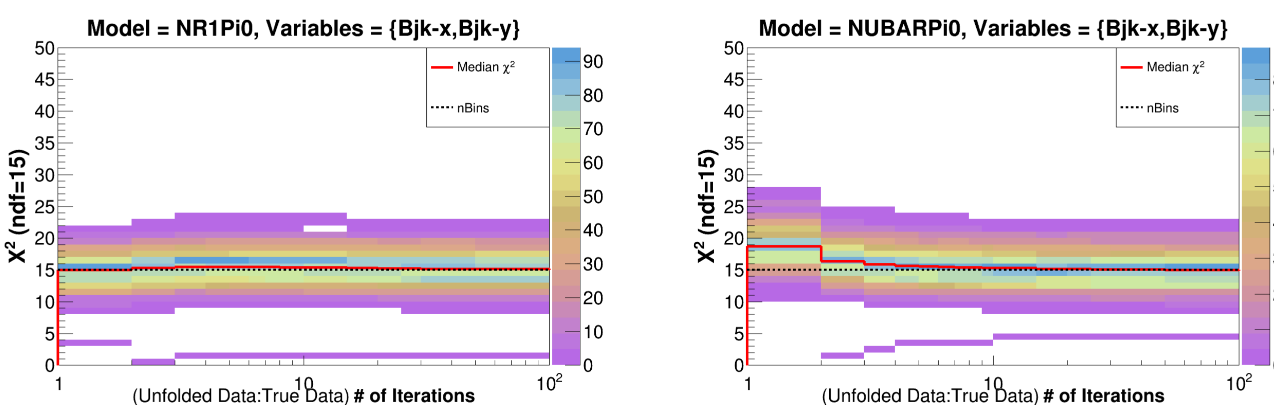

(a) MnvTunev2-NR1Pi warped model.

(b) NUBARPi0 warped model.

Figure 50 – Illustration of two unfolding tests for Bjorken variables analysis. Results are for (a) MnvTunev2-NR1Pi and (b) NUBARPi0 warped simulations, which are described in Tab. 10. The median χ^2 between the unfolded and true component of the simulation is illustrated as a solid red line, with the number of degrees of freedom (15) represented by the horizontal dashed line. For these studies, five low-populated bins were removed.

5.3.4 Unfolded distributions

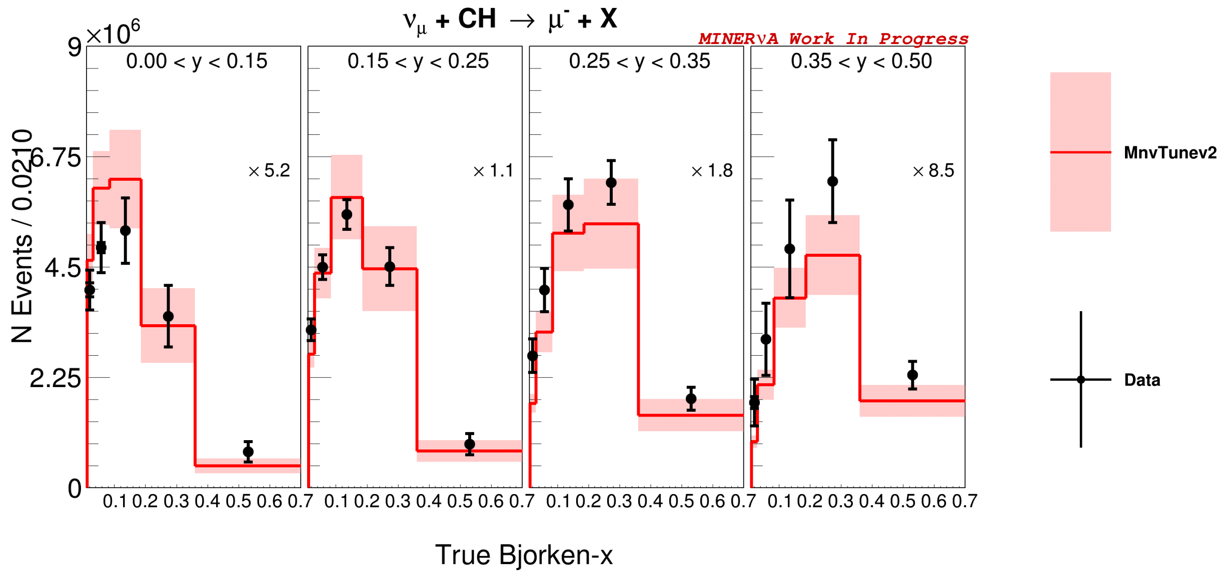

Figure 51 – Unfolded distributions as a function of **Bjorken variables**. The data points (black) include both statistical uncertainties (represented by inner error bars) and total uncertainties, statistical plus systematic (outer error bar). The simulated **neutrino** sample is shown as solid red line, with the surrounding pink band indicating its total (statistical + systematic) uncertainty.

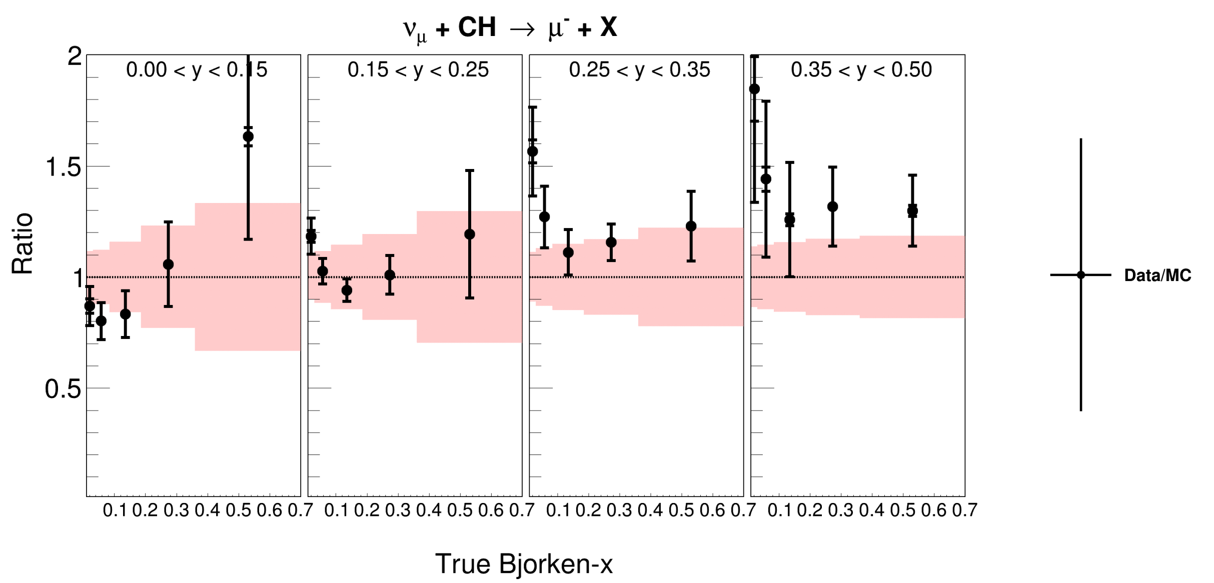

Figure 52 – Unfolded data-to-MC ratios as a function of **Bjorken variables**. The data points (black) carry both statistical (represented by inner error bar) and total (statistical + systematic, represented by outer error bar) uncertainties. The pink error band around line one represents the total (statistical+systematic) uncertainty on the simulation. Results are shown for **neutrino mode**.

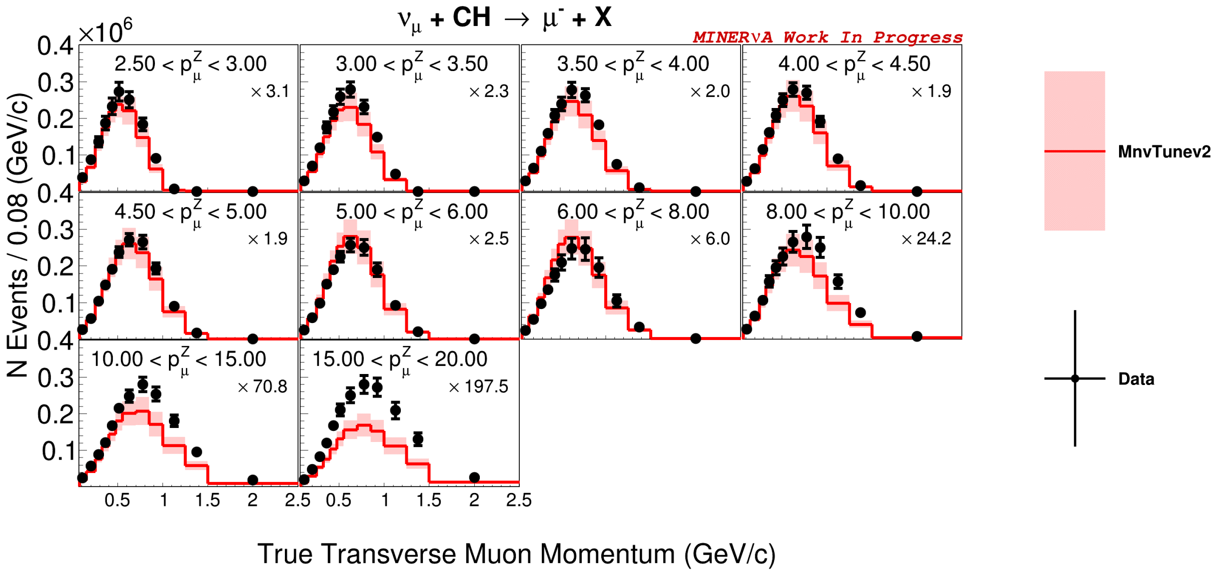

Figure 53 – Unfolded distributions as a function of **muon momentum components**. The data points (black) include both statistical uncertainties (represented by inner error bars) and total uncertainties, statistical plus systematic (outer error bar). The simulated **neutrino** sample is shown as solid red line, with the surrounding pink band indicating its total (statistical + systematic) uncertainty.

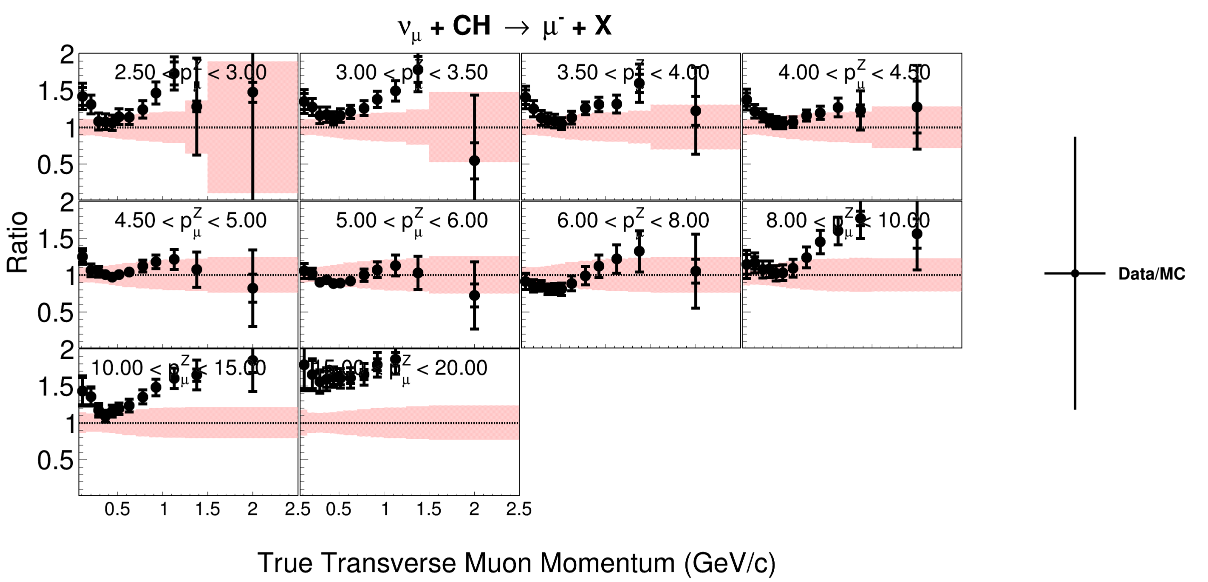

Figure 54 – Unfolded data-to-MC ratios as a function of **muon momentum components**. The data points (black) carry both statistical (represented by inner error bar) and total (statistical + systematic, represented by outer error bar) uncertainties. The pink error band around line one represents the total (statistical+systematic) uncertainty on the simulation. Results are shown for **neutrino mode**.

5.4 Reconstruction efficiency and detector acceptance corrections

After the unfolding procedure, the signal events are now distributed into their correct bins and no longer carry the detector smearing effect. However, these event distributions are affected by the efficiency of the selection/reconstruction and detector acceptance limitations, which cause the number of events in the sample to be underestimated. In fact, some SIS events are not included in the sample either because their final state muons do not have sufficient energy to reach the MINOS spectrometer or they are too energetic to be reconstructed with an acceptable resolution[3]. In addition, signal events may go missing because the reconstruction algorithm may misplace the interaction vertex outside of the fiducial volume. These effects are represented by the ϵ_i term in Eq. 5.1, and are estimated by the simulation to compute Eq. 5.9. In this equation, the numerator is the number of the true events that are reconstructed and pass the full selection, and the denominator is the number of true signal events in fiducial volume.

$$\epsilon_i = \frac{\mathrm{N}_i^{\text{Selected signal}}}{\mathrm{N}_i^{\text{All true signal}}} \tag{5.9}$$

The overall mean efficiency of the SIS neutrino (antineutrino) sample is 32 % (35 %). To assess the impact of the selection on the efficiency, the cuts (previously described in Tab. 6) are ordered and applied in sequence as listed by the first column of Tab. 11. For each k cut, the mean efficiency is computed with respect to the total number of generated SIS events in the fiducial volume as $\mathrm{N}_k/\mathrm{N}^{\text{All true signal}}$. The survival rate (SR) and fraction lost (FL) after each k cut, applied cumulatively, are listed in columns 2-3 for the neutrino sample, and columns 4-5 for the antineutrino sample. The loss of efficiency is mainly driven by the SIS cut, fiducial volume and muon energy cuts.

Table 11 – Survival rate (SR) and fraction lost (FL) after cumulatively applying the selection/reconstructed cuts listed in Tab. 6.

	ν_μ-mode		$\bar{\nu}_\mu$-mode	
Cuts	SR (%)	FL (%)	SR (%)	FL (%)
Fiducial volume	76.14	23.86	78.11	21.89
Muon energy	66.37	33.63	71.02	28.98
Muon angle	65.39	34.61	70.47	29.53
Helicity	63.74	36.26	68.82	31.18
Dead time	62.47	37.53	67.83	32.17
Neutrino energy	62.47	37.53	67.83	32.17
Muon curvature	57.26	42.74	62.81	37.19
Muon coil	52.79	47.21	57.95	42.05
SIS cut	32.25	67.75	35.24	64.76

[3] These are signal events outside the kinematic range $2 < \mathrm{E}_\mu < 20$ GeV or have $\theta_\mu > 20°$.

The bin-by-bin efficiency for Bjorken and muon momentum variables are illustrated in Fig. 55, and the unfolded efficiency-corrected distributions are shown in the next subsection.

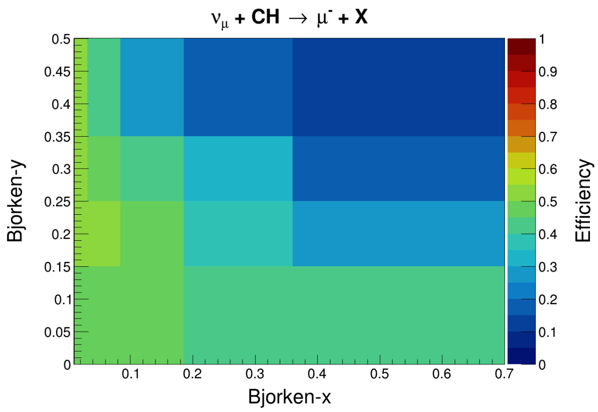

(a) x-y efficiency in **neutrino** mode.

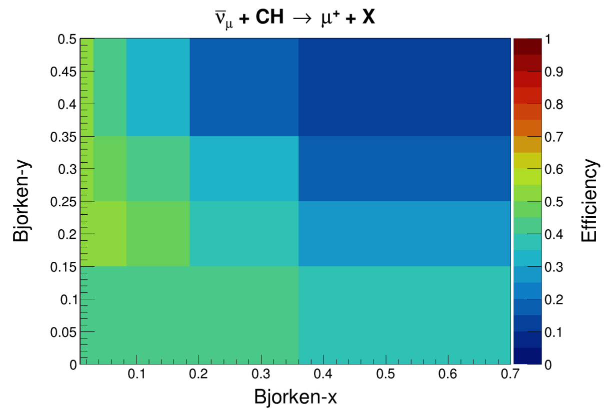

(b) x-y efficiency in **antineutrino** mode.

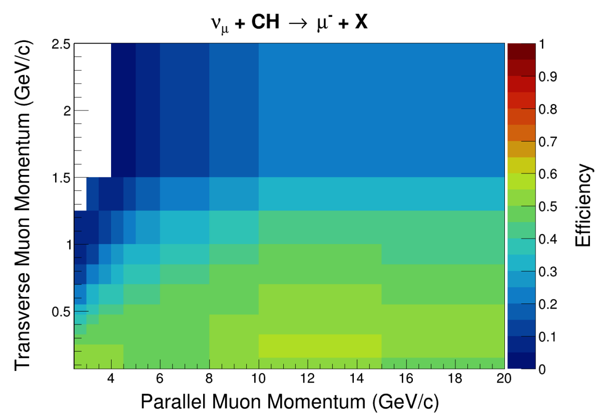

(c) p_μ^Z-p_μ^T efficiency in **neutrino** mode.

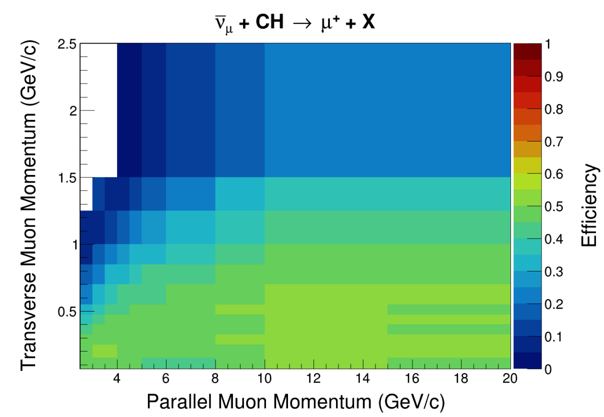

(d) p_μ^Z-p_μ^T efficiency in **antineutrino** mode.

Figure 55 – Efficiency distributions for Bjorken (top) and muon momentum (bottom) variables in neutrino (left) and antineutrino (right) modes.

5.4.1 Unfolded efficiency-corrected distributions

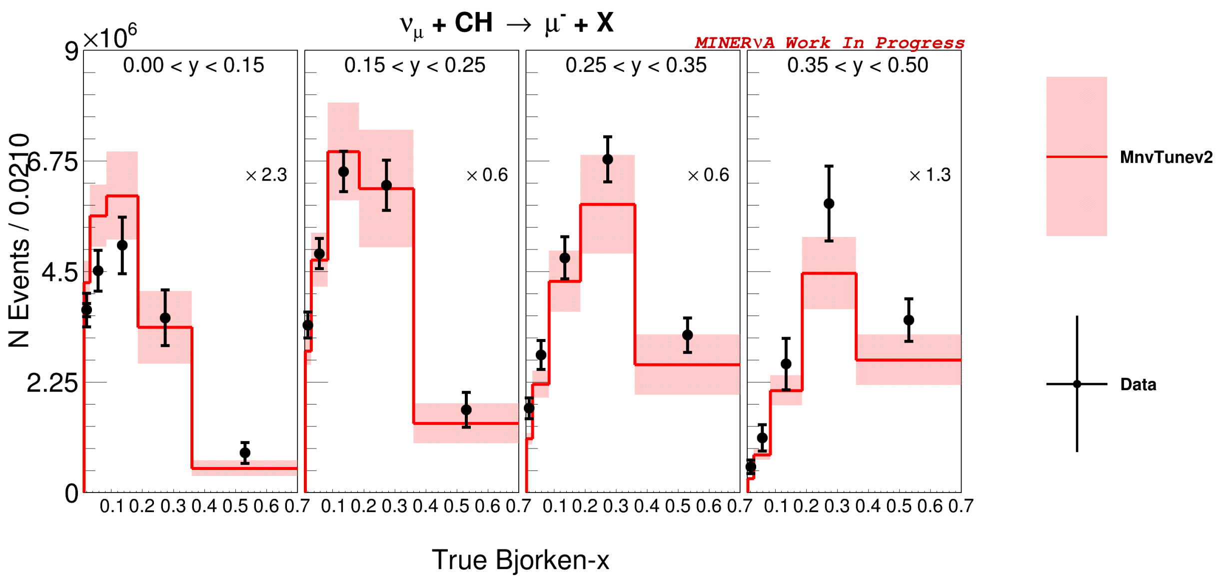

Figure 56 – Unfolded efficiency-corrected distributions as a function of **Bjorken variables**. The data points (black) include both statistical uncertainties (represented by inner error bars) and total uncertainties, statistical plus systematic (outer error bar). The simulated **neutrino** sample is shown as solid red line, with the surrounding pink band indicating its total (statistical + systematic) uncertainty.

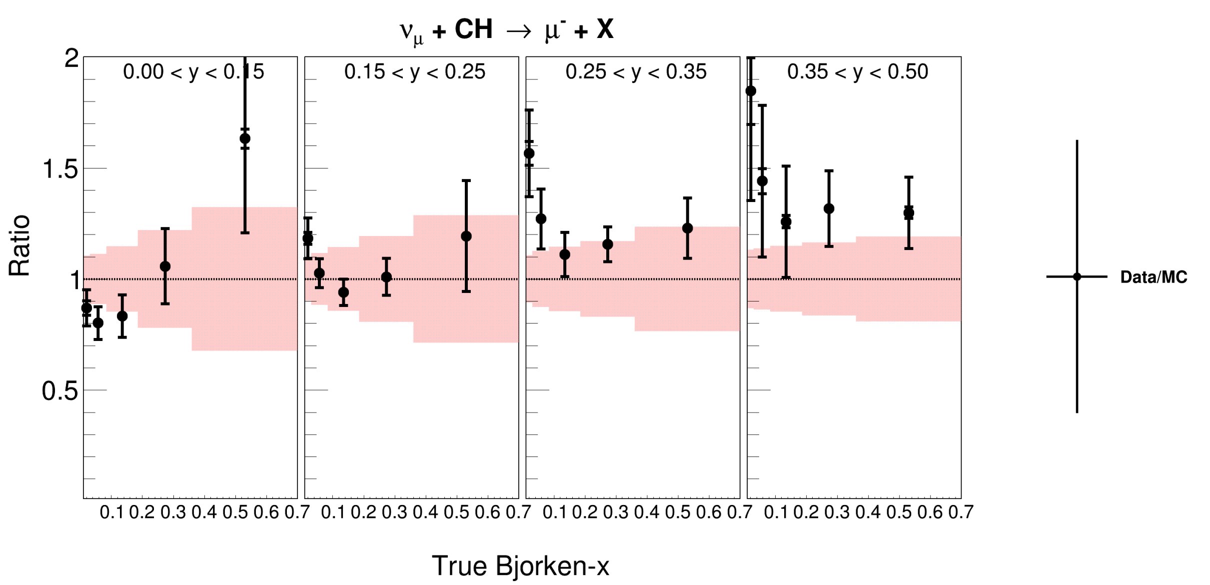

Figure 57 – Unfolded efficiency-corrected data-to-MC ratios as a function of **Bjorken variables**. The data points (black) carry both statistical (represented by inner error bar) and total (statistical + systematic, represented by outer error bar) uncertainties. The pink error band around line one represents the total (statistical+systematic) uncertainty on the simulation. Results are shown for **neutrino mode**.

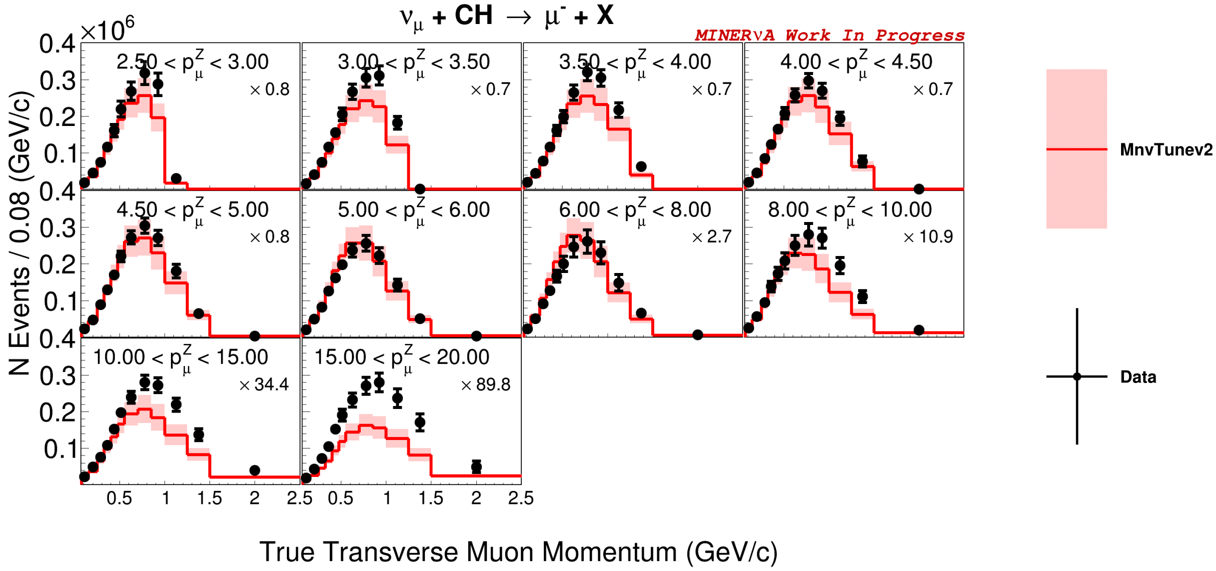

Figure 58 – Unfolded efficiency-corrected distributions as a function of **muon momentum components**. The data points (black) include both statistical uncertainties (represented by inner error bars) and total uncertainties, statistical plus systematic (outer error bar). The simulated **neutrino** sample is shown as solid red line, with the surrounding pink band indicating its total (statistical + systematic) uncertainty.

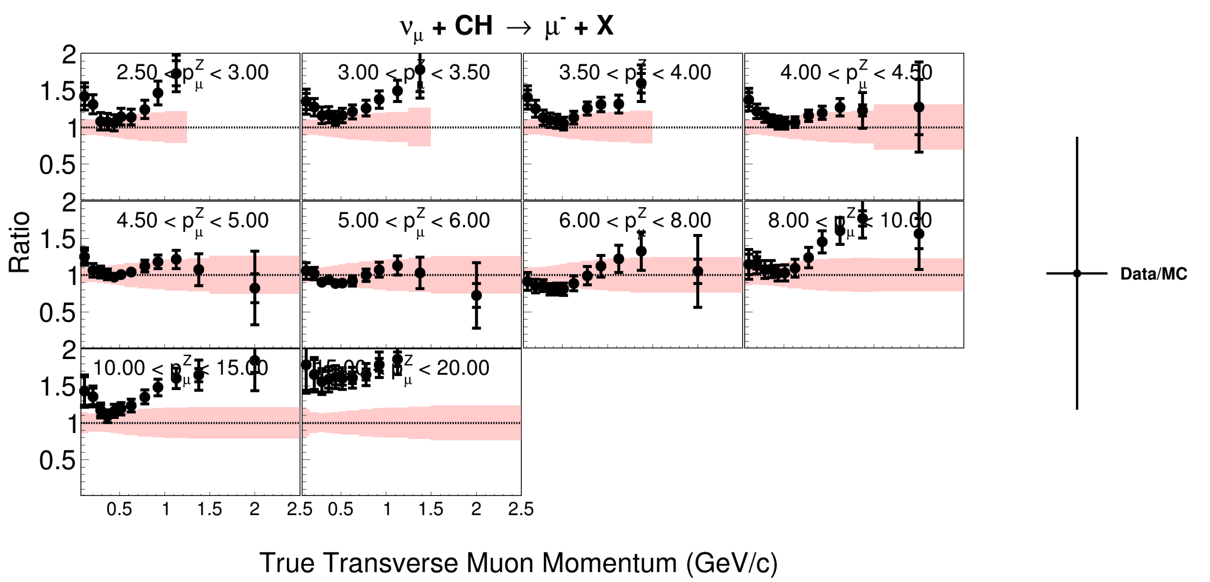

Figure 59 – Unfolded efficiency-corrected data-to-MC ratios as a function of **muon momentum components**. The data points (black) carry both statistical (represented by inner error bar) and total (statistical + systematic, represented by outer error bar) uncertainties. The pink error band around line one represents the total (statistical+systematic) uncertainty on the simulation. Results are shown for **neutrino mode**.

5.5 Normalization factors

The final step of the cross section extraction process consists in dividing the unfolded efficiency-corrected distributions by the integrated flux, Φ, and the number of targets, T. The first factor turns the measured event counts into the actual cross sections, while the division by the number of targets provides detector-independent measurements[4].

The simulated neutrino flux was discussed in Sub-sec. 4.4.1. Since the PPFX flux predicts number of neutrinos per unit of area per number of protons on target (POT) for a given energy, then the total number of incoming neutrinos is the integral of the flux distribution over a specific energy range, multiplied by the data POT. The neutrino energy range over which the integral is performed is $E_\nu = [0, 120]$ GeV. These limits cover all possible neutrino energies originated from the 120 GeV NuMI beam protons. The resulting integrated flux for neutrinos and antineutrinos, as well as the data POTs are listed in Tab. 12. The flux uncertainty is discussed in the next chapter.

The number of targets which neutrinos and antineutrinos interact with is estimated from the density and mass of the material comprising the scintillator tracker. As detailed in [103], the scintillator planes are made from seven elements. Therefore, the number of nucleons is determined by combining individual number of protons and neutrons for each X element using Eq. 5.10, where f_X is the mass fraction of that element X, A_X its atomic mass (g/mol), Z_X its number of protons/neutrons, and M_{target} its total target mass; N_A is the Avogadro number. Then, the total number of nucleons is found to be $T = 3.23478 \times 10^{30}$, and is also included in Tab. 12. The uncertainty in the target mass model is considered in the next chapter.

Table 12 – Cross section normalization factors.

Factor	ν_μ-mode	$\bar{\nu}_\mu$-mode
Integrated flux ($\times 10^{-8}$ ν_μ/cm^2/POT)	6.22992	4.77415
Data POT ($\times 10^{21}$)	1.05689	1.11707
Number of targets ($\times 10^{30}$)	3.23478	

$$n_X = M_{\text{target}} \cdot f_X \cdot \frac{N_A}{A_X} \cdot Z_X \tag{5.10}$$

4 The bin widths, $\Delta x_i, \Delta y_i$, are already accounted for during event selection, ensuring a uniform distribution of event counts.

6 Systematic uncertainties

It is well established by experience that no physical quantity can be measured with complete certainty, and this limitation equally affects the cross section measurements reported in this work. In fact, to estimate how precise and consistent with theoretical models the results are, it is crucial to carefully define and evaluate experimental uncertainties. In general, they are classified as being of *statistical* and *systematic* nature.

The statistical uncertainty is revealed by repeating the measurements, which, in this context, are the number of SIS neutrinos and antineutrinos interacting on the MINERvA hydrocarbon target (see the detailed signal definition in Sub-sec. 5.1.1). Because these measurements follow a Poisson distribution, then the magnitude of the statistical uncertainty for a n_i counts in bin i is $\sigma_{\text{stat}} = \sqrt{n_i}$.

On the other hand, systematic uncertainties are more complex to detect and estimate given the series of variables and conditions under which the experiment is performed. They affect the results in the same way, and cannot be identified by just repeating the measurements. At MINERvA, systematics are evaluated through a technique called many-universe, explained below.

6.1 MINERvA systematics evaluation

The many-universe technique used in MINERvA consists in re-extracting the simulated cross sections multiple times, each time with a model parameter varied within its 1σ uncertainty [134]. This shifted cross section then defines what is called as a *systematic universe*. These systematic universes are used to build a covariance matrix, whose i, j-bin elements are defined in Eq. 6.1. In this equation, N is the total number of systematic universes, x_u is the bin content in universe u, and $\bar{x}$ is the bin content averaged over all universes, including the central value universe, *i.e.* the parameters set to their nominal values, not varied.

$$\text{cov}_{ij} = \frac{1}{N-1} \sum_{u=1}^{N} \left(x_{u,i} - \bar{x}_i\right)\left(x_{u,j} - \bar{x}_j\right). \tag{6.1}$$

Then, the magnitude of the systematic uncertainty for a specific source is calculated as the squared root of the covariance matrix diagonal entries, $\sigma_{\text{sys}} = \sqrt{(\text{cov}_{ii})^2}$. In this analysis, similar error sources are grouped in five categories, listed in Tab. 13, and each of them is discussed in the following sections. As it will be seen in Chap. 7, the "Muon Reconstruction", "Flux" and "Interaction Model" groups figure as the major systematic uncertainties.

Table 13 – Systematic error groups adopted in this work.

Systematic error group	Description
Flux	Uncertainties on the neutrino flux simulation parameters.
Interaction Model	Uncertainties on GENIE cross section models and on the MINERvA Tune v2 reweights.
FSI	Uncertainties on GENIE parameters for final state interactions of pions and nucleons.
Particle Response	Uncertainties on MINERvA calorimetric energy response.
Muon Reconstruction	Uncertainties associated to the muon reconstruction in MINERvA and MINOS detectors.

6.2 Flux

Among the five systematic error groups, the uncertainties associated to the neutrino "Flux" are the most complex ones to be estimated due to the many parameters describing it. While the other error sources are evaluated by shifting their parameters using two or three universes, the flux systematics require at least five hundreds universes to be well-characterized, according to the study illustrated in Fig. 60. The systematic uncertainties on the flux arise from two sources: hadron production and beam focusing, which are described below.

- Hadron production uncertainties

  As detailed in Sec. 4.1, neutrinos observed at the MINERvA detector are produced from 120 GeV protons colliding on the NuMI graphite target. Because the thickness of the target, the primary hadrons generated from the initial interaction can re-scatter on their way out, producing yet more hadrons. The hadron production from proton-carbon interactions is described by phenomenological models [135, 136] and the Bertini cascade physics list [137–139]. These models are implemented in a GEANT4 simulation, and refined using the PPFX tool developed by MINERvA, which computes and propagates their parameter uncertainties based on hadron production datasets [115].

- Beam focusing uncertainties

  The neutrino beam is also sensitive to the beamline geometry. The positions of the target, magnetic horns and the residual water layer from the active cooling are some of the parameters that affect the flux – the complete list of focusing parameters and their corresponding 1σ uncertainties are found in Tab. 14. As for the hadron production, the focusing uncertainties are treated using the PPFX tool.

Table 14 – Beamline and focusing system parameters with their nominal values and corresponding 1σ uncertainties. Each parameter affects the neutrino flux prediction or focusing configuration.

Parameter	**Description**	**Nominal**	**1σ variance**
Beam x-position (mm)	Horizontal position of the neutrino beam center at the target.	0	0.4
Beam y-position (mm)	Vertical position of the neutrino beam center at the target.	0	0.4
Beam spot size (mm)	Transverse Gaussian width of the proton beam at the target, influencing the hadron yield and focusing.	1.4	0.2
Horn 1 x-position (mm)	Horizontal alignment of the first magnetic horn relative to the beam axis.	0	1
Horn 1 y-position (mm)	Vertical alignment of the first magnetic horn relative to the beam axis.	0	1
Horn 1 z-position (mm)	Longitudinal position of the first horn along the beamline, affecting pion focusing and acceptance.	30	2
Horn 2 x-position (mm)	Horizontal alignment of the second magnetic horn relative to the beam axis.	0	1
Horn 2 y-position (mm)	Vertical alignment of the second magnetic horn relative to the beam axis.	0	1
Horn water layer (mm)	Effective thickness of the water layer inside the horn conductor, impacting the magnetic field distribution.	1	0.5
Horn current (kA)	Electric current circulating through the magnetic horns, determining the focusing strength for charged hadrons.	200	1
Target x-position (mm)	Horizontal alignment of the graphite target relative to the beam axis.	0	1
Target y-position (mm)	Vertical alignment of the graphite target relative to the beam axis.	0	1
Target z-position (mm)	Longitudinal placement of the target relative to the horn system along the beamline.	-1433	1
POT counting	Uncertainty in the total number of protons-on-target (POT) used for flux normalization.	—	2% of POT
Baffle scraping	Fraction of proton interactions occurring in the upstream baffle, which modifies the pion yield and flux shape.	—	0.25% of POT

The fractional flux uncertainty in Fig. 60 illustrates both the effect of the number of systematic universes on its magnitude, and the use of data constraints. Increasing the number of systematic universes reduces the flux uncertainty; as after five hundred universes the reduction is tiny, then this number represents an adequate choice to characterize the imprecision on the neutrino flux. Moreover, as described in Sub-sec. 4.4.4, adding neutrino-electron scattering and inverse muon decay data constraints further reduces the flux uncertainty from 7.62% (7.76%) to 3.27% (4.66%) in neutrino (antineutrino) mode [116–118]. Overall, the imprecision on the flux is dominated by hadron production uncertainties.

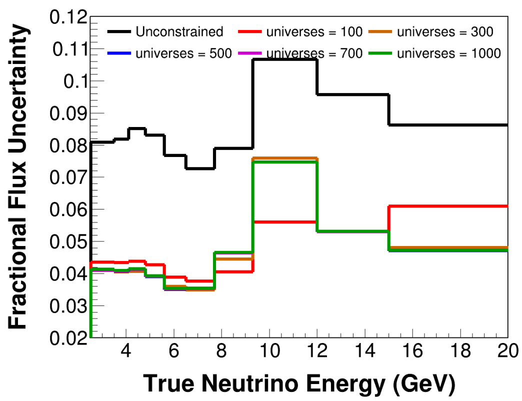

(a) **Neutrino** mode.

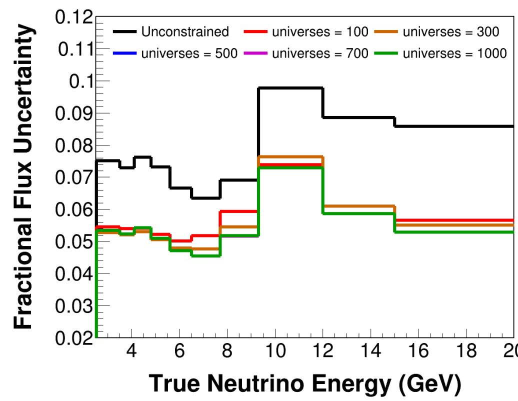

(b) **Antineutrino** mode.

Figure 60 – Fractional flux uncertainty. Black line shows the flux uncertainty prior to the implementation of constraints from neutrino-electron scattering and inverse muon decay data. Color lines include the data constraints discussed in the text, and illustrate how the fractional uncertainty reduces as the number of universes increases, starting from 100 to 1000.

6.3 Interaction Model

As discussed in Sub-sec. 4.4.2, neutrino interactions in MINERvA are simulated using GENIE, which implements models describing primary and final state interactions. These models take as input several experimental parameters (and their uncertainties) to compute the probability and kinematics of those interactions. The systematic uncertainties on the neutrino initial state interaction modeling are evaluated by varying the parameters listed in Tab. 15. In this table, the last four rows refer to the systematic uncertainties coming from the MINERvA tuning adopted in this analysis. Altogether, these systematics comprise the "Interaction Model" error group. Each of them provides two possible variations for the simulated central value, except for the `Low_Recoil_2p2h_Tune` error band, which has three universes (one for each nn, np and pp pairs).

Table 15 – Summary of cross section model error bands, their descriptions, and 1σ variations.

Error band name	**Description**	1σ **shift**
GENIE_CCQEPauliSupViaKF	Variation of Pauli blocking at low-Q^2, implemented by modifying the cutoff in the nucleon momentum distribution, which alters the suppression of low-energy CCQE events.	±30%
GENIE_MaCCQE	Axial mass parameter for CCQE interactions in the Llewellyn-Smith model (nominal 0.99 GeV). Affects both the Q^2 shape and the overall normalisation of the cross section.	+25%/-15%
GENIE_MaRES	Axial mass parameter for resonant pion production (nominal 0.94 GeV) in the Rein–Sehgal model.	±0.05 GeV
GENIE_MvRES	Vector mass parameter for resonant pion production (nominal 0.84 GeV) in the Rein–Sehgal model. Impacts the vector form factors in the cross section.	±3%
GENIE_Rvn1pi	Strength of charged-current and neutral-current single-pion production from non-resonant (Bodek–Yang) interactions on $\nu n/\bar{\nu}p$.	±4%
GENIE_Rvn2pi	Strength of charged-current and neutral-current double-pion production from non-resonant (Bodek–Yang) interactions on $\nu n/\bar{\nu}p$.	±50%
GENIE_Rvp1pi	Strength of charged-current and neutral-current single-pion production from non-resonant (Bodek–Yang) interactions on $\nu p/\bar{\nu}n$.	±4%
GENIE_Rvp2pi	Strength of charged-current and neutral-current double-pion production from non-resonant (Bodek–Yang) interactions on $\nu p/\bar{\nu}n$.	±50%
GENIE_VecFFCCQEshape	Model dependence of the CCQE vector form factor, varied between the BBBA parameterisation and a simple dipole form, primarily impacting the Q^2 dependence.	BBBA $\rightarrow$ dipole
Low_Recoil_2p2h_Tune	Variation of the 2p2h reweighting depending on the final state nucleon pair: nn, np, or pp by the MINERvA Tune.	100%
RPA_HighQ2	Variation of the RPA reweighting for high-Q^2 QE events by the MINERvA Tune.	$\pm100\%$
RPA_LowQ2	Variation of the RPA reweighting for low-Q^2 QE events by the MINERvA Tune.	$\pm100\%$
LowQ2Pi	Variation of the low-Q^2 reweighting for $Q^2 < 0.7$ GeV^2 events by the MINERvA Tune.	$\pm100\%$

6.4 Final State Interaction

The variety of particles produced from the neutrino interaction with nucleons or quarks can re-scatter as they exit the nucleus. GENIE predicts this process using an intranuclear cascade model, which was discussed in Sub-sec. 4.4.2. Several complex effects due to the nuclear medium are simulated − such as absorption, charge-exchange, elastic or inelastic scattering −, and affect the kinematic of the observed particles in the final state. The systematics associated to intranuclear processes are estimated by considering these model parameters, listed in Tab. 16. These sources of systematic were originally proposed by the MINOS Collaboration [140], and are grouped under the "FSI" error name. Their nominal values are varied using two systematic universes.

Table 16 – Summary of intranuclear re-scattering and hadronization error bands, their descriptions, and 1σ variations.

Error band name	**Description**	1σ **shift**
`GENIE_AGKYxF1pi`	Variation of the AGKY hadronisation model for low-multiplicity events, especially affecting the production of nucleons and pions in deep inelastic scattering.	$\pm 20\%$
`GENIE_FrAbs_N`	Probability of absorption for outgoing nucleons as they propagate through the nuclear medium, relative to the total rescattering probability.	$\pm 20\%$
`GENIE_FrAbs_pi`	Probability of absorption for pions in the nuclear medium, reducing the number of observable pions after intranuclear transport.	$\pm 30\%$
`GENIE_FrCEx_N`	Probability of charge exchange for nucleons inside the nucleus (e.g., $p \leftrightarrow n$), relative to the total rescattering probability.	$\pm 50\%$
`GENIE_FrCEx_pi`	Probability of charge exchange for pions in the nucleus (e.g., $\pi^+ \leftrightarrow \pi^0$), relative to the total rescattering probability.	$\pm 50\%$
`GENIE_FrElas_N`	Probability of elastic scattering for nucleons in the nuclear medium, altering their kinematics without absorption.	$\pm 30\%$
`GENIE_FrElas_pi`	Probability of elastic scattering for pions in the nuclear medium, changing their direction and energy while preserving particle identity.	$\pm 10\%$
`GENIE_FrInel_N`	Probability of inelastic scattering for nucleons in the nucleus, potentially producing secondary particles and altering event topology.	$\pm 40\%$
`GENIE_FrPiProd_N`	Probability of pion production from nucleon rescattering in the nuclear medium, introducing additional final-state pions.	$\pm 20\%$
`GENIE_MFP_N`	Modification of the mean free path for nucleons, controlling how far they propagate before undergoing reinteraction.	$\pm 20\%$
`GENIE_MFP_pi`	Modification of the mean free path for pions, affecting their survival probability inside the nucleus.	$\pm 20\%$
`GENIE_Theta_Delta2Npi`	Uncertainty in the anisotropy of the Δ resonance decay angular distribution to $N\pi$, influencing pion emission angles.	$\pm 100\%$

6.5 Particle Response

Whereas systematics for the production of final state particles are estimated using GENIE intranuclear cascade model parameters, uncertainties related to the actual observations of those

FSI particles in the MINERvA detector are inferred from GEANT4 simulation. As discussed in Sub-sec. 4.4.3, GEANT4 takes as input the various GENIE neutrino-nucleus interactions and propagate them through the MINERvA detector. The systematics on the detector response to energy depositions by final state hadrons are treated by varying the GEANT4 inelastic cross section model parameters. The errors on protons, neutrons and pions calorimetry are further constrained by test beam studies [141], and are summarized in Tab. 17. Together, they form the "Particle Response" error group.

Table 17 – Summary of detector response error bands, their descriptions, and 1σ variations.

Error band name	**Description**	1σ **shift**
`response_low_proton`	Uncertainty on the calorimetric response to protons with kinetic energy below 50 MeV, where ionization quenching is significant.	±4.0%
`response_mid_proton`	Uncertainty on the calorimetric response to protons with kinetic energy between 50–100 MeV, covering the transition between highly quenched and minimum-ionizing behavior.	±3.5%
`response_high_proton`	Uncertainty on the calorimetric response to protons with kinetic energy above 100 MeV, where detector response is more linear.	±3.0%
`response_meson`	Uncertainty on the calorimetric response to pions with kinetic energy between 400 MeV and 1.9 GeV, where hadronic shower modeling dominates.	±5.0%
`response_em`	Uncertainty on the detector response to electromagnetic showers, dominated by electrons and photons, primarily from π^0 decay.	±3.0%
`response_other`	Residual response uncertainty assigned to other final-state particles not explicitly covered, including rare hadrons.	±20.0%

6.6 Muon Reconstruction

Muons are an essential part of this cross section analysis. As discussed in Chap. 4, they are reconstructed through combined measurements in both the MINERvA and MINOS near detectors, and subjected to a certain degree of imprecision. The sources of muon reconstruction systematics are listed in Tab. 18. The `Muon_Energy_MINERvA` error refers to the uncertainty associated to the energy reconstruction at MINERvA. Two sources were identified for this component: 40 MeV uncertainty is attributed to the measurement of energy deposition rate, and 11 MeV is assigned to the MINERvA material assay. On the other hand, at MINOS near detector, the `Muon_Energy_MINOS` error source comprises $\sigma_{\text{range}} = 0.98\%$ uncertainty on muons reconstructed by range, and $\sigma_{\text{curv}} = 2.1\%$ (3.2%) uncertainty on muons reconstructed by curvature with momenta above (below) 1 GeV (refer to Sec. 4.3 for details on muon measurement at MINOS spectrometer). Finally, as it affects the muon energy scale, an uncertainty of $\pm$ 1.4% associated to the fiducial volume material, is added to this error group. Together, these sources are categorized as "Muon Reconstruction + Target Mass", and two systematic universes are used for each of them.

Table 18 – Summary of muon reconstruction error bands, their descriptions, and 1σ variations.

Error band name	**Description**	1σ **shift**
`BeamAngleX`	Variation of the muon angle with respect to the neutrino beam along the x-axis.	$\pm$ 1.0 mrad
`BeamAngleY`	Variation of the muon angle with respect to the neutrino beam along the y-axis.	$\pm$ 0.9 mrad
`MINOS_Reconstruction_Efficiency`	Variation of the MINOS tracking efficiency.	Evaluated by considering the parameter errors of a correction function associated to the MINOS matching efficiency; not public available (MINERvA reference DocDB 20760).
`Muon_Energy_MINERvA`	Variation due to muon energy scale in MINERvA.	$\pm$ 40 MeV (dE/dx); 11 MeV (assay)
`Muon_Energy_MINOS`	Variation due to muon energy scale in MINOS.	$\pm$ 0.98% (range); $\pm$ 2.1% / 3.2% (curvature)
`Muon_Energy_Resolution`	Variation due to results of muon energy resolution studies.	$\pm$ 0.4%
`Target_Mass_CH`	Variation of the density of hydrocarbon in the MINERvA detector.	$\pm$ 1.4%

7 Results and discussion

This chapter presents the final results obtained from the cross section extraction procedure detailed in Chap. 5. These results are organized as follows. First, the cross sections as a function of the Bjorken x and y variables are shown, followed by the measurements in terms of the transverse and longitudinal components of the outgoing muon momentum; the distributions are compared for both the neutrino and antineutrino modes for each variable pairings.

In the following plots, the data are represented by black dots whereas a red solid line indicates the simulated cross section by GENIE v2.12.6 reweighted to MnvTunev2. The simulation is broken down into the various GENIE interaction channels, illustrated by dashed lines, and whose relative contributions to the total cross section are listed in Tab. 19. These results are discussed in Sec. 7.3. Additionally to these measurements, the data are used to test alternative cross section interaction models in Appends. A.1 and A.2.

Table 19 – Breakdown of simulated cross section according to GENIE interaction channels.

GENIE channels	%
QE	< 1
Delta RES	8.5
Heavier RES	26.4
DIS	57.1
2p2h	3.4
Other	4.6

7.1 Measurements as a function of Bjorken variables

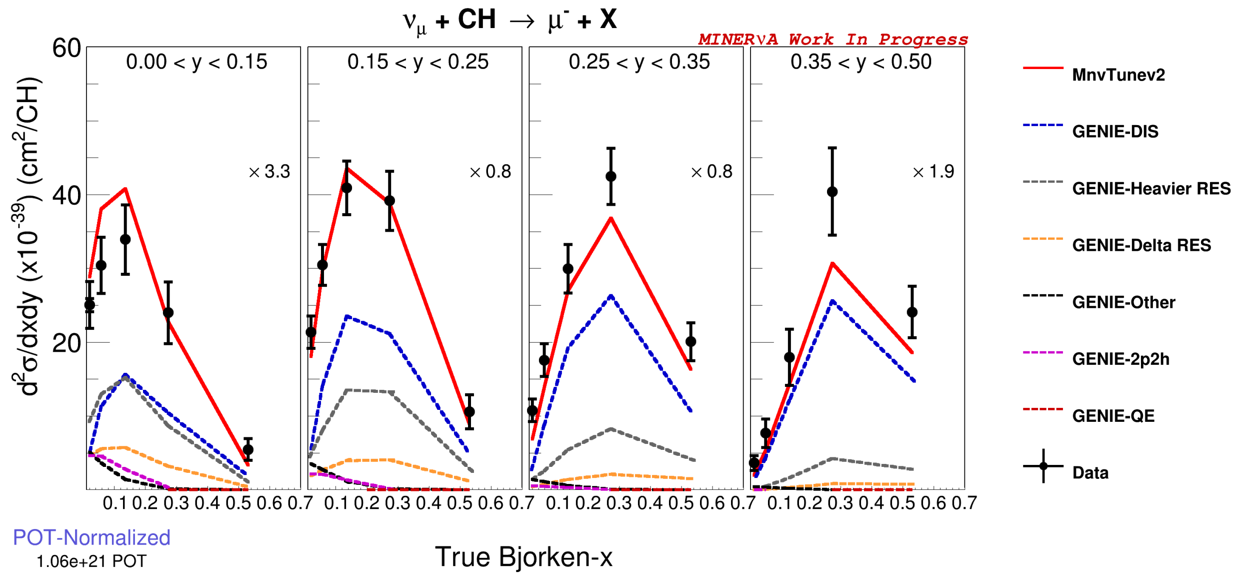

(a) **Neutrino** mode.

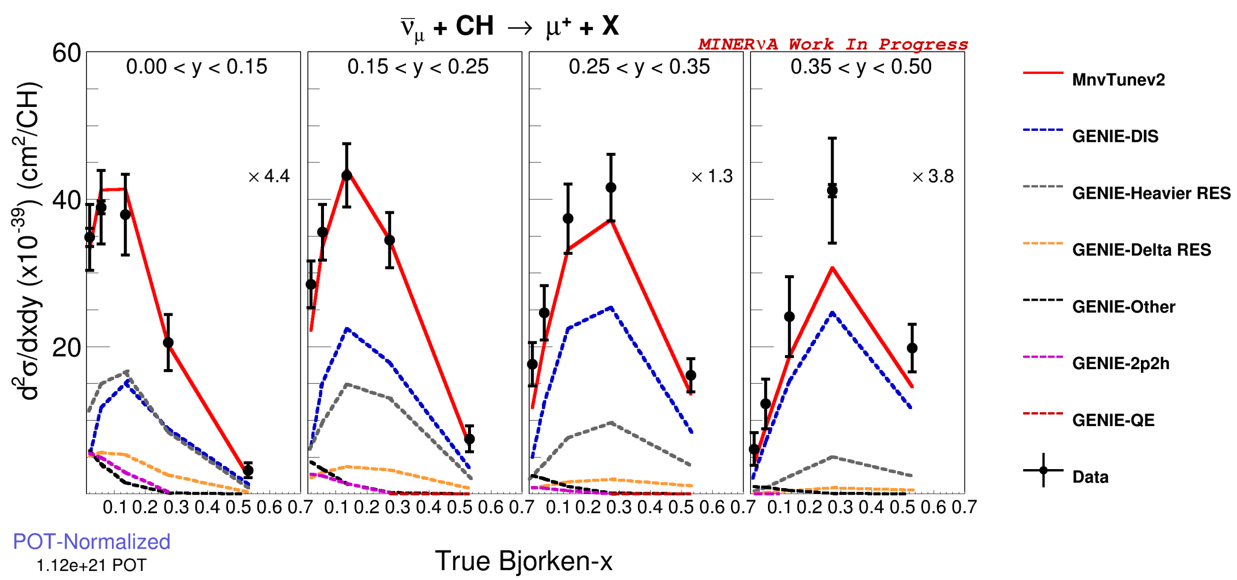

(b) **Antineutrino** mode.

Figure 61 – Cross sections in terms of **Bjorken variables**. Top (bottom) figure shows the result for neutrino (antineutrino) mode. The data points (black) carry both the statistical (inner error bars) and the statistical plus systematic uncertainties (outer error bars). The simulated cross section (solid red line) is split into various GENIE interaction channels.

7.2 Measurements as a function of muon momentum components

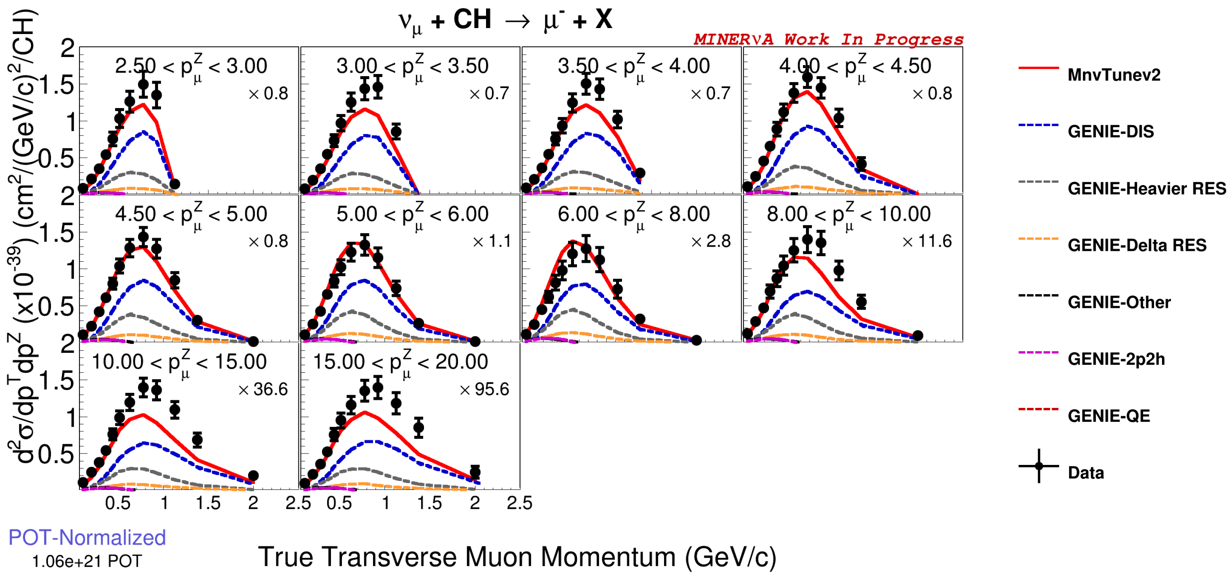

(a) **Neutrino** mode.

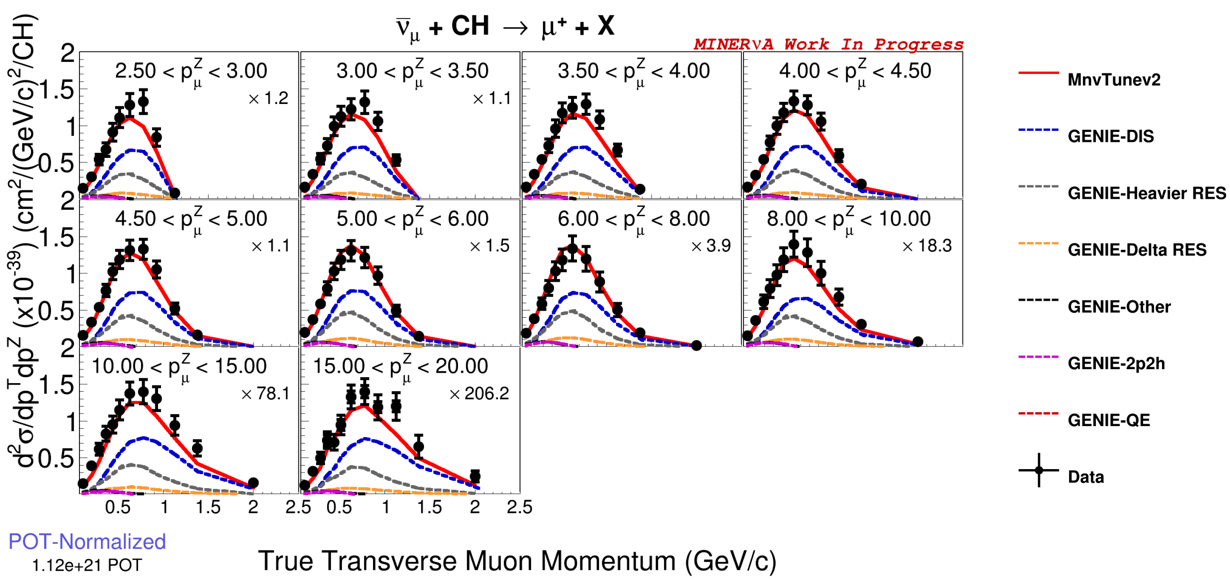

(b) **Antineutrino** mode.

Figure 62 – Cross sections in terms of **muon momentum components**. Top (bottom) figure shows the result for neutrino (antineutrino) mode. The data points (black) carry both the statistical (inner error bars) and the statistical plus systematic uncertainties (outer error bars). The simulated cross section (solid red line) is split into various GENIE interaction channels.

7.3 Discussion

The measured data cross sections are shown in Figs. 61 and 62, and Tab. 19 lists the main interaction channels, predicted by GENIE. According to GENIE, the sample is made primarily of DIS processes (57 %), followed by a resonance background (35 %). Overall, the MnvTunev2 simulation does not describe the measured data across the entire kinematic range, in both Bjorken and muon momentum variables.

In terms of the Bjorken x and y variables, in the first two y-panels, the data in the region $x < 0.2$ are overpredicted by the simulation $-$ y-panel 1 is dominated by muon kinematics, and the low-x region corresponds to DIS events; see Sec. 2.5. On the other hand, the data in last two y-panels are underpredicted, with an noticeable tension with the first two data points.

Moreover, as one moves towards the high energy regime, the relative contribution of GENIE-DIS events (dashed blue line) increases, whereas GENIE-Heavier RES (dashed gray line), and other components, decrease, as expected. In particular, across all panels, the GENIE-DIS prediction falls rapidly as x decreases. This points out to a mismodeling of that cross section channel, and deserves serious thoughts.

Now, considering the cross sections as a function of the outgoing muon momentum components, in Fig. 62, except for some bins in the panels corresponding to the kinematic region $4.50 < p_\mu^\mathsf{Z} < 8.00$ GeV, the simulation underpredicts the data. As p_μ^T increases, the data excess grows, especially for the antineutrino case. Such a trend has been previously observed in other MINERvA measurements, which suggested a mismodeling of the QE and resonant channels [143].

In addition, comparing the neutrino and antineutrino results at intermediate p_μ^Z bins, the data-simulation tension seems to be lower for neutrino data in the $p_\mu^\mathsf{T} < 0.7$ GeV region. A similar feature was also observed in the 1-dimensional SIS publication [20], and is attributed to both the low-Q^2 and the non-resonant pion suppression included in the MnvTunev2 central value (Sub-sec. 4.4.4). That is the reason for the apparent agreement in that region. The pion suppression, derived from neutrino datasets, were propagated to the antineutrino sample, but they do not show to be as effective as for neutrinos.

Regarding the fractional uncertainties, illustrated in Figs. 88 and 93, the magnitude of the error bars on the measured data is bigger for the Bjorken variables analysis than for muon momentum variables. As discussed in Sec. 2.5, the Bjorken variables are derived, model-dependent quantities, whereas the muon momentum is a fundamental physical variable, measured directly in the MINERvA and MINOS near detectors; it does not depend on the recoil energy reconstruction, thereby susceptible to less source of uncertainties.

The leading error groups are the following: “Muon Reconstruction”, “Particle Response”, “Flux” and “Interaction Model”. The first two uncertainties show up in bins dominated by high energy muons (especially low-x and low-y in the Bjorken analysis), which are not well reconstructed due to the detector acceptance (recall the discussion in Sub-sec. 5.1.1); an investigation is being conducted to confirm such an assumption. Additionally, the uncertainties on antineutrino data are slightly higher due to limited statistics, neutron and flux modeling. The breakdown of these error groups, which shows the specific source of uncertainty, is presented in Append. C.

8 Conclusions and future directions

This thesis reported measurements of muon neutrinos and antineutrinos double-differential cross sections in a resonance background-dominated phase space of the shallow inelastic scattering (SIS) region. The measurements were performed using the MINERvA hydrocarbon target exposed to the Fermilab NuMI neutrino flux, with a mean energy of approximately 6 GeV. The cross sections are presented as functions of the Bjorken variables and the longitudinal and transverse components of the outgoing muon momentum, measured with the MINERvA detector and the MINOS near detector.

The SIS data samples are isolated with the application of selection cuts designed using Monte Carlo simulations. The analysis signal and backgrounds are also determined from the simulation, but the latter are validated and constrained using a sideband technique. The detector smearing, present in the background-subtracted samples, is corrected through the D'Agostini unfolding procedure, and reconstruction and detector acceptance limitations are amended through the application of a efficiency correction. The unfolded efficiency-corrected distributions are divided by the integrated flux, number of targets and bin widths yielding to the final results.

Overall, the models implemented in the simulation cannot describe the measured data across the full kinematic range. Alternative simulation programs have also been tested against the data, but all of them struggle to predict interactions in the SIS background region. The understanding of SIS interactions is still incomplete. The results reported in this work contribute to fill the longstanding gap of measurements in such a kinematic regime, and can be used to improve interaction models for current and future oscillation experiments. The extracted double-differential data cross sections can be combined with other samples to fit parton distribution functions, like in Refs. [147, 148], and test alternative (to Rein-Sehgal) resonance models, such as [46, 47].

8.1 Future directions

Several lessons were learned throughout this work, and there is certainly room for improvements and extensions. In fact, a number of studies are already underway that are not included in this thesis, as they were not yet complete at the time of writing, but are planned to be reported in future publications. These studies include: the implementation of a new flux constraint on the SIS sample, derived from work by other MINERvA collaborators; a new Q^2-dependent tuning candidate for the simulated central value, which combines a reduction of the non-resonant pion suppression in selected bins with resonant form factors implemented in GENIE v3; and systematic uncertainties derived from a DIS model proposed by the AMU group, which accounts for higher-twist effects and target-mass corrections (Sub-sec. 3.2.2).

Also, it remains to be seen the version of these measurements that emphasizes the SIS multi-quark contribution to the cross section, defined by the kinematic region above $Q^2 = 1$ GeV^2 (Sec. 3.1), including updated predictions from alternative event generators. Moreover, nuclear medium effects associated to neutrino interactions in the SIS region could be explored using (now publicly) available MINERvA datasets encompassing carbon, lead, and iron nuclear targets [149].

APPENDIX A – Comparisons with other models

A.1 MINERvA tunings comparisons

As seen from the measurements presented in Secs. 7.1 and 7.2, the underlying simulation (MnvTunev2) clearly is unable to describe the data across the full kinematic range. To expand the discussion and make reliable interpretations of these results, a few alternative MINERvA tunings and models are considered. Confronting these measurements with tuned predictions is essential to guide future improvements on the data modeling. Some of these models (*e.g.*, MnvTunev2-NR1Pi and MnvTunev4) have been already used to test the unfolding procedure in Sub-sec. 5.3.3. Below, a summary of their main features is provided.

- MnvTunev2-NR1Pi

  As described in Sub-sec. 4.4.4, the central value of this analysis implements a series of reweights applied to GENIE 2.12.6. Among these ingredients, there is a suppression of 43 % on the non-resonant single pion production (NR1Pi) motivated by a reanalysis of neutrino data from ANL/BNL experiments. Such a suppression is completely removed from MnvTunev2.

- MnvTunev4

  The MnvTunev4 is also a modified version of MnvTunev2: first, the low-Q^2 suppression applied on GENIE resonant single pion production model is switched OFF; second, the value for the resonant axial mass, M_A, changes from 1.12 GeV to 0.94 GeV, and the cross section normalization factor is set to 1.15 based on a reanalysis of deuterium bubble chamber data from ANL/BNL.

- GS Axial FF

  This refers to a implementation of the Graczyk-Sobczyk axial form factor to reweight MnvTunev2 [90]. In this work, the authors refine the Rein-Sehgal model by replacing its *ad-hoc* form factors with theoretically and experimentally motivated ones. The new form factors provide better agreement with neutrino–nucleon and electron–nucleon data. More specifically, what is considered for this model comparison is the term $1-(W^2-Q^2-M_N^2)/8M_N^2$ from Eq. 54 in their paper. This contribution is used to reweight GENIE heavier resonances prediction, such as N*(1440), N*(1520), N*(1535), etc.

- SuSA 2p2h

  The Valencia 2p2h implementation in GENIE is reweighted using the Super-Scaling Approximation (SuSA) 2p2h model [142]. The model uses a superscaling framework constrained by electron scattering data and relativistic mean-field dynamics. While the Valencia approach is a microscopic many-body calculation based on a local Fermi gas, SuSA provides a more data-driven, relativistically consistent description across a broader kinematic range.

A.1.1 MINERvA tunings comparisons as a function of Bjorken variables

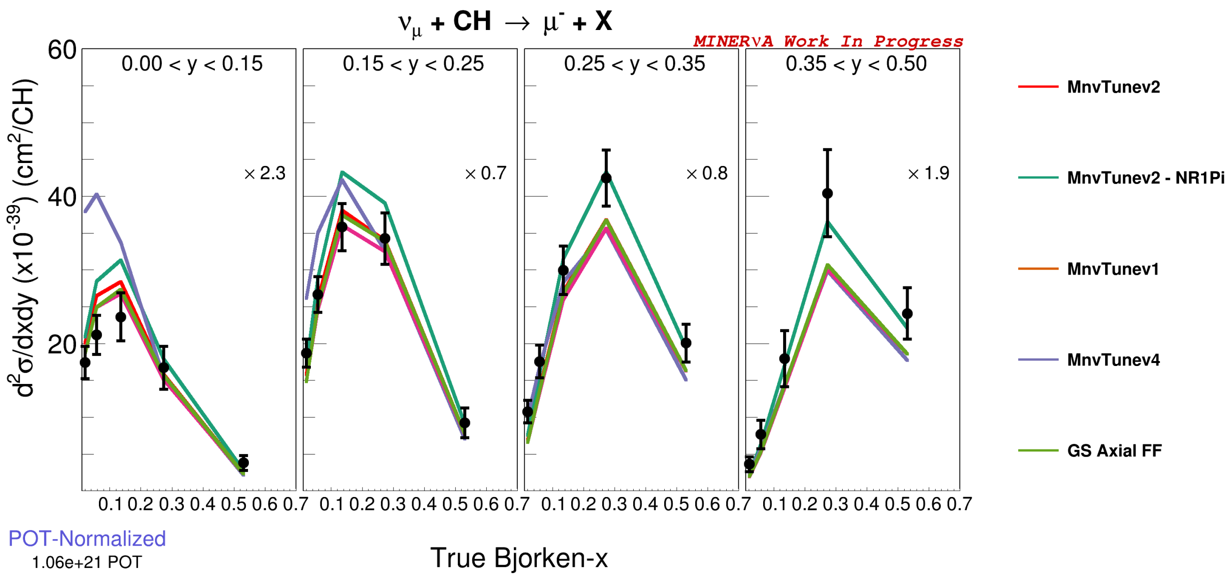

(a) **Neutrino** mode.

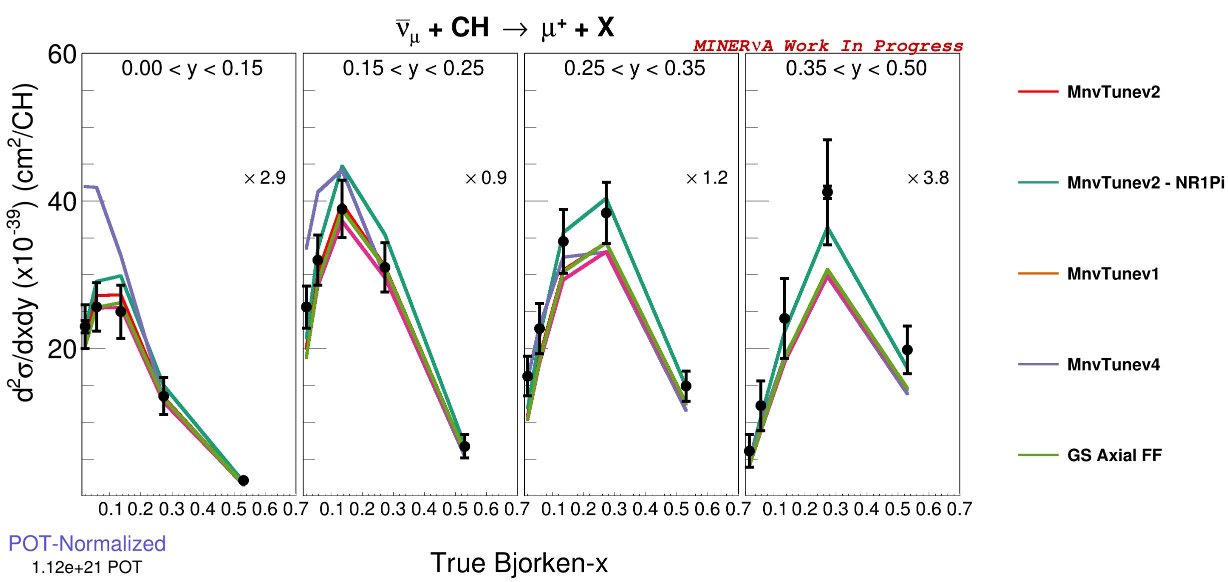

(b) **Antineutrino** mode.

Figure 63 – MINERvA tunings comparisons for extracted data cross sections in terms of **Bjorken variables**. Top (bottom) figure shows the result for neutrino (antineutrino) mode. The simulation baseline (MnvTunev2) is represented by a solid red line. The data points (black) are extracted considering MnvTunev2 as central value, and carry both the statistical (inner error bars) and the statistical plus systematic uncertainties (outer error bars). For better visualization, each panel has been scaled by a specific factor to normalize its height.

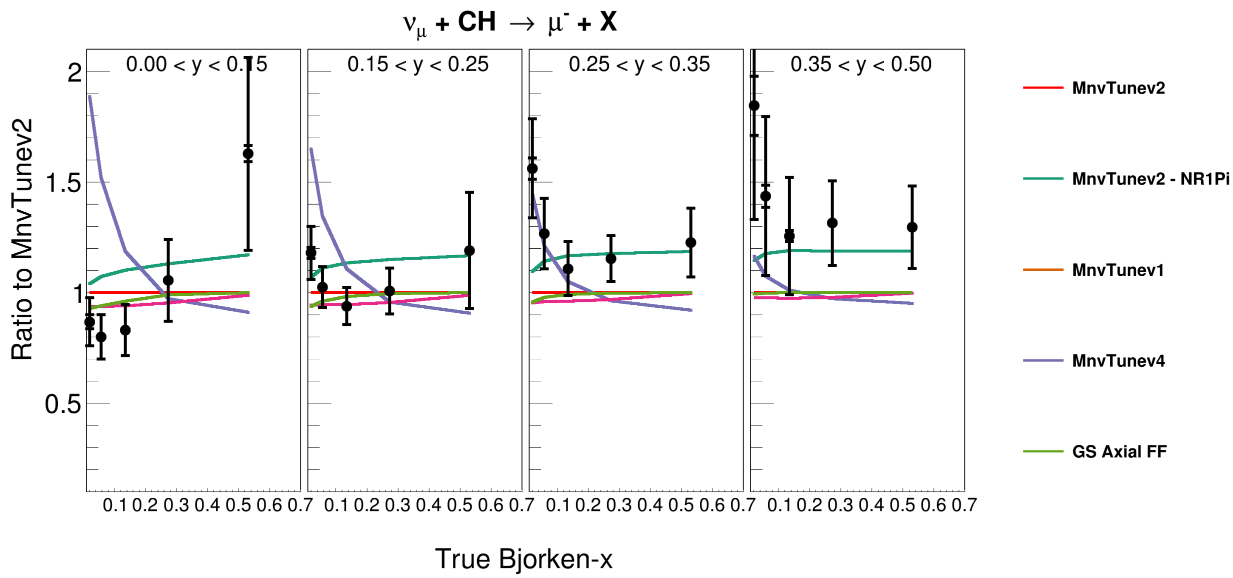

(a) **Neutrino** mode.

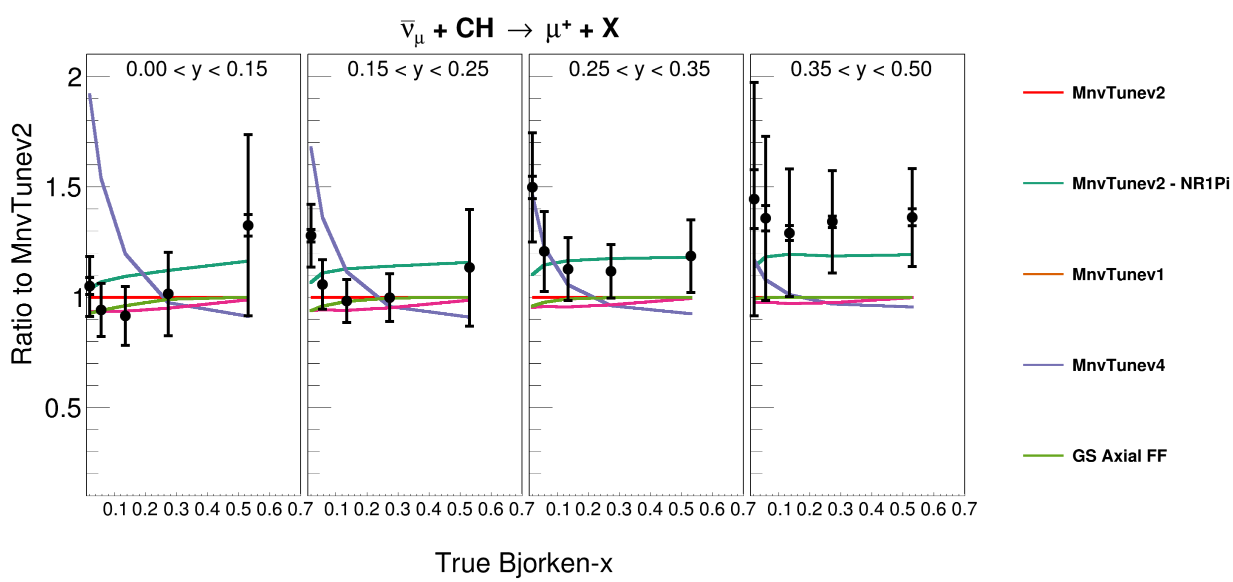

(b) **Antineutrino** mode.

Figure 64 – Ratio of MINERvA tunings to the simulation baseline (MnvTunev2) in terms of **Bjorken variables**. Top (bottom) figure shows the result for neutrino (antineutrino) mode. The data points (black) are extracted considering MnvTunev2 as central value, and carry both the statistical (inner error bars) and the statistical plus systematic uncertainties (outer error bars).

A.1.2 MINERvA tunings comparisons as a function of muon momentum components

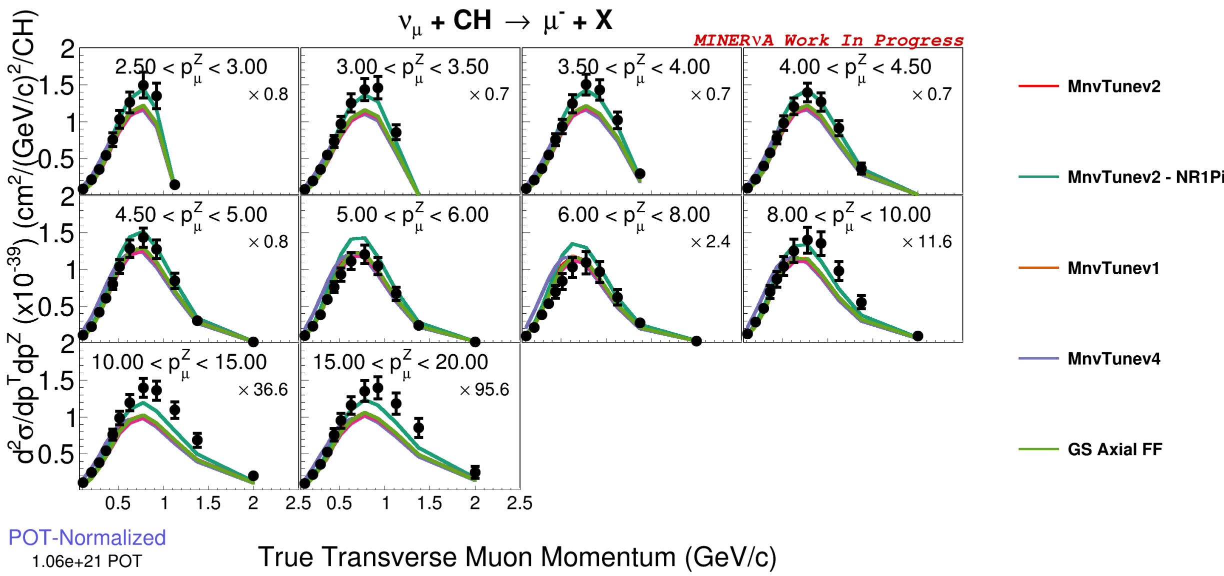

(a) **Neutrino** mode.

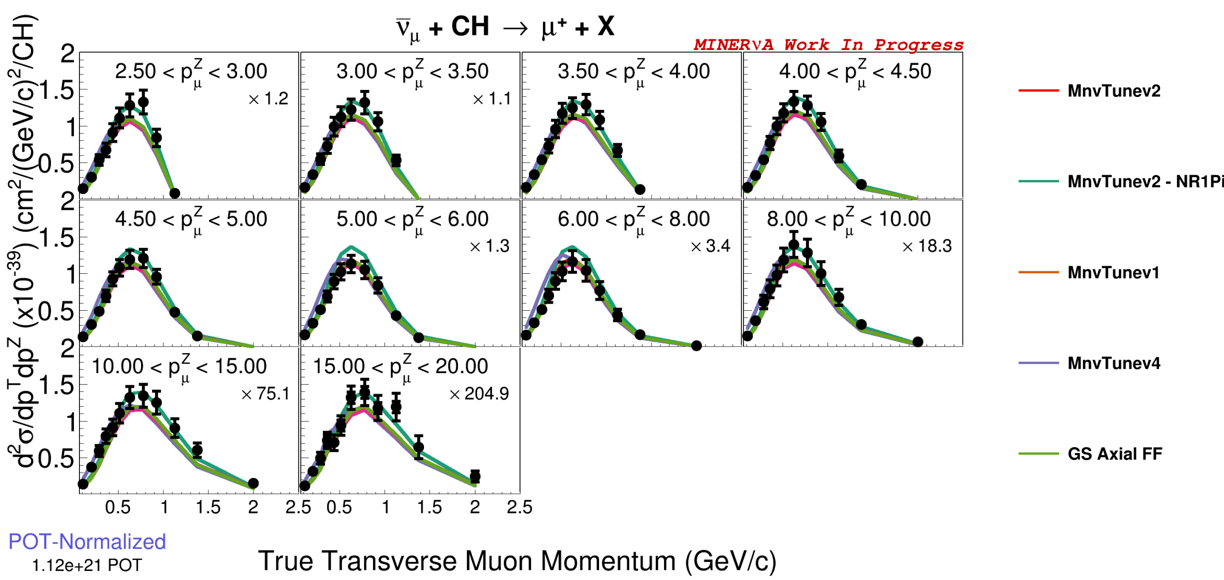

(b) **Antineutrino** mode.

Figure 65 – MINERvA tunings comparisons for extracted data cross sections in terms of **muon momentum components**. Top (bottom) figure shows the result for neutrino (antineutrino) mode. The simulation baseline (MnvTunev2) is represented by a solid red line. The data points (black) are extracted considering MnvTunev2 as central value, and carry both the statistical (inner error bars) and the statistical plus systematic uncertainties (outer error bars). For better visualization, each panel has been scaled by a specific factor to normalize its height.

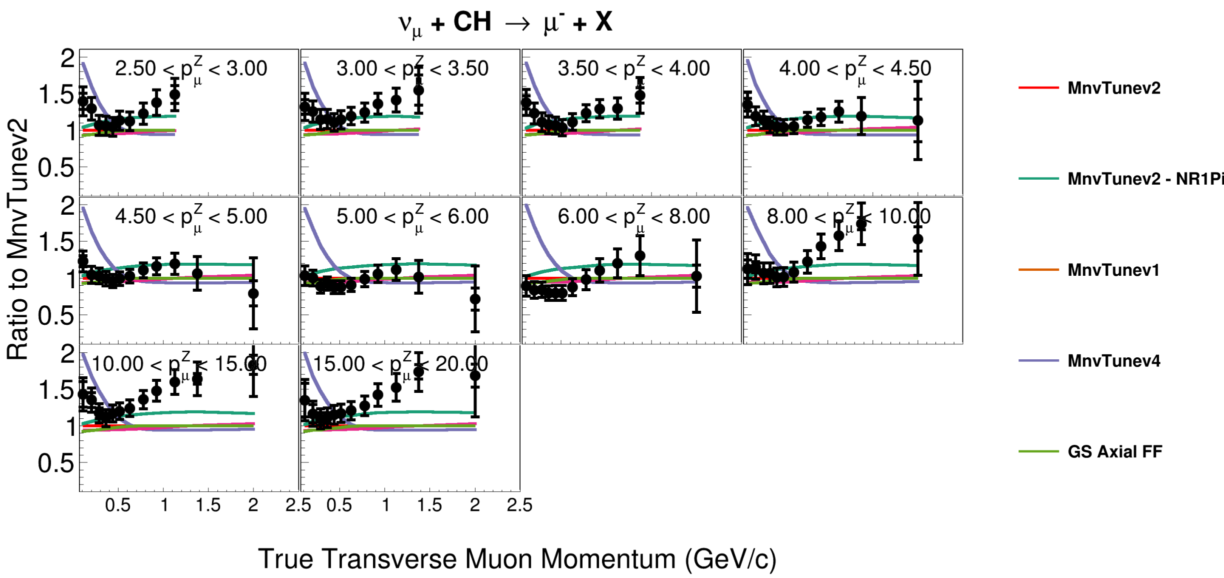

(a) **Neutrino** mode.

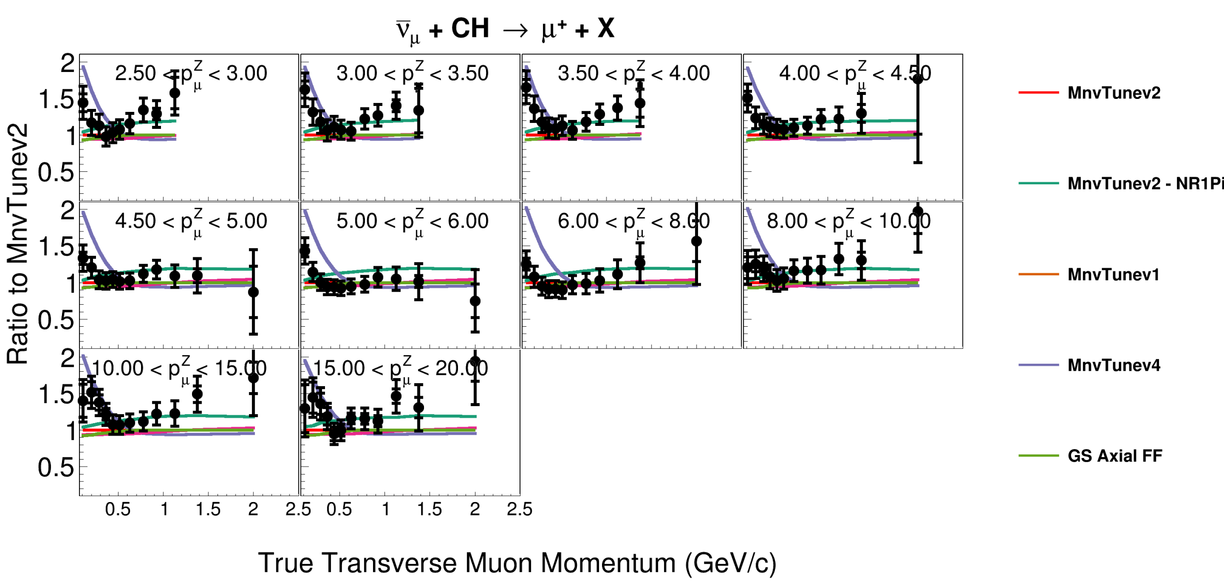

(b) **Antineutrino** mode.

Figure 66 – Ratio of MINERvA tunings to the simulation baseline (MnvTunev2) in terms of **muon momentum components**. Top (bottom) figure shows the result for neutrino (antineutrino) mode. The data points (black) are extracted considering MnvTunev2 as central value, and carry both the statistical (inner error bars) and the statistical plus systematic uncertainties (outer error bars).

A.2 Comparisons to other simulation programs

A.2.1 GENIE v3.0.6

In the GENIE v3.0.6 with RFG initial nucleon state, the QE and 2p2h channels are replaced by the Valencia hadronic tensor framework; resonant, non-resonant, and coherent pion production use the Berger-Sehgal model [146]; FSI are treated with the updated INTRANUKE-hA cascade (2018 revision).

A.2.2 NEUT v5.4.1

NEUT v5.4.1 with LFG nuclear initial state also employs the Valencia/Nieves hadronic tensor framework for multi-nucleon interactions. However, unlike GENIE v3, NEUT uses the Kabirnezhad single-pion production model, which includes a more detailed treatment of the $\Delta(1232)$ resonance and its medium modifications. Coherent pion production is handled using the Berger–Sehgal formulation.

A.2.3 NuWro v19.02

NuWro with an LFG initial state provides modular QE and 2p2h configurations, typically drawing from the Valencia/Nieves framework. For resonant pion production, NuWro uses an explicit $\Delta(1232)$ treatment based on the Adler–Rarita–Schwinger formalism.

A.2.4 GiBUU 2021

GiBUU differs fundamentally from the above, cascade-based neutrino generators. The nuclear initial state is represented using nucleons bound in a mean-field potential, and all hadronic final states are propagated through the nucleus via a Boltzmann–Uehling–Uhlenbeck (BUU) transport equation.

A.2.5 Generator comparisons as a function of Bjorken variables

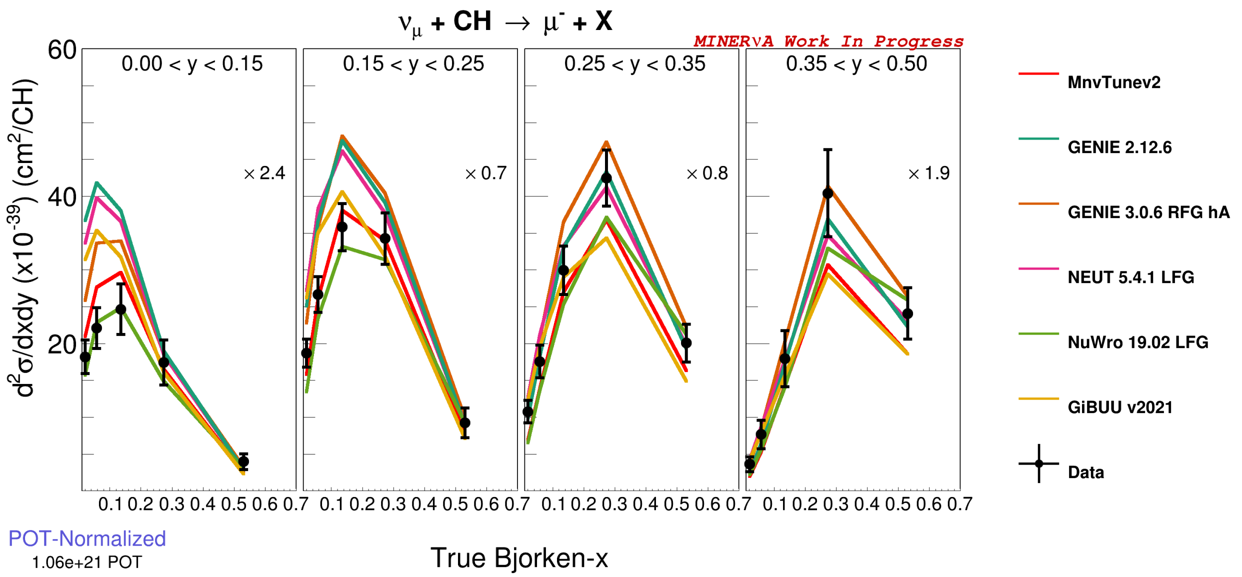

(a) **Neutrino** mode.

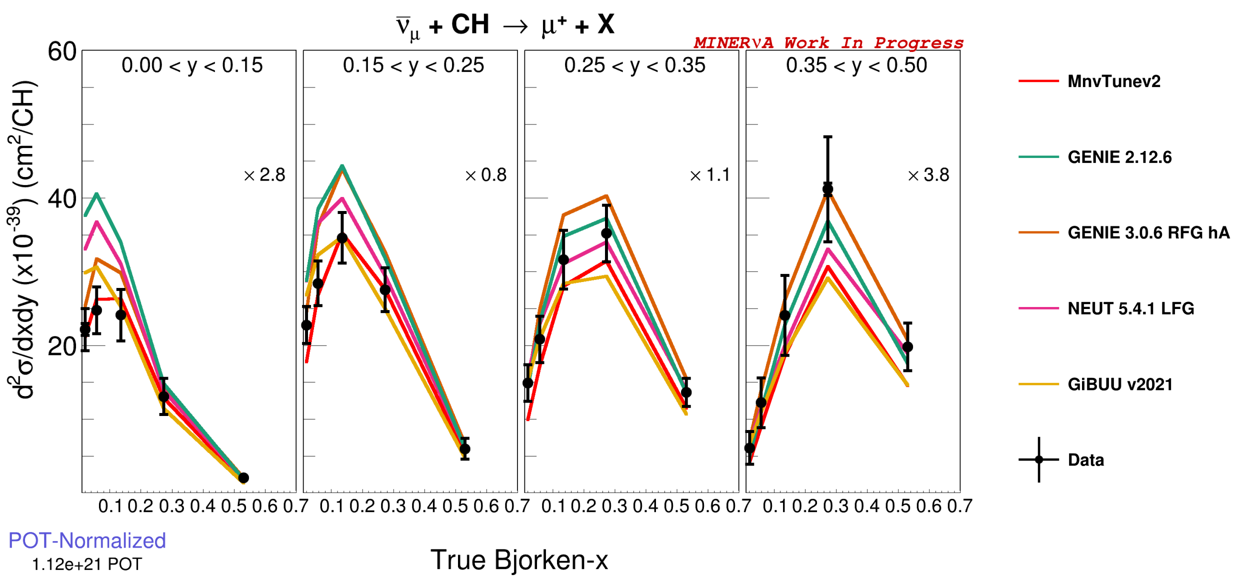

(b) **Antineutrino** mode.

Figure 67 – Generator comparisons against extracted data cross section in terms of **Bjorken variables**. Top (bottom) figure shows the result for neutrino (antineutrino) mode. The MnvTunev2 central value is represented by a red line; GENIE v2 in teal; GENIE v3 in orange; NEUT in magenta; NuWro in light green; GiBUU in yellow. The data points (black), extracted considering MnvTunev2 central value, carry both the statistical (inner error bars) and the statistical plus systematic uncertainties (outer error bars). For better visualization, each panel has been scaled by a specific factor to normalize its height.

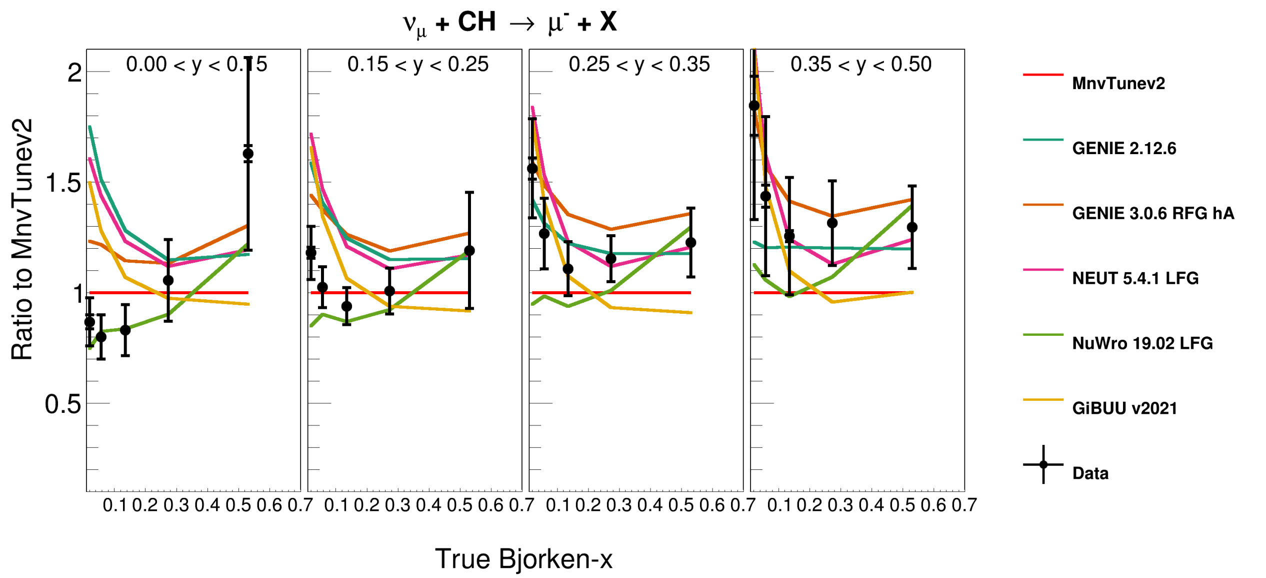

(a) **Neutrino** mode.

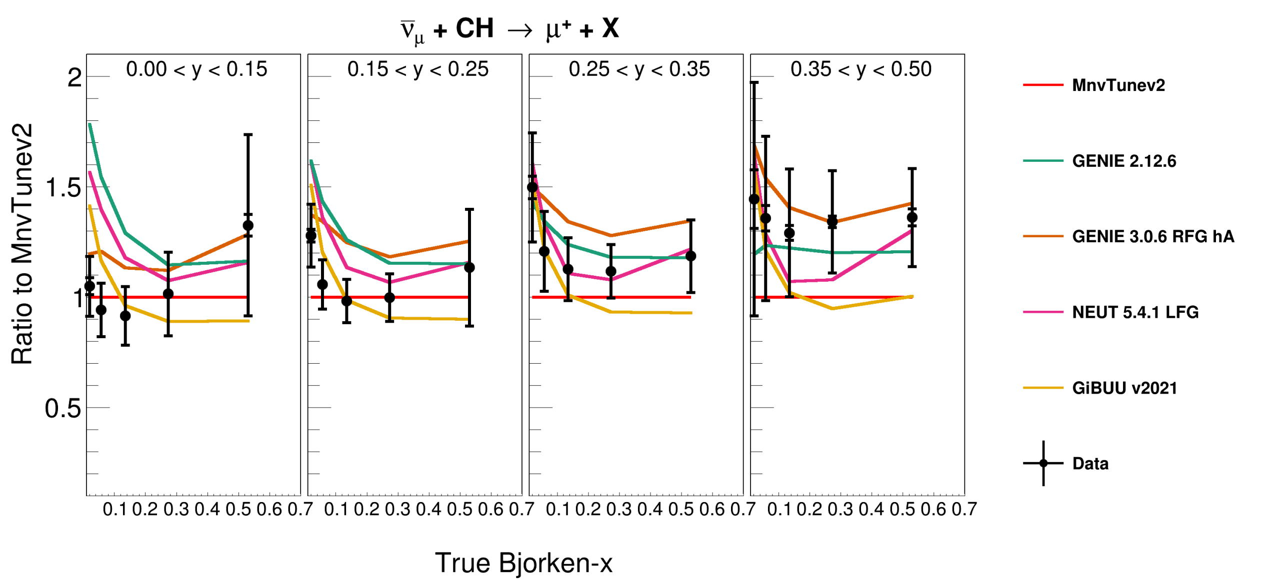

(b) **Antineutrino** mode.

Figure 68 – Ratio of generator predictions to MnvTunev2 in terms of **Bjorken variables**. Top (bottom) figure shows the result for neutrino (antineutrino) mode. The MnvTunev2 central value is represented by a red line; GENIE v2 in teal; GENIE v3 in orange; NEUT in magenta; NuWro in light green; GiBUU in yellow. The data points (black), extracted considering MnvTunev2 central value, carry both the statistical (inner error bars) and the statistical plus systematic uncertainties (outer error bars).

A.2.6 Generator comparisons as a function of muon momentum components

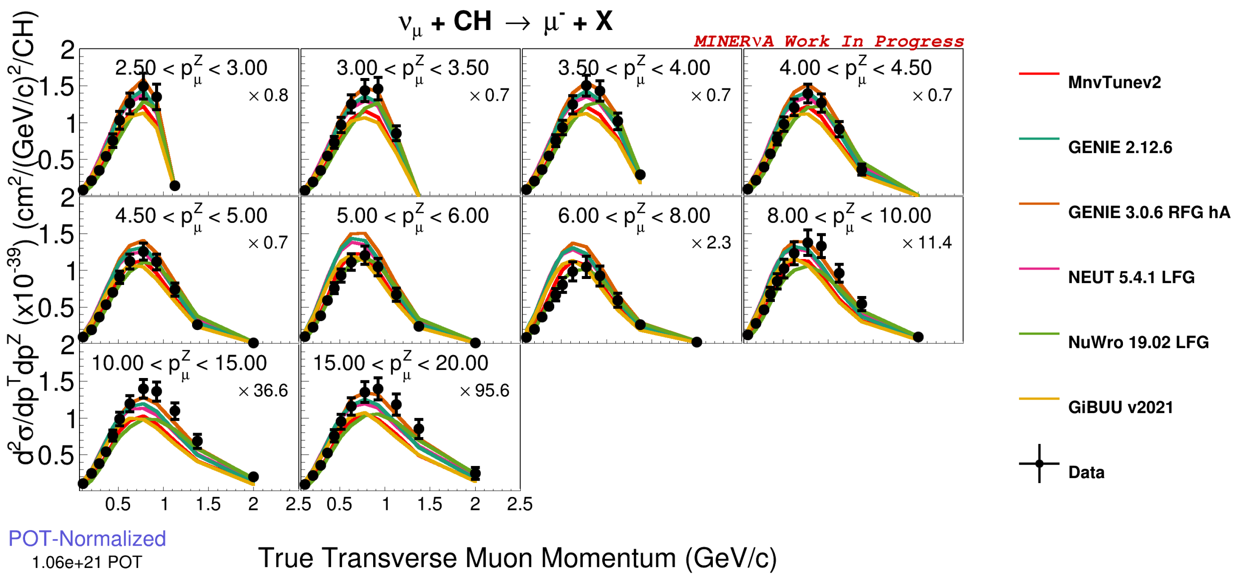

(a) **Neutrino** mode.

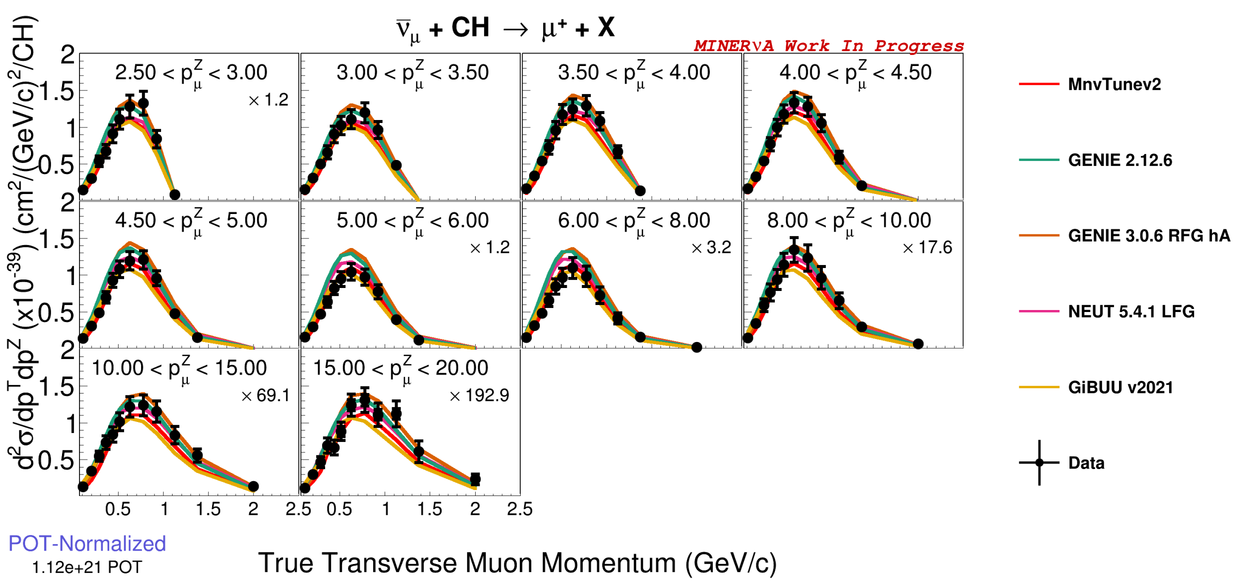

(b) **Antineutrino** mode.

Figure 69 – Generator comparisons against extracted data cross section in terms of **muon momentum components**. Top (bottom) figure shows the result for neutrino (antineutrino) mode. The MnvTunev2 central value is represented by a red line; GENIE v2 in teal; GENIE v3 in orange; NEUT in magenta; NuWro in light green; GiBUU in yellow. The data points (black), extracted considering MnvTunev2 central value, carry both the statistical (inner error bars) and the statistical plus systematic uncertainties (outer error bars). For better visualization, each panel has been scaled by a specific factor to normalize its height.

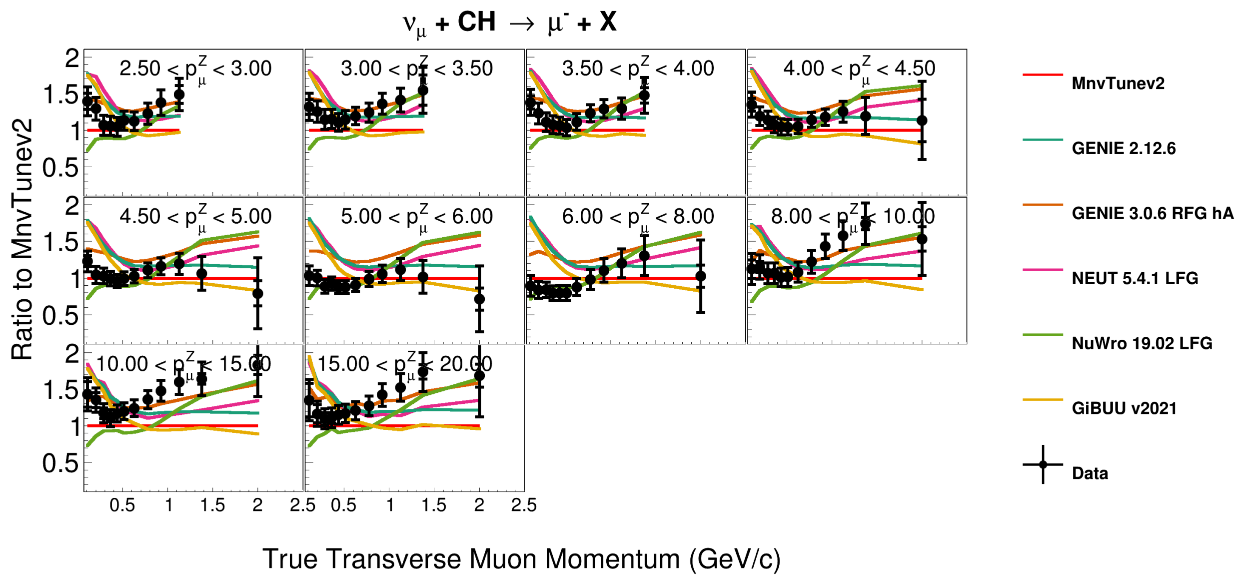

(a) **Neutrino** mode.

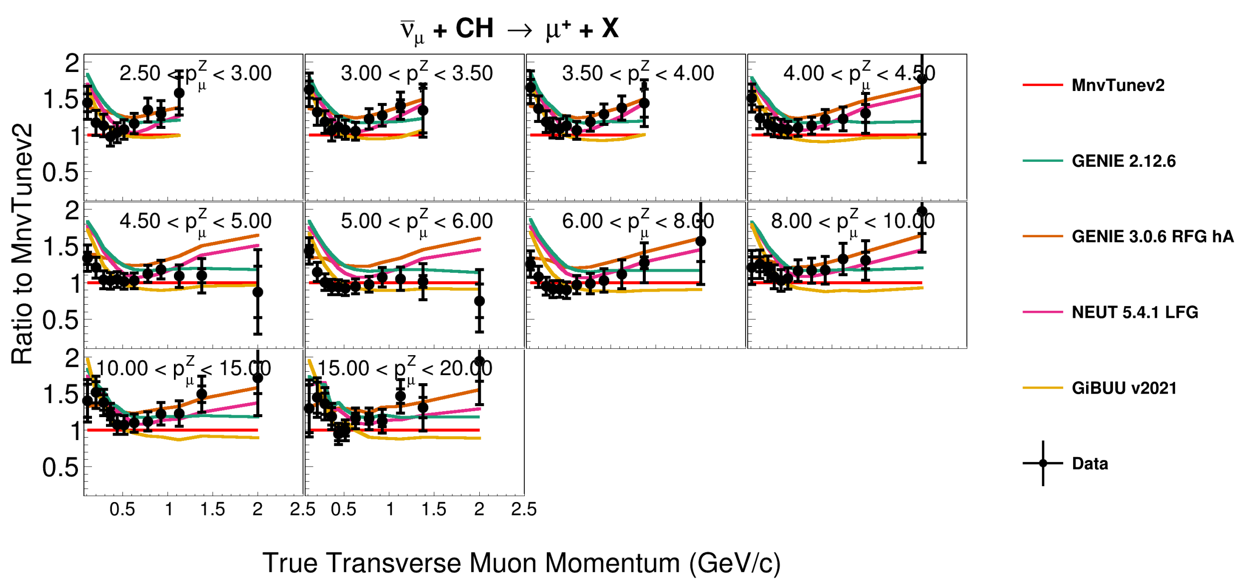

(b) **Antineutrino** mode.

Figure 70 – Ratio of generator predictions to MnvTunev2 in terms of **muon momentum components**. Top (bottom) figure shows the result for neutrino (antineutrino) mode. The MnvTunev2 central value is represented by a red line; GENIE v2 in teal; GENIE v3 in orange; NEUT in magenta; NuWro in light green; GiBUU in yellow. The data points (black), extracted considering MnvTunev2 central value, carry both the statistical (inner error bars) and the statistical plus systematic uncertainties (outer error bars).

A.2.7 Evaluation of MINERvA tunings

Some other MINERvA tunings and models have been considered and confronted against the extracted data cross sections. These alternative tunings and models were summarized in Sec. A.1, and comparisons are shown in Figs. 63-66. According to these results, the MnvTunev2 without the non-resonant pion suppression of 43 % seems to describe better the SIS data. This conclusion is also found in the 1-dimensional measurements publication [20].

A similar conclusion can be drawn for the alternative 2p2h model (SuSA): considering for instance the lowest y-panel in Fig. 64, one can see that the data favors SuSA 2p2h more. MnvTunev4 is clearly not a good tuning candidate for SIS, and emphasizes the need of the low-Q^2 suppression, which was discussed in Sub-sec. 4.4.4.

A.2.8 Performance of neutrino event generators in the SIS region

Finally, the measured data are used to test cross section interaction models implemented in alternative neutrino event generators. The list includes an upgraded version of GENIE [144, 145], NEUT [87], NuWro [88], and GiBUU [76]. The results are shown in Figs. 67-70. Despite non-satisfactory χ^2 per degree of freedom, NuWro provides the best prediction for neutrino data, matching the majority of bins, while GENIE v3 with relativistic fermi gas configuration describes antineutrino interactions best.

As discussed in Sec. 3.3, resonant pion production in NuWro is simulated using the Graczyk and Sobczyk model, with the non-resonant background predicted by the Bodek and Yang model, extended down to the resonance region. In this generator, the transition from resonance to the DIS regime is done smoothly, via a linear function. On the other hand, GENIE v3 uses an improved version of the Rein-Sehgal model (Berger-Sehgal [146]) that accounts for nonzero lepton mass, lepton polarization, and pion pole contribution.

In addition to the cross section distributions, full covariance matrices – including both the statistical and systematic (Eq. 6.1) errors on data – are used to estimate the data-model tension via a χ^2 metric, defined through

$$\chi^2 = \sum_{i=1}^{\text{nBins}} \sum_{j=1}^{\text{nBins}} \left(\text{Data}_i - \text{MC}_i\right) \text{C}_{ij}^{-1} \left(\text{Data}_j - \text{MC}_j\right). \tag{A.1}$$

In Eq. A.1, nBins is the product of the number of bins along the X-, Y- projected distributions, nBins $= xBins * yBins$, corresponding to the number of degrees of freedom (20 and 120 for the Bjorken x and y variables, and outgoing muon momentum components, respectively), and C_{ij}^{-1} is the inverse of the covariance matrix.

Table 20 – Measured χ^2 per degree of freedom, grouped by neutrino modes, for the analysis central value (MnvTunev2) and each alternative MINERvA tuning, models, and generator predictions, described in Secs. A.1 and A.2.

Model	(x,y) ν_μ	(x,y) $\bar{\nu}_\mu$	$(p_\mu^\mathsf{T}, p_\mu^\mathsf{Z})$ ν_μ	$(p_\mu^\mathsf{T}, p_\mu^\mathsf{Z})$ $\bar{\nu}_\mu$
GENIE v2.12.6	29.6	19.1	5.8	5.4
MnvTunev2	15.2	7.0	4.9	3.0
MnvTunev2 - NR1Pi	16.7	9.0	5.4	3.5
MnvTunev4	35.8	26.5	6.6	6.6
SuSA2p2h	14.0	6.4	4.9	2.8
GS Axial FF	12.8	5.1	4.5	2.5
GENIE v3.0.6 RFG hA	13.3	9.1	5.8	4.2
NEUT v5.4.1 LFG	17.8	11.9	7.5	5.3
NuWro v19.02 LFG	7.5	–	4.1	–
GiBUU v2021	20.6	9.1	6.4	3.7

APPENDIX B – Backgrounds constraint and validation

B.1 Definition of sideband regions

The sideband regions used in this analysis were established by considering the backgrounds classification from GENIE 2.12.6 predictions. Three sidebands are defined by kinematic cuts on the reconstructed invariant mass, W_{reco}, listed in Tab. 8.

As illustrated in Fig. 71, the sideband definitions are based on purity, efficiency, and signal contamination (1 - purity) studies. The W_{reco} boundaries are chosen to produce an acceptable purity-efficiency balance, *i.e.* one wants high enough signal purity but not too much efficiency loss. Guided by this criterion, the regions populated by QE and Δ-resonant backgrounds are determined by looking at the fraction of those events together, whereas the W_{reco} cut defining sideband 2 considers the GENIE-DIS category alone.

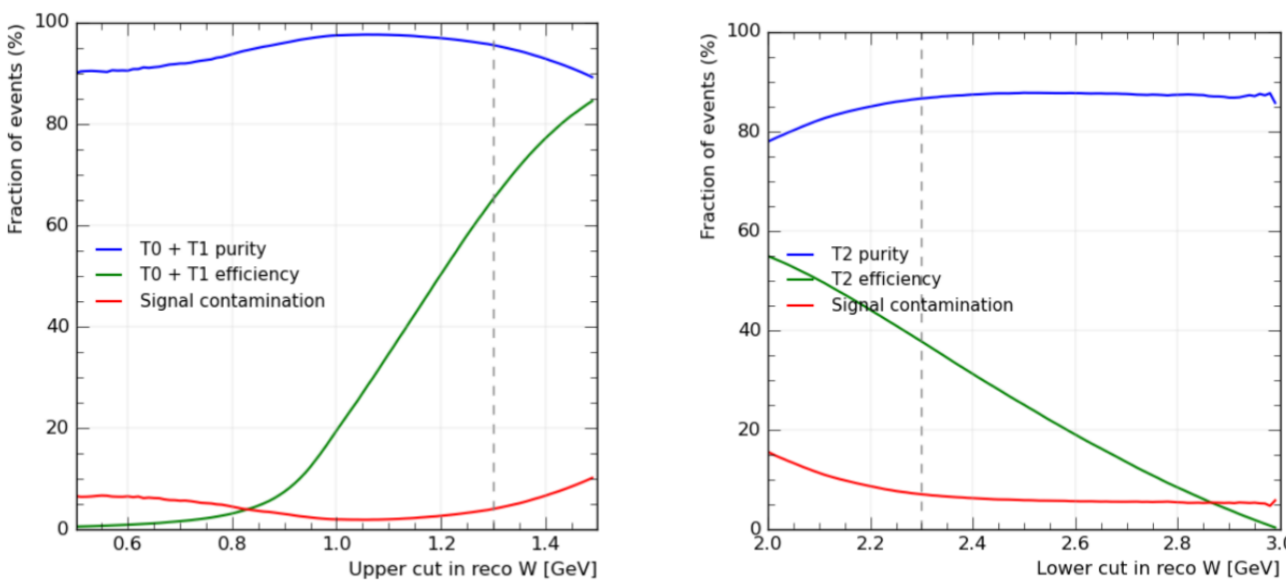

Figure 71 – Sideband regions defined by cuts on the reconstructed invariant mass, W_{reco}. T0, T1 and T2 refer to QE, RES and DIS backgrounds. The solid lines correspond to purity (blue), efficiency (green) and signal contamination (red). The MINERvA document number for this study is 27143.

B.2 Sideband tuning results

B.2.1 Bjorken variables analysis

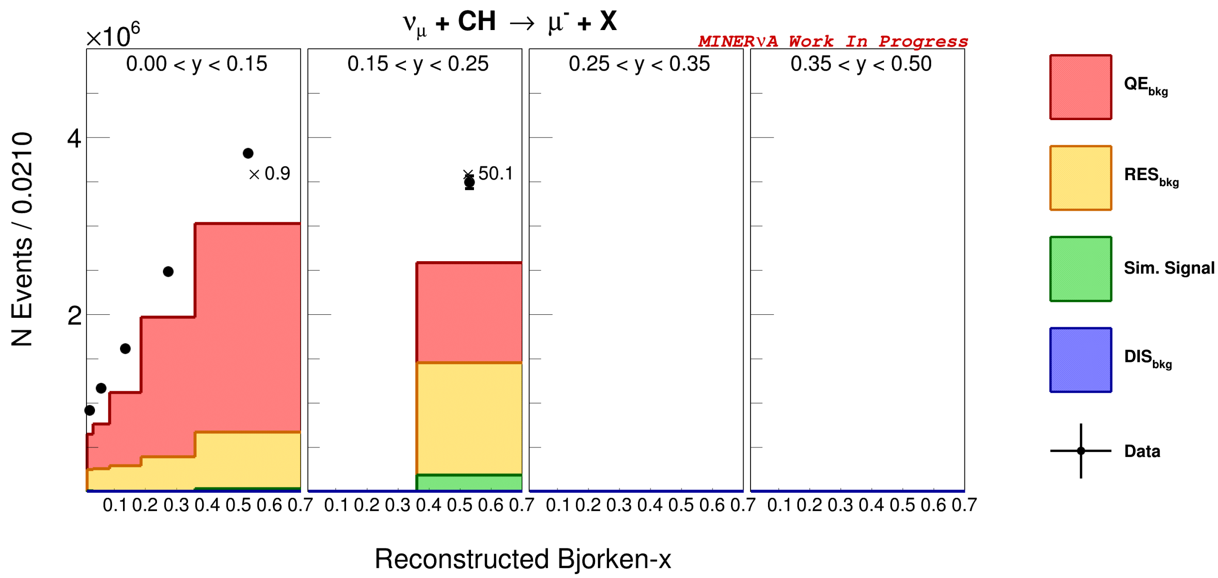

(a) **Neutrino** mode.

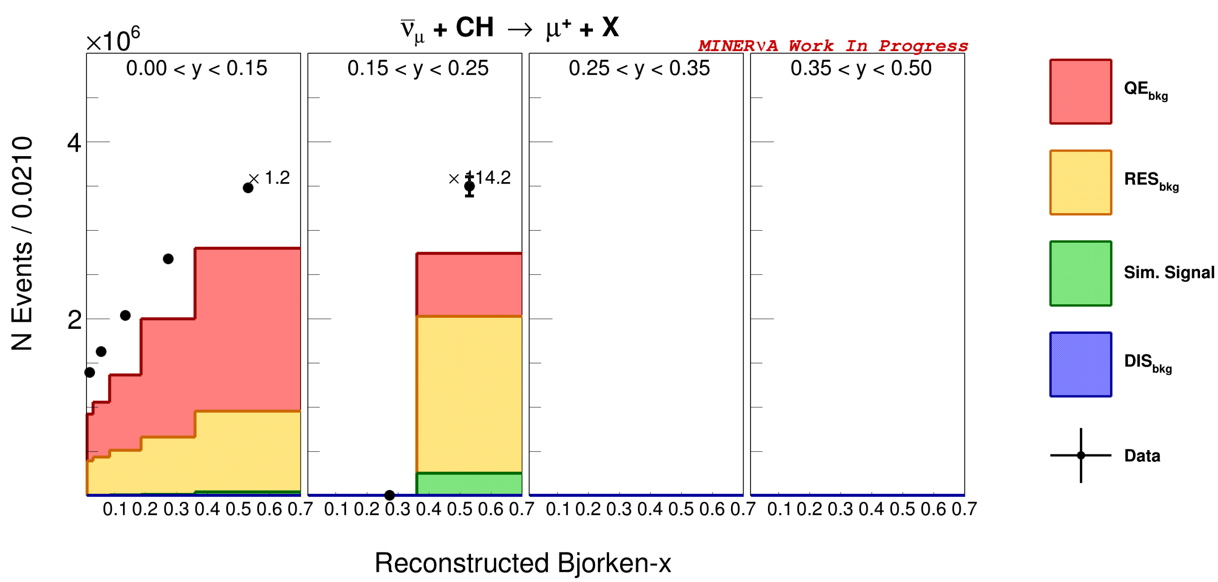

(b) **Antineutrino** mode.

Figure 72 – Selected **events in Sideband 0** (QE-rich) shown in terms of **Bjorken variables**. The top (bottom) plot displays the data (black points) and the simulated events in neutrino (antineutrino) mode, stacked in descending order of contribution: QE$_{bkg}$ (red), RES$_{bkg}$ (yellow), signal (green) and DIS$_{bkg}$ (blue). For better visualization, each panel has been scaled by a specific factor to normalize its height. The error bars on the data represent statistical uncertainties only.

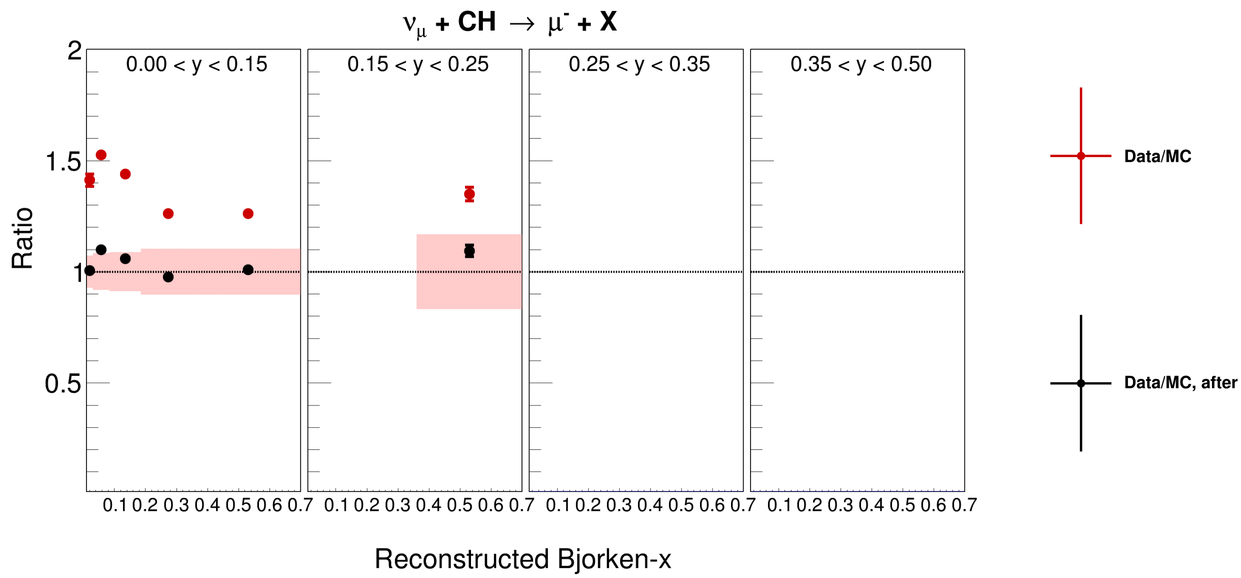

(a) **Neutrino** mode.

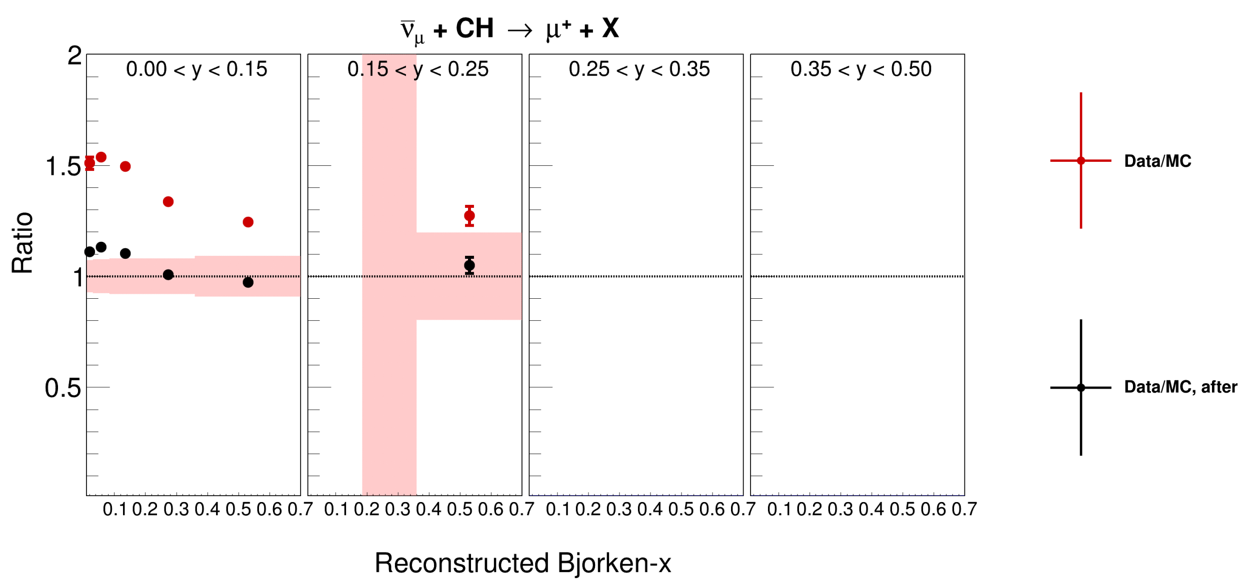

(b) **Antineutrino** mode.

Figure 73 – Data-to-MC ratios in **Sideband 0** as a function of **Bjorken variables**. Red (black) points represent the data/MC ratio before (after) tuning the background. Error bars indicate statistical uncertainty, while the pink error band around line one represents the total (statistical+systematic) uncertainty on the simulation. Top (bottom) plot displays the distribution ratios in neutrino (antineutrino) mode.

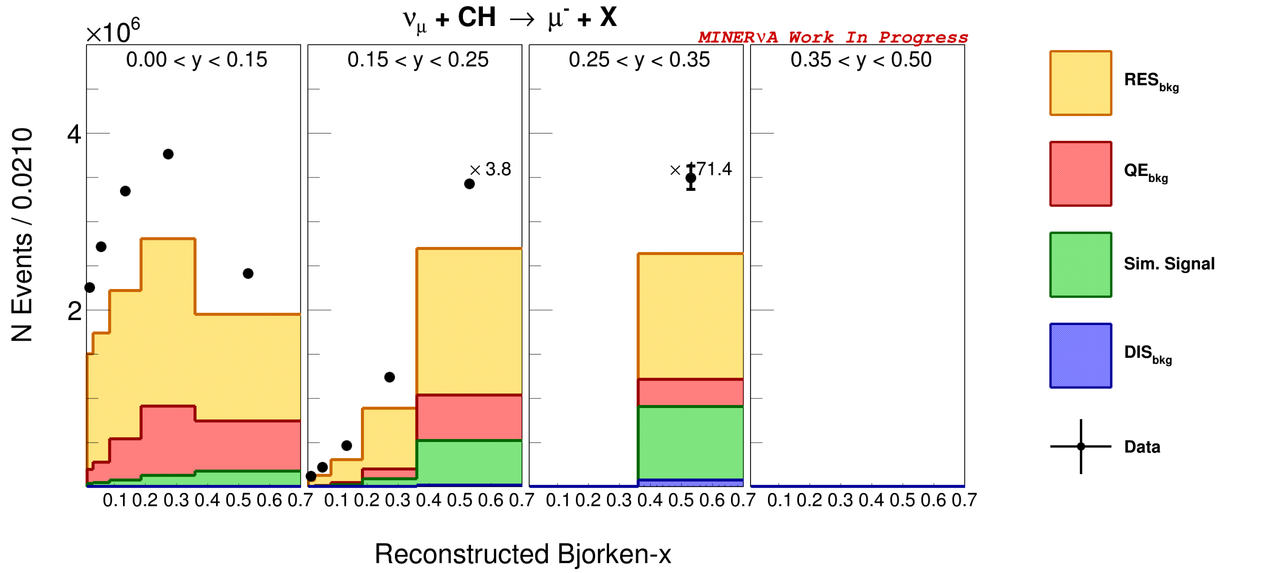

(a) **Neutrino** mode.

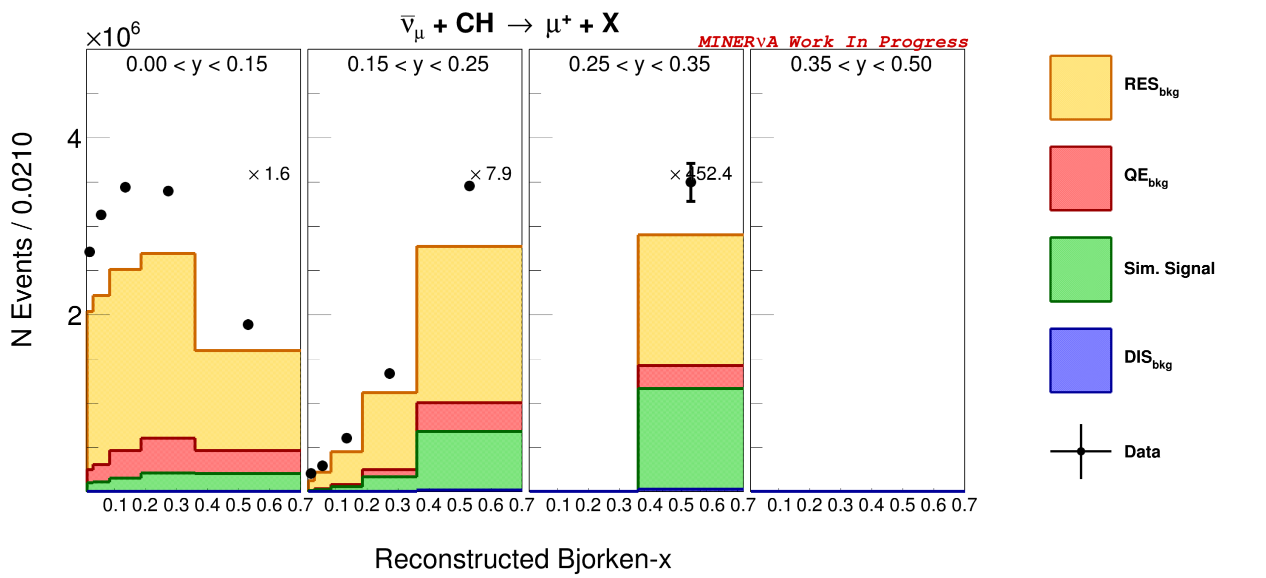

(b) **Antineutrino** mode.

Figure 74 – Selected **events in Sideband 1** (RES-rich) shown in terms of **Bjorken variables**. The top (bottom) plot displays the data (black points) and the simulated events in neutrino (antineutrino) mode, stacked in descending order of contribution: RES_{bkg} (yellow), QE_{bkg} (red), signal (green) and DIS_{bkg} (blue). For better visualization, each panel has been scaled by a specific factor to normalize its height. The error bars on the data represent statistical uncertainties only.

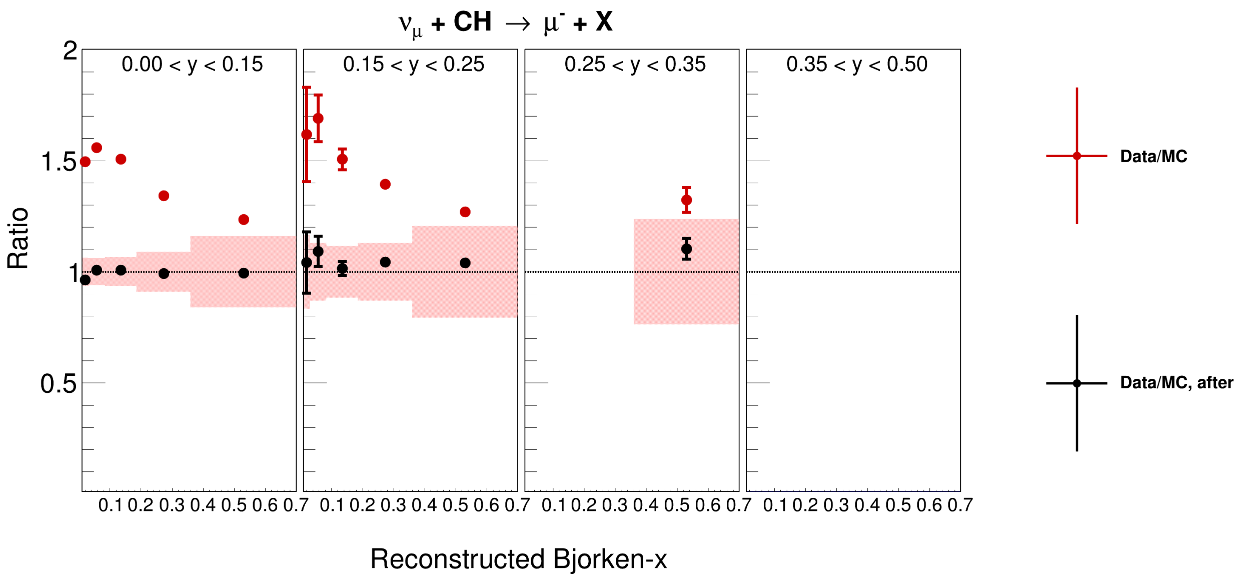

(a) **Neutrino** mode.

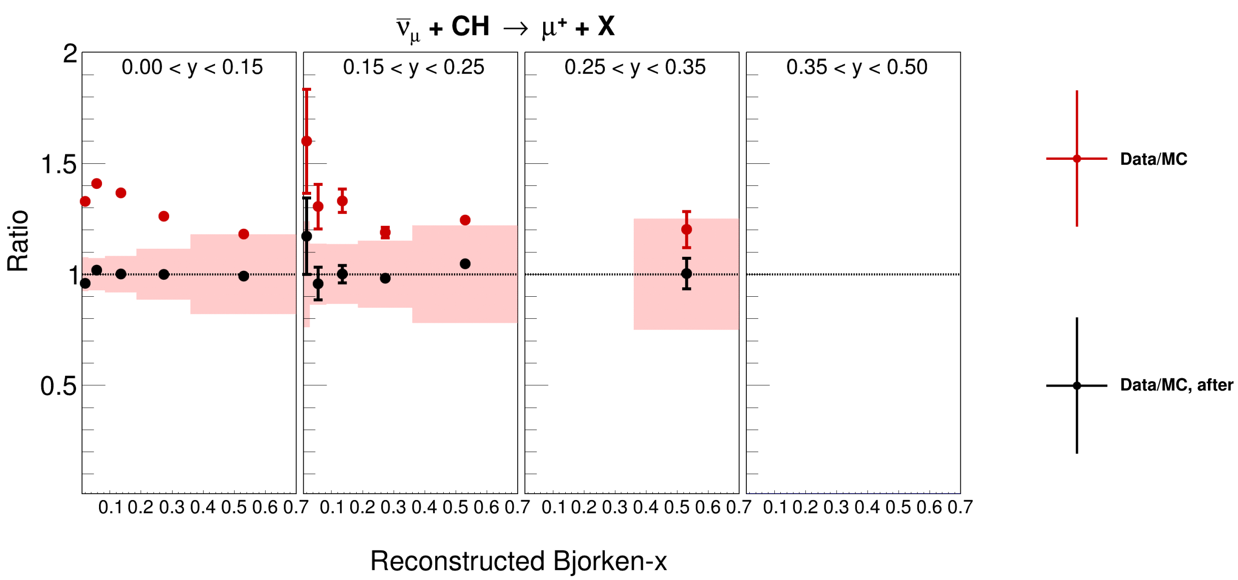

(b) **Antineutrino** mode.

Figure 75 – Data-to-MC ratios in **Sideband 1** as a function of **Bjorken variables**. Red (black) points represent the data/MC ratio before (after) tuning the background. Error bars indicate statistical uncertainty, while the pink error band around line one represents the total (statistical+systematic) uncertainty on the simulation. Top (bottom) plot displays the distribution ratios in neutrino (antineutrino) mode.

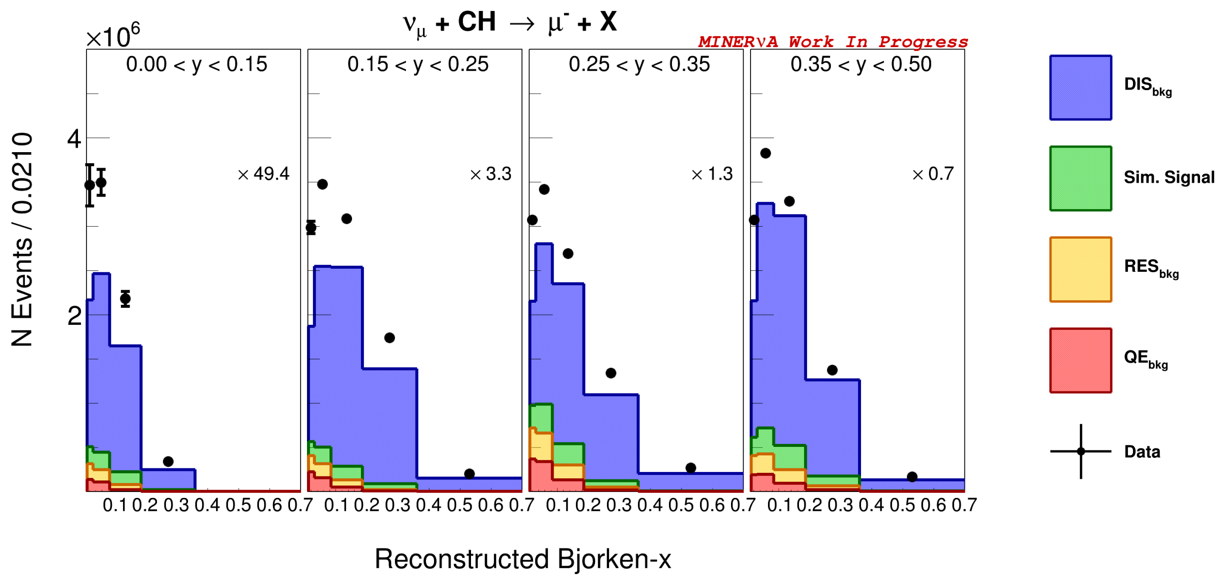

(a) **Neutrino** mode.

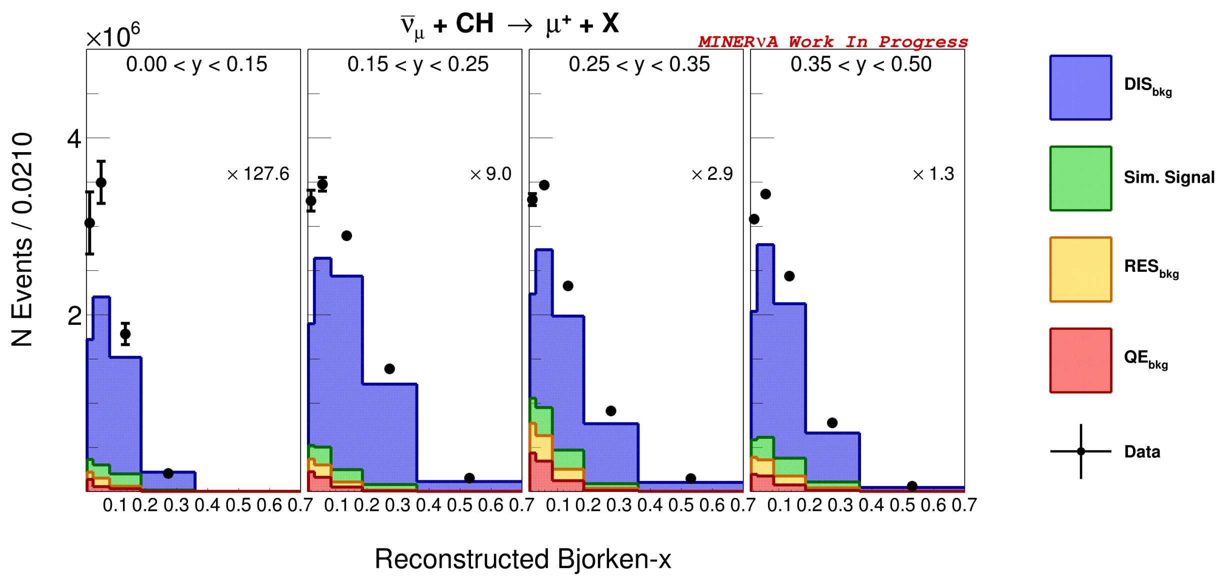

(b) **Antineutrino** mode.

Figure 76 – Selected **events in Sideband 2** (DIS-rich) shown in terms of **Bjorken variables**. The top (bottom) plot displays the data (black points) and the simulated events in neutrino (antineutrino) mode, stacked in descending order of contribution: DIS_{bkg} (blue), signal (green), RES_{bkg} (yellow), and QE_{bkg} (red). For better visualization, each panel has been scaled by a specific factor to normalize its height. The error bars on the data represent statistical uncertainties only.

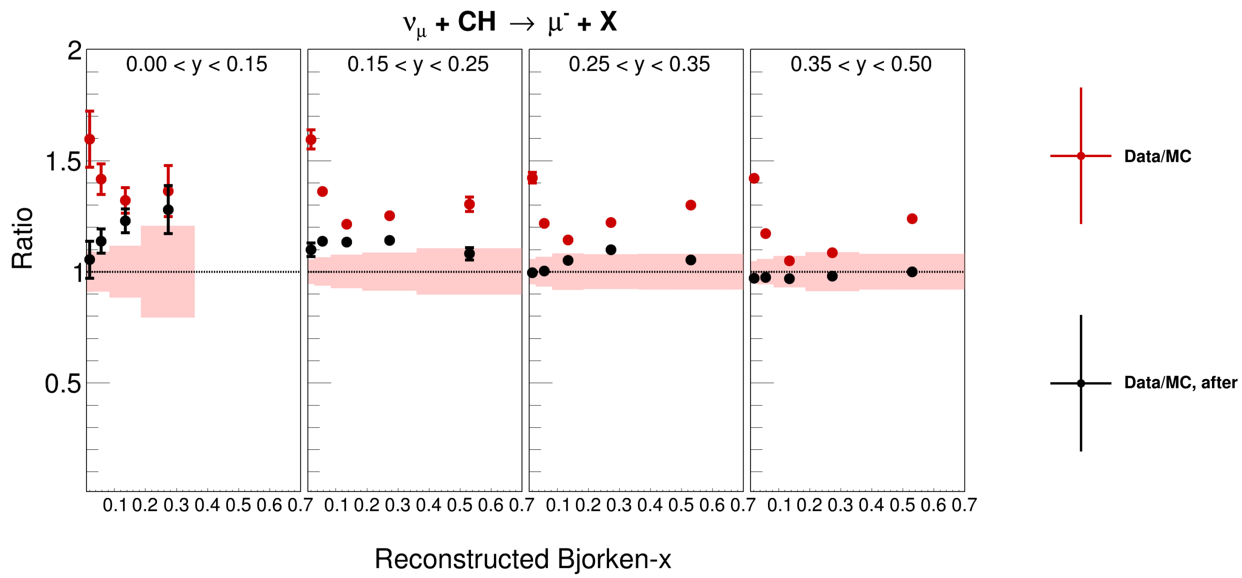

(a) **Neutrino** mode.

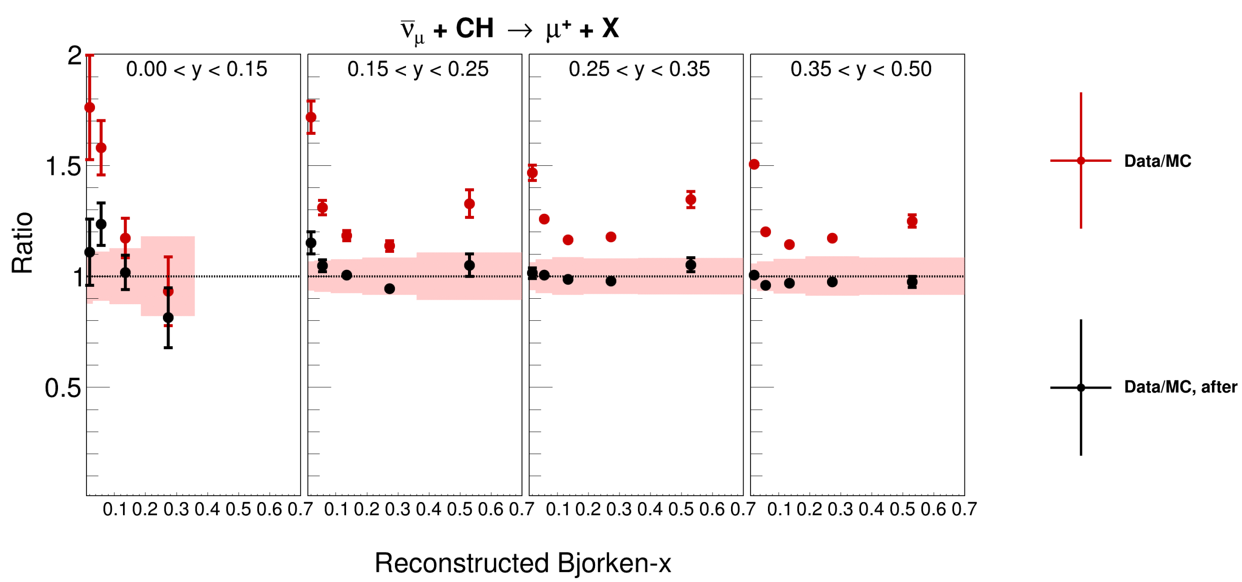

(b) **Antineutrino** mode.

Figure 77 – Data-to-MC ratios in **Sideband 2** as a function of **Bjorken variables**. Red (black) points represent the data/MC ratio before (after) tuning the background. Error bars indicate statistical uncertainty, while the pink error band around line one represents the total (statistical+systematic) uncertainty on the simulation. Top (bottom) plot displays the distribution ratios in neutrino (antineutrino) mode.

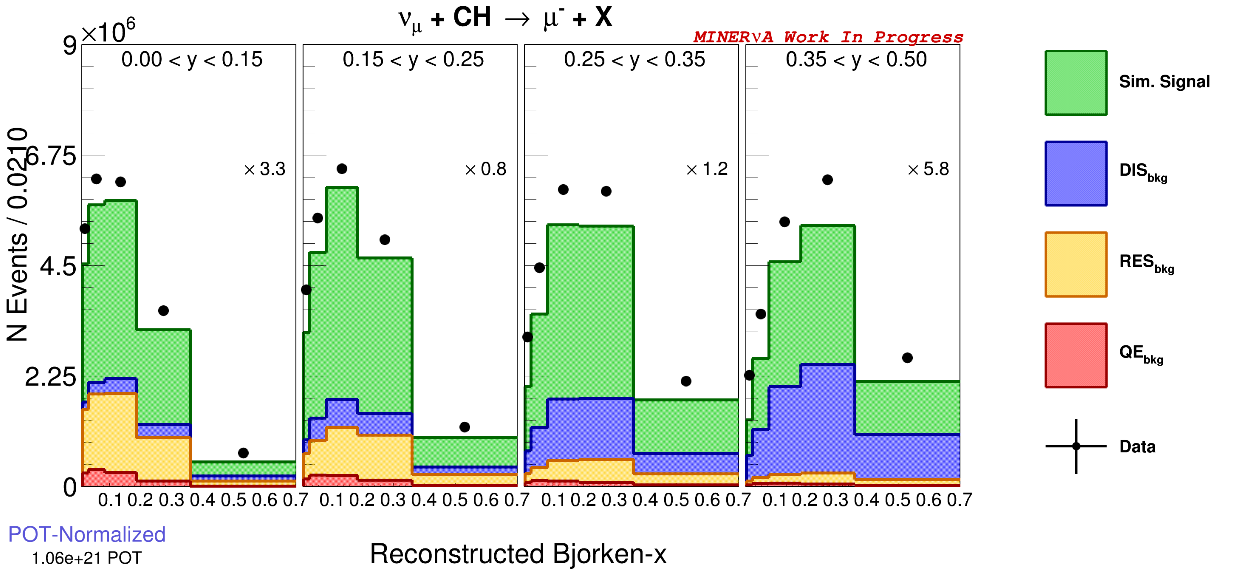

(a) **Neutrino** mode.

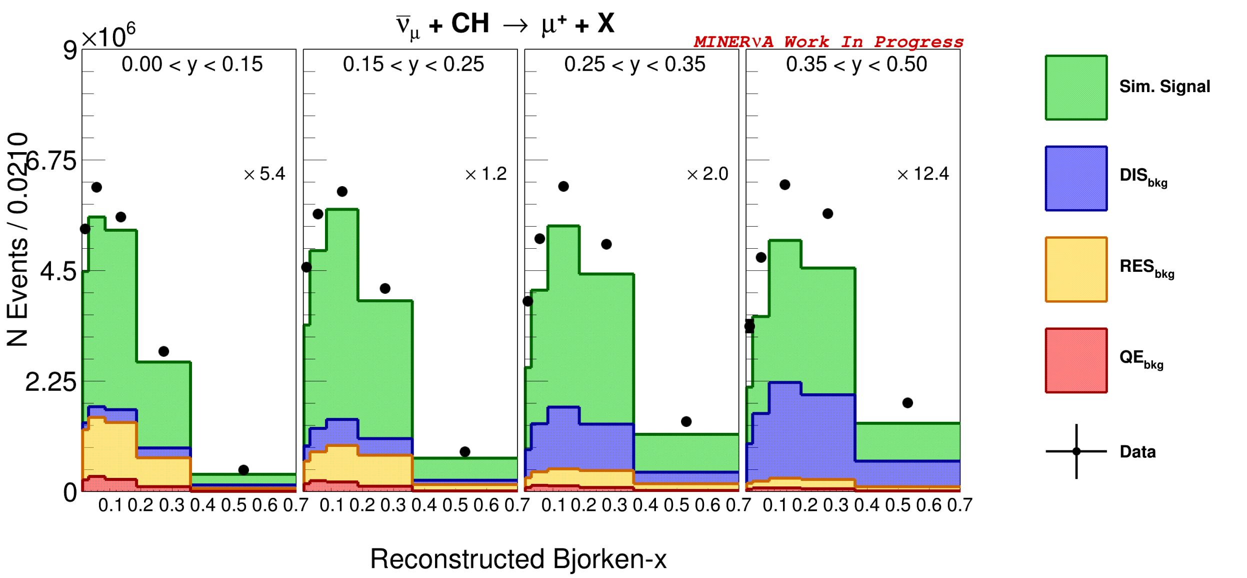

(b) **Antineutrino** mode.

Figure 78 – Selected **events in signal region** shown in terms of **Bjorken variables**. The top (bottom) plot displays the data (black points) and the simulated events in neutrino (antineutrino) mode, stacked in descending order of contribution: signal (green), DIS$_{bkg}$ (blue), RES$_{bkg}$ (yellow) and QE$_{bkg}$ (red). For better visualization, each panel has been scaled by a specific factor to normalize its height. The error bars on the data represent statistical uncertainties only.

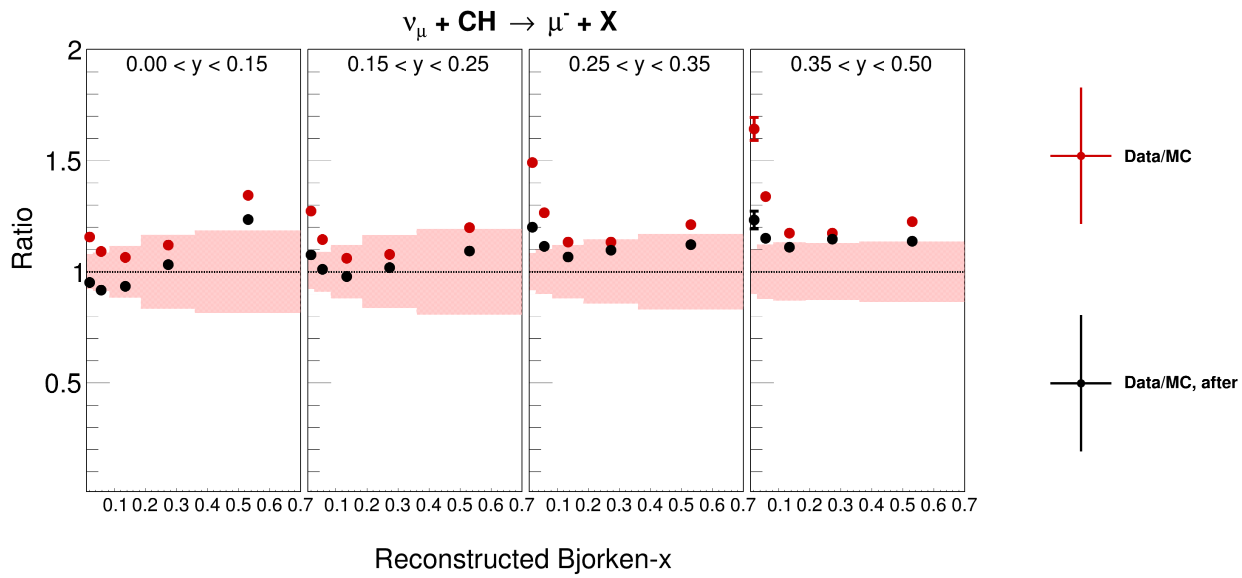

(a) **Neutrino** mode.

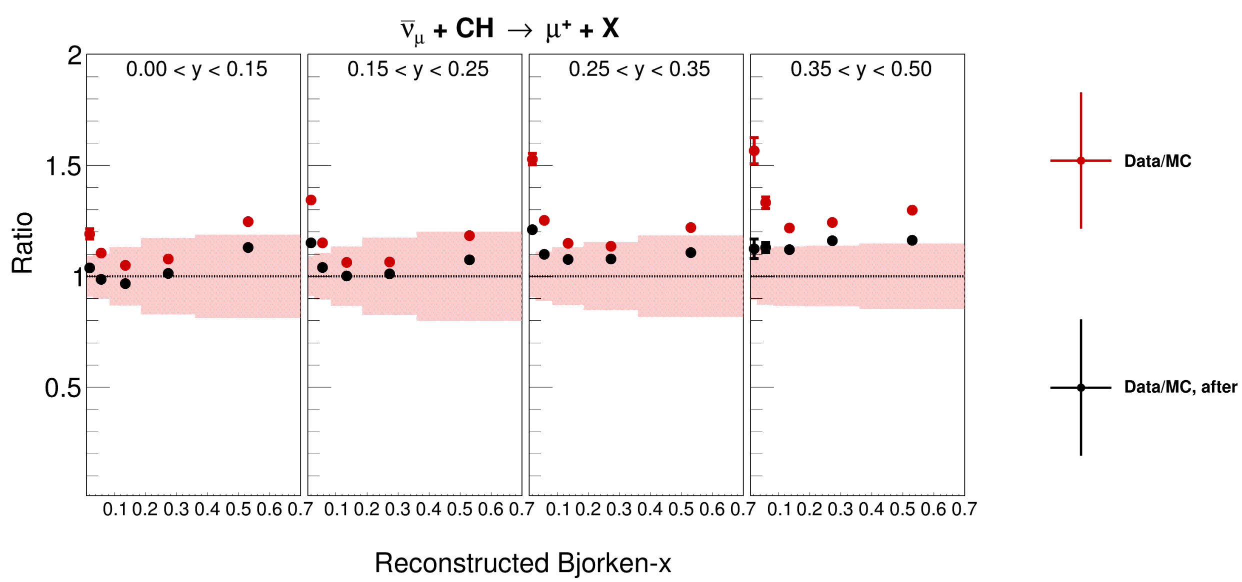

(b) **Antineutrino** mode.

Figure 79 – Data-to-MC ratios in **signal region** as a function of **Bjorken variables**. Red (black) points represent the data/MC ratio before (after) tuning the background. Error bars indicate statistical uncertainty, while the pink error band around line one represents the total (statistical+systematic) uncertainty on the simulation. Top (bottom) plot displays the distribution ratios in neutrino (antineutrino) mode.

B.2.2 Muon variables analysis

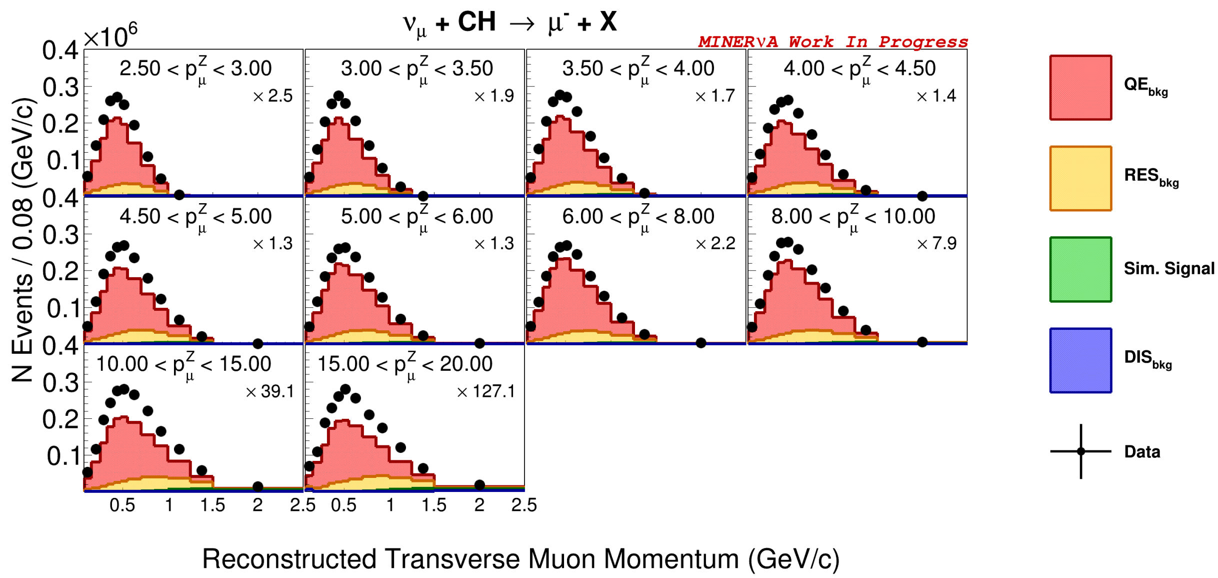

(a) **Neutrino** mode.

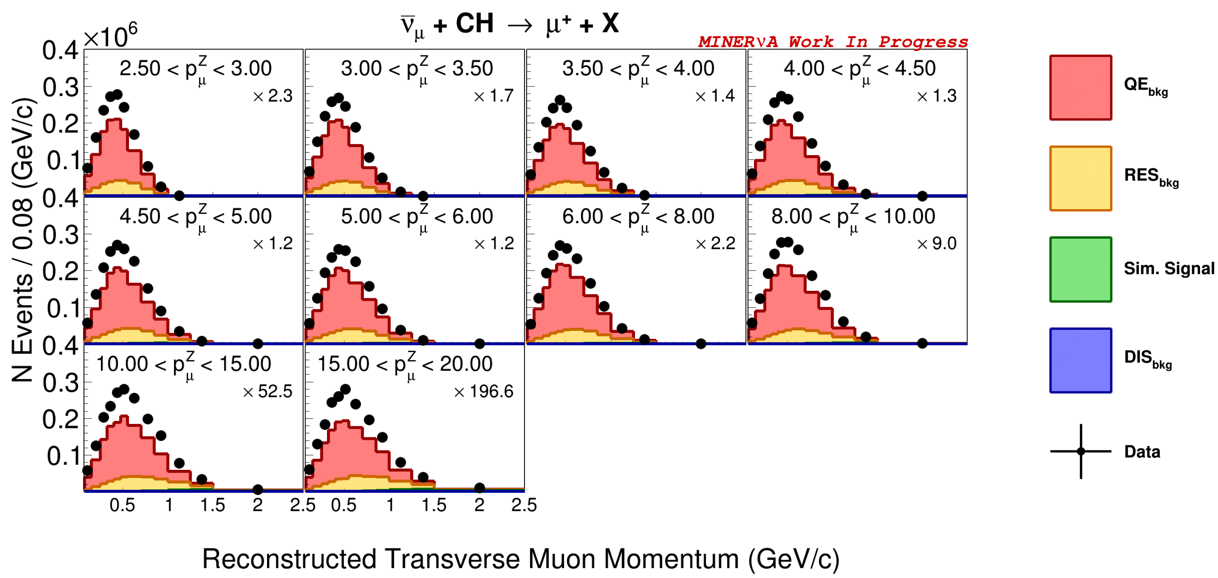

(b) **Antineutrino** mode.

Figure 80 – Selected **events in Sideband 0** (QE-rich) shown in terms of **muon variables**. The top (bottom) plot displays the data (black points) and the simulated events in neutrino (antineutrino) mode, stacked in descending order of contribution: QE$_{bkg}$ (red), RES$_{bkg}$ (yellow), signal (green) and DIS$_{bkg}$ (blue). For better visualization, each panel has been scaled by a specific factor to normalize its height. The error bars on the data represent statistical uncertainties only.

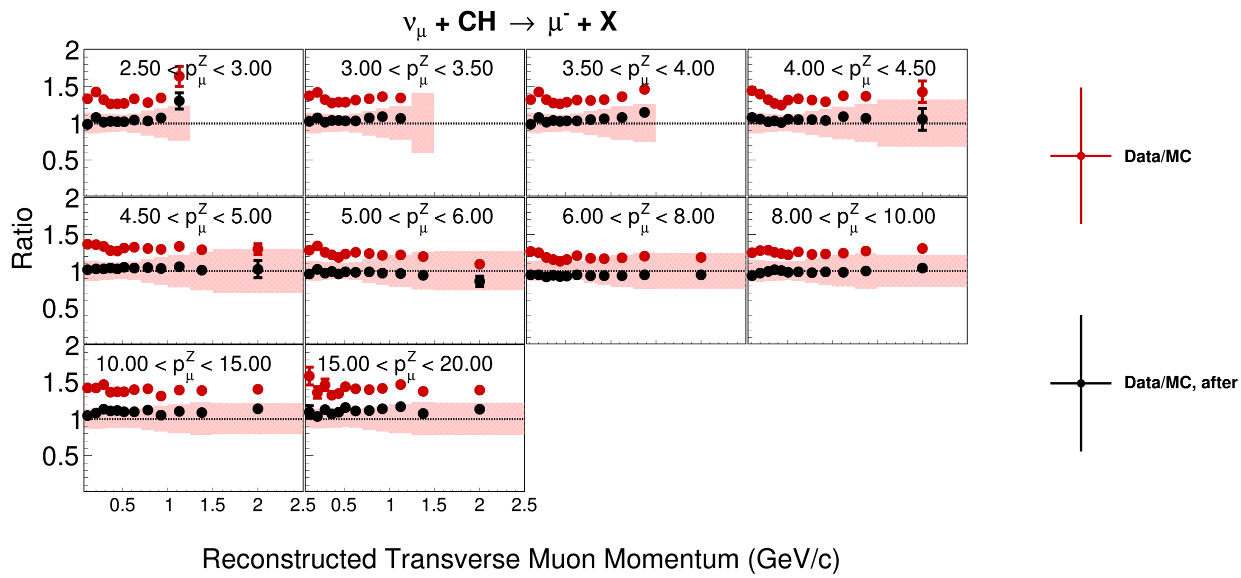

(a) **Neutrino** mode.

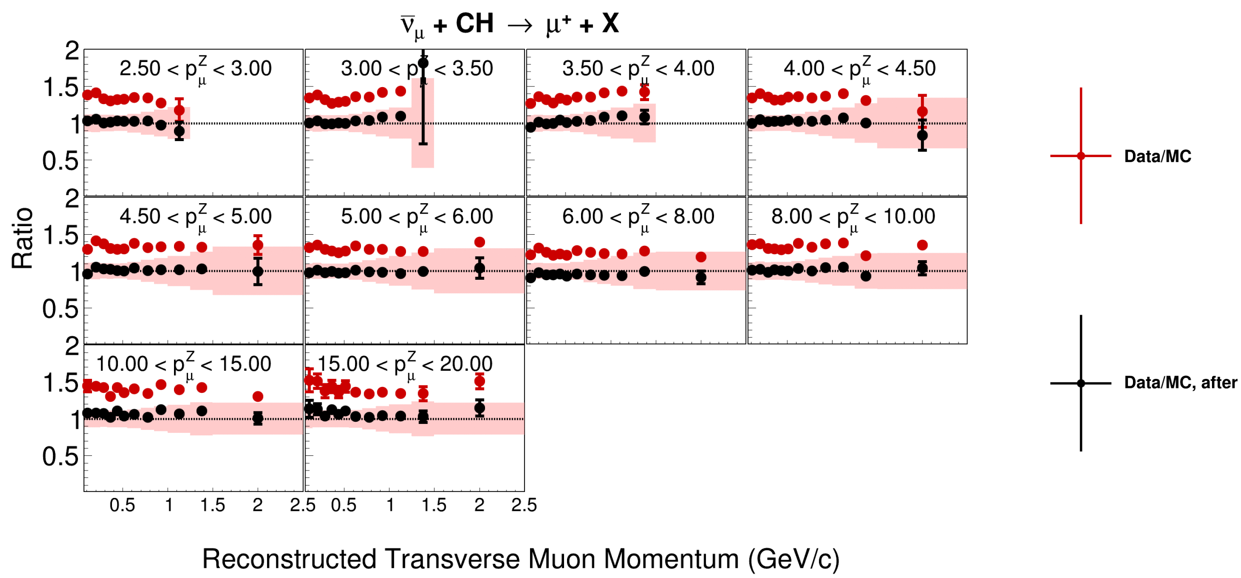

(b) **Antineutrino** mode.

Figure 81 – Data-to-MC ratios in **Sideband 0** as a function of **muon variables**. Red (black) points represent the data/MC ratio before (after) tuning the background. Error bars indicate statistical uncertainty, while the pink error band around line one represents the total (statistical+systematic) uncertainty on the simulation. Top (bottom) plot displays the distribution ratios in neutrino (antineutrino) mode.

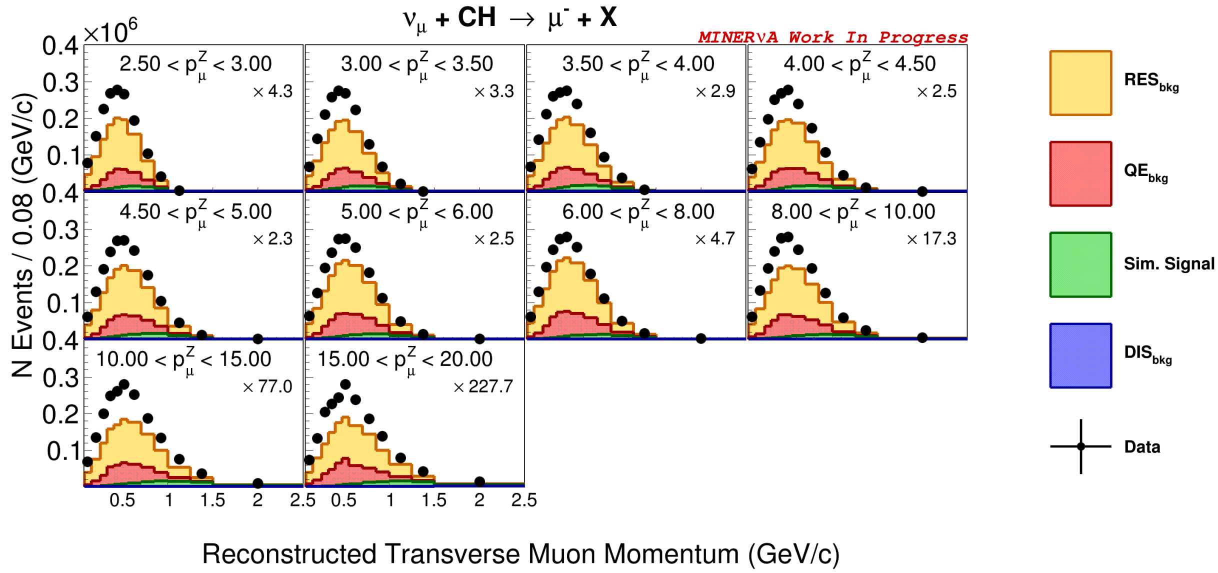

(a) **Neutrino** mode.

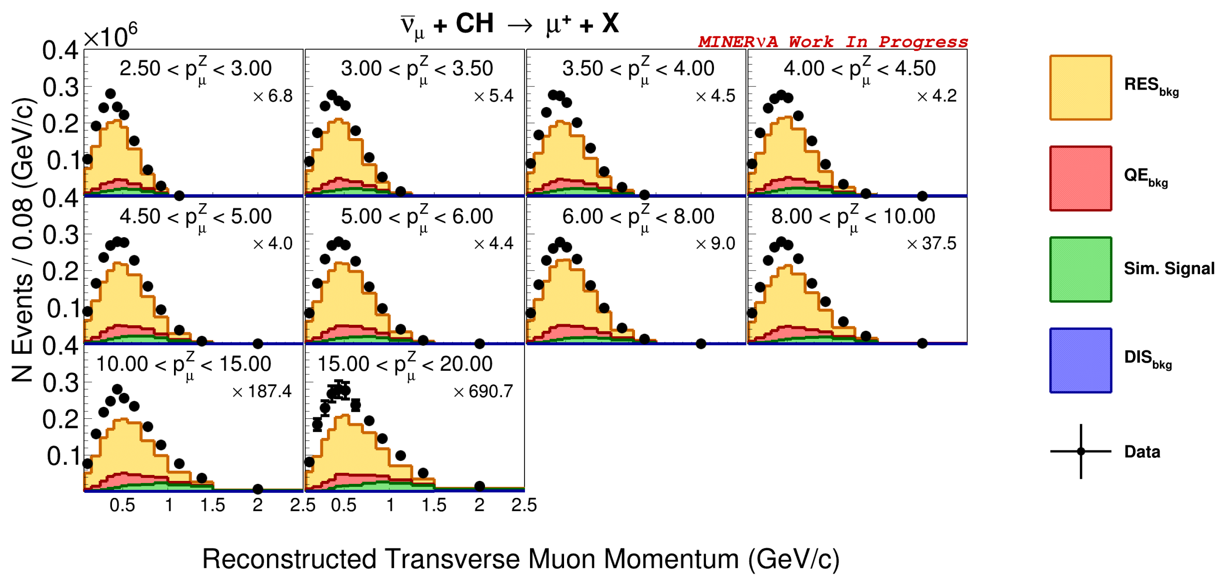

(b) **Antineutrino** mode.

Figure 82 – Selected **events in Sideband 1** (RES-rich) shown in terms of **muon variables**. The top (bottom) plot displays the data (black points) and the simulated events in neutrino (antineutrino) mode, stacked in descending order of contribution: RES_{bkg} (yellow), QE_{bkg} (red), signal (green) and DIS_{bkg} (blue). For better visualization, each panel has been scaled by a specific factor to normalize its height. The error bars on the data represent statistical uncertainties only.

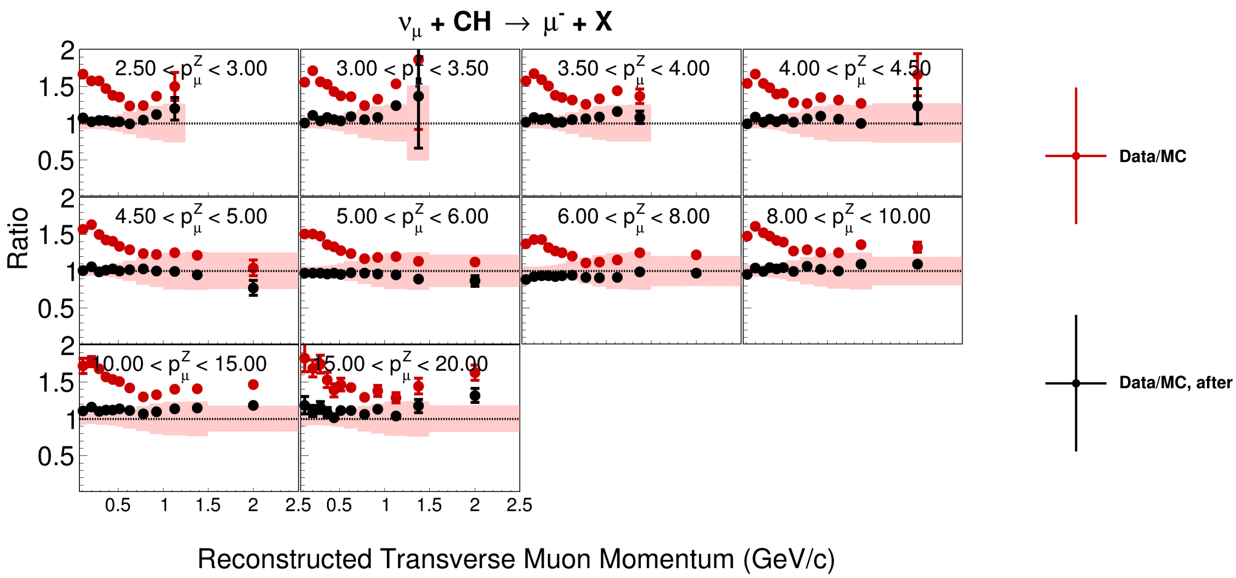

(a) **Neutrino** mode.

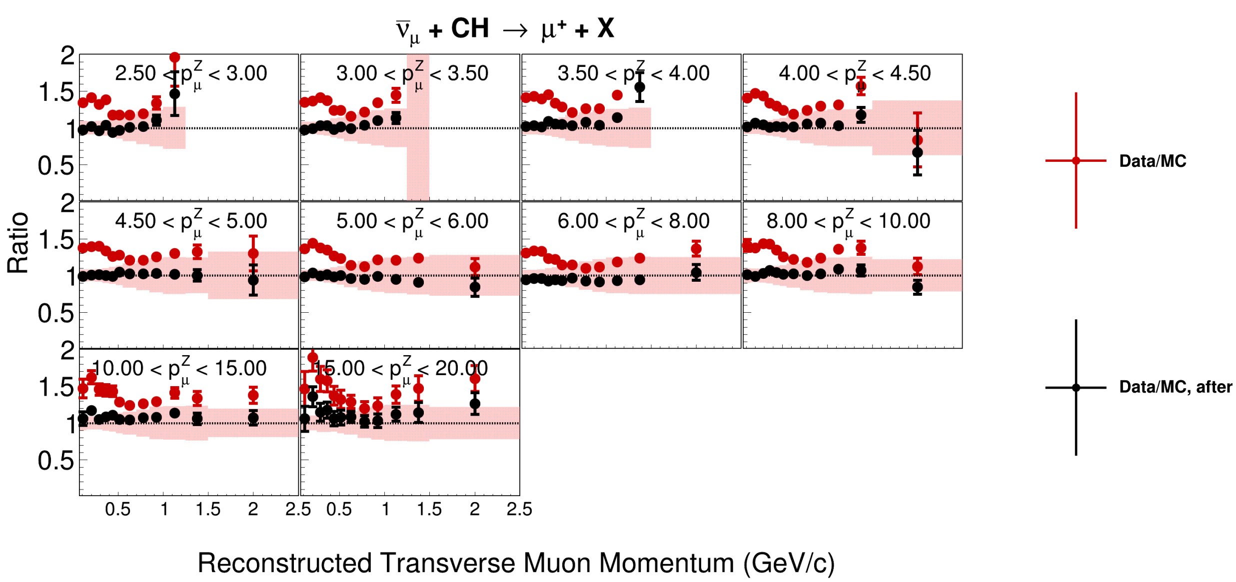

(b) **Antineutrino** mode.

Figure 83 – Data-to-MC ratios in **Sideband 1** as a function of **muon variables**. Red (black) points represent the data/MC ratio before (after) tuning the background. Error bars indicate statistical uncertainty, while the pink error band around line one represents the total (statistical+systematic) uncertainty on the simulation. Top (bottom) plot displays the distribution ratios in neutrino (antineutrino) mode.

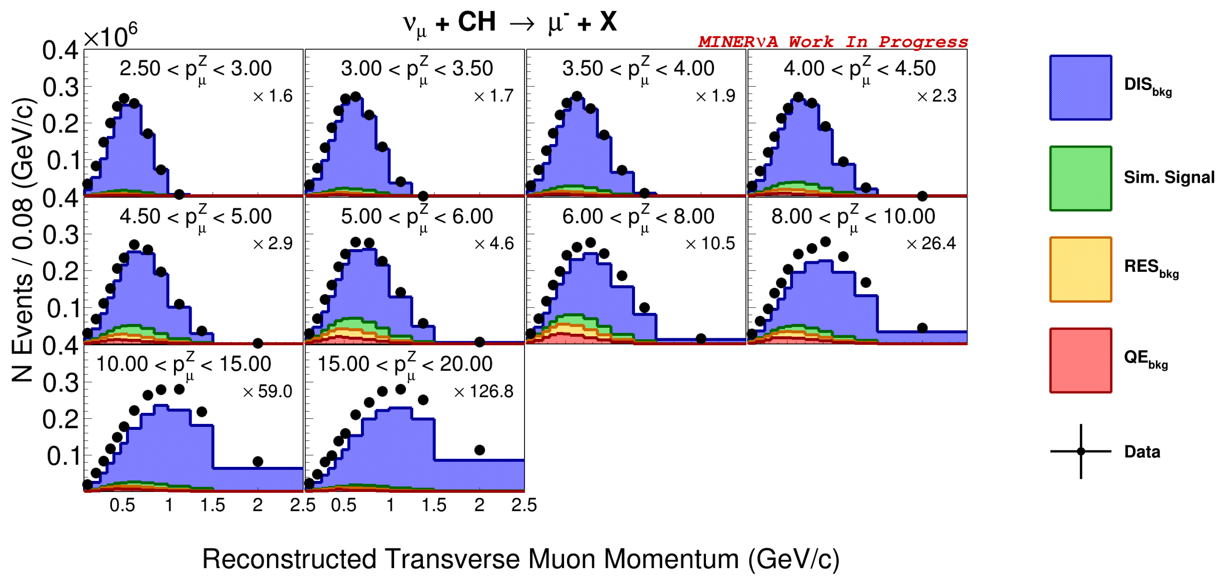

(a) **Neutrino** mode.

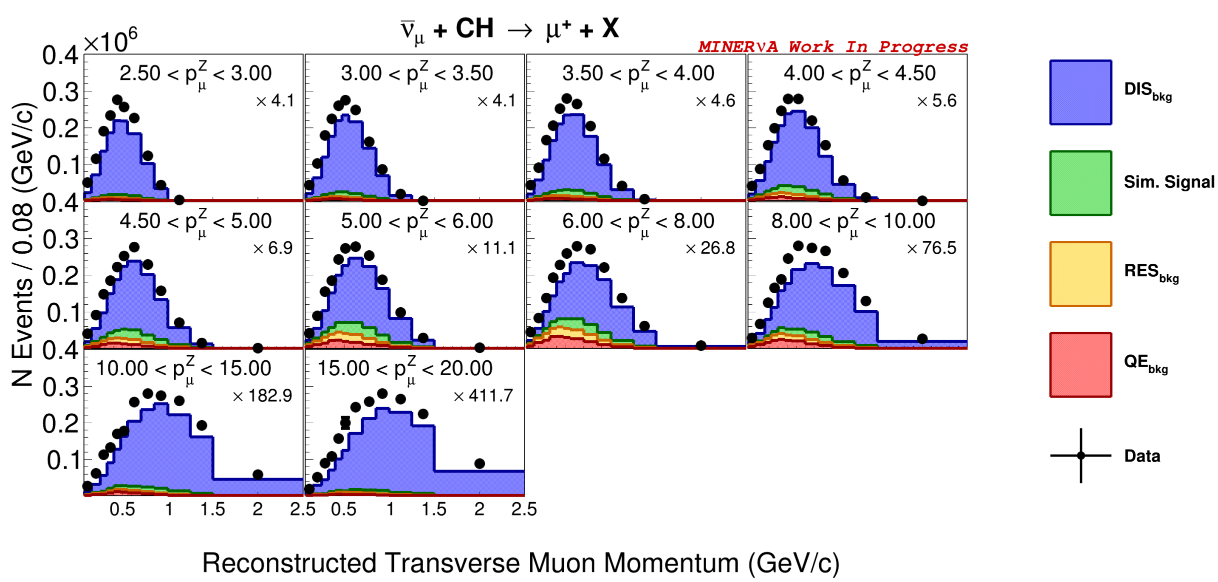

(b) **Antineutrino** mode.

Figure 84 – Selected **events in Sideband 2** (DIS-rich) shown in terms of **muon variables**. The top (bottom) plot displays the data (black points) and the simulated events in neutrino (antineutrino) mode, stacked in descending order of contribution: DIS$_{bkg}$ (blue), signal (green), RES$_{bkg}$ (yellow), and QE$_{bkg}$ (red). For better visualization, each panel has been scaled by a specific factor to normalize its height. The error bars on the data represent statistical uncertainties only.

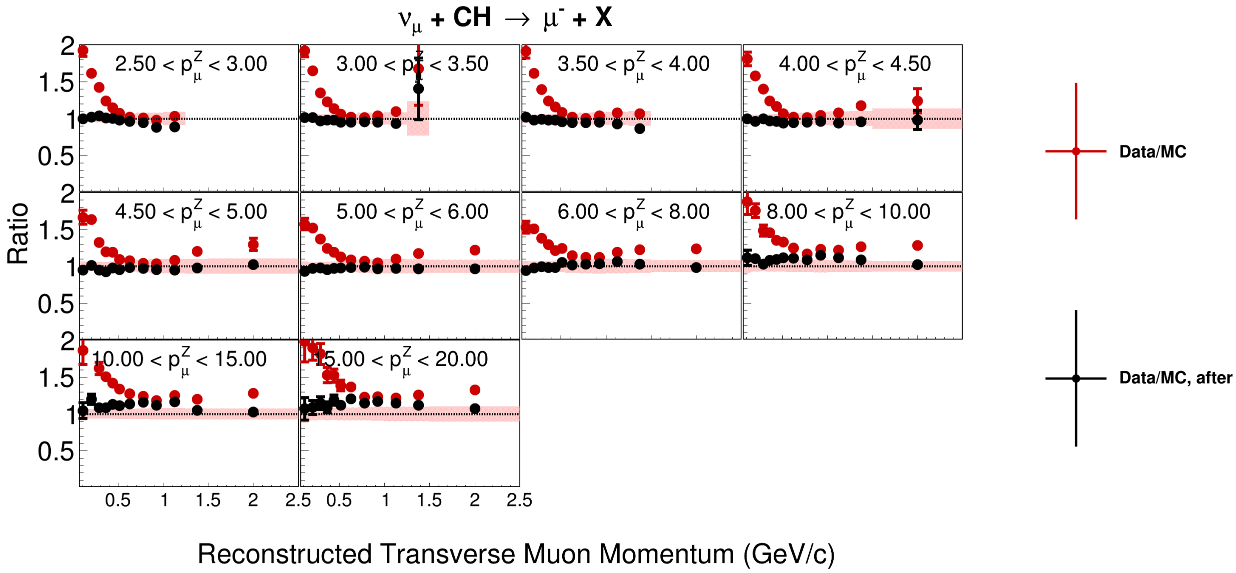

(a) **Neutrino** mode.

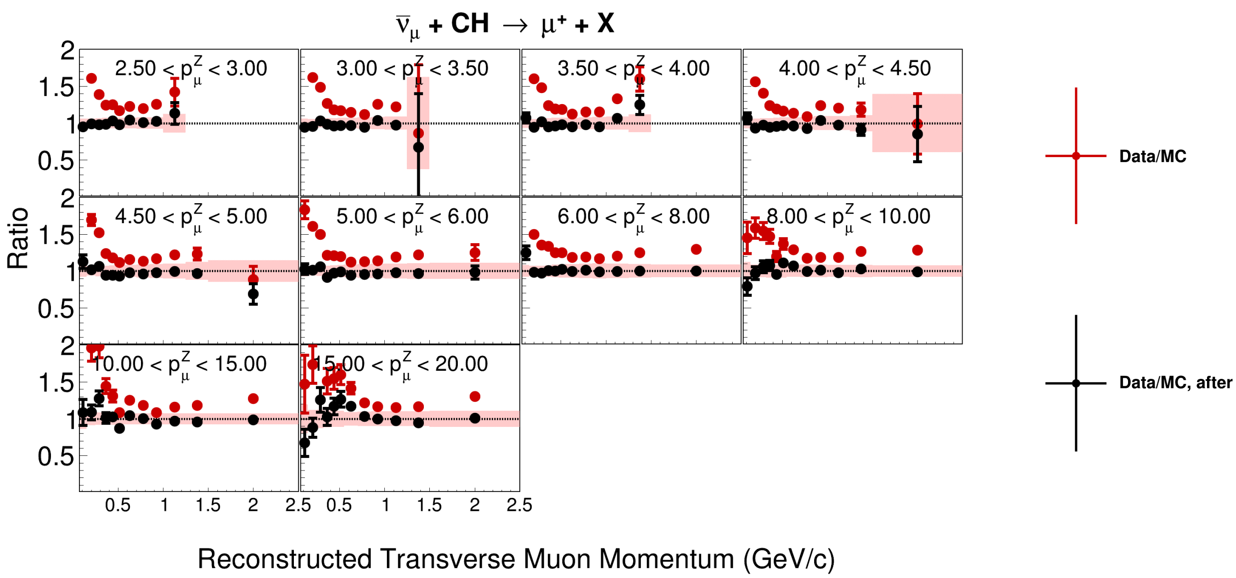

(b) **Antineutrino** mode.

Figure 85 – Data-to-MC ratios in **Sideband 2** as a function of **muon variables**. Red (black) points represent the data/MC ratio before (after) tuning the background. Error bars indicate statistical uncertainty, while the pink error band around line one represents the total (statistical+systematic) uncertainty on the simulation. Top (bottom) plot displays the distribution ratios in neutrino (antineutrino) mode.

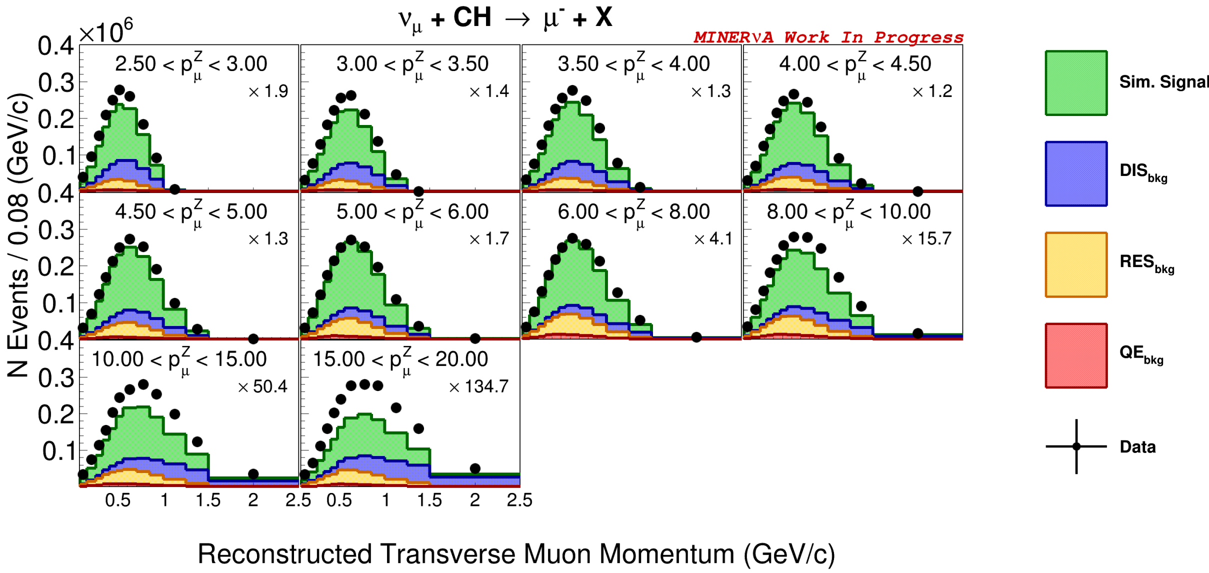

(a) **Neutrino** mode.

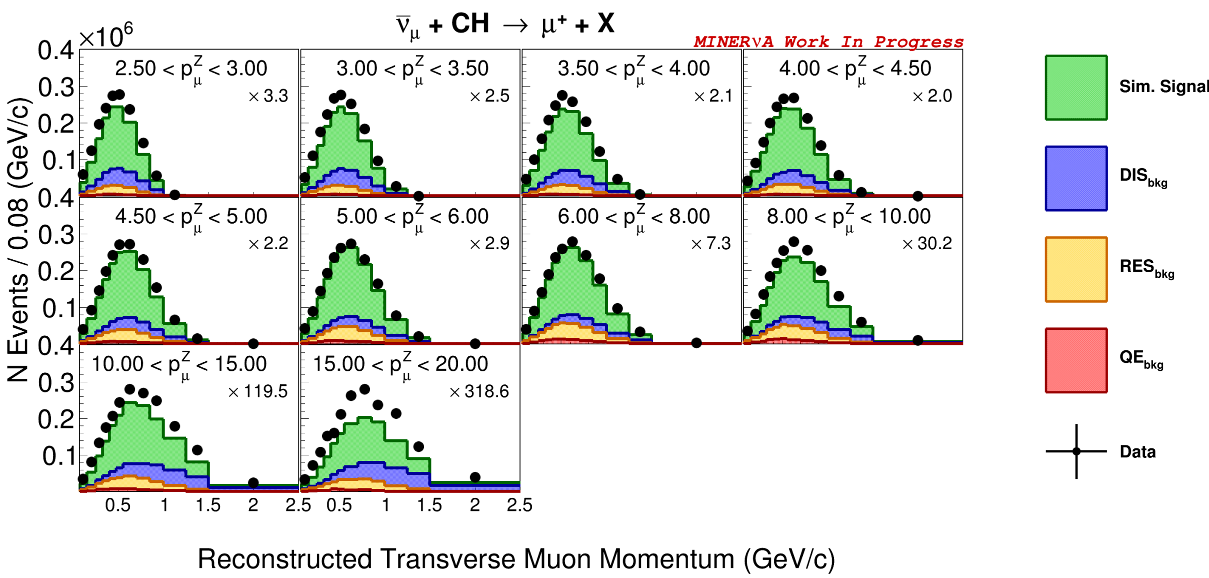

(b) **Antineutrino** mode.

Figure 86 – Selected **events in signal region** shown in terms of **muon variables**. The top (bottom) plot displays the data (black points) and the simulated events in neutrino (antineutrino) mode, stacked in descending order of contribution: signal (green), DIS_{bkg} (blue), RES_{bkg} (yellow) and QE_{bkg} (red). For better visualization, each panel has been scaled by a specific factor to normalize its height. The error bars on the data represent statistical uncertainties only.

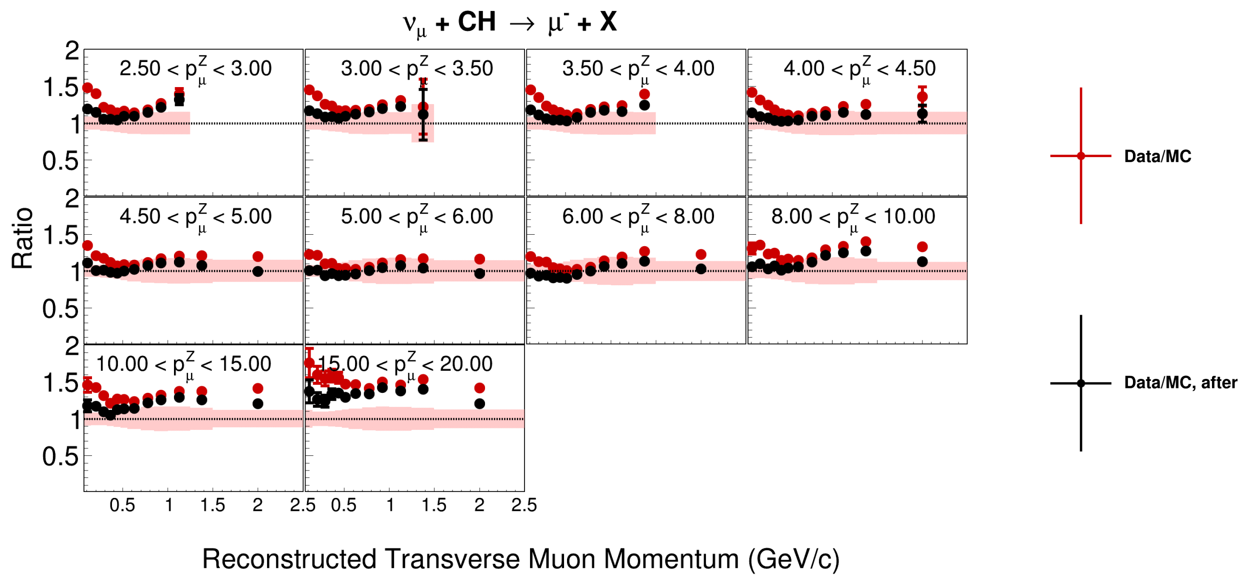

(a) **Neutrino** mode.

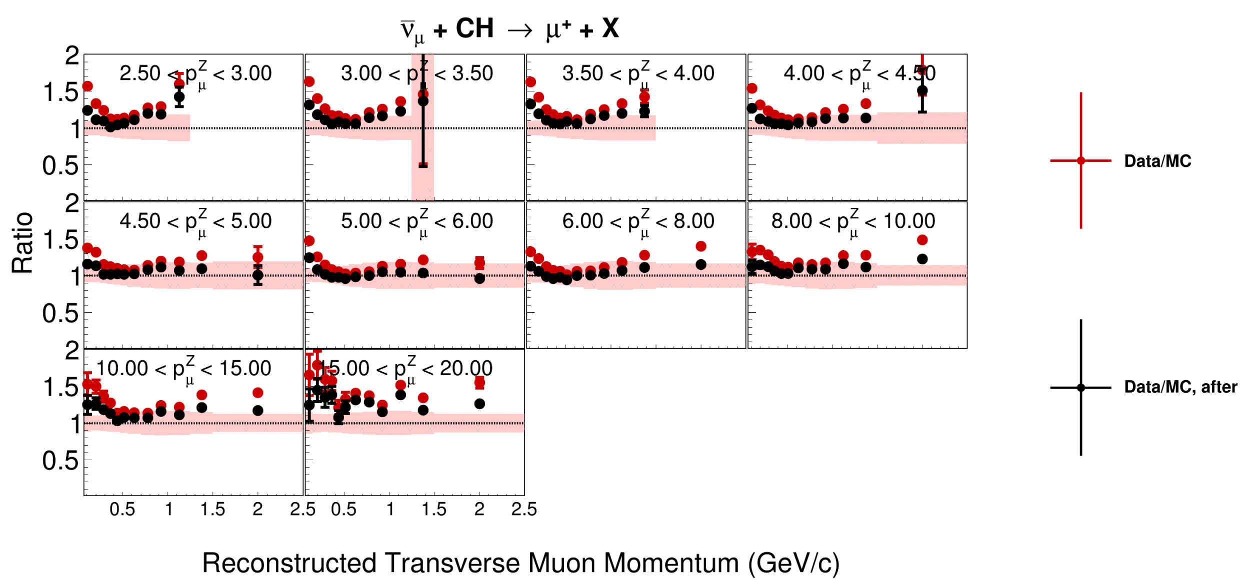

(b) **Antineutrino** mode.

Figure 87 – Data-to-MC ratios in **signal region** as a function of **muon variables**. Red (black) points represent the data/MC ratio before (after) tuning the background. Error bars indicate statistical uncertainty, while the pink error band around line one represents the total (statistical+systematic) uncertainty on the simulation. Top (bottom) plot displays the distribution ratios in neutrino (antineutrino) mode.

APPENDIX C – Uncertainty groups breakdown

C.1 Bjorken variables

C.1.1 Fractional uncertainties

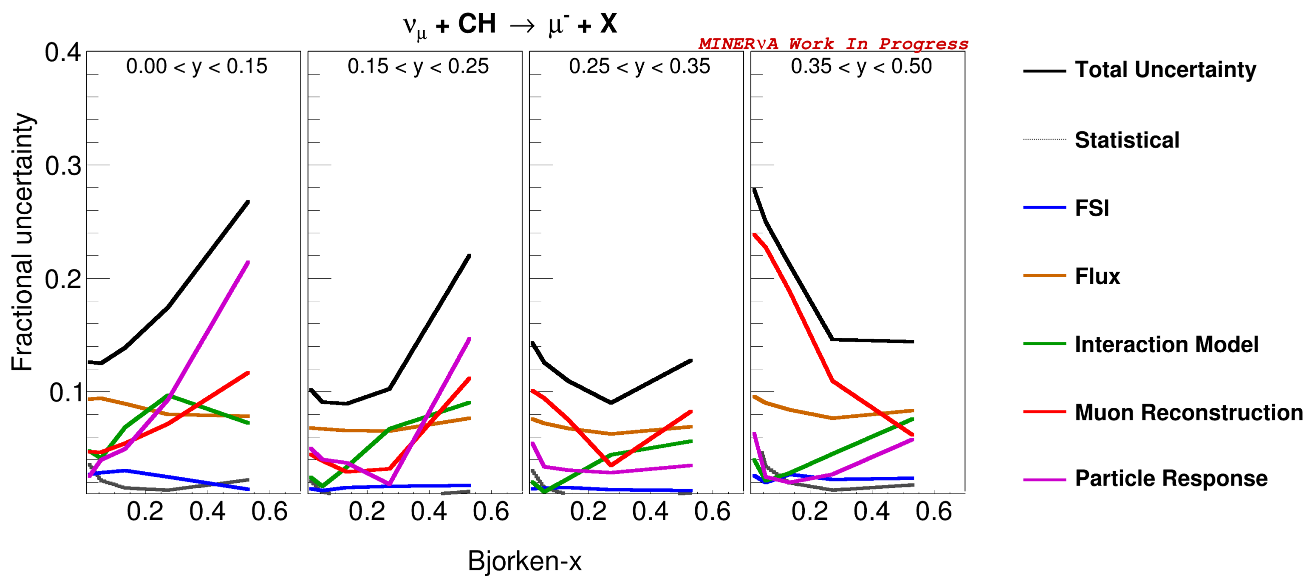

(a) **Neutrino** mode.

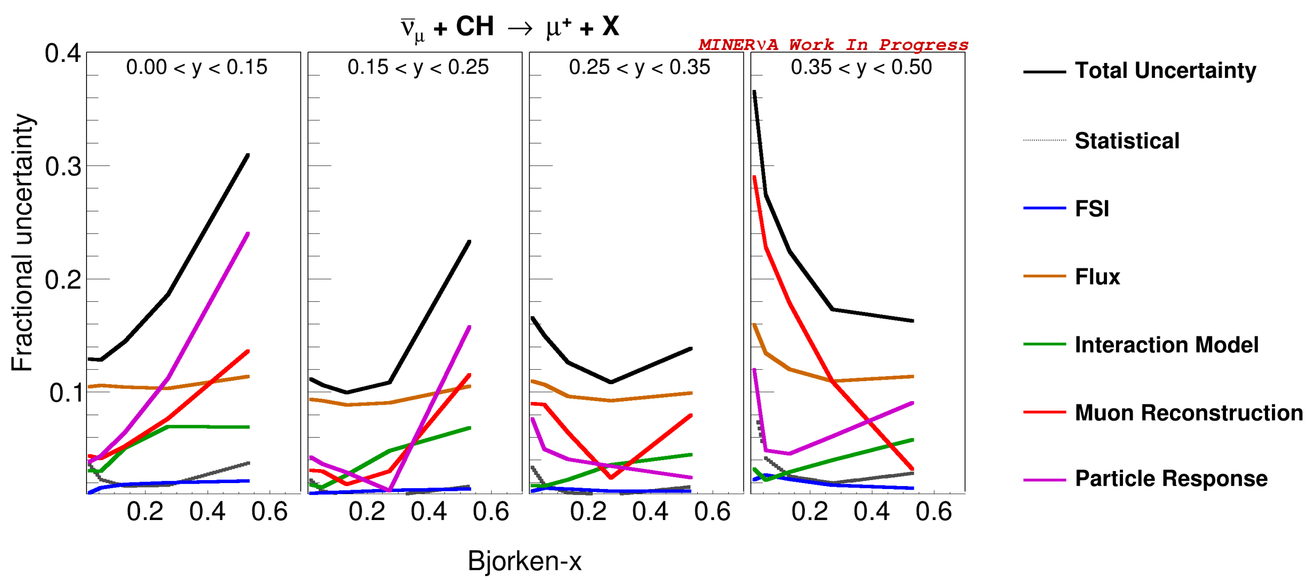

(b) **Antineutrino** mode.

Figure 88 – Fractional uncertainties on data cross section as a function of **Bjorken variables**. Top (bottom) figure shows the result for neutrino (antineutrino) mode. The five error groups comprising the systematic uncertainty budget are described in Chap. 6. The fractions are computed with respect to the MnvTunev2 central value.

C.1.2 Interaction Model error group

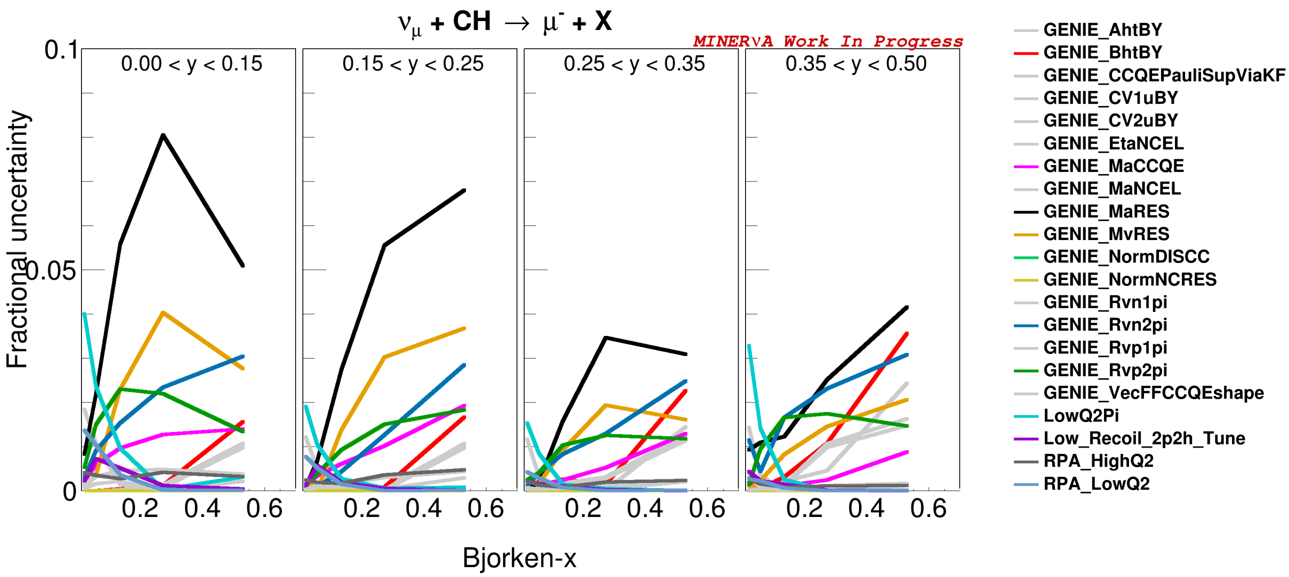

(a) **Neutrino** mode.

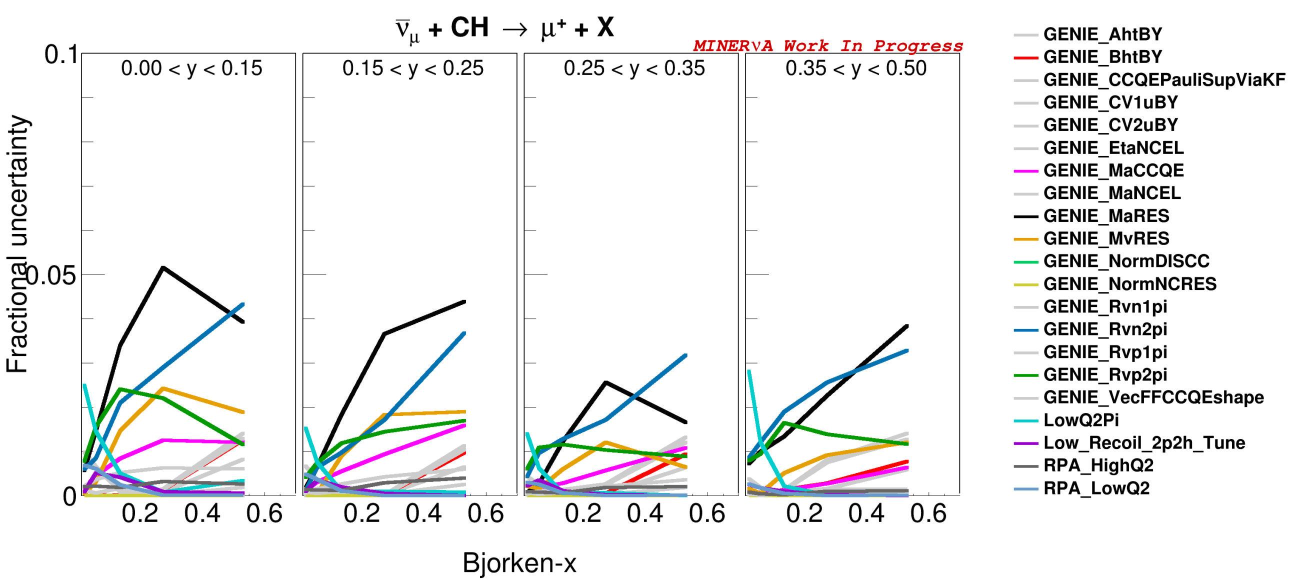

(b) **Antineutrino** mode.

Figure 89 – Fractional systematic uncertainties breakdown corresponding to the **Interaction Model** error group. The top (bottom) plot illustrates the errors on the extracted neutrino (antineutrino) data cross sections in terms of the **Bjorken variables**. The dominant sources of uncertainty are attributed to the following simulated cross section model parameters: `GENIE_MaRES` (black), `GENIE_MvRES` (yellow), and `GENIE_Rvn2pi` (blue); refer to Tab. 15 for further details.

C.1.3 Muon Reconstruction error group

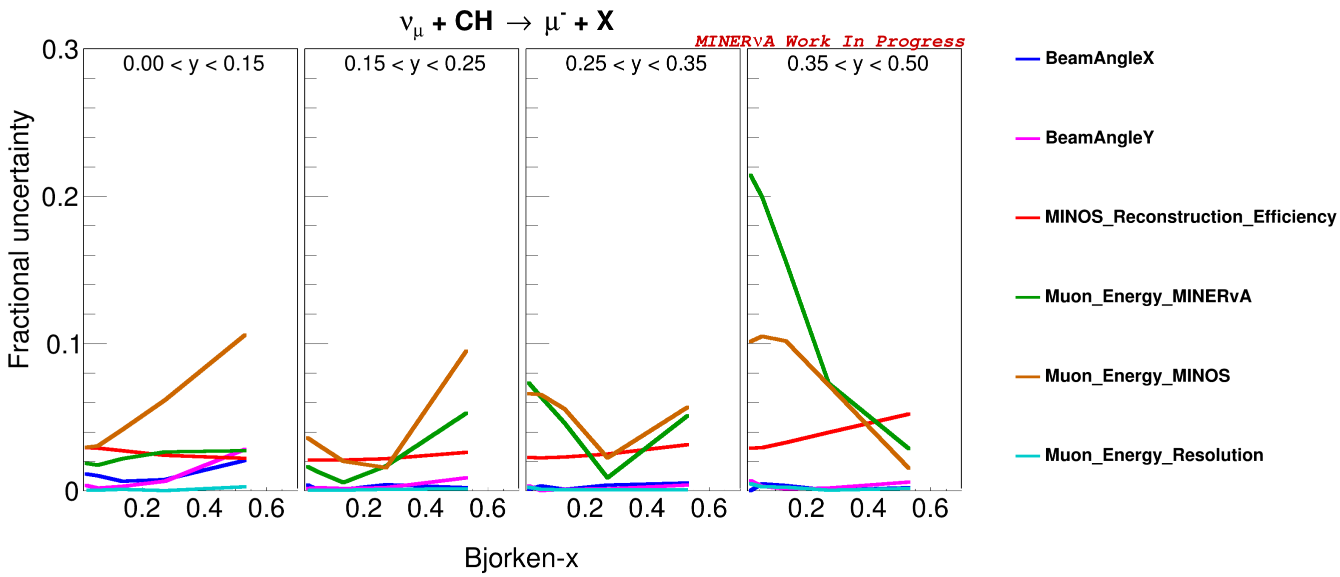

(a) **Neutrino** mode.

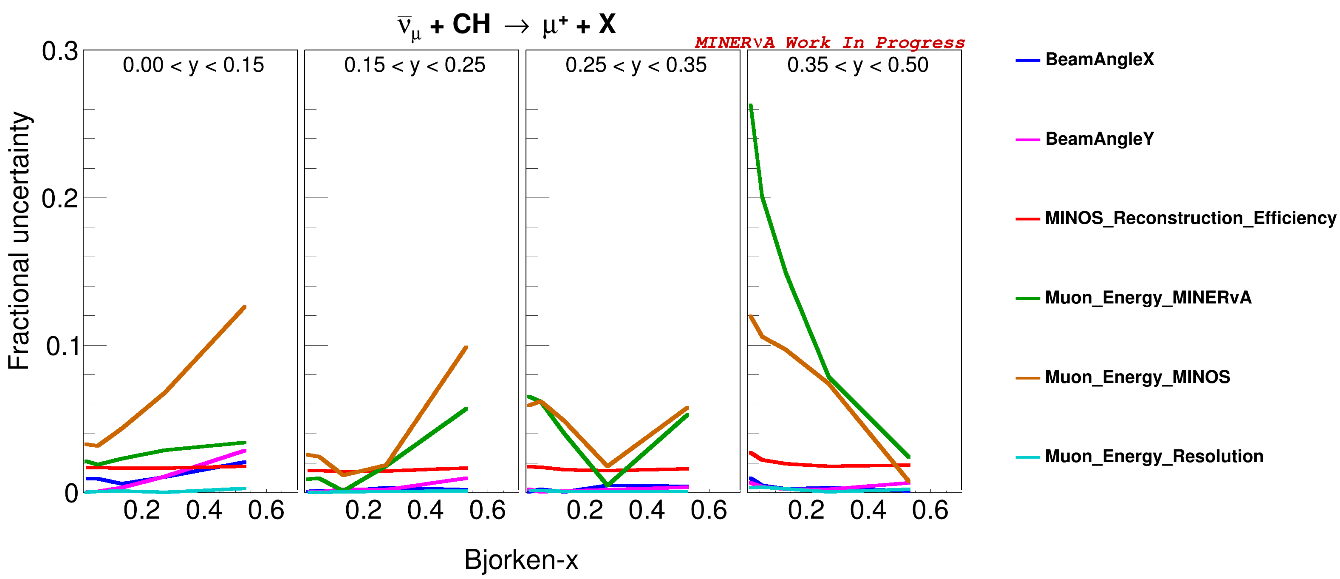

(b) **Antineutrino** mode.

Figure 90 – Fractional systematic uncertainties breakdown corresponding to the **Muon Reconstruction** error group. The top (bottom) plot illustrates the errors on the extracted neutrino (antineutrino) data cross sections in terms of the **Bjorken variables**. The dominant sources of uncertainty are `Muon_Energy_MINERvA` (gree), `Muon_Energy_MINOS` (orange), and `MINOS_Reconstruction_Efficiency` (red); refer to Tab. 18 for further details.

C.1.4 FSI error group

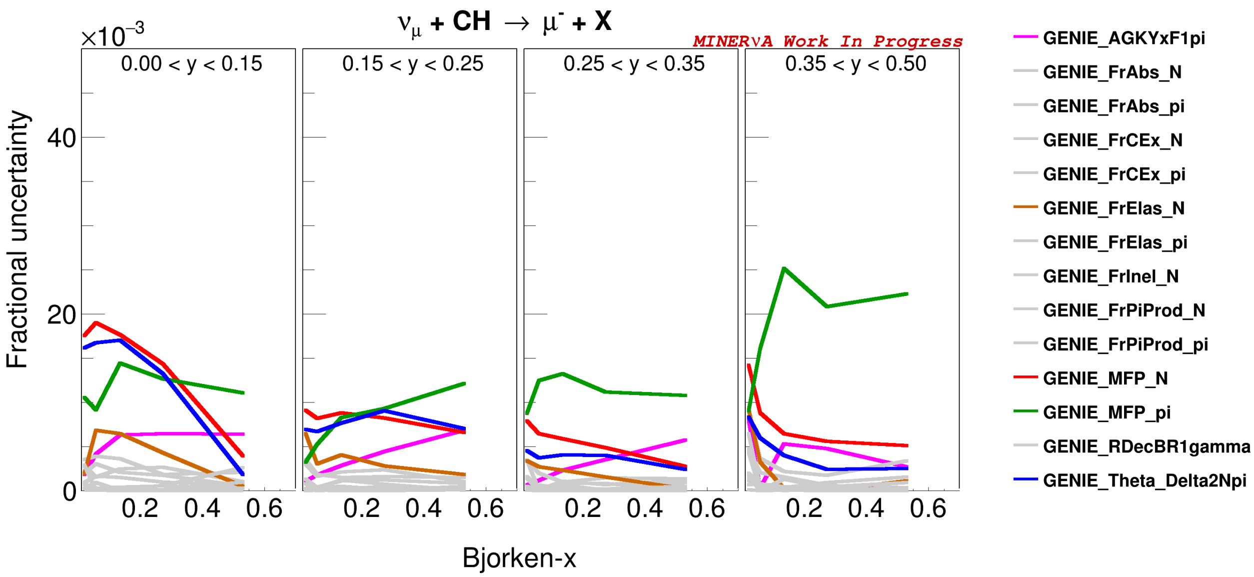

(a) **Neutrino** mode.

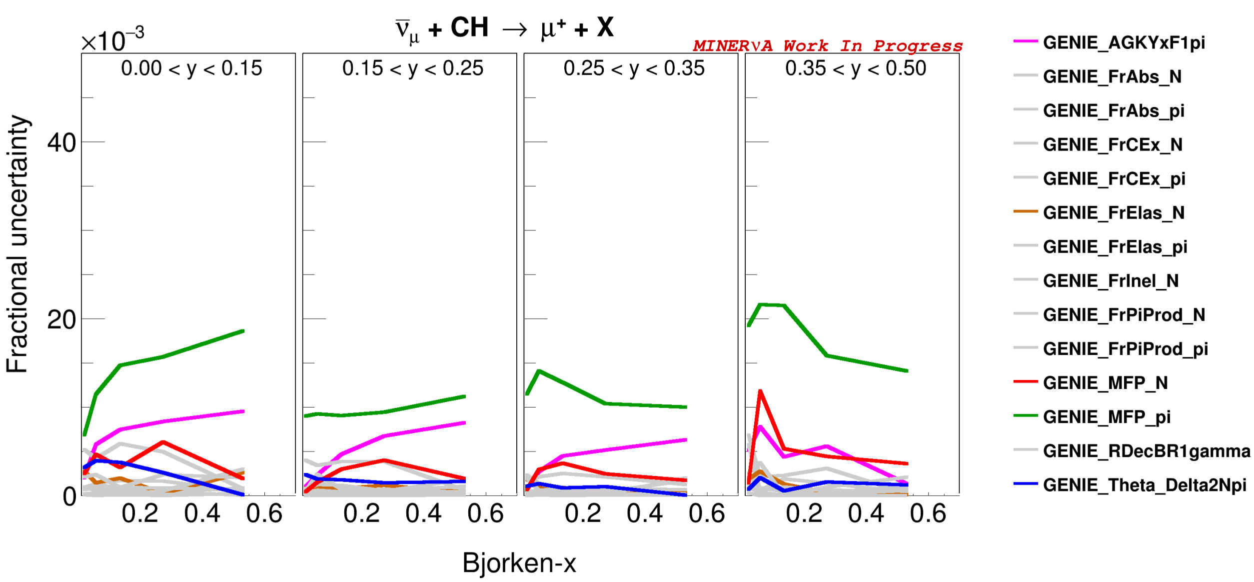

(b) **Antineutrino** mode.

Figure 91 – Fractional systematic uncertainties breakdown corresponding to the **FSI** error group. The top (bottom) plot illustrates the errors on the extracted neutrino (antineutrino) data cross sections in terms of the **Bjorken variables**. The dominant sources of uncertainty are `GENIE_MFP_pi` (gree), `GENIE_MFP_N` (red), and `GENIE_Theta_Delta2Npi` (blue) for neutrinos, and `GENIE_AGKYxF1pi` (pink) for antineutrinos; refer to Tab. 16 for further details.

C.1.5 Particle Response error group

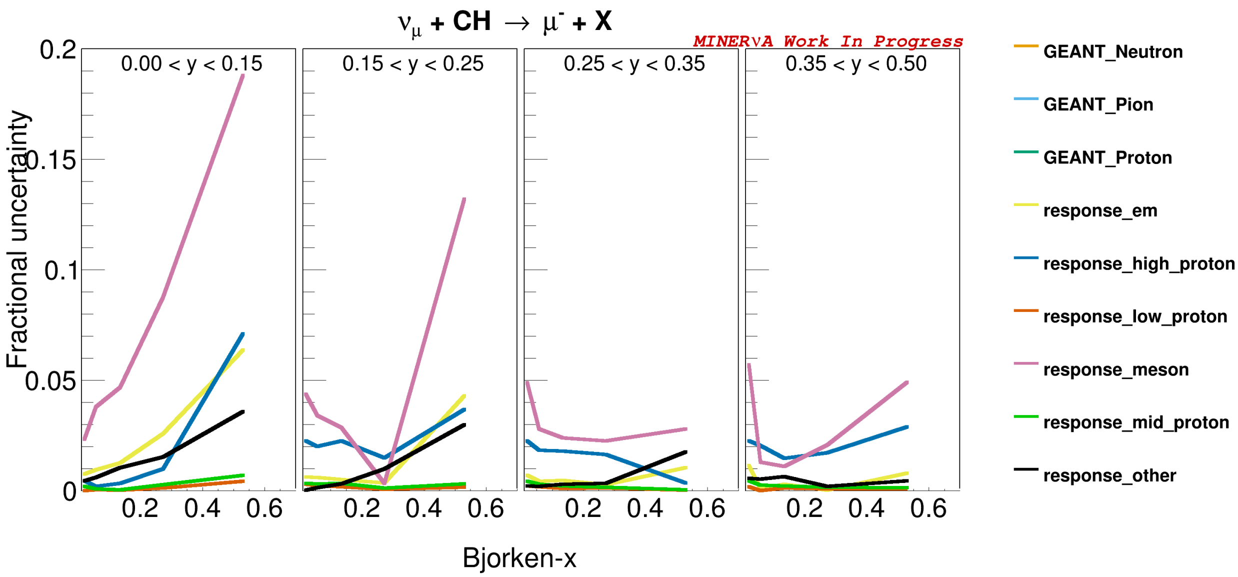

(a) **Neutrino** mode.

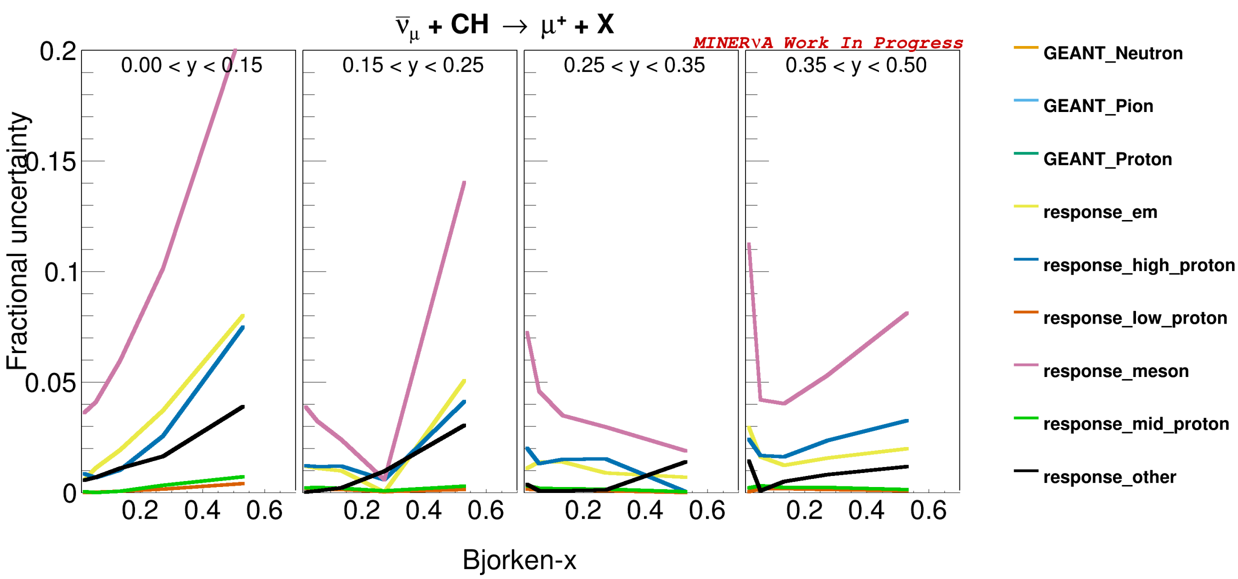

(b) **Antineutrino** mode.

Figure 92 – Fractional systematic uncertainties breakdown corresponding to the **Particle Response** error group. The top (bottom) plot illustrates the errors on the extracted neutrino (antineutrino) data cross sections in terms of the **Bjorken variables**. The dominant sources of uncertainty are `response_meson` (magenta), `response_em` (light yellow), and `response_high_proton` (blue); refer to Tab. 17 for further details.

C.2 Muon momentum components

C.2.1 Fractional uncertainties

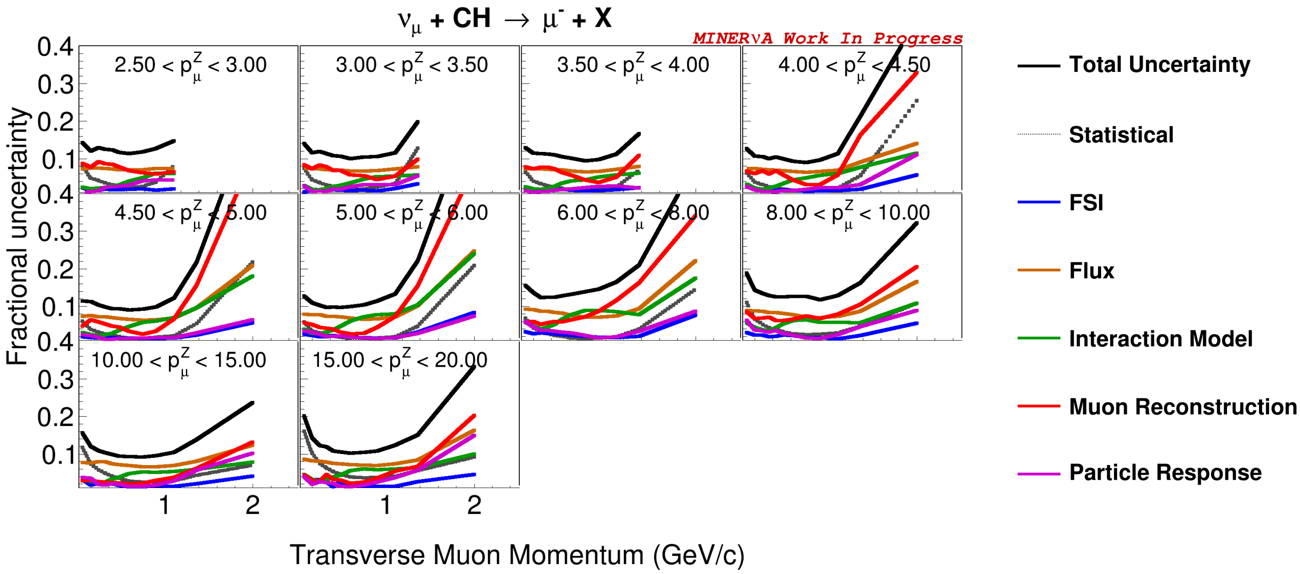

(a) **Neutrino** mode.

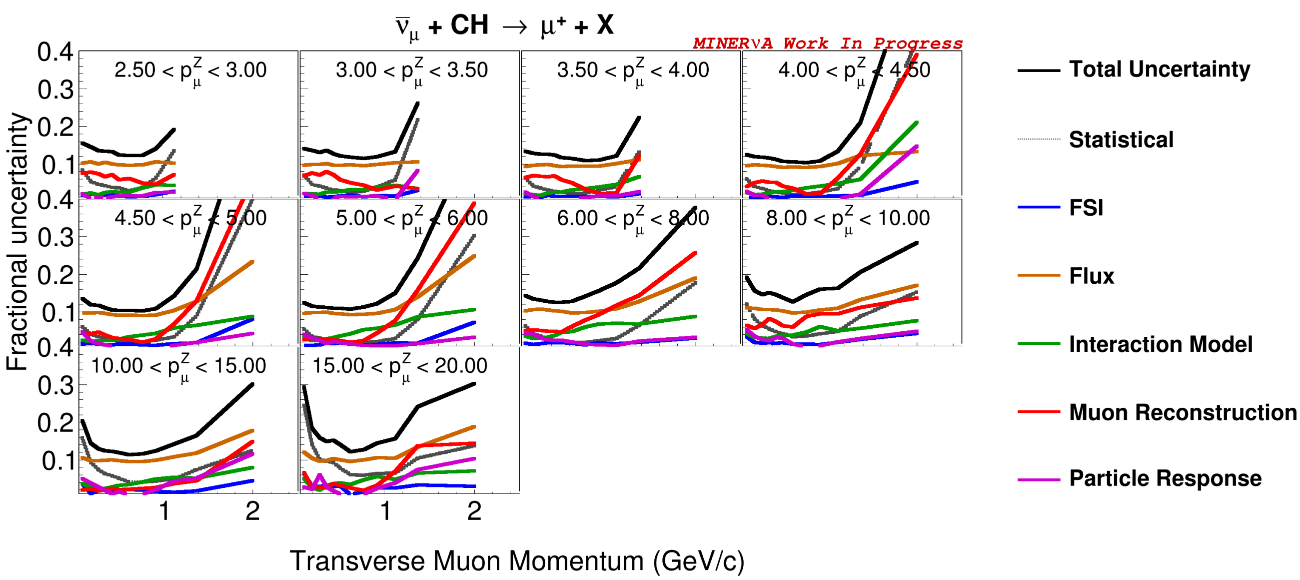

(b) **Antineutrino** mode.

Figure 93 – Fractional uncertainties on data cross section as a function of **muon momentum components**. Top (bottom) figure shows the result for neutrino (antineutrino) mode. The five error groups comprising the systematic uncertainty budget are described in Chap. 6. The fractions are computed with respect to the MnvTunev2 central value.

C.2.2 Interaction Model error group

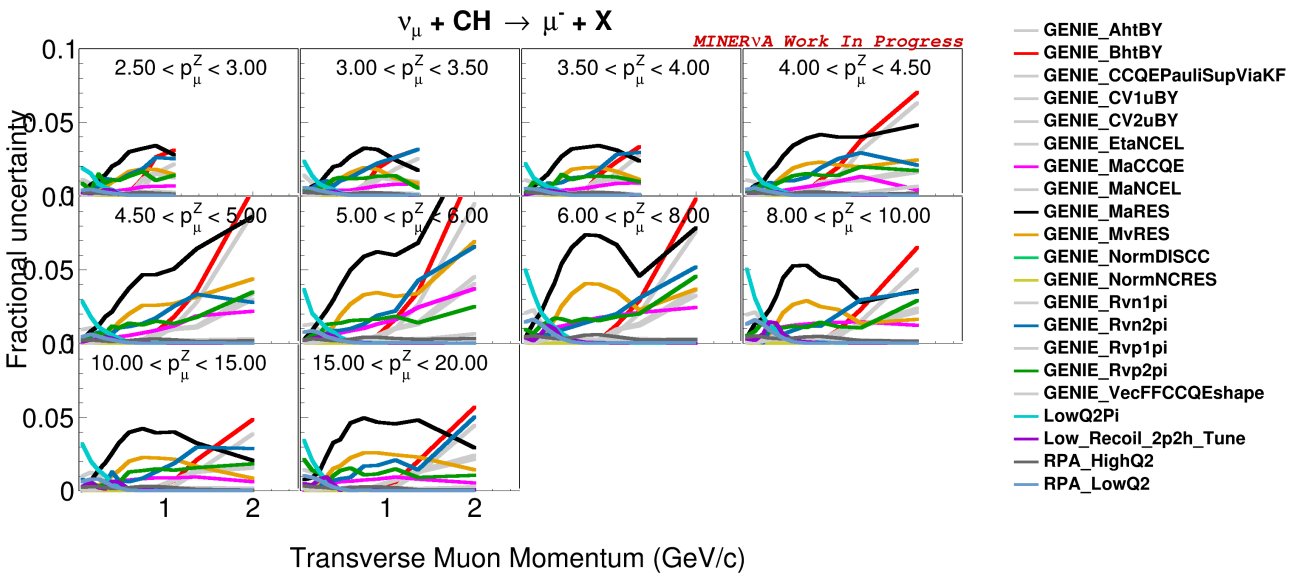

(a) **Neutrino** mode.

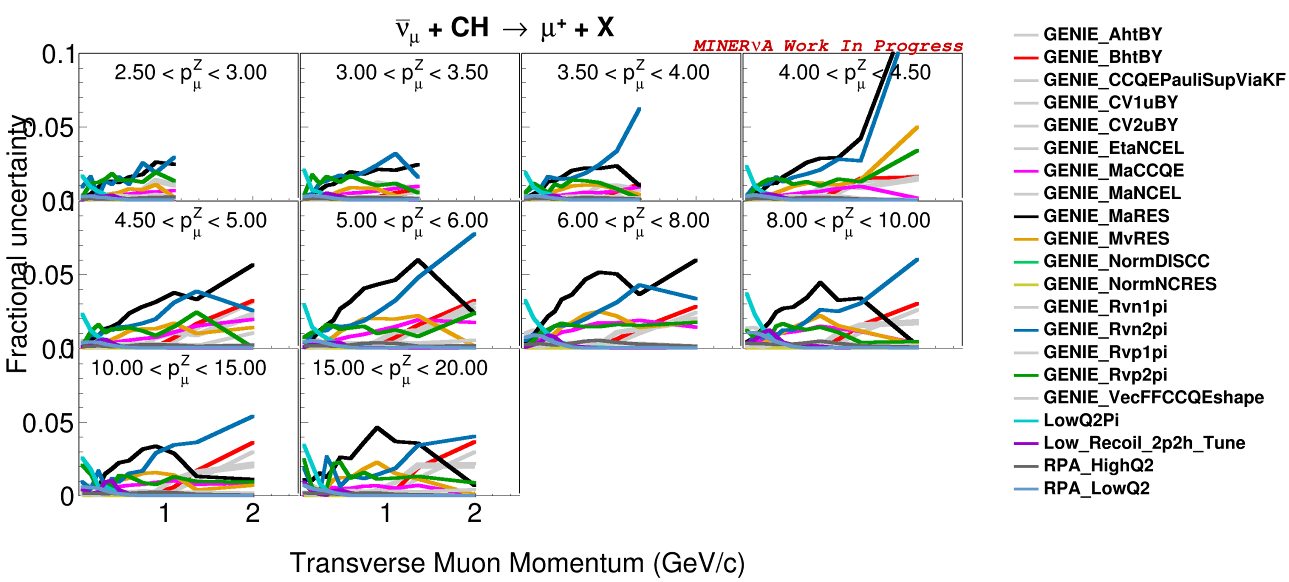

(b) **Antineutrino** mode.

Figure 94 – Fractional systematic uncertainties breakdown corresponding to the **Interaction Model** error group. The top (bottom) plot illustrates the errors on the extracted neutrino (antineutrino) data cross sections in terms of the **muon momentum components**. The dominant sources of uncertainty are attributed to the following simulated cross section model parameters: `GENIE_MaRES` (black), `GENIE_MvRES` (yellow), and `GENIE_Rvn2pi` (blue); refer to Tab. 15 for further details.

C.2.3 Muon Reconstruction error group

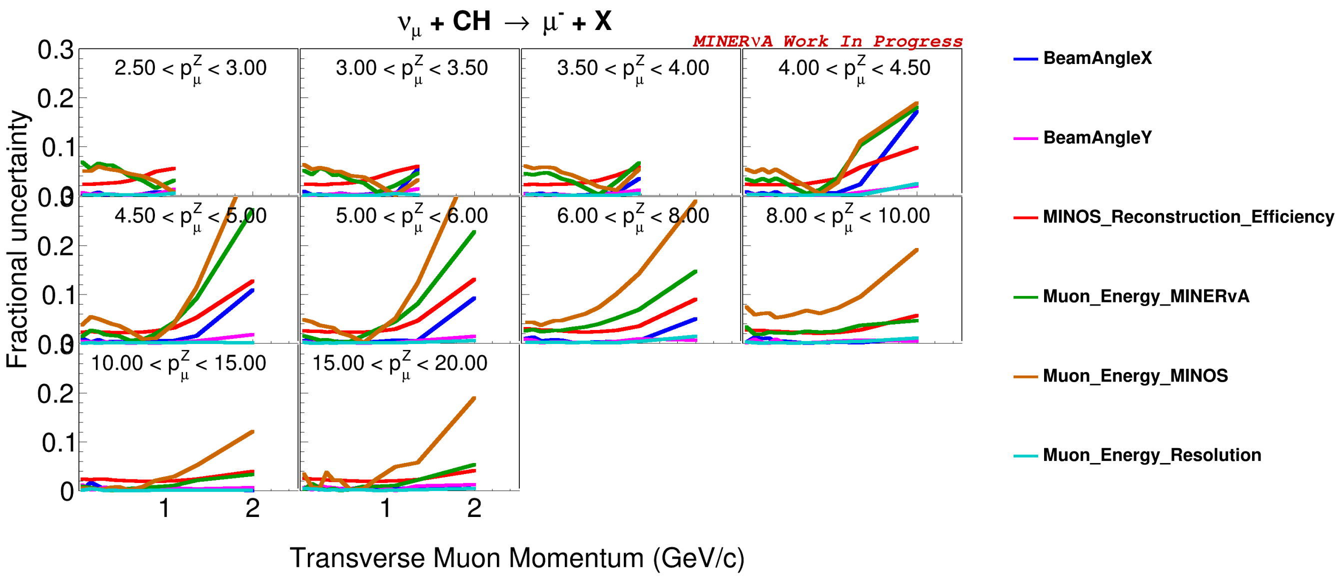

(a) **Neutrino** mode.

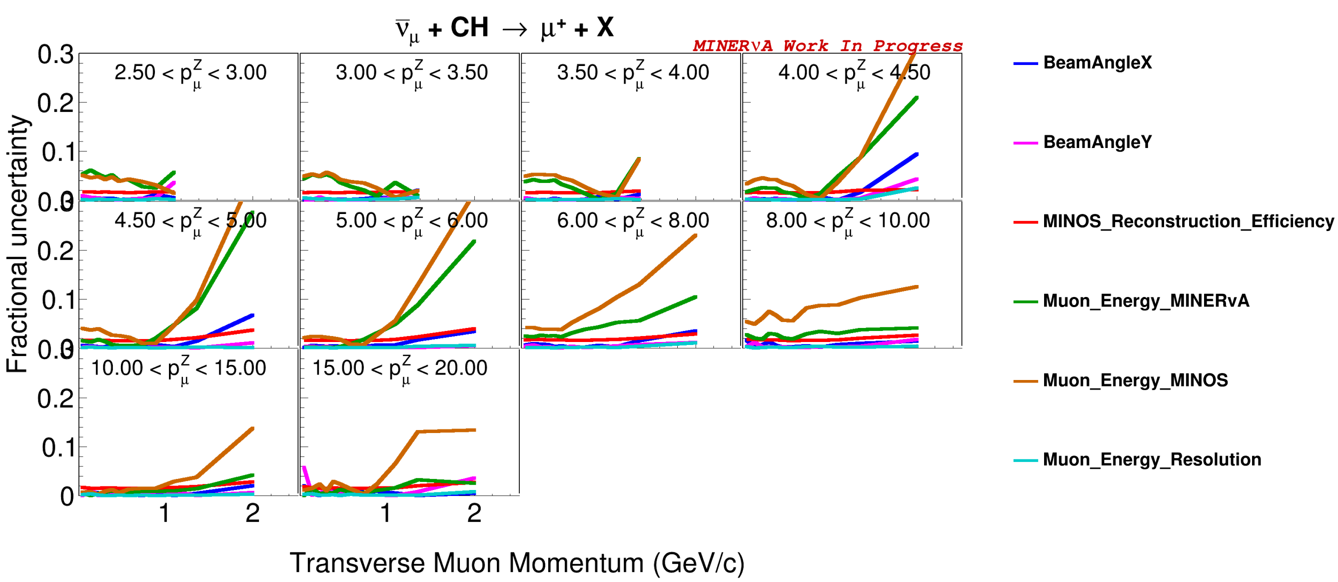

(b) **Antineutrino** mode.

Figure 95 – Fractional systematic uncertainties breakdown corresponding to the **Muon Reconstruction** error group. The top (bottom) plot illustrates the errors on the extracted neutrino (antineutrino) data cross sections in terms of the **muon momentum components**. The dominant sources of uncertainty are `Muon_Energy_MINERvA` (gree), `Muon_Energy_MINOS` (orange), and `MINOS_Reconstruction_Efficiency` (red); refer to Tab. 18 for further details.

C.2.4 FSI error group

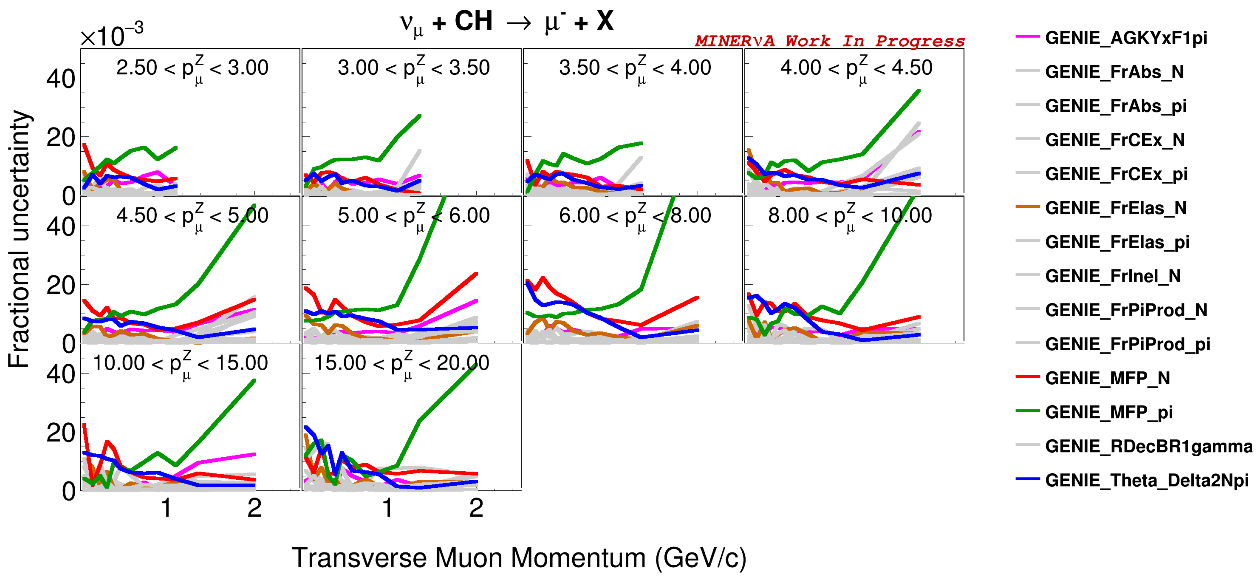

(a) **Neutrino** mode.

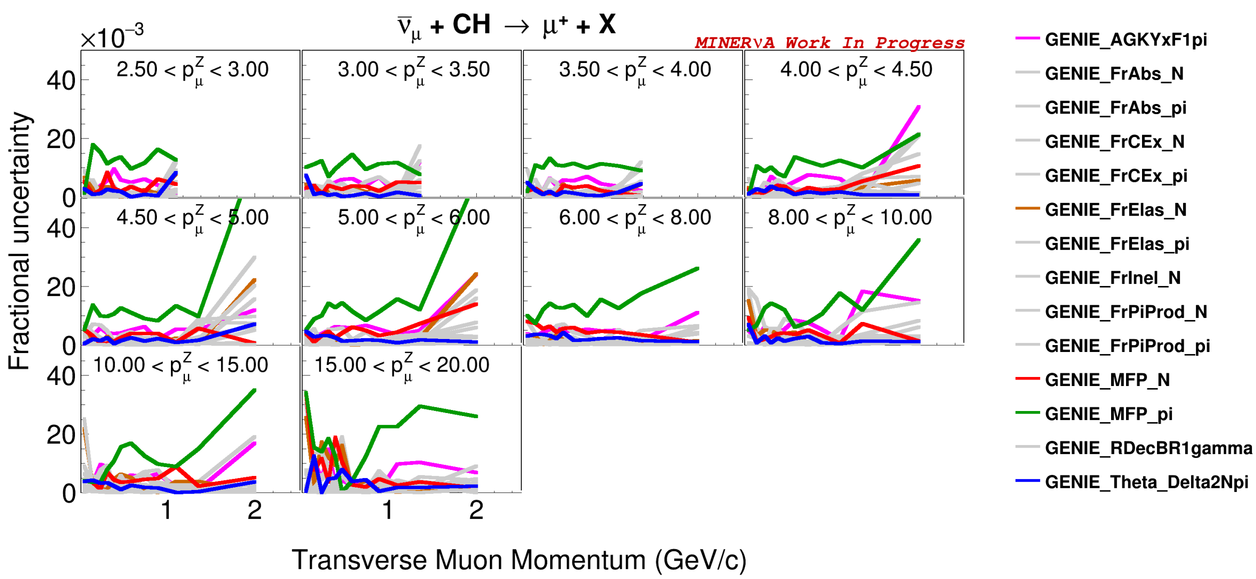

(b) **Antineutrino** mode.

Figure 96 – Fractional systematic uncertainties breakdown corresponding to the **FSI** error group. The top (bottom) plot illustrates the errors on the extracted neutrino (antineutrino) data cross sections in terms of the **muon momentum components**. The dominant sources of uncertainty are `GENIE_MFP_pi` (gree), `GENIE_MFP_N` (red), and `GENIE_Theta_Delta2Npi` (blue) for neutrinos, and `GENIE_AGKYxF1pi` (pink) for antineutrinos; refer to Tab. 16 for further details.

C.2.5 Particle Response error group

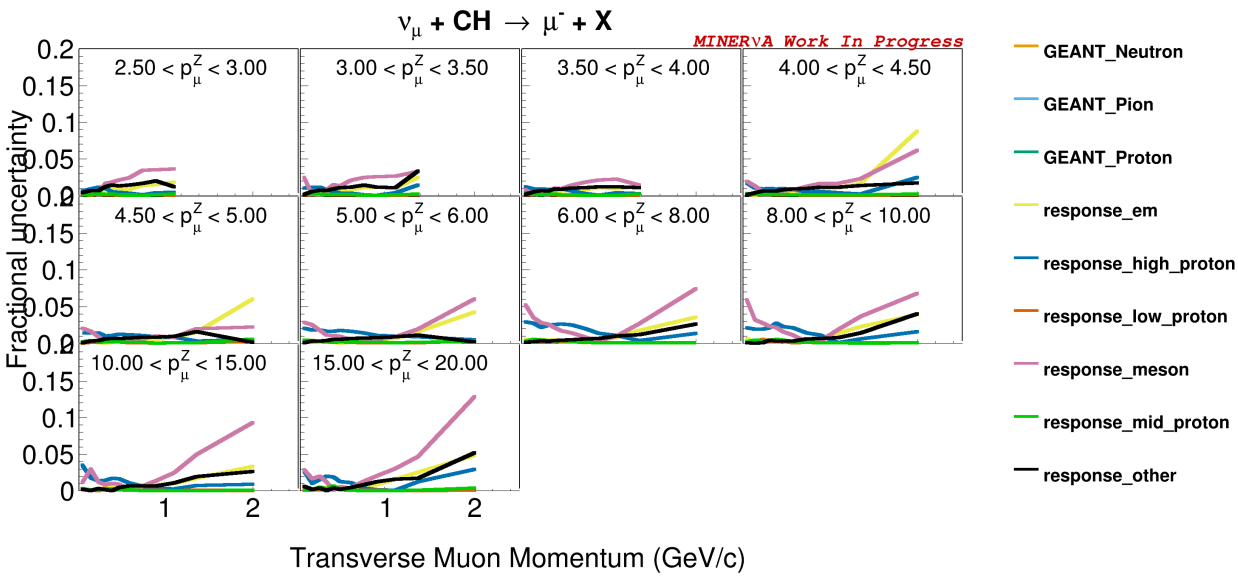

(a) **Neutrino** mode.

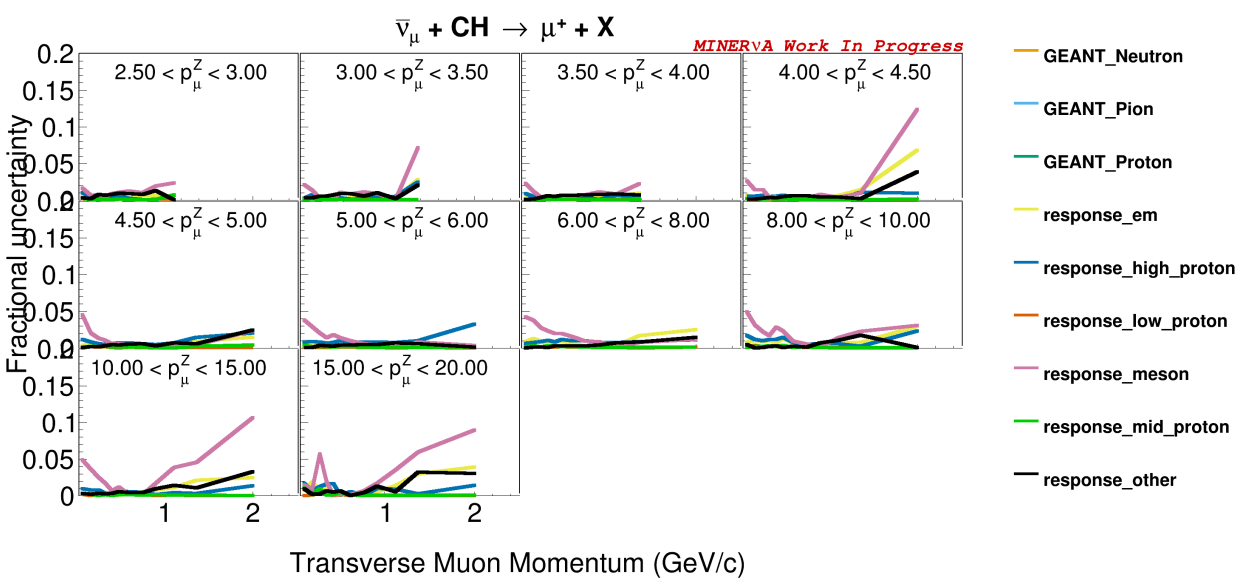

(b) **Antineutrino** mode.

Figure 97 – Fractional systematic uncertainties breakdown corresponding to the **Particle Response** error group. The top (bottom) plot illustrates the errors on the extracted neutrino (antineutrino) data cross sections in terms of the **muon momentum components**. The dominant sources of uncertainty are `response_meson` (magenta), `response_em` (light yellow), and `response_high_proton` (blue); refer to Tab. 17 for further details.

APPENDIX D – LArTPC detector studies

This Appendix documents the main results obtained over the course of one year (2023) from studies of a purification system for liquid argon time projection chamber (LArTPC) neutrino detectors. The work was conducted at the Leptons Laboratory at the University of Campinas (Unicamp), Brazil, and at the Noble Liquid Test Facility at Fermilab, USA.

My contributions to this project resulted in a few publications, some of which are listed at the beginning of this thesis (Publication List). The proposed purification system demonstrated the capability to significantly reduce nitrogen contamination in commercial liquid argon, and is expected to be deployed in the 70 kton LArTPC modules of the DUNE experiment.

The proposal for these studies began several years before I joined the collaboration, and involved researchers from multiple Brazilian institutions, with primary funding provided by the São Paulo Research Foundation. The collaborators involved in the project's Phase I are listed below:

- Dilson Cardoso, José Mansur Assaf, Ivana Cruz, Rosemberg Gonçalves (UFSCar)
- Magda Fontes and Krystal Brant (CBPF)
- Pascoal Pagliuso, Ettore Segreto, Ana Machado, Thiago Alegre, Cris Adriano, Dirceu Noriler, Gustavo Wiederhecker, Ana Caffer, Heriques Frandini, Renato Soccol, Pedro Bianchi, Cezar Aguiar, Frederico Demolin (Unicamp)
- Elisabete Assaf (USP–São Carlos)
- Cristhiane Reis (UFSJ)

D.1 Introduction

Liquid argon (LAr) has been widely adopted in neutrino and dark matter experiments because of its favorable detection properties. Final-state charged particles traversing the medium produce both scintillation light and ionization electrons. By collecting scintillation photons and drifting the ionization charge under an electric field, these detectors enable precise reconstruction of interaction topologies.

Despite that, the performance of LAr detectors strongly depends on the purity of the argon. Contaminants such as nitrogen, oxygen, and water reduce scintillation light yield and capture drifting electrons, degrading detector resolution. Therefore, impurity levels must be minimized through continuous filtration. This Appendix presents results from a novel purification technology developed in Brazil, and tested in the Purification Liquid Argon Cryostat (PuLArC) at IFGW–Unicamp, and in the ICEBERG setup at the Fermilab Noble Liquid Test Facility [151].

D.2 LAr scintillation light theory

When ionizing particles traverse LAr, recombination and de-excitation processes produce ultraviolet scintillation light through the reaction $Ar_2^* \rightarrow 2Ar + 1\gamma$. The observed signal consists of two characteristic components associated with the excited dimer states: singlet (S) and triplet (T). In pure LAr, their populations follow first-order decay kinetics ($i = S, T$):

$$\frac{d[Ar_2^*]_i}{dt} = -\frac{1}{\tau_i}[Ar_2^*]_i \qquad \Rightarrow \qquad [Ar_2^*]_i(t) = [Ar_2^*]_i(0)e^{-t/\tau_i}. \tag{D.1}$$

Typical decay constants reported in the literature are $\tau_S = 2$–6 ns and $\tau_T = 1100$–1600 ns [152, 153]. The presence of contaminants such as N_2 or O_2 introduces non-radiative quenching processes that reduce the scintillation yield and modify the decay time according to

$$\frac{1}{\tau_i'}([X_2]) = \frac{1}{\tau_i} + [X_2] \cdot k, \tag{D.2}$$

where k is the quenching rate constant and τ_i corresponds to the decay time in purified argon.

D.3 Experimental apparatus

D.3.1 PuLArC - UNICAMP

The experiment is composed of two main components: a **vessel** and a **dewar**. The vessel contains 100 L of LAr (grade 6.0) and houses two purity monitors and one photomultiplier tube (PMT). The dewar, filled with 250–270 L of LAr (grade 5.0), acts as a thermal bath and accommodates up to two filters. These components are illustrated in Fig. 98.

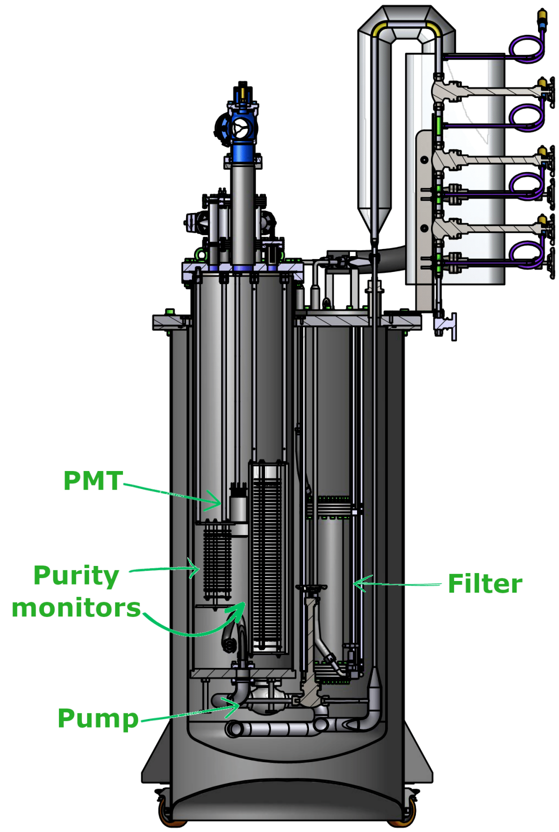

Figure 98 – Schematics of the cryogenic system. Reproduced from K. Brandt, C. Santos, H. Frandini, and A. Augusto [154].

Additional components include:

- Pump (Barber Nichols FSCM 57377)
- Two power supplies (CAEN 1370 and 1471)
- Oscilloscope (Tektronix MDO 3034)
- Level sensors and signal amplifier
- Xenon lamp and optical fibers

The novel nitrogen filter, Li-FAU, was tested and its performance compared with commercial BASF and 4A media. Detailed descriptions of their properties can be found in Refs. [155–158].

The PMT and the purity monitors provide a cross-check to each other in assessing the concentration of LAr contaminants. The PMT detects scintillation light from cosmic muons. On the other hand, the purity monitors count the number of free (drifted) electrons, generated from flashlights of an external Xenon lamp (photo-electric effect).

The contaminants concentration is then evaluated by computing the Ar and electron constants time. In this report, only PMT-based measurements are presented. The structure of the purity monitor and one of the tested filters are shown in Fig. 99.

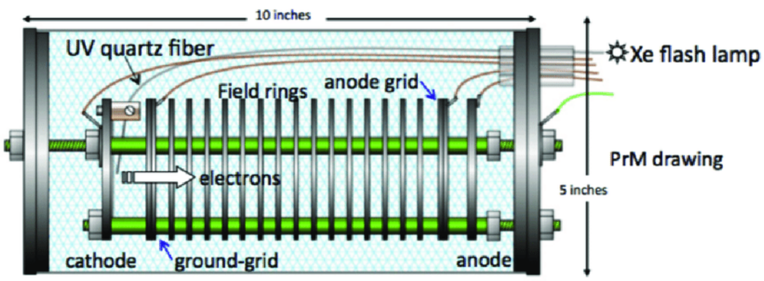

Figure 99 – *Left*: Purity monitor structure. *Right*: Assembled filter.

Fig. 100 illustrates a typical PMT signal (voltage *vs.* time). The PMT signals were acquired by setting the following parameters: Power supply (CAEN 1370) = -1200 V; Oscilloscope: Channel = 3, Channel Termination = 50 Ω, Vertical Scale = 200 mV, Horizontal Scale = 400 ns, Slope = Negative-going edge, Trigger Level = -76 mV, Trigger Coupling = DC; signal amplifier turned ON.

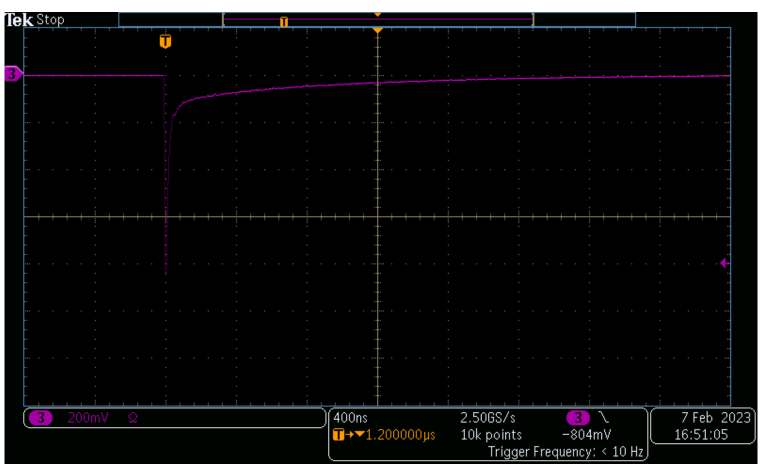

Figure 100 – Signal waveform from the PMT.

After the filter was activated and placed in the cryostat, the N_2 filtration tests followed a general procedure, described below:

i) With the pump ON at 45 Hz, 1 filter (BASF or 4A) is used to purify the LAr 6.0 until its decay time reaches $\sim$ 1000 ns;

ii) With the pump ON at 45 Hz, the valves to the first filter are closed, and a controlled amount (0.5 L/min) of N_2 contaminant is flushed into the vessel for about 10 s;

iii) Then, the mixture is left circulating for 10 min from when a PMT measurement is taken and the decay time computed;

iv) The last 2 steps are repeated until the decay time drops below $\sim$ 200 ns;

v) Finally, the valves to the filter being tested (Li-FAU) are opened, and PMT signals are recorded at each 15 min lasting 3 hours in total.

Fig. 101 shows how the PMT signals evolves with the pumping time for a typical LAr purification test. Notice that, the slow component is more pronounced, and so this is used as a proxy to the LAr purity.

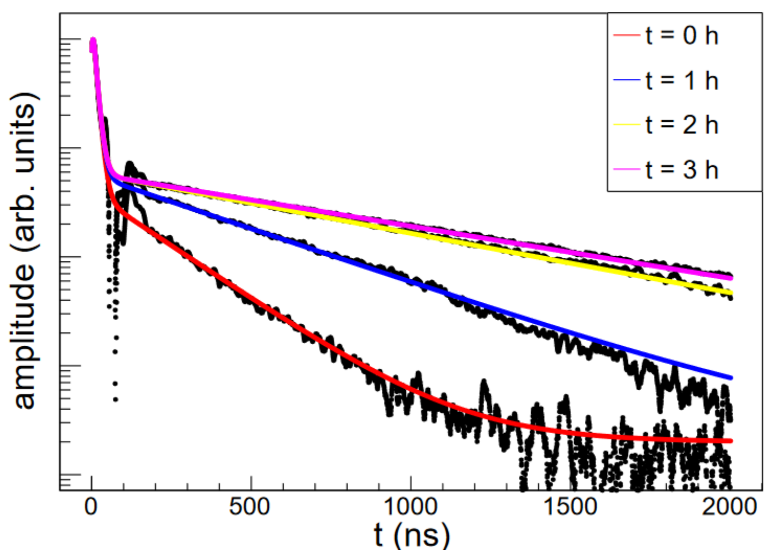

Figure 101 – PMT acquired signals during the LAr purification.

D.3.2 ICEBERG - Fermilab

The results from PuLArC, presented in Sec. D.4, motivated further investigations in a large scale setup. ICEBERG, a 3,000-liter cryostat at Fermilab, was used to test the Li-FAU filter. The list of materials used in the experiment is given below, and Fig. 102 illustrates the cryostat: blue color represents the LAr volume; the compartment on the right houses the Li-FAU the filter and an heater..

1) 5 kg of Li-FAU;

2) 2,625 L of LAr;

3) 70 L of gas nitrogen;

4) 2 gas analyzers (ServoPro and LDetek).

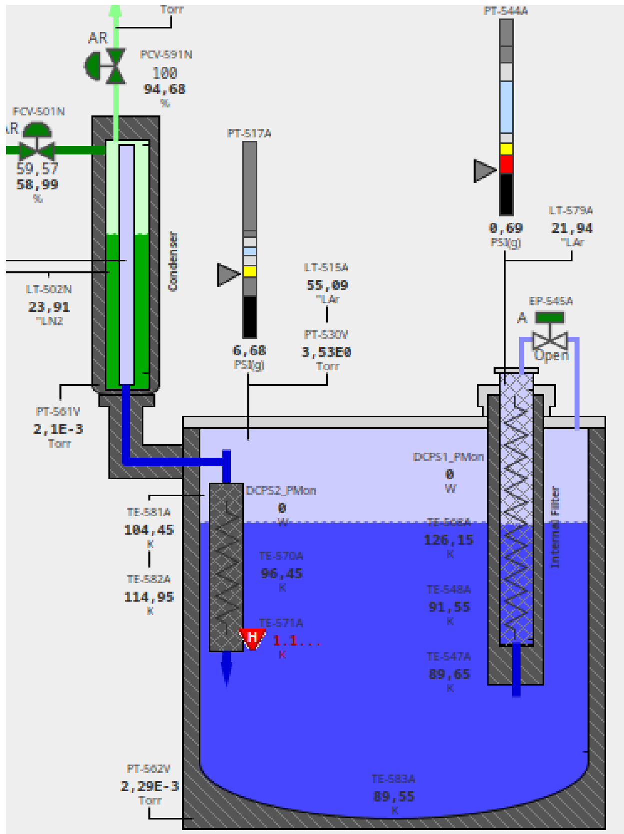

Figure 102 – ICEBERG cryostat.

The filtering process in ICEBERG is described as follows: once the injection procedure is completed, the heater is turned ON, which makes the internal pressure of the filter rise, flushing out the LAr through a duct located on the bottom; then the heater is switched OFF, and an automatic valve on the top connecting the internal part of the filter to the cryostat is opened. This allows the internal pressure to decrease, and the mixture N_2+LAr enter the filter compartment from the bottom. Once the mixture reaches a defined level in the filter, the heater is switched ON again, and the cycle is repeated until the N_2 concentration drops below 1 ppm. Each cycle took approximately 8 minutes considering the parameter settings.

D.4 Results from PuLArC

Fig. 103 shows the results from the experiments at PuLArC. Starting with the frame (a), the LAr 6.0 is purified through BASF filter until the decay time reaches 1000 ns. Then, the system is contaminated with 1 L of N_2, and the filtering process is transferred to the Li-FAU media (b). This filter has been shown to be capable of purify the LAr, by reducing significantly the concentration of N_2 in the system. A counter proof was performed with the 4A filter (c), which cannot absorb N_2, and again Li-FAU successfully filtered the system, mitigating the N_2 contaminant (d).

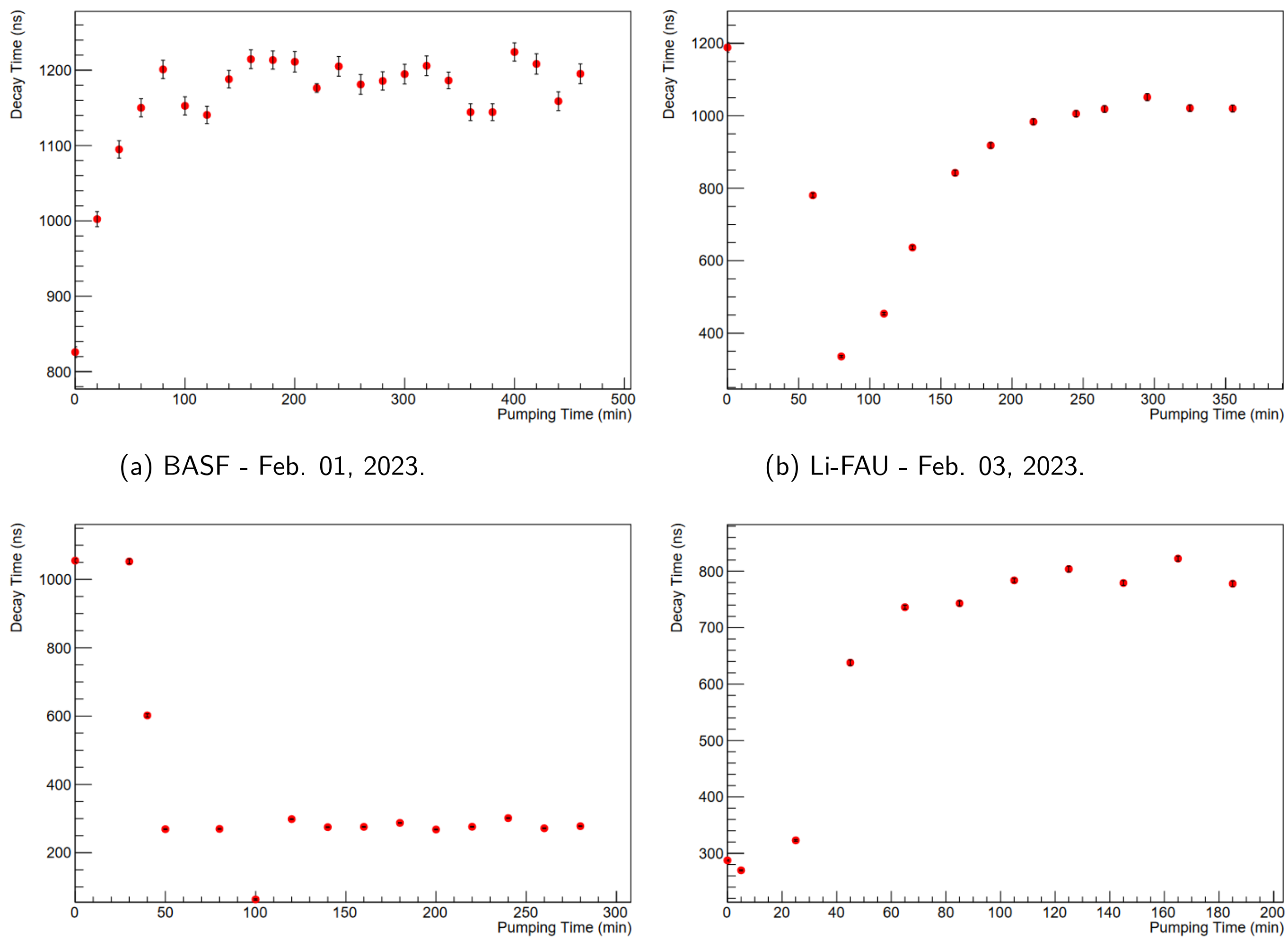

(a) BASF - Feb. 01, 2023.

(b) Li-FAU - Feb. 03, 2023.

(c) 4A - Feb. 09, 2023.

(d) Li-FAU - Feb. 10, 2023.

Figure 103 – Results for LAr filtering at PuLArC through different medias.

D.5 Results from ICEBERG

The N_2 concentration over time was measured using 2 gas analyzers, and recorded in real time using the Seeq online server. Fig. 104 shows the measurements corresponding to a 4-day period.

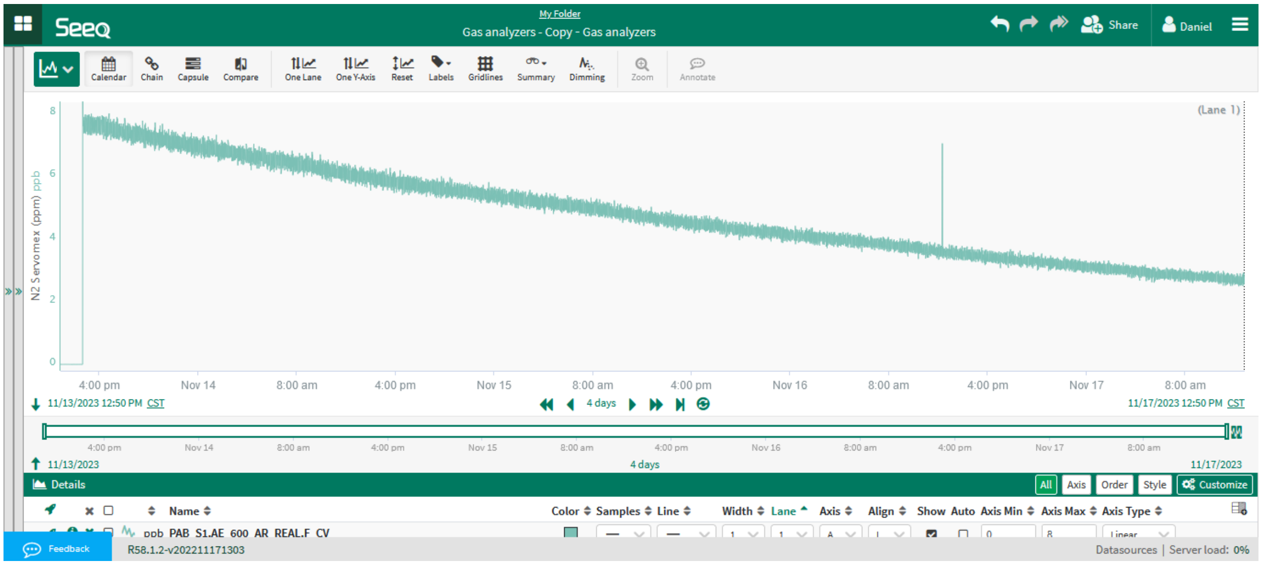

Figure 104 – N_2 concentration (ppm) in ICEBERG using Li-FAU purification system.

The data were analyzed for 3 hour batches, assuming the N_2 concentration as the mean value from 10-second adjacent measurements, and the error computed as the standard deviation. Fig. 105 shows the resulting N_2 concentration as a function of purification time (error bars are statistical only), and Tab. 21 the initial and final N_2 concentrations.

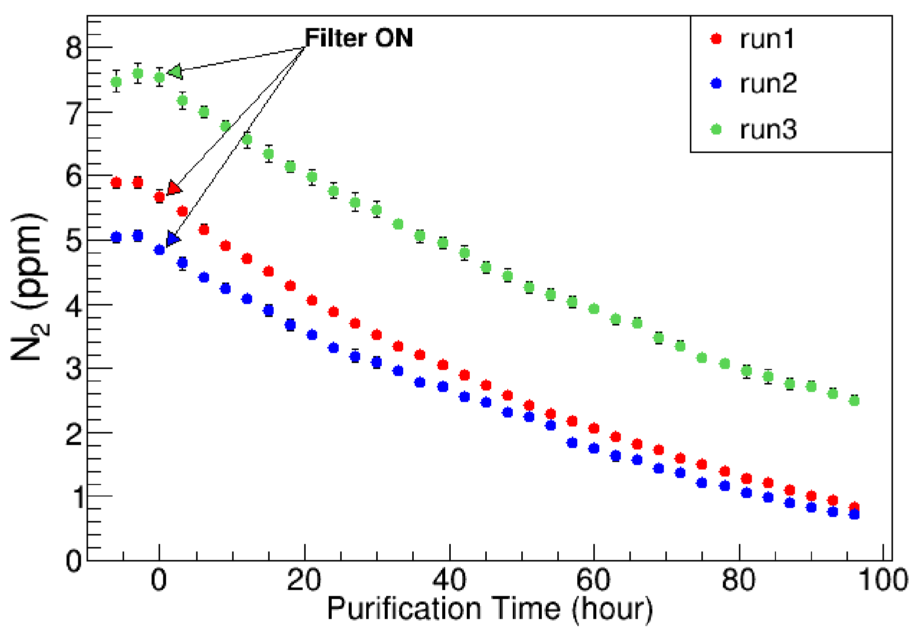

Figure 105 – N_2 concentration (ppm) vs. purification time (h).

Table 21 – Initial and final N_2 concentration (ppm).

Runs	$t = 0$ h	$t = 96$ h
run1	5.68 $\pm$ 0.10	0.84 $\pm$ 0.04
run2	4.84 $\pm$ 0.07	0.71 $\pm$ 0.03
run3	7.54 $\pm$ 0.14	2.50 $\pm$ 0.07

D.6 Final Remarks

In this study, an innovative filtering technology for nitrogen removal from liquid argon was investigated. The datasets analyzed from experiments conducted in two different cryogenic setups demonstrate the filter's capability to significantly mitigate nitrogen impurities in commercial liquid argon, thereby helping to control detector response systematics in neutrino experiments such as DUNE.

Bibliography

[1] J. N. Bahcall *et al.*, Rev. Mod. Phys. **54**, 767 (1982), doi:10.1103/RevModPhys.54.767;

[2] W. Pauli, "Letter addressed to the participants of the Tübingen conference on β-radioactivity" (4 Dec 1930), Physics Institute of the Federal Institute of Technology, Zürich. Translated copy available online: https://www.math.utah.edu/~beebe/talks/2015/qtm/pdf/pauli-1930-ltc.pdf (accessed Feb 10, 2026);

[3] C. Cowan *et al.*, Science **124**, 103 (1956), doi:10.1126/science.124.3212.103;

[4] K. Zuber, Neutrino Physics 3rd ed. (2020), doi:10.1201/9781315195612;

[5] R. Davis, Jr., D. S. Harmer, and K. C. Hoffman, Phys. Rev. Lett. **20**, 1205 (1968), doi:10.1103/PhysRevLett.20.1205;

[6] Y. Fukuda *et al.*, Phys. Rev. Lett. **81**, 1562 (1998), doi:10.1103/PhysRevLett.81.1562;

[7] Q. R. Ahmad *et al.* (SNO Collaboration), Phys. Rev. Lett. **87**, 071301 (2001), doi:10.1103/PhysRevLett.87.071301;

[8] K. Kodama *et al.*, Phys. Lett. B **504**, 218 (2001), doi:10.1016/S0370-2693(01)00307-0;

[9] N. Agafonova *et al.* (OPERA Collaboration), Phys. Rev. Lett. **120**, 211801 (2018), doi:10.1103/PhysRevLett.120.211801;

[10] A. Ereditato, Nucl. Phys. B **908**, 116 (2016), doi:10.1016/j.nuclphysb.2016.03.014;

[11] The Double Chooz Collaboration, Nat. Phys. **16**, 558–564 (2020), doi:10.1038/s41567-020-0831-y;

[12] NOvA and T2K Collaborations, Nature **646**, 818–824 (2025), doi:10.1038/s41586-025-09599-3;

[13] MicroBooNE Collaboration, Nature **648**, 64–69 (2025), doi:10.1038/s41586-025-09757-7;

[14] K. Abe *et al.* (T2K Collaboration), Phys. Rev. D **108**, 072011 (2023), doi:10.1103/PhysRevD.108.072011;

[15] S. Abubakar *et al.* (NOvA Collaboration), arXiv:2509.04361v1 [hep-ex] (2025);

[16] Y. Liu, L. Munteanu, and S. Dolan, arXiv:2511.03964v1 [hep-ex] (2025);

[17] C. M. G. Lattes, H. Muirhead, G. P. S. Occhialini, and C. F. Powell, Nature **159**, 694–697 (1947), doi:10.1038/159694a0;

[18] C. M. G. Lattes, G. P. S. Occhialini, and C. F. Powell, Nature **160**, 453–456 (1947), doi:10.1038/160453a0;

[19] M. S. Athar and J. G. Morfín, Journal of Physics G: Nuclear and Particle Physics **48**, 034001 (2021), doi:10.48550/arXiv.2006.08603;

[20] A. Lozano *et al.* (MINERvA Collaboration), arXiv=2503.20043 (2025);

[21] A. A. Aguilar-Arevalo *et al.* (MiniBooNE Collaboration), Phys. Rev. D **83**, 052007 (2011), doi:10.1103/PhysRevD.83.052007;

[22] O. Altinok *et al.* (MINERvA Collaboration), Phys. Rev. D **96**, 072003 (2017), doi:10.1103/PhysRevD.96.072003;

[23] S. Abbaslu *et al.* (DUNE Collaboration), arXiv:2511.11925v1 [nucl-ex] (2025);

[24] C. M. Marshall *et al.* (MINERvA Collaboration), Phys. Rev. D **94**, 012002 (2016), doi:10.1103/PhysRevD.94.012002;

[25] P. Abratenko *et al.* (MicroBooNE Collaboration), Phys. Rev. Lett. **135**, 251804 (2025), doi:10.1103/96vx-gq2g;

[26] E. Bloom and F. Gilman, Phys. Rev. Lett. **25**, 1140 (1970), doi:10.1103/PhysRevLett.25.1140;

[27] L. Alvarez-Ruso *et al.*, NuSTEC White Paper: Neutrino–Nucleus Interactions, Prog. Part. Nucl. Phys. **100**, 1 (2018), doi:10.1016/j.ppnp.2018.01.006;

[28] J. Formaggio and G. Zeller, Rev. Mod. Phys. **84**, 1307 (2012), doi:10.1103/RevModPhys.84.1307;

[29] S. L. Glashow, Nucl. Phys. **10**, 107–117 (1959), doi:10.1016/0029-5582(59)90196-8;

[30] A. Salam and J. C. Ward, Il Nuovo Cimento **11**, 568–577 (1959), doi:10.1007/BF02726525;

[31] S. Weinberg, Phys. Rev. Lett. **19**, 1264–1266 (1967), doi:10.1103/PhysRevLett.19.1264;

[32] C. S. Wu *et al.*, Phys. Rev. **105**, 1413–1415 (1957), doi:10.1103/PhysRev.105.1413;

[33] C.H. Llewellyn Smith, Phys. Rep. **3**, 261–379 (1972), doi:10.1016/0370-1573(72)90010-5;

[34] A. A. Aguilar-Arevalo *et al.*, Phys. Rev. D **81**, 092005 (2010), doi:10.1103/PhysRevD.81.092005;

[35] X. G. Lu *et al.*, Phys. Rev. D **92**, 051302 (2015), doi:10.1103/PhysRevD.92.051302;

[36] X. G. Lu *et al.*, Phys. Rev. C **94**, 015503 (2016), doi:10.1103/PhysRevC.94.015503;

[37] J. Kleykamp *et al.* (MINERvA Collaboration), Phys. Rev. Lett. **130**, 161801 (2023), doi:10.1103/PhysRevLett.130.161801;

[38] J. Kleykamp *et al.* (MINERvA Collaboration), Phys. Rev. D **112**, 052005 (2025), doi:10.1103/h9vz-x4xf;

[39] S. J. Barish *et al.*, Phys. Rev. D **16**, 3103 (1977), doi:10.1103/PhysRevD.16.3103;

[40] N. J. Baker *et al.*, Phys. Rev. D **23**, 2499 (1981), doi:10.1103/PhysRevD.23.2499;

[41] T. Kitagaki *et al.*, Phys. Rev. D **42**, 1331 (1990), doi:10.1103/PhysRevD.42.1331;

[42] A. S. Meyer, M. Betancourt, R. Gran, and R. J. Hill, Phys. Rev. D **93**, 113015 (2016), doi:10.1103/PhysRevD.93.113015;

[43] A.S. Meyer *et al.* (MINERvA Collaboration), arXiv:2512.14097 [hep-ex] (2025);

[44] C. Patrignani *et al.* (Particle Data Group), Chin. Phys. C **40**, 100001 (2016), doi:10.1088/1674-1137/40/10/100001;

[45] D. Rein and L. M. Sehgal, Ann. Phys. **133**, 79–153 (1981), doi:10.1016/0003-4916(81)90242-6;

[46] R. González-Jiménez *et al.*, Phys. Rev. D **95**, 113007 (2017), doi:10.1103/PhysRevD.95.113007;

[47] M. Kabirnezhad, Phys. Rev. D **102**, 053009 (2020), doi:10.1103/PhysRevD.102.053009;

[48] A. Bodek and U.K. Yang, Journal of Physics G: Nuclear and Particle Physics **29**, 1899 (2003);

[49] R. Smith and E. Moniz, Nucl. Phys. B. **43**, 605 (1972), doi:10.1016/0550-3213(72)90040-5;

[50] A. Bodek and J. L. Ritchie, Phys. Rev. D **24**, 1400 (1981), doi:10.1103/PhysRevD.24.1400;

[51] J. P. Stowell, Effects of Nucleon and Nuclear Structure in Neutrino Interactions. PhD thesis, The University of Sheffield, UK (2019);

[52] M. Martini *et al.*, Phys. Rev. C **80**, 065501 (2009), doi:10.1103/PhysRevC.80.065501;

[53] J. Nieves *et al.*, Phys. Rev. C **83**, 045501 (2011), doi:10.1103/PhysRevC.83.045501;

[54] P. A. Rodrigues *et al.*, Phys. Rev. Lett. **116**, 071802 (2016), doi:10.1103/PhysRevLett.116.071802;

[55] S. Dytman *et al.*, Phys. Rev. D **104**, 053006 (2021), doi:10.1103/PhysRevD.104.053006;

[56] S. Dytman, 6th International Workshop on Neutrino-nucleus interactions in the few GeV region (NUINT 09), AIP Conf. Proc. 1189, 51 (2009), doi:10.1063/1.3274190;

[57] R. P. Feynman, Photon-hadron Interactions (1st ed.). CRC Press (1972), doi:10.1201/9780429493331;

[58] M. Breidenbach *et al.*, Phys. Rev. Lett. **23**, 935 (1969), doi:10.1103/PhysRevLett.23.935;

[59] J. D. Bjorken, Phys. Rev. **163**, 1767 (1967), doi:10.1103/PhysRev.163.1767;

[60] M. Gell-Mann, Phys. Lett. **8**, 214 (1964), doi:10.1016/S0031-9163(64)92001-3;

[61] G. Zweig, Developments in the Quark Theory of Hadrons **1**, 22 (1964);

[62] R. P. Feynman, Phys. Rev. Lett. **23**, 1415 (1969), doi:10.1103/PhysRevLett.23.1415;

[63] R. Dolen, D. Horn, C. Schmid, Phys. Rev. **166**, 1768 (1968), doi:10.1103/PhysRev.166.1768;

[64] I. Niculescu *et al.*, Phys. Rev. Lett. **85**, 1186 (2000), doi:10.1103/PhysRevLett.85.1186;

[65] Y. Liang *et al.* (The Jefferson Lab Hall C E94-110 Collaboration), arXiv=nucl-ex/0410027 (2004);

[66] W. Melnitchouk *et al.*, Physics Reports **406**, 127 (2005), doi:10.1016/j.physrep.2004.10.004;

[67] S. P. Malace *et al.*, Phys. Rev. C **80**, 035207 (2009), doi:10.1103/PhysRevC.80.035207;

[68] I. Niculescu, arXiv=1509.07795 (2015);

[69] C. E. Carlson and N. C. Mukhopadhyay, Phys. Rev. D **47**, R1737 (1993), doi:10.1103/PhysRevD.47.R1737;

[70] S. J. Barish *et al.*, Phys. Rev. D **16**, 3103 (1977), doi:10.1103/PhysRevD.16.3103;

[71] G. M. Radecky *et al.*, Phys. Rev. D **25**, 1161 (1982), doi:10.1103/PhysRevD.25.1161;

[72] A. Rodriguez *et al.* (K2K Collaboration), Phys. Rev. D **78**, 032003 (2008), doi:10.1103/PhysRevD.78.032003;

[73] K. M. Graczyk, C. Juszczak and J. T. Sobczyk, Nucl. Phys. A **781**, 227 (2007), doi:10.1016/j.nuclphysa.2006.10.036;

[74] O. Lalakulich, W. Melnitchouk, and E. A. Paschos, Phys. Rev. C **75**, 015202 (2007), doi:10.1103/PhysRevC.75.015202;

[75] O. Lalakulich *et al.*, AIP Conf. Proc. **1189**, 276 (2009), doi:10.1063/1.3274170;

[76] O. Buss *et al.*, Physics Reports **512**, 1 (2012), doi:10.1016/j.physrep.2011.12.001;

[77] O. Lalakulich *et al.*, Phys. Rev. C **79**, 015206 (2009), doi:10.1103/PhysRevC.79.015206;

[78] D. J. Gross, S. B. Treiman, Phys. Rev. D **4**, 1059 (1971), doi:10.1103/PhysRevD.4.1059;

[79] V. M. Braun, EPJ Web of Conferences **274**, 01012 (2022), doi:10.1051/epjconf/202227401012;

[80] S. Alekhin *et al.*, AIP Conference Proceedings **967**, 215 (2007), doi:10.1063/1.2834481;

[81] S. Alekhin *et al.*, Phys. Rev. D **89**, 054028 (2014), doi:10.1103/PhysRevD.89.054028;

[82] A. Accardi *et al.*, Phys. Rev. D **93**, 114017 (2016), doi:10.1103/PhysRevD.93.114017;

[83] I. Schienbein *et al.*, Journal of Physics G: Nuclear and Particle Physics **35**, 053101 (2008), doi:10.1088/0954-3899/35/5/053101;

[84] H. Georgi and H. D. Politzer, Phys. Rev. D **14**, 1829 (1976), doi:10.1103/PhysRevD.14.1829;

[85] R. Ruiz *et al.*, Progress in Particle and Nuclear Physics **136**, 104096 (2024), doi:10.1016/j.ppnp.2023.104096;

[86] C. Bronner, JPS Conf. Proc. **12**, 010025 (2016), doi:10.7566/JPSCP.12.010025;

[87] Y. Hayato, Acta Phys. Polon. B **40**, 2477 (2009);

[88] J. A. Nowak, Phys. Scr. **2006**, 70 (2006);

[89] Z. Koba, H.B. Nielsen and P. Olesen, Nucl. Phys. B **40**, 317 (1972), doi:10.1016/0550-3213(72)90551-2;

[90] K. M. Graczyk and J. T. Sobczyk, Phys. Rev. D **77**, 053001 (2008), doi:10.1103/PhysRevD.77.053001;

[91] C. Juszczak, J. A. Nowak and J. T. Sobczyk, Nuclear Physics B - Proceedings Supplements 159, 211 (2006), doi:10.1016/j.nuclphysbps.2006.08.069;

[92] J. Kopp, Diploma Thesis, Phenomenology of Three-Flavour Neutrino Oscillations, Technische Universität München (2006);

[93] W. Wu *et al.* (The NOvA Collaboration), arXiv=2511.05807 (2025);

[94] C.L. McGivern *et al.* (MINERvA Collaboration), Phys. Rev. D **94**, 052005 (2016), doi:10.1103/PhysRevD.94.052005;

[95] K. Abe *et al.* (T2K Collaboration) Nucl. Instrum. Methods **659**, 106 (2011), doi:10.1016/j.nima.2011.06.067;

[96] D. S. Ayres *et al.* (NOvA Collaboration), Report No. FERMILAB-DESIGN-2007-01 (2007);

[97] R. Acciarri *et al.* (DUNE Collaboration), arXiv=1601.05471 (2016);

[98] K. Abe *et al.* (Hyper-Kamiokande Proto-Collaboration), Prog. Theor. Exp. Phys. **2015**, 053C02 (2015), doi:10.1093/ptep/ptv061;

[99] Y. CHEN, Neutrino interactions in a modularised-LArTPC demonstrator for the DUNE near detector, NuInt 2022 (2022);

[100] Adrian Lozano Sánchez, *Cross Sections Measurement of $\nu/\bar{\nu}$ Interactions in CH in the Shallow Inelastic Scattering Region at $\langle E_\nu \rangle \sim$ 6 GeV in the MINERvA Experiment*, Ph.D. thesis, Centro Brasileiro de Pesquisas Físicas (2022);

[101] Gian Fredy Ricardo Caceres Vera, *Measurement of Neutrino Cross Sections interactions in the Shallow Inelastic Scattering region in Hydrocarbon at $\langle E_\nu \rangle \sim 6$ GeV in the MINERvA experiment*, Ph.D. thesis, Centro Brasileiro de Pesquisas Físicas (2020);

[102] H. Bethe and R. Peierls, Nature **133**, 532 (1934), doi:10.1038/133532a0;

[103] L. Aliaga *et al.* (MINERvA Collaboration), Nucl. Instrum. Methods Phys. Res. A **743**, 130–159 (2014), doi:10.1016/j.nima.2013.12.053;

[104] J. A. Mousseau, *First Search for the EMC Effect and Nuclear Shadowing in Neutrino Nuclear Deep Inelastic Scattering at MINERvA*, Springer Theses (Springer International Publishing, Cham, 2017), ISBN: 978-3-319-44841-1;

[105] C. E. Patrick, *Measurement of the Antineutrino Double-Differential Charged-Current Quasi-Elastic Scattering Cross Section at MINERvA*, Springer Theses (Springer International Publishing, Cham, 2018), ISBN: 978-3-319-69087-2;

[106] P. Adamson *et al.*, Nucl. Instrum. Methods Phys. Res. A **806**, 279–306 (2016), doi:10.1016/j.nima.2015.08.063;

[107] V. Shiltsev, arXiv:1906.07324v1 [physics.acc-ph, hep-ex] (2019);

[108] A. Klustová, *Measurement of Nuclear Dependence in Inclusive Antineutrino Scattering*, Ph.D. thesis, Imperial College London and Fermi National Accelerator Laboratory (2024), FERMILAB-THESIS-2024-08;

[109] D. G. Michael *et al.* (MINOS Collaboration), Nucl. Instrum. Methods Phys. Res., Sect. A **596**, 190–228 (2008), doi:10.1016/j.nima.2008.08.003;

[110] P. Adamson *et al.* (MINOS Collaboration), Phys. Rev. D **81**, 072002 (2010), doi:10.1103/PhysRevD.81.072002;

[111] R. Ospanov, *A measurement of muon neutrino disappearance with the MINOS detectors and NuMI beam*, Ph.D. thesis, The University of Texas at Austin, FERMILAB-THESIS-2008-04 (2008);

[112] *Fermilab bids a fond farewell to MINOS*, Fermilab News, August 1, 2016;

[113] S. Agostinelli *et al.*, Nucl. Instrum. Methods Phys. Res., Sect. A **506**, 250–303 (2003), doi:10.1016/S0168-9002(03)01368-8;

[114] J. Allison *et al.*, IEEE Trans. Nucl. Sci. **53**, 270–278 (2006), doi:10.1109/TNS.2006.869826;

[115] L. Aliaga, *Neutrino Flux Prediction for the NuMI Beamline*, Ph.D. thesis, The College of William and Mary in Virginia (2016);

[116] L. Zazueta *et al.* (MINERvA Collaboration), Phys. Rev. D **107**, 012001 (2023), doi:10.1103/PhysRevD.107.012001;

[117] E. Valencia *et al.* (MINERvA Collaboration), Phys. Rev. D **100**, 092001 (2019), doi:10.1103/PhysRevD.100.092001;

[118] D. Ruterbories *et al.* (MINERvA Collaboration), Phys. Rev. D **104**, 092010 (2021), doi:10.1103/PhysRevD.104.092010;

[119] C. Andreopoulos *et al.*, Nucl. Instrum. Meth. A **614**, 87 (2010), doi:10.1016/j.nima.2009.12.009;

[120] G. Diaz Bautista, *Measurement of ν_μ CC1π^0 Cross Section on Heavy Nuclei in MINERvA*, Ph.D. thesis, University of Rochester, Fermi National Accelerator Laboratory, FERMILAB-THESIS-2023-01 (2023);

[121] J. Nieves, J. E. Amaro, and M. Valverde, Phys. Rev. C **70**, 055503 (2004), doi:10.1103/PhysRevC.70.055503;

[122] R. Gran *et al.* (MINERvA Collaboration), Phys. Rev. Lett. **120**, 221805 (2018), doi:10.1103/PhysRevLett.120.221805;

[123] R. Gran *et al.* (MINERvA Collaboration), Phys. Rev. Lett. **120**, 221805 (2018), doi:10.1103/PhysRevLett.120.221805;

[124] P. Rodrigues, C. Wilkinson, and K. McFarland, Eur. Phys. J. C **76**, 474 (2016), doi:10.1140/epjc/s10052-016-4314-3;

[125] P. Stowell *et al.* (MINERvA Collaboration), Phys. Rev. D **100**, 072005 (2019), doi:10.1103/PhysRevD.100.072005;

[126] R. Bradford, A. Bodek, H. Budd, and J. Arrington, Nucl. Phys. B Proc. Suppl. **159**, 127–132 (2006), doi:10.1016/j.nuclphysbps.2006.08.028;

[127] S. Gardiner, arXiv:2401.04065 (2024);

[128] F. James and M. Roos, Computer Physics Communications **10**, 343 (1975), doi:10.1016/0010-4655(75)90039-9;

[129] G. D'Agostini, Nucl. Instrum. Methods Phys. Res. A **362**, 487 (1995), doi:10.1016/0168-9002(95)00274-X;

[130] T. Adye, arXiv:1105.1160 (2011);

[131] H. Haider *et al.*, Nuclear Physics A **955**, 58 (2016), doi:10.1016/j.nuclphysa.2016.06.006;

[132] M. Tzanov *et al.*, Phys. Rev. D **74**, 012008 (2006), doi:10.1103/PhysRevD.74.012008;

[133] M. Kabirnezhad, Phys. Rev. D **97**, 013002 (2018), doi:10.1103/PhysRevD.97.013002;

[134] B. Messerly *et al.*, EPJ Web of Conferences **251**, 03046 (2021), doi:10.1051/epjconf/202125103046;

[135] B. Andersson *et al.*, Nucl. Phys. B **281**, 289 (1987), doi:10.1016/0550-3213(87)90257-4;

[136] B. Nilsson-Almqvist and E. Stenlund, Comput. Phys. Commun. **43**, 387 (1987), doi:10.1016/0010-4655(87)90056-7;

[137] H. W. Bertini, Phys. Rev. **131**, 1801 (1963), doi:10.1103/PhysRev.131.1801;

[138] H. W. Bertini, Phys. Rev. **188**, 1711 (1969), doi:10.1103/PhysRev.188.1711;

[139] H. W. Bertini, Nucl. Phys. A **169**, 670 (1971), doi:10.1016/0375-9474(71)90710-X;

[140] S. Dytman *et al.*, arXiv:0806.2119 (2008);

[141] L. Aliaga *et al.*, Nucl. Instrum. Meth. A **789**, 28 (2015), doi:10.1016/j.nima.2015.04.003;

[142] G. D. Megias *et al.*, Phys. Rev. D **94**, 093004 (2016), doi:10.1103/PhysRevD.94.093004;

[143] A. Bashyal *et al.* (MINERvA Collaboration), Phys. Rev. D **108**, 032018 (2023), doi:10.1103/PhysRevD.108.032018;

[144] L. Alvarez-Ruso *et al.*, Eur. Phys. J. Spec. Top. **230**, 4449–4467 (2021), doi:10.1140/epjs/s11734-021-00295-7;

[145] J. Tena-Vidal *et al.* (GENIE Collaboration), Phys. Rev. D **106**, 112001 (2022), doi:10.1103/PhysRevD.106.112001;

[146] Ch. Berger and L. M. Sehgal, Phys. Rev. D **76**, 113004 (2007), doi:10.1103/PhysRevD.76.113004;

[147] K. Kovařík *et al.*, Phys. Rev. D **93**, 085037 (2016), doi:10.1103/PhysRevD.93.085037;

[148] E. P. Segarra *et al.*, Phys. Rev. D **103**, 114015 (2021), doi:10.1103/PhysRevD.103.114015;

[149] R. Gran, Data Preservation at MINERvA, NuInt 2025 (2025).

[150] DUNE Collaboration. B. Abi *et al.*, *The DUNE Far Detector Interim Design Report Volume 1: Physics, Technology and Strategies*. ArXiv=1807.10334 (2018);

[151] D. Cardoso *et al.*, *Innovative proposal for N_2 capturing in Liquid Argon using the Li-FAU molecular Sieve*, in preparation to submission on the Journal of Instrumentation.

[152] R. Acciarri *et al.* Journal of Instrumentation **5**, P06003-P06003 (2010), doi:10.1088/1748-0221/5/06/P06003;

[153] R. Acciarri *et al.* Journal of Instrumentation **5**, P05003-P05003 (2010), doi:10.1088/1748-0221/5/05/P05003;

[154] Technical Note CRYOFRABR004/2021, *A cryostat for liquid argon purification.* url=https://edms.cern.ch/ui/#!master/navigator/document?D:101077088:101077088:subDocs;

[155] Technical Note CRYOFRABR003/2021, *Determination of nitrogen physisorption properties by zeolites for argon purification*. url=https://edms.cern.ch/ui/#!master/navigator/document?D:101081172:101081172:subDocs;

[156] Technical Note CRYOFRABR007/2021, *Activated-copper-coated alumina granules synthesis*. url=https://edms.cern.ch/ui/#!master/navigator/document?D:101081173:101081173:subDocs;

[157] Technical Note CRYOFRABR008/2021, *Effects of zeolite particle size on Nitrogen Adsorption Isotherms*. url=https://edms.cern.ch/ui/#!master/navigator/document?D:101081178:101081178:subDocs;

[158] Technical Note CRYOFRABR009/2021, *Nitrogen Adsorption Modeling*. url=https://edms.cern.ch/ui/#!master/navigator/document?D:101077087:101077087:subDocs;